



HAL
open science

Earthquake-induced soil liquefaction under drained conditions

Shahar Ben-Zeev

► **To cite this version:**

Shahar Ben-Zeev. Earthquake-induced soil liquefaction under drained conditions. Earth Sciences. Université de Strasbourg; Hebrew University (Jérusalem), 2023. English. NNT : 2023STRAH011 . tel-04648092

HAL Id: tel-04648092

<https://theses.hal.science/tel-04648092>

Submitted on 15 Jul 2024

HAL is a multi-disciplinary open access archive for the deposit and dissemination of scientific research documents, whether they are published or not. The documents may come from teaching and research institutions in France or abroad, or from public or private research centers.

L'archive ouverte pluridisciplinaire **HAL**, est destinée au dépôt et à la diffusion de documents scientifiques de niveau recherche, publiés ou non, émanant des établissements d'enseignement et de recherche français ou étrangers, des laboratoires publics ou privés.

ÉCOLE DOCTORALE 413 - Sciences de la Terre et de l'Environnement

L'Institut Terre et Environnement de Strasbourg (ITES) (UMR7063)

THÈSE présentée par :

Shahar BEN-ZEEV

soutenue le : 17 avril 2023

pour obtenir le grade de : **Docteur de l'université de Strasbourg**

Discipline/ Spécialité : Géophysique

**Liquéfaction du sol induite par tremblement
de terre dans des conditions drainées**

THÈSE dirigée par :

M. TOUSSAINT Renaud
Mme. AHARONOV Einat
Mme. GOREN Liran

Directeur de recherche CNRS, université de Strasbourg
Professeur, université Hébraïque de Jérusalem
Professeur, université Ben-Gourion du Néguev

RAPPORTEURS :

M. EINAV Itai
M. FLEKKØY Eirik G.

Professeur, université de Sydney
Professeur, université d'Oslo

AUTRES MEMBRES DU JURY :

M. MANGA Michael
M. SALAMON Amos

Professeur, UC Berkeley
Dr., Commission géologique d'Israël

Earthquake-induced soil liquefaction under drained conditions

Thesis for the degree of "Doctor of Philosophy"

By

Shahar Ben-Zeev

Submitted to

the Senate of the Hebrew University of Jerusalem

and to

Université de Strasbourg

December 2022

Earthquake-induced soil liquefaction under drained conditions

Thesis for the degree of "Doctor of Philosophy"

By

Shahar Ben-Zeev

Submitted to

the Senate of the Hebrew University of Jerusalem

and to

Université de Strasbourg

December 2022

**This work was carried out under the
supervision of:**

Prof. Einat Aharonov

Prof. Liran Goren

Prof. Renaud Toussaint

Acknowledgements

”Panta rhei” (Heraclitus), everything flows, including soils.

First and foremost, I express my deepest gratitude to my advisors Einat Aharonov, Liran Goren, and Renaud Toussaint, for their patient guidance and the long hours spent on discussions. Their enthusiasm and curiosity inspired my journey.

I thank Dr. Stanislav Perez, who guided me and helped me at the beginning of my journey into the world of numerical modeling, specifically the coupled discrete elements and fluid code.

I am grateful for the doctoral advisory committee members: DR-CNRS Valérie Vidal and Prof. Yossi Hatzor, who gave much good advice and encouragement and helped me sharpen my scientific message. I thank Prof. Amotz Agnon, who joined Prof. Yossi Hatzor in evaluating my progression lecture at The Hebrew University of Jerusalem.

I thank Prof. Assaf Klar and Dr. Eithan Cohen from the Technion, for a fruitful discussion.

I acknowledge the financial support of Campus France as a ”Chateaubriand Fellow” via the Institut français d’Israël. Special thanks to Mrs. Daphna Leibowitz for her dedicated work regarding the fellowship.

I thank the administrative and technical staff of the Institute of Earth Sciences at The Hebrew University of Jerusalem: Maguiy Perkin, Sandara Kaplan, Batya Zaken, Keren Mimran, Keren Shoshana, Shani Israelowitz, Yossi Shrer, Adam Levi and Helena Kirmayer. Each has helped me in his field of expertise at some point during my Ph.D. track.

On the other side of the Mediterranean Sea, I am in great debt to the personnel of ITES (formerly IPGS): Binta Mosmaqe and Dilek Kiryegat for their administrative help. Alain Steyer, Miloud Talib, and Martine Trautman greatly assisted with the experiments, and I am grateful for that.

The joint Ph.D. imposed administrative and academic challenges. I express a special thanks to the many people who helped solve those challenges: The personnel of the Research Students Authority of the Hebrew University of Jerusalem (Prof. Zach Adam, Netta Weiss, Galit Chen, Sharon Haliva, Veronica Golsberg), and the excellent people from the University of Strasbourg (Jerome van der Wored, Hanna Eriksson, and the staff of the Collège doctoral, Maurice Tripad, Fayza Fallah and Ali Amir).

It was a pleasure to work, eat, chat or drink (coffee or beer) with my lab mates, friends, research and teaching colleagues: Mathilde Desrues, Myriam Lajaunie, Tom Vincint-Dospital, Laciél Alonso, Monem Ayaz, Anner Paldor, Itzik Hamdani, Yoni Israeli, Yevgeny Kreisserman, Amit Meltzer, May Laor, Yechiel Ben-Zeev, Elchanan Zucker, Natalie Neagu, Jonathan Keinan, Nadav Kedem, Pritom Sarma, Osnat Barnea, Yaniv Darvasi, Itamar Yaacobi, Rawi Dawood, Shalev Siman-Tov, and Zohar Katzin.

Lastly, my dear family: Renana, Gili, and Hallel. Words cannot express my gratitude for carrying the burden with me.

”It is not for you to complete the work, but neither you are free to desist from it.”

(Mishnah, Avot 2, 16)

Abstract

Earthquake-induced soil-liquefaction is a common and devastating phenomenon, which causes casualties, economic losses, and destruction of lifelines. During liquefaction, earthquake-shaking induces loss of soil rigidity, producing liquid-like behavior and a sudden loss of soils ability to support infrastructure load, leading to failure of structures such as buildings and bridges. Liquefaction can also be recognized in the geological record as soft sediment deformation. The classical mechanism used to explain this phenomenon assumes an undrained response, i.e., that during earthquake shaking, fluid-filled pores in the soil tend to collapse and reduce volume so quickly that fluid cannot escape, resulting in a pore pressure increase. The overburden load is transmitted from the grain contacts to the interstitial fluid, which cannot support shear; hence, the soil layer liquefies and fails. Recent studies have questioned whether the undrained response is the sole mechanism that can lead to soil liquefaction. Particularly, the undrained hypothesis fails to explain observations of liquefaction beyond the earthquake near-field, where the seismic energy density is low, and recurrent liquefaction events. The undrained model further struggles to explain observations of co-seismic fluid expulsion from the subsurface, and co-seismic soil settlement produced in the lab.

This work utilizes a physics-based formulation of pore pressure evolution in a deforming granular layer, numerical simulations and shaking table experiments to show that pore fluid pressurization can be achieved via a drained end member in addition to the known undrained end member. The term "drained" is adopted in this study to describe the end member in which the time scale of pore pressure dissipation is much shorter than the time scale of forcing. The dissertation shows that fluid flow relative to the soil grains is immanent under drained conditions. The flow is accompanied by excess pore pressure gradients and pore pressure values that liquefy the soil. The dynamics of drained liquefaction are controlled by an upward-moving compaction (solidification) front, which separates a compacted non-liquefied sub-layer at the bottom from a settling-liquefied sub-layer at the top. The compaction front travels upward at a velocity dictated by the rate by which the seismic energy density

(the seismic power) is imposed. The duration of the drained liquefaction event and the accompanying process of soil compaction are found to be controlled mainly by the relations between the seismic power, the front velocity, the layer's thickness, and the soil characteristic permeability.

Drained liquefaction is further found to occur even at very low seismic energy, providing an explanation for previously puzzling liquefaction events beyond the earthquake near-field. The unique interplay between the amount of compaction and the imposed power during an earthquake can also explain previously enigmatic recurrent liquefaction events, that occur despite the expected natural remediation against reliquefaction.

The practical implications of this study are that well-drained (e.g., high permeability) soils, sites which are not expected to experience large shaking intensity, and soils that were liquefied in the past, should not be a-priori assumed liquefaction resistant.

Résumé

La liquéfaction des sols induite par les tremblements de terre est un phénomène courant et dévastateur, qui cause de graves pertes économiques et des victimes. Au cours de la liquéfaction, les secousses sismiques provoquent une perte de rigidité du sol, produisant un comportement de type liquide et une perte soudaine de la capacité du sol à supporter la charge des infrastructures, entraînant la défaillance de structures telles que des bâtiments et des ponts. La liquéfaction peut également être reconnue dans les archives géologiques comme une déformation des sédiments mous. Le mécanisme classique utilisé pour expliquer ce phénomène suppose une réponse non drainée, c'est-à-dire que pendant les secousses sismiques, les pores remplis de fluide dans le sol ont tendance à s'effondrer et à réduire leur volume si rapidement que le fluide ne peut pas s'échapper, ce qui entraîne une augmentation de la pression interstitielle. Le poids des couches supérieures transmise des contacts de grain au fluide interstitiel, qui ne peut pas supporter le cisaillement ; par conséquent, la couche de sol se liquéfie et échoue. Des études récentes ont remis en question si la réponse non drainée est le seul mécanisme qui peut conduire à la liquéfaction du sol. En particulier, l'hypothèse non drainée ne parvient pas à expliquer les observations de liquéfaction au-delà du champ proche du tremblement de terre où la densité d'énergie sismique est faible, et les événements de liquéfaction récurrents. Le modèle non drainé a en outre du mal à expliquer les observations d'expulsion de fluide co-sismique du sous-sol, le tassement co-sismique du sol produit en laboratoire et les formulations théoriques qui permettent la pressurisation dans des conditions drainées.

Ce travail utilise une formulation basée sur la physique de l'évolution de la pression interstitielle dans une couche granulaire déformable, des simulations numériques et des expériences de table vibrante pour montrer que la pressurisation du fluide interstitiel peut être obtenue via un cas extrême drainé en plus du cas extrême non drainé connu. La thèse montre que l'écoulement des fluides par rapport aux grains du sol est inhérent en conditions drainées. L'écoulement s'accompagne de gradients de surpression interstitielle et de

valeurs de pression interstitielle qui liquéfient le sol. La dynamique de liquéfaction drainée est contrôlée par un front de compaction (solidification) ascendant, qui sépare une sous-couche compactée non liquéfiée en bas d'une sous-couche liquéfiée (en décantation) en haut. Le front de compaction se déplace vers le haut à une vitesse dictée par la vitesse à laquelle la densité d'énergie sismique est imposée (la puissance sismique). La durée de l'événement de liquéfaction drainée et le processus de compaction du sol qui l'accompagne sont contrôlés principalement par les relations entre la puissance sismique, la vitesse du front, l'épaisseur de la couche et la perméabilité caractéristique du sol.

La liquéfaction drainée s'avère en outre se produire même à une énergie sismique très faible, fournissant une explication aux événements de liquéfaction précédemment déroutants au-delà du champ proche du tremblement de terre. L'interaction unique entre la quantité de compaction et la puissance imposée lors d'un tremblement de terre peut également expliquer des événements de liquéfaction récurrents auparavant énigmatiques, qui se produisent malgré la remédiation naturelle attendue contre la reliquéfaction.

A letter of contribution

This doctoral dissertation consists of three research chapters (as well as an introduction, a concluding chapter, and an appendix).

I (Shahar Ben-Zeev) am the main scientific contributor to every one of the chapters. All the analyses, interpretation, simulations, processing, visualizations and writing were conducted by me (in collaboration with my advisors and our co-author). As so, I am the first author of every one of the chapters included in this work. My advisors helped me with interpretation of the results, with fruitful discussions, with research planning and with the writing.

Dr. Stanislav Parez helped with code modifications, and contributed to the writing of Chapter 1 (Compaction front and pore fluid pressurization in horizontally shaken drained granular layers).

Contents

Acknowledgements	v
Abstract	vii
Résumé	ix
A letter of contribution	x
Introduction	1
0.1 Liquefaction initiation under undrained conditions	4
0.2 Liquefaction initiation under drained conditions	5
0.3 Earthquake ground motion parameters controlling liquefaction initiation . .	9
0.3.1 Implications of the seismic energy approach for liquefaction beyond the earthquake near field	11
0.4 Recurrent liquefaction	13
0.5 Research goals and questions	14
0.6 Methods	14
0.6.1 Numerical Simulations	14
0.6.2 Shaking table experiments	17
0.7 Dissertation overview	18
1 Compaction front and pore fluid pressurization in horizontally shaken	

drained granular layers	19
2 Drainage explains soil liquefaction beyond the earthquake near-field	46
3 Recurrent soil liquefaction under drained conditions	85
Discussion, future perspectives, and conclusions	113
Appendix A The Combined Effect of Buoyancy and Excess Pore Pressure in Facilitating Soil Liquefaction	123
Bibliography	134

Introduction

Earthquake-induced soil liquefaction is one of the major earthquake-induced secondary natural hazards, along with tsunamis, landslides and fire (Marano et al., 2010). During liquefaction, soils that exhibited load-supporting elasto-plastic rheology, lose their shear strength and stiffness and behave in a fluid-like manner, that cannot support load anymore (Kramer, 1996; National Academies of Sciences Engineering and Medicine, 2016). Soil liquefaction can result in (Fig. 1) buildings and infrastructures sinking (Ishihara et al., 2011), floating and tilting (Ishihara et al., 2011), ground lateral spreading (Ishihara et al., 2011), settlement (Bray et al., 2014), and landsliding (Bradley et al., 2019). Liquefaction damage often leads to extensive human casualties (Gautam et al., 2017; Bradley et al., 2019), destruction of lifelines (Ishihara et al., 2011; Cubrinovski et al., 2012a), and economic losses (Cubrinovski et al., 2012a; Cox et al., 2012; National Academies of Sciences Engineering and Medicine, 2016; Wood et al., 2016), outcomes that can result in complete abandonment of formerly inhabited areas (Cox et al., 2012), posing a significant challenge to community resilience (Jones et al., 2021). Liquefaction-induced soft sediment deformations in the geological record play a significant role in earthquake science (Obermeier, 1996; Tuttle et al., 2019), as they are regarded as rare markers of paleoseismicity, from which site ground-motion parameters can be deduced (ground motion can be deduced also from landslides, but those are not uniquely related to seismic events) (Rasanen et al., 2021).

Two components are generally considered necessary for soil liquefaction triggering: a soil that is susceptible to liquefaction and a seismic forcing that triggers it. To evaluate the soil



Figure 1: Liquefaction manifestations and damage. (a) floating of sewage manhole in Urayasu Japan; 2011 Great east Japan earthquake (photo from (Ishihara et al., 2011)) . (b) tilted buildings in Niigata, Japan; 1964 Niigata earthquake (photo from Wikipedia). (c) Sand blows (water escape features) in Christchurch, New Zealand; Canterbury earthquake sequence 2010-2011 (photo from (Quigley et al., 2013)). (d) Ground settlement in Kamisu, Japan; 2011 Great east Japan earthquake (photo from (Oregon State University, 2011)). (e) ground lateral spreading in the Christchurch area, New Zealand; 2010 Darfield earthquake (photo from (Cubrinovski et al., 2012b)). (f) a completely abandoned neighborhood, 11 years after the 2011 liquefaction event (Avonside, Christchurch New Zealand; Photos: Google Earth). (g) before and after a liquefaction event that initiated massive gentle-slope landslides in September 2018 in Palu, Indonesia (Photos: Google Earth).

susceptibility to liquefaction, the main parameters to be considered are soil density (de Alba et al., 1976), soil type and composition (Andrews and Martin, 2000), initial shear stress (e.g., on sloping ground and in the proximity to structural load; National Academies of Sciences Engineering and Medicine, 2016), age (Youd and Hoose, 1977; Schmertmann, 1991; Olson et al., 2001, 2005), hydraulic conditions ((Cox et al., 2012)), and the geological-geometrical setup such as the depositional environment, layering and depth ((Youd and Hoose, 1977; Youd and Perkins, 1978; Beyzaei et al., 2018)). It is important to note that many of these properties are not evaluated as part of the common geotechnical practice. Instead, they are replaced by in-situ profiles of proxies that are more cost-and-time-effective, such as SPT (standard penetration test), CPT (cone penetration test) and shear wave velocity (National Academies of Sciences Engineering and Medicine, 2016). To evaluate the ground motion required to trigger liquefaction, the main parameters to be considered are shaking intensity as measured for example via ground displacement, velocity and acceleration (expressed by their peak value, PGD, PGV, PGA or other representative value such as the root mean square of the respective waveform), the spectral composition of the shaking waveform (Kostadinov and Towhata, 2002; Wong and Wang, 2007), and strong shaking duration (Youd et al., 2001; Greenfield, 2017), all of which are derivatives of the earthquake epicenter location (or distance from a site), the earthquake magnitude and the seismic velocities in the wave pathway (velocity model).

Overall, liquefaction hazard is at its peak with the combination of an active seismic region and a soil that is shallowly buried, loose, young (especially man-made fill and reclaimed land), granular non-plastic (sands, gravel, some silts) and saturated (riverbanks, coastlines, irrigated areas).

Reclaimed lands deserve a special attention as they are young and commonly fully saturated due to high ground water level, and hence are at great risk for soil liquefaction. The massive liquefaction that occurred in Kobe port (Japan), following the $M_w = 6.9$ Kobe earthquake in 1995 (Yamashita et al., 2004), is a prime example of liquefaction under such

conditions. The port was built on reclaimed land and despite extensive soil improvement, extensive liquefaction occurred (Soga, 1998), causing many casualties and a total shutdown of the port facilities creating a large economic loss.

Global urbanization processes drive mega-cities to rise in number and size, and since many of them are coastal, it is expected that the use of reclaimed land will become more prevalent at a global scale (Sengupta et al., 2018). This has the potential to increase the size of the population and the number of infrastructures placed at risk from soil liquefaction hazard.

0.1 Liquefaction initiation under undrained conditions

Since the conception of soil liquefaction studies, mainly after the Good Friday earthquake in 1964 (Alaska) and Niigata earthquake in 1964 (Japan) (Kramer, 1996), liquefaction has been considered as an undrained phenomenon (Martin et al., 1975). Granular materials in general, and soils specifically, tend to reduce their volume under cyclic shear. This is true even for dense soils that will dilate under monotonic shearing (Sawicki and Mierczynski, 2006). If the cyclically sheared soil is saturated, it is assumed that drainage is unable to occur during the time span of the loading sequence, hence, the tendency for volume reduction results in an increase in the pore fluid pressure (Martin et al., 1975). Once the pore pressure is elevated to the solid stress values, the grains lose their stress-transmitting contacts and the load is carried solely by the fluid (zero effective stress), that cannot support shear, i.e., has no shear strength. This mechanistic view led to extensive "soil element tests", commonly using jacketed samples to ensure undrained conditions. Those undrained tests form the basis for the common understanding of soil liquefaction initiation (Adamidis and Madabhushi, 2018).

A typical behavior of liquefiable soil subjected to harmonic undrained loading in cyclic simple shear test is presented in Fig. 2 (numbered red markers indicate the number of cycle). The test starts with no excess pore pressure (rightmost end of panels b&d). During the first

~ 22 cycles, the soil is stiff (high shear modulus) with steep shear stress-strain curve (panel a), minimal strain (panel c) and with pore pressure that increases (and effective normal stress decreases) incrementally in each cycle (panels b&d), while the shear stress amplitude is high (panels a&b). After ~ 22 cycles the soil reaches the "phase transformation line" (panel b), the shear strain becomes larger (panel c) and the stiffness is decreased steadily in every cycle (panel a) until the soil reaches the failure envelope (panel b), the pore pressure becomes close or equal to the vertical normal stress and the soil is liquefied (panel b&d).

"Cyclic resistance curves" (Fig. 3) from undrained laboratory test (de Alba et al., 1976) shows that the number of cycles required to initiate undrained soil liquefaction (proportional to the time elapsed from the onset of shaking, assuming one dominant frequency), depends on the amplitude of the applied shear stress (normalized by the initial effective normal stress) and the initial relative density of the soil (see Fig. 3). It is evident that under most scenarios, at least several shear cycles are needed to initiate undrained liquefaction in loose soils that experience large shear stresses. Smaller shear stress and denser soil will require many cycles until undrained liquefaction is initiated.

0.2 Liquefaction initiation under drained conditions

Goren et al. (2010, 2011) formulated from basic physics a pore-pressure diffusion equation in deforming granular material:

$$\frac{\partial P'}{\partial t} - \frac{1}{\beta_f \eta \phi} \nabla \cdot [\kappa \nabla P'] + \frac{1}{\beta_f \phi} \nabla \cdot u_s = 0, \quad (1)$$

where P' is the dynamic pore pressure deviation from hydrostatic value ($P' = P - P_{hyd}$), β_f and η are the fluid compressibility and viscosity, respectively, κ is the permeability, t is time and ∇ is a spatial derivative. The third term in eq. (1) describes the internal source for dynamic pore pressure, due to divergence of solid grain velocities (u_s). This term can be approximated (Goren et al., 2011) as the compaction and dilation rate of the pore space,

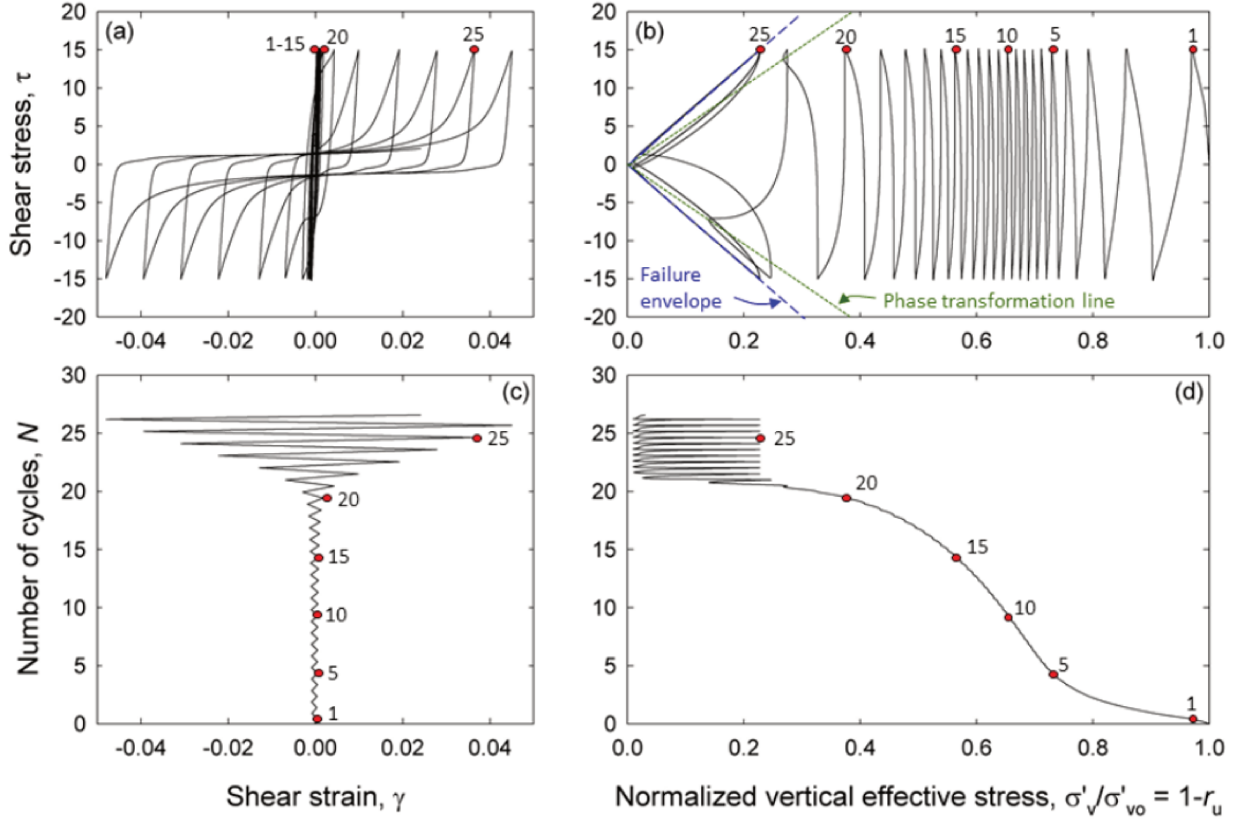


Figure 2: A typical behavior of liquefiable soil under cyclic loading. (a) Shear stress-strain hysteresis curve. The shear modulus of the soil (the average slope during one cycle) is degraded after ~ 22 cycles (numbered red markers indicate cycle number), i.e., the strains are large even under low shear stress. (b) Shear stress vs. the vertical effective stress normalized by its initial value. The origin of the horizontal axis represents pore pressure that is equal to the initial vertical stress. (c) Number of cycles vs. the shear strain. The strain was almost constant during the first ~ 22 cycles, than it increased rapidly due to liquefaction initiation. (d) Number of cycles vs. the vertical effective stress normalized by its initial value. Figure from National Academies of Sciences Engineering and Medicine (2016)

i.e., $\nabla \cdot u_s \simeq (1/(1 - \phi))(\partial\phi/\partial t)$, where ϕ is the porosity.

By carefully choosing scale factors for eq. (1), the authors identified an emergent non-dimensional number called the Deborah number (De (Reiner, 1964)), that serves as metric for drainage conditions:

$$\text{De} = \frac{t_d}{t_0}. \quad (2)$$

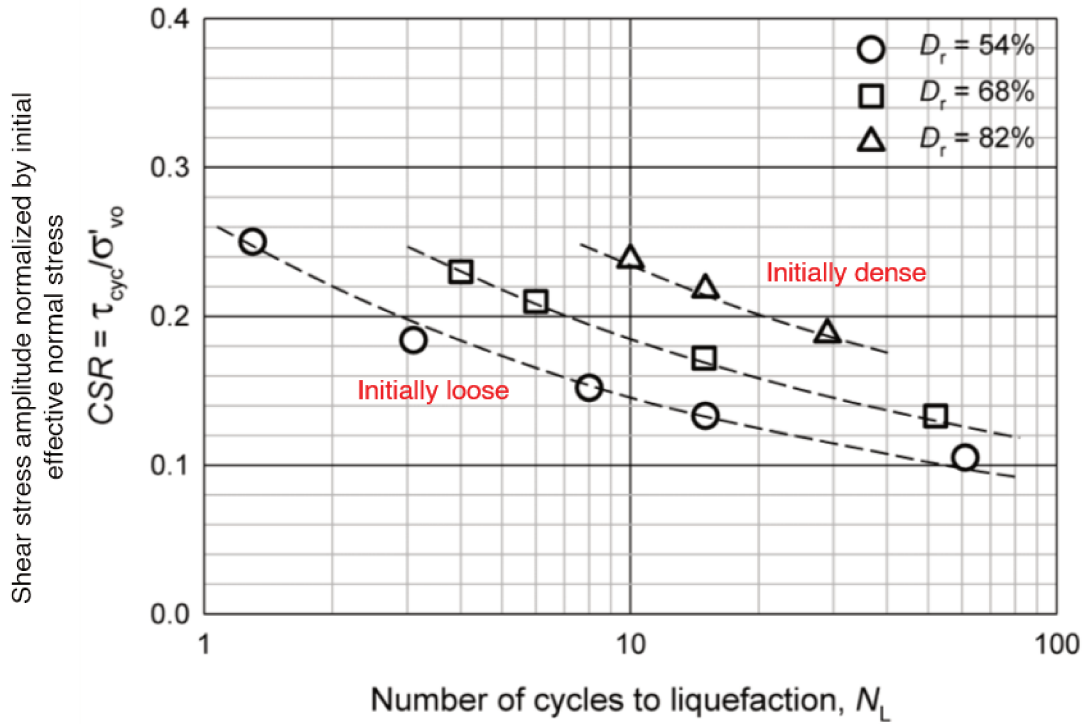


Figure 3: "Cyclic Resistance Curve", i.e., the number of shear cycles required to initiate liquefaction in a given cyclic shear stress and initial relative density (low D_r means loose sand), under undrained conditions. Loose soil and large cyclic shear stress are the optimal conditions for undrained liquefaction initiation. In most scenarios, more than a few shear cycles are required to initiate liquefaction. Modified from de Alba et al. (1976); National Academies of Sciences Engineering and Medicine (2016)

In this context, the De number is the ratio between the pore pressure diffusion time scale (t_d) and the time scale of deformation (t_0). Goren et al. (2010, 2011) further showed that for the undrained end member (when $De \gg 1$ and the second term in eq. (1) can be neglected) the solution of eq. (1) relates the change in pressure to the change in pore volume, and the fluid compressibility plays a major role (Fig. 4a). On the other hand, in the drained end member (when $De \ll 1$ and the first term in eq. (1) can be neglected), the pore pressure is related to the rate of compaction of the granular media (Fig. 4b). This highlights the possibility of pressure and pressure gradients generation due to fast changes in pore volume that promote fluid flow under drained conditions.

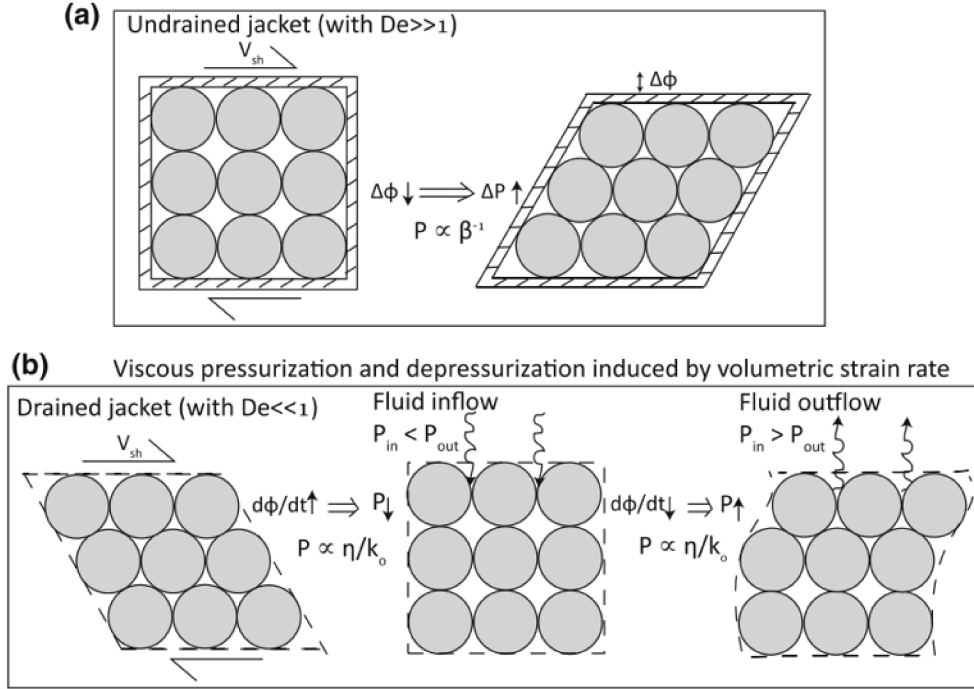


Figure 4: Conceptual demonstration of the two end members of pore pressure change in deforming granular media. (a) Under undrained conditions with $De \gg 1$, the pore pressure change is proportional to the volumetric strain (the change in porosity, $\Delta\phi$) and the fluid compressibility (β_f). (b) Under drained conditions with $De \ll 1$, the pore pressure change is proportional to the instantaneous volumetric strain rate (the compaction rate $d\phi/dt$) and is related to the viscous flow parameters viscosity (η) and skeleton permeability (κ). Figure from Goren et al. (2011)

Lakeland et al. (2014) reached similar conclusions regarding the role of fluid flow and grain rearrangement in liquefaction, and pointed out that fluid flow during liquefaction is expected to occur even across thin regions of low-permeability soil (that naively should prevent fluid flow).

The development of centrifuge tests allowed the observations of fluid migration and water film generation during liquefaction (Fiegel and Kutter, 1994; Kokusho and Kojima, 2002), but those observations were explained locally, without questioning the undrained assumption in general.

Madabhushi and Haigh (2012) in a paper titled "How well do we understand earthquake induced liquefaction?", pointed out that co-seismic soil settlement observed in centrifuge

tests *”is only possible if the liquefied soil is not behaving in an undrained fashion”*. This conclusion is based on simple mass conservation. If the soil layer settles, the fluid must drain out of the pores to accommodate it.

Beyond the scientific discussion regarding the undrained assumption, testimonies exist for drained liquefaction in the field. A relatively rare filmed testimony (Kooi, 2011) captured fluid seeping at the ground while the earth is still shaking at the *”Makuhari Seaside Park”* in Chiba (Japan), during the $M_w = 9.0 - 9.1$ Tohoku earthquake (2011, also known as the Great East Japan Earthquake) (Konagai et al., 2013). If not strict evidence, this at least raises doubts regarding the validity of the undrained assumption and the possibility that liquefaction could also initiate under well-drained conditions.

0.3 Earthquake ground motion parameters controlling liquefaction initiation

Liquefaction susceptibility evaluation is a common procedure in areas that are prone to earthquakes. Specifically, in sites that are pre-screened as requiring detailed evaluation (e.g, after eliminating sites with bedrock exposure or deep groundwater table). The common geotechnical engineering practice utilizes the concept of the *”factor of safety”* (FS), which is the ratio between the expected seismic loading to the seismic resistance of a specific examined site and depth (Kramer, 1996). When $FS < 1$ liquefaction triggering is expected under the examined seismic loading. When $FS > 1$ liquefaction is not expected.

The most popular scheme for liquefaction susceptibility evaluation is the *”simplified procedure for evaluating soil liquefaction potential”* (Seed and Idriss, 1971; Youd et al., 2001). In this scheme, the expected horizontal peak ground acceleration (PGA), and a factor that represents the expected strong motion duration (MSF), are taken into account in the factor of safety. This echoes the expectation (derived from undrained soil element experiments, Fig. 3) that both the number of shear cycles and the shear stress control the

initiation of liquefaction (de Alba et al., 1976; National Academies of Sciences Engineering and Medicine, 2016). The PGA, which is proportional to the maximum transient shear stress during shaking (from simple mechanics, mass times acceleration equals the sum of forces), is also set as a threshold in building codes (e.g., Eurocode 8, 2004), so that if PGA is below this threshold, no further geotechnical examination is needed. Yet, de Magistris et al. (2013, 2014) found that many liquefaction events occur below the stated threshold, with critical implications for infrastructure built where ground motion is expected to be smaller than the code defined threshold. Interestingly, this includes the famous 1964 Niigata earthquake, mentioned above as one of the major events that instigated liquefaction studies. This hints to the possibility that the PGA may be only one of several ground motion parameters controlling a liquefaction threshold.

Dobry et al. (1982) suggested that the shear strain is the controlling parameter on liquefaction initiation, following identification of a threshold strain for sufficient pressurization in strain-controlled tests (Dobry et al., 1982) and field measurements (Dobry and Abdoun, 2015). It is noted that this approach has an advantage over the stress (PGA) approach, in that the shear strain is mechanically closer to the volumetric strain associated with pore space compaction than the shear stress. Yet, this is only relevant under the undrained assumption, where the pressurization is expected to be proportional to the volumetric strain (Goren et al., 2010, 2011).

Several studies (Nemat-Nasser and Shokooh, 1979; Berrill and Davis, 1985; Law et al., 1990; Figueroa et al., 1994; Liang et al., 1995; Green and Mitchell, 2004; Dief and Figueroa, 2007; Jafarian et al., 2014) have suggested that the seismic energy (or the dissipated energy) is the controlling parameter on liquefaction initiation. The energy approach has the advantages of being able to accommodate nonuniform loading such as earthquake loading (Figueroa et al., 1994), at least in its cumulative form, and is measurable in the field (Wang and Manga, 2021) while the strain and even the stress are only approximated.

Arias intensity, which is defined as the time integral of the squared ground acceleration

over the duration of ground shaking ($I_A = (\pi/2g) \int_0^{T_d} a(t)^2 dt$), can be interpreted as a cumulative energy measure. As other cumulative energy measures, it depends on the amplitude, frequency content, and duration of the earthquake ground motion, and hence represents a more holistic metric than the single values metrics as PGA or PGV. For this property, Arias intensity has also been suggested as the controlling ground motion parameter in liquefaction evaluation (Kayen and Mitchell, 1997; Green and Mitchell, 2003).

0.3.1 Implications of the seismic energy approach for liquefaction beyond the earthquake near field

Wang (2007) (updated in Wang and Manga (2021)) compared ~ 240 naturally occurring liquefaction events with the seismic energy density that induced the events. To do this, they combined an analytical formulation (Lay and Wallace, 1995) relating the seismic energy density to the squared peak ground velocity ($e = \rho/4 \text{ PGV}^2$), with empirical laws and case history database of liquefaction events, triggered under a variety of earthquake magnitudes and distances from the source. The result of the analysis is depicted in Fig. 5. The figure shows the distance of each recorded liquefaction event from the earthquake epicenter that produced it, vs. the earthquake magnitude. The contours of the seismic energy density are plotted as sloping black lines, showing that the seismic energy density decays away from the earthquake. This presentation shows that liquefaction has not been observed in the field below a minimum seismic energy of 0.1 J m^{-3} .

Wang (2007) further reports an experimentally observed minimum energetic threshold to trigger liquefaction by undrained consolidation of 30 J m^{-3} (Green, 2001; Green and Mitchell, 2004), which roughly coincides with the border of the earthquake near-field (hypocentral distance of one ruptured fault length, red sloped line in Fig. 5). Yet, in contrast to this prediction, many of the liquefaction events in his compilation (Fig. 5) were triggered by an energy density, which is smaller by orders of magnitude with respect to the energetic threshold, and beyond the earthquake near field (e.g., at a hypocentral distance greater than ~ 10

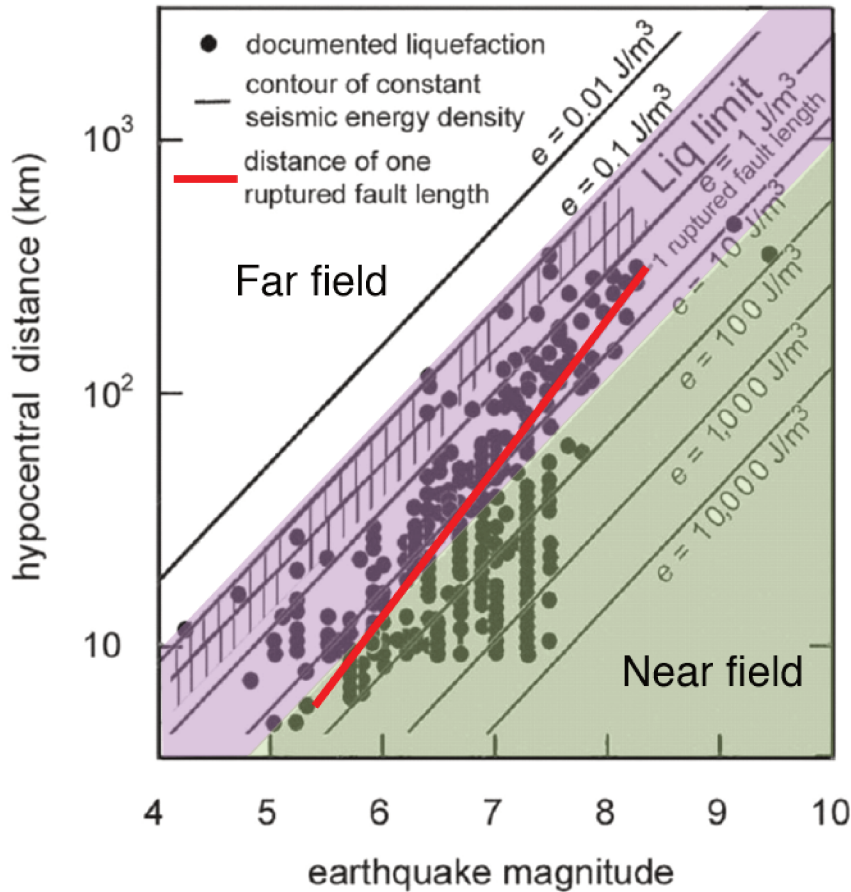


Figure 5: Field liquefaction events, as a function of the magnitude and hypocentral distance of the earthquakes that triggered them. Sloped lines are contours of seismic energy density. Red line marks the border of the near field. Only about 40% of the recorded liquefaction events (green area) were triggered by an energy density that exceeded the empiric minimum energetic threshold for undrained liquefaction (Green, 2001), yet about 60% of the events occurred below the minimum energetic threshold (purple area), and are thus unexplained by undrained liquefaction. Modified from Wang (2007).

kilometers in $M = 6$ earthquake, or greater than ~ 100 kilometers in $M = 8$ earthquake). To solve this discrepancy, the author and others (Wang, 2007; Wang and Manga, 2011; Manga et al., 2012; M. Manga and C.-Y. Wang, 2015) suggested that seismically-enhanced-permeability allows an efficient flow path between deep pressurized aquifers, and the surface soil layers. Fluid release and upward fluid flow is expected to aid soil layers to liquefy under smaller energy density than expected by the conventional view. Cox et al. (2012) examined

the hydrological response of the Christchurch region after the Darfield (2010) earthquake, and postulated that artesian release from pressurized aquifers was a key mechanism for the extensive liquefaction event that occurred in the Christchurch region.

Still, dynamic permeability increase and the availability of buried pressure sources represent unique hydrological settings, and a general mechanism to explain liquefaction beyond the near field is still missing.

0.4 Recurrent liquefaction

Liquefaction often occurs repeatedly at the same site (Obermeier, 1996). In the field, it is common to observe soils that were liquefied more than once in a mainshock-aftershocks sequence, as in Watsonville, California (Sims and Garvin, 1995), following the 1989 Loma Prieta earthquakes sequence, and in Christchurch, New Zealand (Quigley et al., 2013), following the 2010-2011 Canterbury earthquake sequence.

It is well established from undrained tests (de Alba et al., 1976) that the relative density of the soil is a key factor in its liquefaction potential, where a loose soil (low relative density) is more susceptible to liquefaction than densely packed soil (see Fig. 3). On the other hand, soils have been shown to densify during and after liquefaction (Obermeier, 1996; Ha et al., 2011), which is expected to reduce their susceptibility to liquefy again. This is an apparent paradox, since liquefaction is expected to be less probable in already liquefied soils, yet it tends to reoccur at the same sites.

Many soil remediation techniques aim to increase the density of the soil as a countermeasure against liquefaction (Besharat, 2012). In that sense, liquefaction of pre-improved soils (e.g., Wotherspoon et al., 2014) is very similar to natural reliquefaction, i.e., they both pose the same problem of liquefaction of soil that was already compacted.

0.5 Research goals and questions

The aim of this dissertation is to show that in contrast to the previous prevailing hypothesis, soil liquefaction can be initiated under drained conditions, and that this new end-member liquefaction process can be invoked to explain puzzling field observations. The following research questions are specifically addressed:

1. Can liquefaction occur under drained conditions? And what is this drained mechanism?
2. What are the controlling dynamics and parameters of drained liquefaction and how do they differ from the dynamics of undrained liquefaction?
3. Can drained liquefaction explain observed, but previously unexplained, intermediate-field and far-field liquefaction cases?
4. Can drained liquefaction explain observed, previously enigmatic, recurrent liquefaction events and define the conditions that favor reliquefaction?

0.6 Methods

To simulate a saturated soil layer that is horizontally shaken by an earthquake, I conduct numerical simulations and shaking table experiments. Here I provide a short overview of the methods. More detailed information is provided in the following chapters. Specifically, the numerical method is detailed in the methods section of Chapter 1 and the experimental method, in the methods section of Chapter 2.

0.6.1 Numerical Simulations

The numerical approach is based on a two-phase coupled model (Fig. 6a). The grains are modeled using the discrete element method (Cundall and Strack, 1979), and the interstitial pore fluid is modeled as a continuum on a superimposed Eulerian grid (McNamara et al.,

2000; Johnsen et al., 2006; Vinningland et al., 2007a,b; Niebling et al., 2010a,b; Goren et al., 2011).

In the discrete element method (Cundall and Strack, 1979), each grain is modeled as a sphere, which experiences the forces of gravity, buoyancy (static pressure gradient force), contact forces from neighboring grains, and the drag force exerted by the seepage of the fluid (dynamic pressure gradient force, interpolated from the nearest grid nodes). The linear and rotational momentum conservation equations are solved for each grain in every time step, yielding its' velocity and displacement.

The fluid solver solves the pressure diffusion equation (eq. (1)) on a 2D grid, where the porosity, grain size and velocities are interpolated into the grid (also allowing the calculation of the local permeability).

The geometry of the numerical layer (Fig. 6b) is a Hele-Shaw cell comprising spherical grains with grain radii between 0.8 – 1.2 cm, drawn from a normal distribution with a mean of 1 cm and a standard deviation of 1 cm. The bottom wall of the numerical layer, which is impermeable for the fluid flow, is made of half grains glued together and is cyclically displaced with an harmonic function ($A \sin(\omega t)$ or $A[1 - \cos(\omega t)]$), with a predetermined amplitude (A) and frequency ($\omega = 2\pi f$). The top boundary is a free surface. No normal or shear stresses are applied on the grains. No non-zero pressure or pressure gradient are applied on the fluid. The layer is periodic in the horizontal direction, making it virtually infinite long in that dimension.

The advantage of this coupled numerical scheme in soil liquefaction study, specifically when pursuing an uncharted domain as drained liquefaction, is that the emergent dynamics arise from basic physics, without assuming constitutive relations. Thus, a simulation may be seen as a numerical experiment, with the advantage (over a physical experiment) of repeatability and easy access to "measurements". Specifically, The macro-scale rheology of the solid granular phase arises naturally in response to the imposed boundary conditions, without the uncertainties arising from imposing constitutive rheologies, such as $\mu(I)$ (Jop

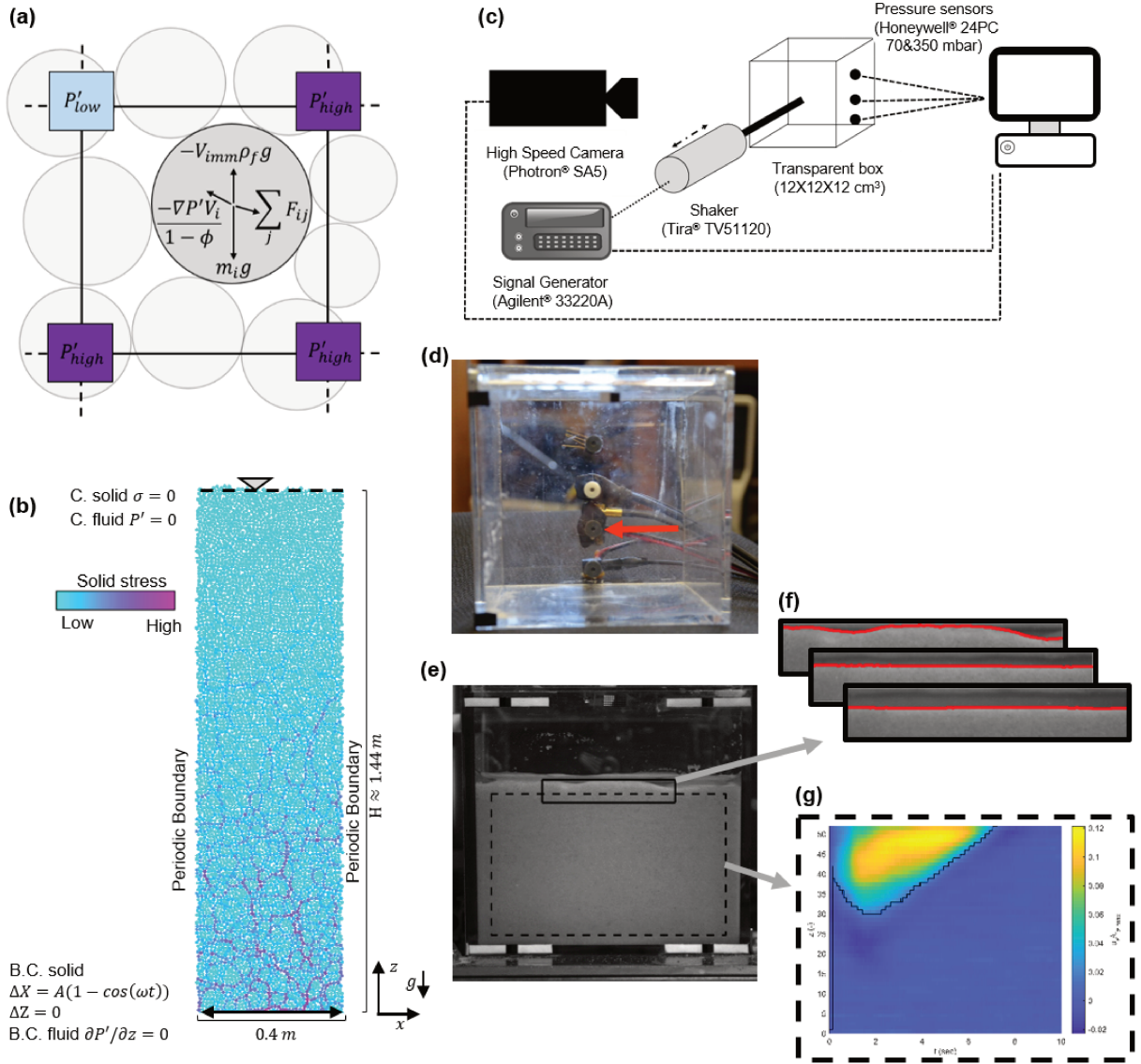


Figure 6: (a) Schematics of the numerical method: coupled discrete elements and fluid on a grid. Arrows are the different forces on a grain (gravity, buoyancy, contact forces and drag force). (b) A typical simulation setup. The boundary conditions are indicated. (c) The experimental setup. (d) Empty experimental box, the red arrow points to the pressure sensors mounted on the far face of the box. (e) A frame from the high-speed camera movie. (f) Three magnified sub-frames showing the edge detected in each frame (red line), representing the layer's height over time. (g) Grain velocity (color) as function of depth and time, achieved by horizontal spatial averaging of the instantaneous grain velocity detected by correlation in time of sub-frames (PIVlab).

et al., 2006; Parez et al., 2021), which is applicable only in a limited range of the phase space. The fluid drainage (see Eqs. (1)-(2) and Fig. 4) also emerges naturally in response to the boundary conditions and the simulated parameters. In each simulation, the full three-terms-diffusion-equation (eq. (1)) is solved, and no assumption is made regarding the relative importance of the three terms. Therefore, when a particular dynamic is observed, it is an emergent (rather than a pre-set) behavior of the system. More specifically, when drained dynamics emerge from simulations that are characterized by $De \ll 1$ (i.e., the coupled grain-fluid dynamics follow the prediction of eq. (1) when the first term is neglected), then the numerical model serves as a validation for the theoretical prediction. One disadvantage of the coupled discrete element and fluid method is that its computational cost is relatively high compared to pure continuum models. This limits the number of grains in a simulation, and consequently limits the size and depth of the simulated layers.

0.6.2 Shaking table experiments

The main objective of the set of experiments is to validate the insights gained from the numerical simulations and theoretical analysis. The experiments (Fig. 6c) comprise a square transparent box ($12 \times 12 \times 12\text{cm}^3$), filled with saturated sand (with a mean grain radius of 0.01 cm), and is harmonically shaken in the horizontal direction. An array of three pressure transducers is mounted vertically on one face of the box to allow pore pressure measurement during the experiment (Fig. 6d). The box's face perpendicular to the shaking direction is filmed by a high-speed camera (Fig. 6e) and the frames are analyzed by edge detection methods to identify changes in the layer's height over time (Fig. 6f), and by Particle Image Velocimetry (Thielicke and Stamhuis, 2014; Thielicke and Sonntag, 2021) method to quantify the instantaneous grain velocity (Fig. 6g).

0.7 Dissertation overview

The work is divided into three chapters:

1) The first chapter develops the theoretical framework for the physics that governs cyclically sheared, unconfined, saturated granular layer under drained conditions, and validates the theory using numerical simulations. This chapter identifies a feedback mechanism between the compacting soil grains and the interstitial fluid flow. The numerical simulations provide further insights that allow the introduction of the compaction front model to describe the layer's dynamics in response to cyclical shear. The role of the layer permeability is explored.

2) The second chapter expands the understanding of the compaction front dynamics and drained liquefaction. Results from both shaking table experiments and numerical simulations are presented. The experimental results are shown to agree and validate the numerical simulations. The rate of seismic energy density input (seismic power) is found to be an important controlling parameter on the duration and magnitude of drained liquefaction. This chapter proposes a solution for the enigmatic liquefaction triggering under low seismic energy density (beyond the earthquake near-field).

3) The third chapter shows how the drained liquefaction and the compaction front model can be invoked to explain the puzzling recurrence of liquefaction in the same site, despite the expected reliquefaction resistance in the aftermath of liquefaction.

A fourth published paper, which deals with the penetration of an intruder into a liquefied granular layer, including the development of the numerical method to treat the intruder, is supplemented as an appendix.

The reader should note that this dissertation is a "collection of papers". This means that the three chapters are independently published, under revision, or soon-to-be-submitted journal articles (as specified in the title page of each chapter). As such, the styling, numbering, and referencing inside each chapter are independent of the other chapters. The dissertation's introduction and closing chapter share numbering, referencing, and a bibliography list.

Chapter 1

Compaction front and pore fluid pressurization in horizontally shaken drained granular layers

Ben-Zeev, S., Aharonov, E., Toussaint, R., Perez, S., & Goren, L. (2020).
Compaction front and pore fluid pressurization in horizontally shaken drained
granular layers. *Physical Review Fluids*, 5(5), 054301.
doi:10.1103/PhysRevFluids.5.054301



Published article in *Physical Review Fluids*.

(Published on May 4, 2020. doi:10.1103/PhysRevFluids.5.054301)

Résumé

Dans de nombreux systèmes granulaires naturels, les pores interstitiels sont remplis d'un fluide. La déformation de ce système diphasique est complexe, fortement couplée et dépend des conditions initiales et aux limites. Ici, nous étudions le compactage granulaire et l'écoulement de fluide dans une couche granulaire saturée, secouée horizontalement et non confinée, où le fluide est libre de s'écouler dans et hors de la couche à travers la surface supérieure libre pendant la secousse (c'est-à-dire la condition aux limites drainée). La géométrie, les conditions aux limites et les paramètres sont choisis pour ressembler à une couche de sol peu profonde, soumise à une accélération cyclique horizontale simulant celle d'un tremblement de terre. Nous développons une théorie et effectuons des simulations numériques couplées éléments discrets et fluides. Les résultats théoriques et de simulation montrent que dans des conditions drainées et au-dessus d'une accélération critique, la couche de grains se compacte à un taux régié par les paramètres d'écoulement du fluide de perméabilité et de viscosité et est indépendante des paramètres d'agitation de fréquence et d'accélération. Un front de compaction se développe, se propageant vers le haut à travers le système. Au-dessus du front, la compaction se produit et le fluide subit une surpression. Les gradients de pression entraînent la filtration de fluide vers le haut et hors de la couche de compaction tout en soutenant le squelette granulaire. Le taux de compaction et le gradient de pression du fluide interstitiel coévoluent jusqu'à ce que les forces exercées par le fluide lors de la filtration équilibrent le poids du solide et que les contacts avec les grains disparaissent. En conséquence, les ondes de cisaillement imposées ne sont pas transmises et la région est liquéfiée. En dessous du front de compaction (c'est-à-dire après son passage), les grains sont bien compactés et les secousses sont transmises vers le haut. Nous concluons que la condition drainée pour le fluide interstitiel est un ingrédient essentiel pour la formation d'un front de compaction ascendant, qui sépare une région granulaire qui présente une rhéologie de type liquide d'une région de type solide.

Compaction front and pore fluid pressurization in horizontally shaken drained granular layers

Shahar Ben-Zeev ^{1,2,*}, Einat Aharonov,¹ Renaud Toussaint,^{2,3}
Stanislav Perez ⁴, and Liran Goren⁵

¹*Institute of Earth Sciences, The Hebrew University of Jerusalem, 91904, Israel*

²*Université de Strasbourg, CNRS, Institut de Physique du Globe de Strasbourg, UMR7516,
F-67000 Strasbourg, France*

³*PoreLab, SFF, the Njord Centre, Department of Physics, University of Oslo, P.O. Box 1048 Blindern,
NO-0316 Oslo, Norway*

⁴*Czech Academy of Sciences, Institute of Chemical Process Fundamentals, 165 02 Prague, Czech Republic*

⁵*The Department of Geological and Environmental Sciences, Ben-Gurion University of the Negev,
84105, Israel*



(Received 15 March 2019; accepted 18 March 2020; published 4 May 2020)

In many natural granular systems, the interstitial pores are filled with a fluid. Deformation of this two-phase system is complex, is highly coupled, and depends on the initial and boundary conditions. Here we study granular compaction and fluid flow in a saturated, horizontally shaken, unconfined granular layer, where the fluid is free to flow in and out of the layer through the free upper surface during shaking (i.e., drained boundary condition). The geometry, boundary conditions, and parameters are chosen to resemble a shallow soil layer, subjected to horizontal cyclic acceleration simulating that of an earthquake. We develop a theory and conduct coupled discrete element and fluid numerical simulations. Theoretical and simulation results show that under drained conditions and above a critical acceleration, the grain layer compacts at a rate governed by the fluid flow parameters of permeability and viscosity and is independent of the shaking parameters of frequency and acceleration. A compaction front develops, swiping upward through the system. Above the front, compaction occurs and the fluid becomes pressurized. Pressure gradients drive fluid seepage upward and out of the compacting layer while supporting the granular skeleton. The rate of compaction and the interstitial fluid pressure gradient coevolve until fluid seepage forces balance solid contact forces and grain contacts disappear. As an outcome, the imposed shear waves are not transmitted and the region is liquefied. Below the compaction front (i.e., after its passage), the grains are well compacted, and shaking is transmitted upward. We conclude that the drained condition for the interstitial pore fluid is a critical ingredient for the formation of an upward-moving compaction front, which separates a granular region that exhibits a liquidlike rheology from a solidlike region.

DOI: [10.1103/PhysRevFluids.5.054301](https://doi.org/10.1103/PhysRevFluids.5.054301)

I. INTRODUCTION

Deformation of densely packed granular media is a subject of great complexity, with applications ranging from industry to natural hazards. In particular, the mechanics of shearing granular media has been shown to control earthquakes (e.g., [1–5]), lead to soil liquefaction (e.g., [6–8]), and control the initiation and movement of landslides (e.g., [9–14]). Granular shear exhibits rich and

* shahar.benzeev@mail.huji.ac.il

not-well-understood behavior even when the grain layers are dry [15–22]. The deformation becomes more complicated when a viscous fluid is present in the pore space between grains, as occurs in most geological systems (e.g., [7,23,24]). Interstitial pore fluid may greatly affect granular deformation because shear deforms the granular skeleton, causing pore-space compaction and dilation [25–27]. These porosity variations lead to pore pressure changes [28], which drive fluid flow [24] and feed back into the granular deformation by imposing forces on grains [29]. These coupled interactions have been studied in various geometrical settings, including continuous horizontal shear under imposed normal stresses [25,30–33], compaction and decompaction due to fluid flow [34,35], vertical discrete tapping [36], impacting intruders [37], vertical continuous shaking [38], and cyclic horizontal shear [8,39] of a horizontally confined layer.

Here, we aim to study the coupled interactions between grains and interstitial pore fluid in a setting that corresponds to saturated soils undergoing earthquake shaking. The soil is represented as a horizontally unconfined layer, with a finite thickness and a free surface at the top. The fluid fully occupies the pore space in the layer. The earthquake shaking is represented as horizontal cyclic shear at accelerations that are well below the gravitational acceleration. In this paper, we use the terms “cyclic shear” and “horizontal shaking” interchangeably to describe this boundary condition.

Natural soils under low overburden stresses, as exist at the shallow subsurface, tend to compact during cyclic shear [40]. We expect that when a viscous interstitial fluid is present, compaction will be accompanied by fluid outflow and pressurization [38]. Here, the fluid drainage conditions (i.e., its ability to flow in and out of the layer) play a key role in controlling both the grain layer dynamics and the fluid pressure and flow. It is usually believed that during the rapid shaking that characterizes earthquakes, fluid cannot drain out of the layer and hence fluid flow does not play an important role in the development of pore pressure or in the compaction process [7]. However, recently it has been suggested [24,33,39,41,42] that even during rapid cyclic shearing, upward fluid flow may be crucial for the coupled deformation, motivating a reevaluation of the effect of fluid flow on pressure changes and compaction during horizontal cyclic shear.

A critical application of the geometry and dynamics that we study here is the hazardous natural phenomenon called “soil liquefaction,” which is often triggered by earthquakes. During liquefaction, soils exhibit an abrupt rheological change where they transition from elastoplastic stress-supporting solid layers to a liquidlike granular phase that flows easily under small applied shear stresses [43,44]. Observations indicate that liquefaction is associated with soil compaction and settlement [45], and pore fluid pressurization is considered as a major driving mechanism for this rheological change [40]. The coupled dynamics that emerge from our idealized shaken saturated grain layer is thus highly relevant to the process of liquefaction.

In the following, we develop a theory for such systems, i.e., unconfined saturated grain layers subjected to horizontal cyclic shear. We establish the conditions under which the proximity to the surface allows fluid to flow in and out of the layer during the imposed deformation, namely, when the grain layer is effectively well drained. These drainage conditions impose a particular form of fluid-grain coupling. We then present a numerical discrete element method (DEM) and computational fluid dynamics framework to study the coupling between compacting grains and fluid flow and pressurization. The agreement between simulation results and theory allows us to present a fully consistent framework of drained granular dynamics in response to cyclic horizontal shaking.

II. GRAIN-FLUID COUPLING UNDER DRAINED CONDITIONS

To identify the dominant interactions between a compacting grain layer and the interstitial fluid flow and pressurization, we develop a theory for the pore fluid response to a general deformation of the grain skeleton. Previous general formulations [24,33] are adopted to the setting of a shallow saturated soil column: The nondimensional analysis is tailored for low stresses with respect to the

fluid bulk modulus. Based on this analysis, the dominant interactions under well-drained conditions are identified.

We start with mass conservation equations over a representative elementary volume for the solid [Eq. (1)] and the fluid [Eq. (2)] phases:

$$\frac{\partial[(1 - \phi)\rho_s]}{\partial t} + \nabla \cdot [(1 - \phi)\rho_s \mathbf{u}_s] = 0, \quad (1)$$

$$\frac{\partial[\phi\rho_f]}{\partial t} + \nabla \cdot [\phi\rho_f \mathbf{u}_f] = 0, \quad (2)$$

where ρ_s and ρ_f are the solid and fluid material densities, respectively, ϕ is the porosity, \mathbf{u}_s and \mathbf{u}_f are the solid grain and fluid velocities, respectively, and t stands for time (vectors are represented in boldface). Grains are assumed to be incompressible with respect to the pore fluid. This assumption is valid, for example, for quartz grains and interstitial water with compressibilities of 2.7×10^{-11} and $4.5 \times 10^{-10} \text{ Pa}^{-1}$, respectively. With this assumption, Eq. (1) is rewritten as

$$\frac{\partial\phi}{\partial t} = \nabla \cdot [(1 - \phi)\mathbf{u}_s]. \quad (3)$$

Further assuming that fluid inertia is negligible compared to the viscous forces, the fluid momentum equation reduces to the Darcy flux law [46]. When the solid grain skeleton is deformable, this law is expressed as

$$\phi(\mathbf{u}_f - \mathbf{u}_s) = -\frac{\kappa}{\eta} \nabla P', \quad (4)$$

where κ is the permeability, η the fluid dynamic viscosity, and P' the fluid pressure deviation from hydrostatic values such that $\nabla P' = \nabla P - \rho_f \mathbf{g}$. The right-hand side of Eq. (4) is commonly referred to as the ‘‘Darcy flux.’’ The fluid density is described by a state equation of the form

$$\rho_f = \rho_{f,0}(1 + \beta P'), \quad (5)$$

where $\rho_{f,0}$ is the fluid density under hydrostatic conditions, with atmospheric pressure on top, and $\beta = (1/\rho_f)(\partial\rho_f/\partial P)$ is the adiabatic fluid compressibility. Next we assess the magnitude of $\beta P'$ in Eq. (5) for the shallow, saturated, and cohesionless soil layer considered here. The pore water compressibility is $O(10^{-10}) \text{ Pa}^{-1}$, and P' cannot significantly exceed the value of the effective static normal stress. To evaluate its value we assume that the top of the water column is exactly at the surface and consider a reference case without dynamic pressure,

$$\begin{aligned} \sigma_0 &= \rho_{\text{eff}} g y - \rho_f g y \\ &= [(1 - \phi)\rho_s + \phi\rho_f - \rho_f] g y \\ &= (1 - \phi)(\rho_s - \rho_f) g y, \end{aligned} \quad (6)$$

where ρ_{eff} is the effective density of a saturated porous layer and y is the downward vertical coordinate, zeroed at the surface. In Eq. (6), σ_0 increases with the depth and its maximal value within a vertically finite domain occurs at depth h , the base of the domain, $\sigma_0^h = \sigma_0(y = h)$. For a layer with quartz grains ($\rho_s = 2640 \text{ kg m}^{-3}$) that extends down to 1 km (much deeper than the systems we consider here), $\sigma_0^h \lesssim O(10^7) \text{ Pa}$, and therefore $\beta P' \ll 1$ and

$$(1 + \beta P') \approx 1. \quad (7)$$

Multiplying Eq. (3) by ρ_f , subtracting it from Eq. (2), and combining it with Eqs. (4), (5), and (7) leads to

$$\phi\beta \frac{\partial P'}{\partial t} + \phi\beta \mathbf{u}_s \cdot \nabla P' - \nabla \cdot \left[\frac{\kappa}{\eta} \nabla P' \right] + \nabla \cdot \mathbf{u}_s = 0. \quad (8)$$

In Eq. (8), the first term describes the temporal derivative of the dynamic pore fluid pressure, the second term describes the dynamic pore pressure advection, the third term is the dynamic pore pressure Laplacian, corresponding to the divergence of the Darcy flux, and the last term describes the effect of the granular skeleton deformation on the fluid pressure via compaction and dilation.

The relative importance of the different terms in Eq. (8) is evaluated using a nondimensional analysis. We choose the system height, h , as the length scale such that $\nabla = \hat{\nabla}/h$, where a caret denotes nondimensional operators and variables. The time and permeability scale factors are t_0 and κ_0 , respectively, such that $t = \hat{t}t_0$ and $\kappa = \hat{\kappa}\kappa_0$. The pore pressure is scaled with the maximum effective static normal stress as $P' = \hat{P}'\sigma_0^h$. The velocity scale factor, $u_0 = (\kappa_0\sigma_0^h)/(\phi\eta h)$, is chosen based on Darcy's flux [Eq. (4)] when $\nabla P' = \nabla\sigma_0 = \sigma_0^h/h$, such that $\mathbf{u}_s = \hat{\mathbf{u}}_s u_0$. This choice reflects our expectations for the importance of fluid flow in our system. In other settings, where fluid flow is vanishingly small with respect to the rate of deformation, a different velocity scale factor should be used [24,33]. Following these definitions, Eq. (8) becomes

$$\frac{\partial \hat{P}'}{\partial \hat{t}} + \frac{\kappa_0 t_0 \sigma_0^h}{\phi \eta h^2} \hat{\mathbf{u}}_s \cdot \hat{\nabla} \hat{P}' - \frac{\kappa_0 t_0}{\phi \beta \eta h^2} \hat{\nabla} \cdot [\hat{\kappa} \hat{\nabla} \hat{P}'] + \frac{\kappa_0 t_0}{\phi^2 \beta \eta h^2} \hat{\nabla} \cdot \hat{\mathbf{u}}_s = 0. \quad (9)$$

The parametric group $t_d = (h^2 \beta \eta \phi)/(\kappa_0) = h^2 D^{-1}$ has the meaning of a diffusion time scale over the layer depth, where $D = (\kappa_0)/(\beta \eta \phi)$ is the pore pressure diffusion coefficient. With this definition, Eq. (9) is written as

$$\frac{\partial \hat{P}'}{\partial \hat{t}} + \frac{t_0}{t_d} \beta \sigma_0^h \hat{\mathbf{u}}_s \cdot \hat{\nabla} \hat{P}' - \frac{t_0}{t_d} \hat{\nabla} \cdot [\hat{\kappa} \hat{\nabla} \hat{P}'] + \frac{t_0}{t_d} \frac{1}{\phi} \hat{\nabla} \cdot \hat{\mathbf{u}}_s = 0. \quad (10)$$

Since we focus on a setting where $\beta \sigma_0^h \ll 1$, the second term in Eq. (10) becomes negligible relative to the third and fourth terms, and Eq. (10) is approximated as

$$\frac{t_d}{t_0} \frac{\partial \hat{P}'}{\partial \hat{t}} - \hat{\nabla} \cdot [\hat{\kappa} \hat{\nabla} \hat{P}'] + \frac{1}{\phi} \hat{\nabla} \cdot \hat{\mathbf{u}}_s = 0. \quad (11)$$

We choose t_0 to represent the process time scale, which in the current system relates to the deformation of the grain skeleton [the third term in Eq. (11)]. A natural choice is the periodicity of the imposed cyclic shear, $t_0 = T$. The coefficient in front of the first term of Eq. (11) then becomes the Deborah number (De) [47], which is the ratio between the relaxation time scale of a system and the process time scale:

$$\text{De} = \frac{t_d}{t_0} = \frac{h^2 \beta \eta \phi}{t_0 \kappa_0}. \quad (12)$$

Hence, Eq. (11) is written as

$$\text{De} \frac{\partial \hat{P}'}{\partial \hat{t}} - \hat{\nabla} \cdot [\hat{\kappa} \hat{\nabla} \hat{P}'] + \frac{1}{\phi} \hat{\nabla} \cdot \hat{\mathbf{u}}_s = 0. \quad (13)$$

When $\text{De} \gg 1$ the diffusion time scale is significantly larger than the process time scale, and the pore pressure will not relax significantly during a single shaking period, leading to “undrained” conditions. When $\text{De} \ll 1$ the diffusion time scale is significantly smaller than the periodicity, leading to “drained” conditions. The De number dictates the relative importance of the terms in Eq. (13). Leaving the third term aside as the source for any dynamics that originates from deformation of the grain skeleton, we note that when $\text{De} \gg 1$ (undrained), the second term in Eq. (13) can be neglected and the temporal evolution of the pore pressure directly correlates with the overall compaction and dilation of the grains skeleton. When $\text{De} \ll 1$ (drained), the first term in Eq. (13) becomes negligible, and Eq. (13) reduces to a Poisson-type equation of the form

$$\hat{\nabla} \cdot [\hat{\kappa} \hat{\nabla} \hat{P}'] = \frac{1}{\phi} \hat{\nabla} \cdot \hat{\mathbf{u}}_s, \quad (14)$$

and in a dimensional form,

$$\nabla \cdot \left[\frac{\kappa}{\eta} \nabla P' \right] = \nabla \cdot \mathbf{u}_s. \quad (15)$$

Integrating Eq. (15) while assuming that $\kappa \approx \kappa_0$ leads to

$$\frac{\kappa_0}{\eta} \nabla P' = \mathbf{u}_s + C(t). \quad (16)$$

Equation (16) reveals the dominant solid-fluid coupling in the drained setting studied here. The equation predicts that the solid velocity depends linearly on the dynamic fluid pressure gradient. When combined with Eq. (4) it becomes a statement of mass conservation, where any solid flux must be compensated by an equal and opposite fluid flux. The details of this dependency in a horizontally shaken layer is the focus of the current work.

III. A COUPLED GRAIN-FLUID MODEL

A. The model

We implement a numerical model that fully couples two phases: a solid phase, which is modeled using the discrete element method [48], and a fluid phase, which is modeled as a continuum on a superimposed Eulerian grid [24,33,49–63]. The core functionality of the code has been verified and used in previous studies. The granular dynamics module was used in [13,14,16–18,64] and coupling with the continuum module was used in [33,59,60,65].

The grains are simulated as interacting spheres using a linear elastic frictional contact model. A velocity-dependent damping is added to the normal contact force, and a threshold friction law based on the ratio of tangential and normal forces between grains is considered, allowing sliding when the shear force surpasses a frictional criterion [16–18]. Grain motion is determined by time integration of the linear [Eq. (17)] and rotational [Eq. (18)] momentum conservation equations,

$$m_i \dot{\mathbf{u}}_{s,i} = m_i \mathbf{g} - V_{\text{imm},i} \rho_f \mathbf{g} + \sum_j \mathbf{F}_{ij} - \frac{\nabla P' \cdot V_i}{1 - \phi}, \quad (17)$$

$$I_i \dot{\boldsymbol{\omega}}_{s,i} = \sum_j R_i \hat{\mathbf{n}}_{ij} \times \mathbf{F}_{ij}, \quad (18)$$

where $\dot{\mathbf{u}}_{s,i}$ and $\dot{\boldsymbol{\omega}}_{s,i}$ are the translational and rotational accelerations of grain i (an overdot indicates a time derivative) and m_i and I_i are the mass and moment of inertia of grain i . In Eq. (17), the first term on the right-hand side is the gravitational force, and \mathbf{g} is the gravitational acceleration. The second term is the buoyancy force, induced by the hydrostatic fluid pressure gradient, whose magnitude depends on the immersed volume of the grain $V_{\text{imm},i}$ and the fluid density ρ_f [66]. The third term is the sum of contact forces (\mathbf{F}_{ij}) of all grains j that are in contact with grain i . The fourth term is the drag force exerted by the fluid dynamic pressure gradient ($\nabla P'$), where V_i is the volume of grain i . In Eq. (18), R_i is the radius of grain i and $\hat{\mathbf{n}}_{ij}$ is a unit vector along the direction connecting the centers of grains i and j .

The evolution of the dynamic pore fluid pressure is found by an implicit numerical solver of Eq. (13) over a square grid, with a grid spacing of two average grain diameters [24,33,54,55]. Importantly, we do not *a priori* assume the state of drainage, and the full three-term equation is solved.

In order to achieve a two-way coupling between the solid and the fluid phases, the grain volumes and velocities are interpolated via a bilinear interpolation scheme into smooth velocity (\mathbf{u}_s) and porosity (ϕ) fields on the grid. Those quantities are used for solving the fluid equation [Eq. (13)]. To solve the solid grain linear momentum equation [Eq. (17)], the dynamic pore pressure gradient ($\nabla P'$) along with the local average porosity (ϕ) is interpolated using an inverse scheme, from the grid to each grain (Fig. 1). In the model, the permeability and the porosity are related by the three-

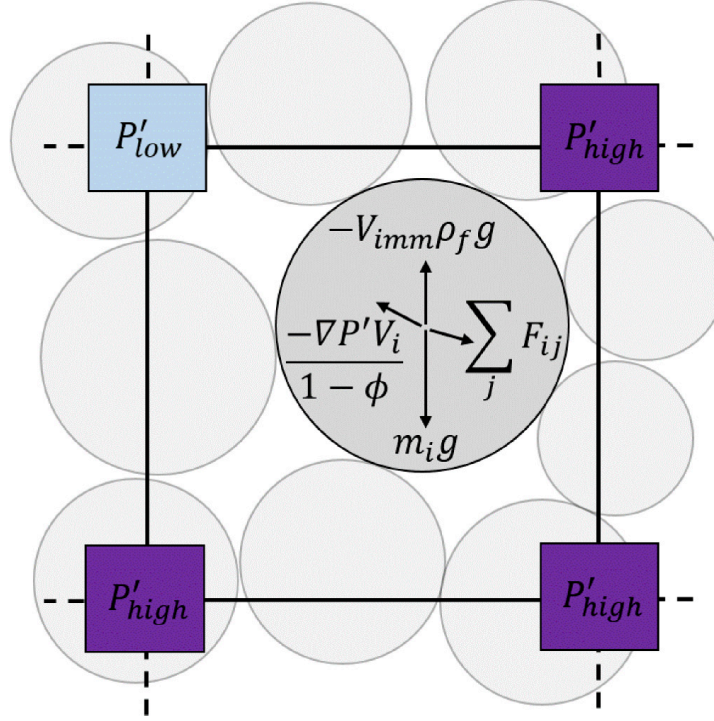


FIG. 1. Schematic of the forces in the model. Dynamic pore pressure gradients exert forces on each grain $[-(\nabla P' V_i)/(1 - \phi)]$. These forces are inferred based on an interpolation scheme that interpolates the pressure gradients from grid nodes to the individual grains. As stated in Eq. (17), this force is added to the gravity ($m_i g$), the buoyancy ($-V_{imm,i}\rho_f g$), and the sum of contact forces ($\sum_j F_{ij}$).

dimensional (3D) Kozeny-Carman relationship [67],

$$\kappa = \kappa_1 \kappa'(x, y, t) = \alpha \bar{r}^2 \frac{\phi^3}{(1 - \phi)^2}, \quad (19)$$

where \bar{r}^2 is the spatial average of the squared grain radii in the surroundings. $\kappa_1 = \alpha \langle r \rangle^2$ is a constant prefactor, while $\kappa' = r'^2 f(\phi)$ captures permeability variations in space and time ($\langle r \rangle$ is the mean grain radius in the system and r' is the local deviation from it, such that $r = \langle r \rangle r'$). In the original Kozeny-Carman relation, $\alpha = 1/45$ [67] is a geometrical prefactor for spheres. In our simulations, we vary α to directly control the order of magnitude of the permeability between different simulations, independent of the grain size. This approach was suggested in [50–53,56] and allows us to overcome the numerical limitations on the usage of small numerical grains, with realistic radii, representative of experiments or field conditions. Varying α allows us to combine numerically feasible grain sizes with permeability values that represent natural systems. We stress that permeability changes due to skeleton deformation are accurately resolved through changes in the porosity. Appendix A presents numerical relations between grain size, time step, and permeability and discusses the validity of the grain size–permeability decoupling.

B. Setup of the numerical simulations

The numerical system (Fig. 2) represents a thin Hele-Shaw cell of spherical grains with grain radii between 0.8 and 1.2 cm drawn from a distribution with a mean of 1 cm and a standard deviation of 1 cm. The system horizontal dimension is $L = 0.8$ m, and its height is $h \approx 0.28$ m. We ran simulations under two distinct modes: The first mode is *hydrostatic pore pressure* (HPP), in which the fluid exerts a buoyancy force due to the constant hydrostatic pressure gradient on the grains

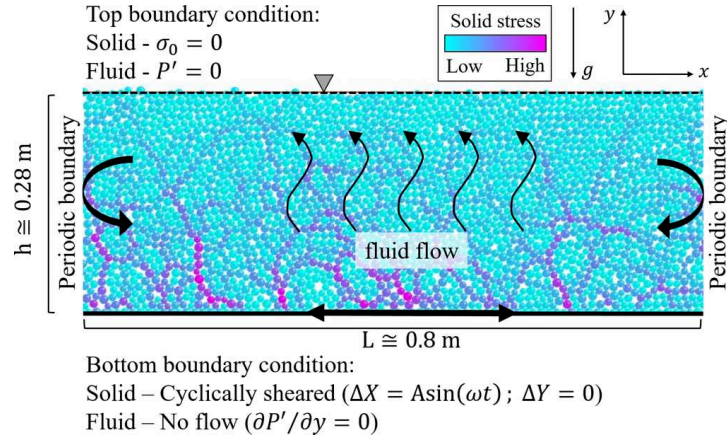


FIG. 2. Numerical system setup. The domain represents a Hele-Shaw cell. The bottom wall is constructed of half-grains, glued together. At the top, there is no wall and the grains are free to move. The grains' color code corresponds to their relative solid normal stress. The dashed line marked by the triangle denotes the fluid level. In “hydrostatic pore pressure” simulations, the fluid exerts only buoyancy on the grains. In “dynamic pore pressure” simulations, deviations from hydrostatic conditions develop. The bottom wall is a no-flow boundary and the upper fluid interface is a zero-pressure boundary, allowing the fluid to drain. In the horizontal direction (x), the system is periodic. The dynamics is induced by cyclic shearing (horizontal shaking) of the bottom solid wall at a preset amplitude (A) and frequency (ω). Vertical displacement of the bottom wall is not allowed.

($-\rho_f g$), regardless of the grain dynamics. In this mode, we do not solve the fluid Eq. (13) and the last term in Eq. (17) is omitted, i.e., we neglect the dynamic forces between the fluid and the solid. The second mode is *dynamic pore pressure* (DPP), in which the fluid and the grains are fully coupled. The local compaction/dilatation affects the fluid pressure and the local dynamic fluid pressure gradients exert forces on the grains in addition to the constant buoyancy force.

The bottom wall is constructed of half-grains (drawn from the same distribution as the internal grains) glued together and a sinusoidal cyclic shear (horizontal shaking) is imposed on it, $X = A \sin(\omega t)$, where X is the bottom wall horizontal displacement, A is the amplitude, and $\omega = 2\pi f$ is the angular frequency ($f = T^{-1}$ is the temporal frequency and T is the periodicity). Vertical displacement of the bottom wall is not allowed. At the top boundary, there are no normal or shear stresses on the solid phase. For the fluid phase, the bottom wall imposes a no-flow boundary condition ($\partial P' / \partial y = 0$) and the top is a constant-pressure boundary ($P' = 0$). The water level is set to be approximately equal to the height of the top grains in the initial configuration, and due to mass conservation, it does not change during the simulations. For both phases, the horizontal direction is periodic, allowing us to simulate a laterally extensive and unconfined layer. The dynamics are limited to a 2D space but the porosity in the simulations is calculated as a 3D porosity, assuming a monolayer of spheres occupying a cell one mean grain diameter in width.

All of our simulations start with the same initial configuration, characterized by a porosity of $\phi_0 = 0.434$, which is denser than a 3D random loose packing. This initial configuration is generated by sedimenting grains on top of the bottom wall, shaking it for 0.53 s at a low normalized acceleration of $\Gamma = A\omega^2/g = 0.042$ ($g = 9.81 \text{ m s}^{-2}$), and allowing complete relaxation. Each simulation is characterized by a single shaking frequency (ω) and by a single low horizontal displacement amplitude of $A = 0.0431 \text{ cm}$ or $A = 0.431 \text{ cm}$, corresponding to 4.31% or 43.1% of the mean grain diameter. Different combinations of frequency and amplitude provide a range of normalized accelerations of $\Gamma = 0.06$ – 0.3 .

The DPP simulations target drained conditions, characterized by $De \ll 1$. To achieve this, we modify α in Eq. (19) and choose relatively high permeabilities, though still within the natural range for soils (κ_0 ranges between 3.1×10^{-12} and $6.1 \times 10^{-11} \text{ m}^2$). With $\eta = 10^{-3} \text{ Pa} \cdot \text{s}$ as the water dynamic viscosity and $t_0 = T$ (single shaking period), De ranges between $O(10^{-4})$ and $O(10^{-2})$,

TABLE I. Physical values used in the model.

Parameter	Value
Grain density	$\rho_s = 2640 \text{ kg m}^{-3}$
Grain Young's modulus	$E = 10^{10} \text{ Pa}$
Grain mean radius	$r_s = 0.5 \text{ cm}$
Grain friction coefficient	$\mu = 0.5$
Grain normal stiffness	$k_n = 10^8 \text{ N m}^{-1}$
Grain tangential stiffness	$k_s = 2.64 \times 10^8 \text{ N m}^{-1}$
Grain damping coefficient	$\gamma = 2.16 \times 10^5 \text{ s}^{-1}$
Fluid density	$\rho_f = 1000 \text{ kg m}^{-3}$
Fluid compressibility	$\beta = 4.5 \times 10^{-10} \text{ Pa}^{-1}$
Fluid dynamic viscosity	$\eta = 10^{-3} \text{ Pa s}$
Gravitational acceleration	$g = 9.81 \text{ m s}^{-2}$

which means that our simulations indeed represent well-drained systems. Table I summarizes the parameter values used in the model.

IV. RESULTS

Figure 3 depicts trends of grain layer compaction in our simulations. The compaction is presented as the deviation of the average porosity from its initial value, $\Delta\langle\phi\rangle = \langle\phi(t)\rangle - \phi_0$, normalized by the initial value, ϕ_0 . The observed compaction trends may be categorized into two representative end members divided by $\Gamma_c \simeq 0.15$: At low accelerations ($\Gamma < \Gamma_c$; red and blue curves in Fig. 3), neither simulation setup, of hydrostatic pore pressure [Fig. 3(a)] or dynamic pore pressure [Fig. 3(b)], shows significant compaction. At $\Gamma \geq \Gamma_c$ (black, gray, pink, and green curves in Fig. 3) both HPP and DPP simulations show significant compaction, where the porosity decreases by more than $\sim 1\%$ with respect to its initial value.

The dynamics of the compaction (that occurs for $\Gamma \geq 0.15$) differs between the HPP and the DPP cases: In HPP simulations, the rate of compaction decreases with time, and the compaction trend varies between simulations. In contrast, the initial compaction rate of DPP simulations is constant and approximately the same across runs, despite the different shear parameters. The linear trend continues for about 5 s, after which the rate of compaction gradually decreases. For $\Gamma \simeq \Gamma_c$, the DPP compaction trend is amplitude dependent. For a low shaking amplitude [solid black curve in Fig. 3(b)], both the final compaction and the transient time are lower. Importantly, all the simulations shown in Fig. 3(b) were conducted with a permeability of the same order of magnitude. When the permeability is changed, the compaction curves change dramatically, as we demonstrate next.

Figure 4 shows the compaction curves of high-acceleration DPP simulations ($\Gamma = 0.2\text{--}0.25$), with amplitudes $A = 0.0431\text{--}0.431 \text{ cm}$ and variable characteristic permeabilities $\kappa_0 = 3.1 \times 10^{-12}\text{--}6.1 \times 10^{-11} \text{ m}^2$, which leads to variable De values, from 0.00094 to 0.054. Note that despite the order-of-magnitude change in the permeability, De remains $\ll 1$, which ensures that the system is well drained. The figure shows that for a given permeability (equal κ_0 values are represented by the same symbols in Fig. 4), the compaction curves collapse and show a similar linear rate of compaction, regardless of the acceleration, frequency, and shearing amplitude. Furthermore, a positive correlation is observed between the permeability and the compaction rate during the initial phase of compaction, whereby in simulations with a lower permeability, the layer compacts more slowly and, consequently, for a longer duration.

In order to explore differences in both the solid and the fluid variables, between compactive behavior that occurs under high cyclic accelerations and noncompactive behavior under low accelerations (as shown in Fig. 3), Figs. 5 and 6 explore representative simulations with low and high accelerations in DPP and HPP cases. The low-acceleration simulation ($\Gamma = 0.1 < \Gamma_c$) exhibits

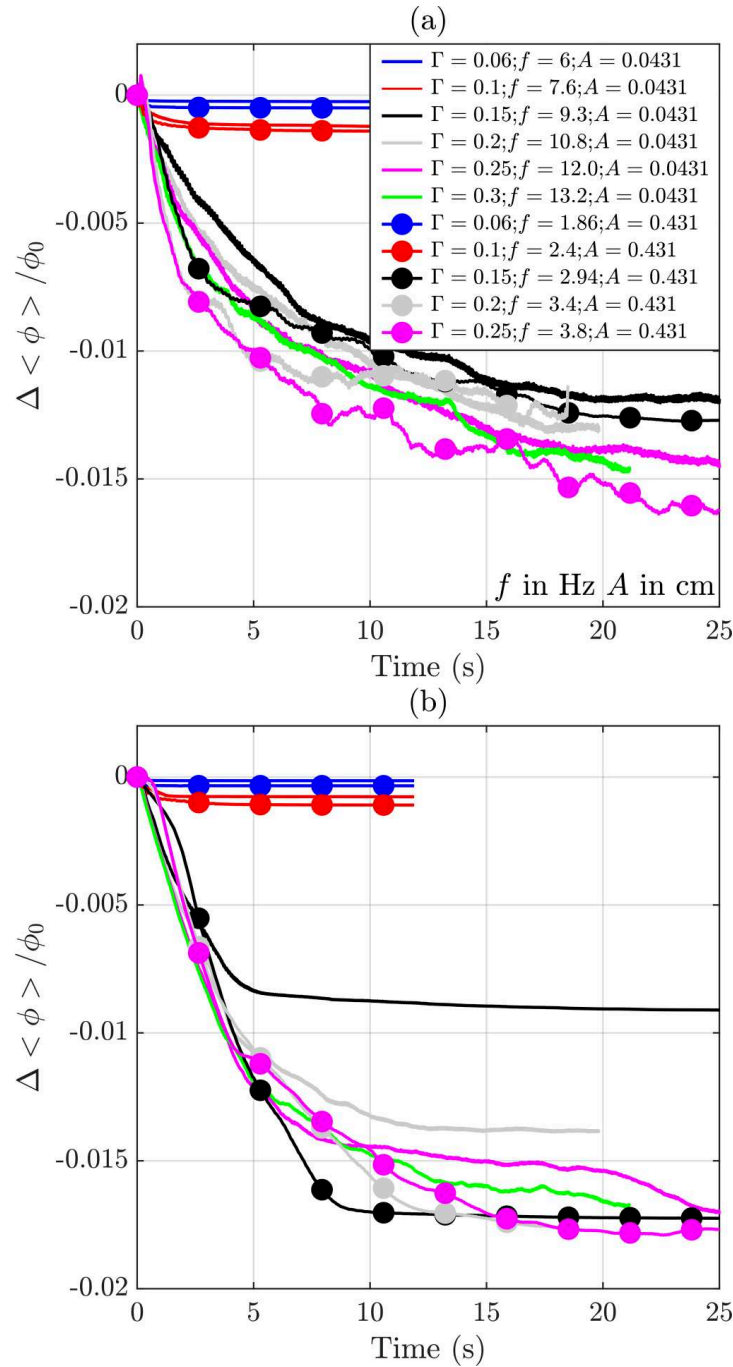


FIG. 3. Normalized average porosity change as a function of time. Two shaking amplitudes (low amplitude $A = 0.0431$ cm, solid line; and high amplitude $A = 0.431$ cm, circles) are compared for variable acceleration, Γ . (a) Hydrostatic pore pressure (HPP) simulations. Compaction occurs only when acceleration exceeds a critical value, $\Gamma_c = 0.15$ (black, gray, pink, and green curves). (b) Dynamic pore pressure (DPP) simulations with a high permeability ($\kappa_0 = 6.1 \times 10^{-11} \text{ m}^2$, $De = 3 \times 10^{-3} - 4.6 \times 10^{-4}$). As in the HPP simulations, compaction occurs only when acceleration exceeds $\Gamma_c = 0.15$. High-acceleration DPP simulations initially follow a single linear compaction trend. When Γ is close to Γ_c (black curves) compaction depends on the shaking amplitude.

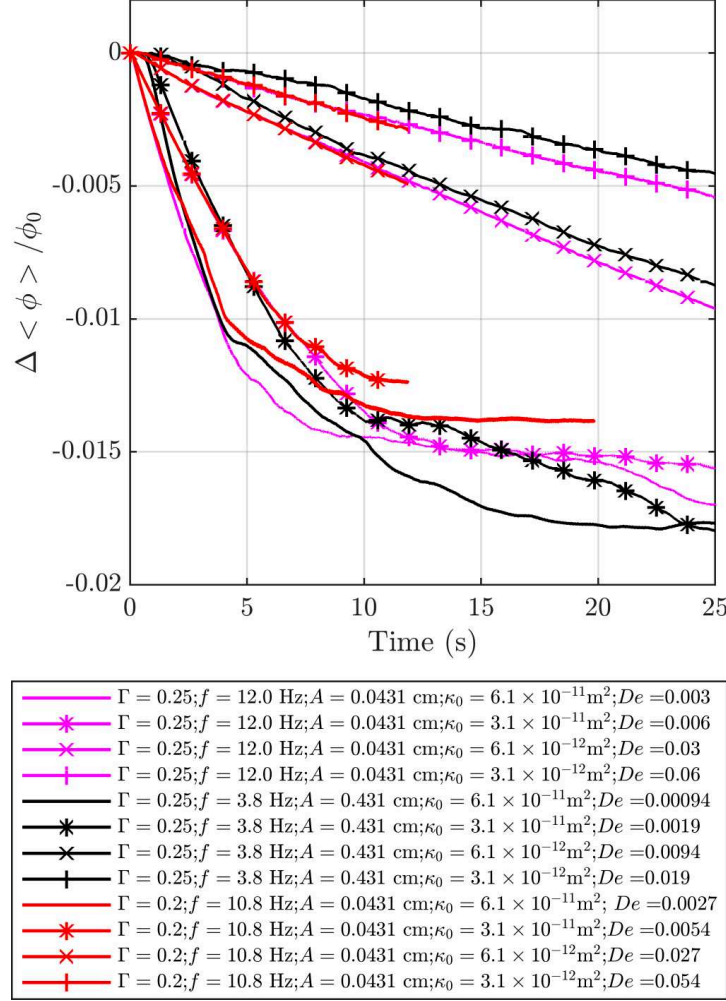


FIG. 4. Normalized average porosity change as a function of time for high-acceleration, dynamic pore pressure simulations with variable permeability. Simulations of equal characteristic permeability (κ_0 ; depicted by the same symbol) have roughly the same compaction rate during the initial rapid linear compaction phase, regardless of the acceleration (Γ), frequency (f), and amplitude (A). All the simulations are well drained ($De \ll 1$).

rigid body translation, with almost no internal strain. More specifically, Figs. 5(a) and 5(b) and the inset show that the horizontal grain velocity is independent of the depth, i.e., $\partial u_{sx}/\partial y = 0$, for both HPP and DPP. In contrast, for high acceleration ($\Gamma = 0.25 > \Gamma_c$), in both the HPP and the DPP simulations the dynamics is radically different. In the HPP simulation, Fig. 6(a) and its inset show a clear delay between the bottom wall velocity, where the strain is imposed, and the layers above it. This reflects the fact that the shear velocity imposed on the bottom wall is transmitted upward via a shear wave. In contrast, the DPP response to the same high acceleration ($\Gamma = 0.25$) [Fig. 6(b)] includes the formation of a zone with nearly zero horizontal grain velocity [$u_{sx}(y, t) \simeq 0$; orange zone bordered by a black line in Fig. 6(b)]. When this zone forms (after a few shearing cycles), it extends from near the bottom wall to the free surface. However, its thickness shrinks with time, until it disappears completely. In the case depicted in Fig. 6(b), this occurs after 5 s. A zone with zero horizontal velocity means that the horizontal shear strain imposed at the bottom wall does not propagate through this horizontal transiently stagnant layer. After this episode, the DPP simulation behaves similarly to the HPP simulation, with propagating shear waves from the base to the top. The episode of nearly zero horizontal grain velocity correlates temporally and spatially with a rapid

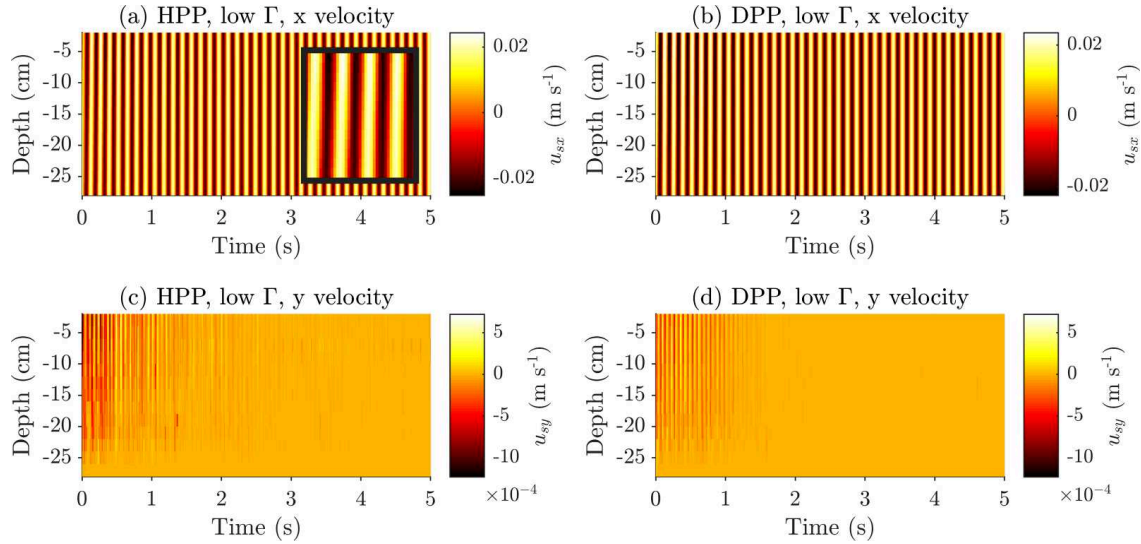


FIG. 5. Horizontally averaged solid grain velocity as a function of depth (y) and time (t) for a low-acceleration simulations ($\Gamma = 0.1$, $A = 0.0431$ cm). The bottom wall is at $y = -28$ cm where the horizontal displacement is imposed, and $y = 0$ cm is the free surface. (a, b) The horizontal grain velocity (u_{sx}) in a hydrostatic pore pressure (HPP) simulation (a) and a dynamic pore pressure (DPP) simulation (b). The grain layers move as a rigid body following the imposed velocity at the bottom, as shown by the inset in (a), which focuses on several cycles. (c, d) The vertical velocity (u_{sy}) in the HPP (c) and the DPP (d) simulations. Minor fluctuations occur during the first second, and afterwards the grains are stagnant in the vertical direction (orange regions).

downward vertical solid grain velocity (u_{sy}) as depicted in Fig. 6(d) by the orange zone bordered by a black line.

To clarify the micromechanics related to this behavior, Fig. 7 presents snapshots of the grain dynamics during a DPP high-acceleration simulation ($\Gamma = 0.25$). Immediately after the imposed shaking starts [Fig. 7(b)] the grain skeleton is solid (the stress chains transmit large stresses, as indicated by their purple color) and horizontal shear deformation is transmitted from the bottom wall via transient granular vortices [as indicated by the black arrows in Fig. 7(c)]. After a few cycles [Fig. 7(d)], the stress chains almost vanish and shear is not transmitted upward. The thickness of the sheared layer gradually increases [Fig. 7(e)] until the whole layer regains its strength and is sheared as in the very beginning [Fig. 7(f)].

To identify the role that fluid pressure plays in this behavior, we follow the spatial and temporal evolution of the dynamic pore pressure gradient ($\nabla P'$, where P' is the pressure deviation from hydrostatic) in the DPP simulations. Figure 8 depicts its vertical component, averaged horizontally and normalized by the static effective vertical stress gradient ($\nabla P'_y / \nabla \sigma_0$). For the low-acceleration simulation ($\Gamma = 0.1$), with the exception of the first few cycles, $\nabla P'_y$ is close to 0 [Fig. 8(a)]. When the acceleration is high ($\Gamma = 0.25 > \Gamma_c$), the gradients of the dynamic pore pressure rise until they become comparable to the static effective vertical stress ($\nabla P'_y / \nabla \sigma_0 \approx 1$; white zone bordered by a black line). This high-pressure-gradient zone progressively shrinks with time until it disappears. In the simulation presented in Fig. 8, the zone disappears about 5 s after the onset of shaking. This transient zone of high pressure gradient correlates spatially and temporally with the high-vertical-grain-velocity episode shown in Fig. 6(d) and with the zero horizontal grain velocity depicted in Fig. 6(b). Outside of this zone, the mean value of $\nabla P'_y$ decreases towards 0, although the instantaneous values are fluctuating and episodically may reach $\nabla P'_y / \nabla \sigma_0 \approx 1$. The same behavior is shown in Fig. 9, where the dynamic pore pressure (P') is plotted vs time at three depths in the layer. Upon the initiation of shaking, the pressure at each depth (solid curves) rises towards the static normal effective solid stress value (dashed lines), and then it decreases back to 0. The closer

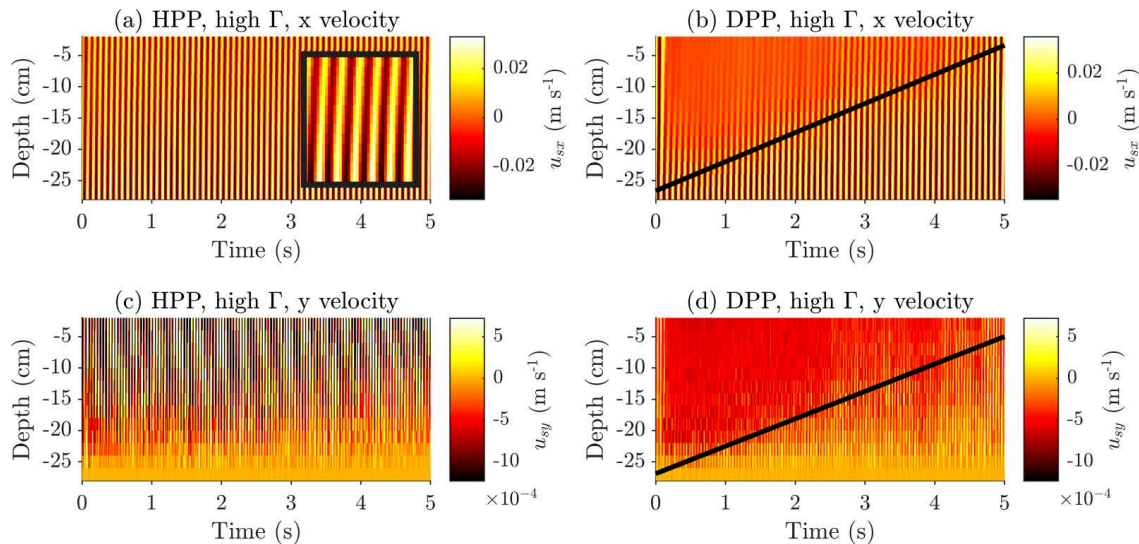


FIG. 6. Horizontally averaged solid grain velocity as a function of depth (y) and time (t) for high-acceleration simulations ($\Gamma = 0.25$, $A = 0.0431$ cm) under both hydrostatic pore pressure (HPP) and dynamic pore pressure (DPP) conditions. The top panels depict the horizontal velocity (u_{sx}). (a) In an HPP simulation, internal strain is observed, where the shear is transmitted from the bottom wall upward, as shown in the inset, which focuses on several cycles. (b) In a DPP simulation, a similar internal strain is observed, yet it is limited to a lower zone, overlain by an upper stagnant domain of nearly zero horizontal velocity (orange regions). The bold black line marks the border between the straining, oscillating domain and the stagnant domain, and its slope is approximated by Eq. (24). This line depicts an upward-propagating front that swipes through the DPP system, separating two dynamical regimes. The bottom panels show the vertical velocity (u_{sy}). (c) In an HPP simulation, we observe oscillatory change in the velocity with positive and negative values (i.e., upward and downward, respectively) that continues throughout the simulation. (d) In a DPP simulation, the same upward-propagating front (bold line) is observed. The front separates a domain with a sustained rapid downward velocity (dark-red region) from an underlying stagnant layer that is no longer compacting.

the point is to the surface, the longer is the duration of the elevated pore pressure. This observed trend in pore fluid pressure evolution is in excellent agreement with the numerical study in [8].

V. DISCUSSION

Three important outcomes arise from our theoretical analysis and simulation results. The outcomes apply specifically to the dynamics of a saturated grain layer that is cyclically sheared in the horizontal direction, when fluid can freely drain from the layer during the time scale set by the shearing periodicity, i.e., where $De \ll 1$.

First, we find an acceleration-controlled transition at $\Gamma_c \approx 0.15$, between noncompactive and compactive behaviors, both in HPP and in DPP simulations. A similar acceleration-dependent threshold that separates rigid from liquidlike behavior was observed previously by Clément *et al.* [66] in DEM simulations, using a different code that implements only HPP conditions. They identified a threshold that corresponds to $\Gamma_c = \mu_a(\rho_s - \rho_f)/\rho_s$, where μ_a is the macroscopic apparent friction coefficient, above which grains slide past each other and initiate grain rearrangement. In DEM simulations, μ_a is smaller than the assigned surface grain friction, and in our case $\mu = 0.5$ and $\mu_a \approx 0.25$ [69]. The acceleration threshold for compaction of grains arises from a force balance between friction (when the normal force is modified by buoyancy) and imposed inertia. Our simulations show that the same criterion and threshold are applicable also in DPP simulations, where dynamic pore pressure gradients develop. This occurs because at the beginning of a DPP simulation, before any dynamic pore pressure or fluid flow evolves, the system is similar to an HPP

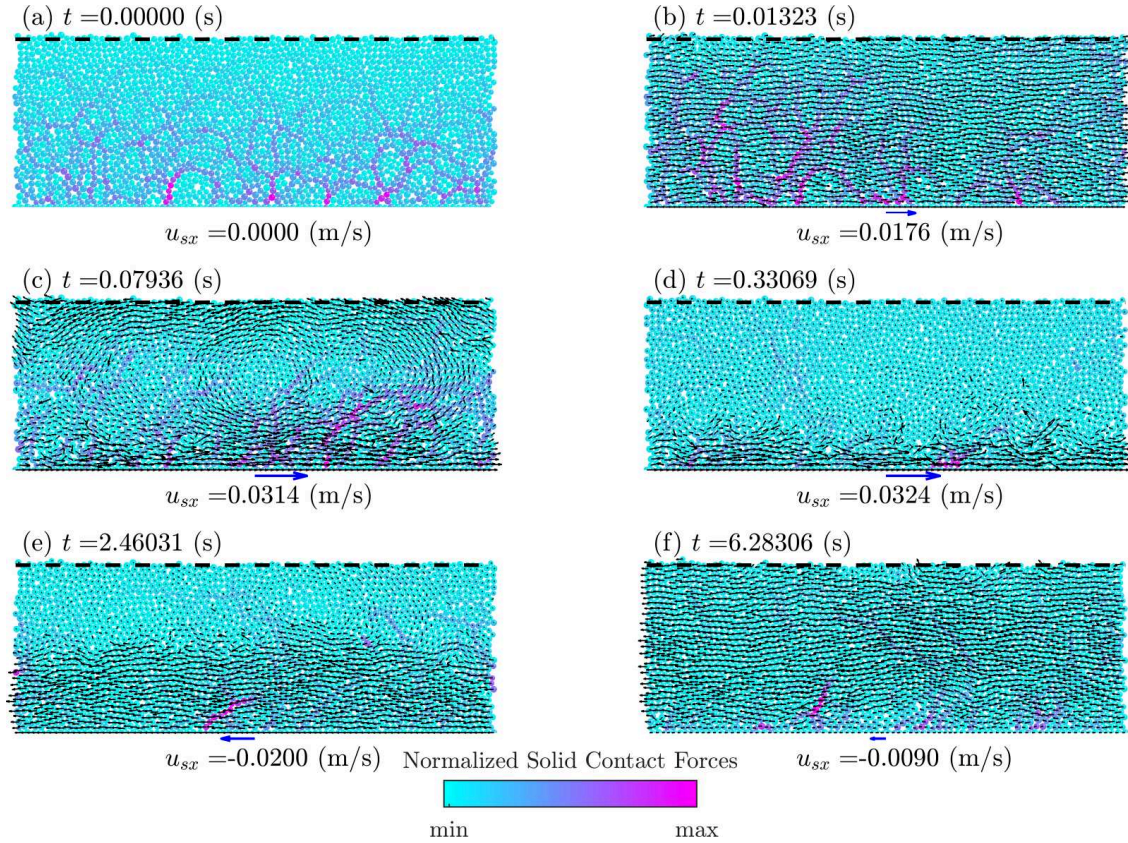


FIG. 7. Snapshots of granular dynamics during a high-acceleration simulation ($\Gamma = 0.25$) with dynamic pore pressure. The colors of the grains indicate their relative solid normal contact force, normalized to the maximum normal force in each frame: (a) 3.5 N, (b) 0.7 N, (c) 7.5 N, (d) 1.7 N, (e) 2.6 N, and (f) 1.0 N. Black arrows depict the solid grain velocity. The blue arrow at the base indicates the imposed bottom wall velocity, exaggerated by a factor of 5 with respect to the black arrows. The dashed black line shows the position of the fluid top surface. (a) Before the initiation of shear, the layer is at rest. (b) When the imposed shaking starts, the grain skeleton behaves in a solid manner, with percolating stress chains capable of transmitting the shear waves from the bottom wall. (c) Some of the motion occurs via transient granular vortices. (d) After a few cycles, the stress chains almost vanish and shear is not transmitted through the upper parts of the layer. (e) The thickness of the bottom sheared zone gradually increases. (f) The whole layer is sheared as in the very beginning. See also a video in the Supplemental Material [68].

system, in which the pressure-gradient drag force is neglected. Hence, the initiation of compaction by sliding obeys the same threshold acceleration predicted for an HPP setting. We note that close to the critical acceleration, the behavior can be more complex. Particularly, our simulations show that the shearing amplitude may control the specific dynamics when $\Gamma = \Gamma_c$ [see Fig. 3(b); black curves].

Second, we reach the important conclusion that fluid pressure evolution is controlled by, and coupled to, the compaction dynamics of grains. Compaction generates high pore pressures, high pressure gradients, and, as an outcome, fluid outflow. At the same time, pressure gradients weaken (and even completely diminish) the solid contacts in between the grains, which facilitates grain rearrangement in the form of compaction. We find that despite the drained conditions, which are achieved since the layer can drain at the time scale of a single cycle of shaking ($De \ll 1$), the pore pressure rises for a substantial duration to a value that is equal to the lithostatic stress. The physics of this pressure rise and its coupling to compaction is concluded from simulations and, also, from the following theoretical analysis.

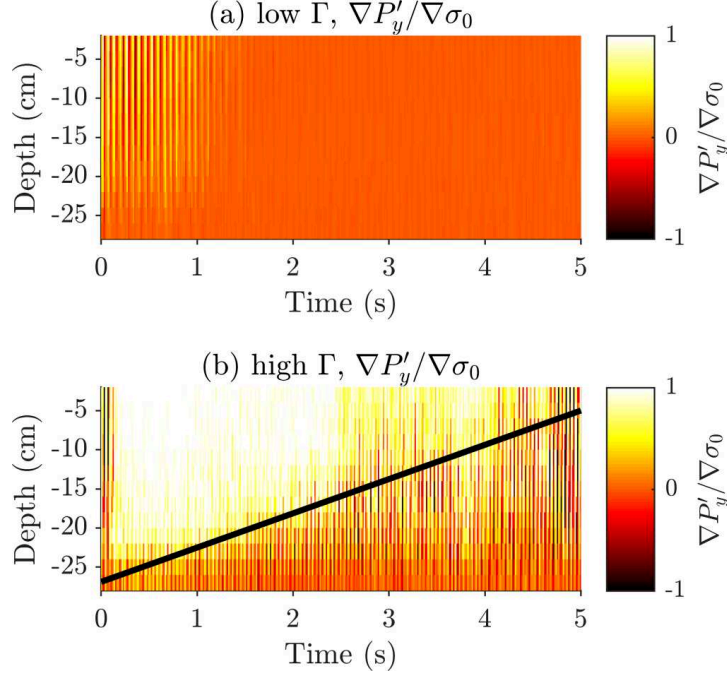


FIG. 8. Dynamic vertical pore pressure gradient ($\nabla P'_y$) normalized by the gradient of the effective static normal stress ($\nabla \sigma_0$) for a low-amplitude simulation ($A = 0.0431$ cm). This ratio is expected to be unity when $\nabla P'_y = \nabla \sigma_0$ (white region), 0 in the hydrostatic case (orange regions), and negative when the pressure is below the hydrostatic value (dark-red regions). (a) At low acceleration ($\Gamma = 0.1$), after some initial fluctuations, the pore pressure gradients vanish. (b) At high acceleration ($\Gamma = 0.25$), a domain where $\nabla P'_y = \nabla \sigma_0$ develops after several cycles. The thickness of this domain decreases with time (white region). The domain is bordered by the bold black line, whose slope is given by Eq. (24). This line represents an upward-moving front, separating a high-pressure-gradient zone from a zone of hydrostatic pressure gradient on average. The high-pressure-gradient zone is temporally and spatially correlated with the high-vertical-velocity zone in Fig. 6(d) and with the vanishingly low-horizontal-velocity zone in Fig. 6(b).

Assuming that significant pressure gradients develop only in the vertical direction, and applying the boundary condition of a vertical stationary and impermeable bottom boundary wall, Eq. (16) reduces to

$$u_{sy} = \frac{\kappa_0}{\eta} \frac{\partial P'}{\partial y}. \quad (20)$$

This relation is depicted in Fig. 10, where the two sides of Eq. (20) are plotted for a high-acceleration DPP simulation, normalized by their theoretical maximum values. A linear relation with a close-to-unity slope emerges even for the raw fluctuating data [Fig. 10(a)]. When the fluctuations are filtered [Fig. 10(b)], an additional trend appears, where at the beginning of the simulation (blue symbols), the values are close to their expected maximum, at the end of the simulation they are equal to 0 (yellow symbols), and the transition between these extreme values is continuous in time. The agreement between the numerical results that are based on the full three-term fluid equation, (13), and the theoretical prediction, Eq. (20), which neglects the time-dependent term when $De \ll 1$, confirms that the nondimensional Deborah number controls the dominant coupled dynamics of the system. More specifically, for drained conditions, the dynamic pressure gradient is exactly proportional to the grain velocity.

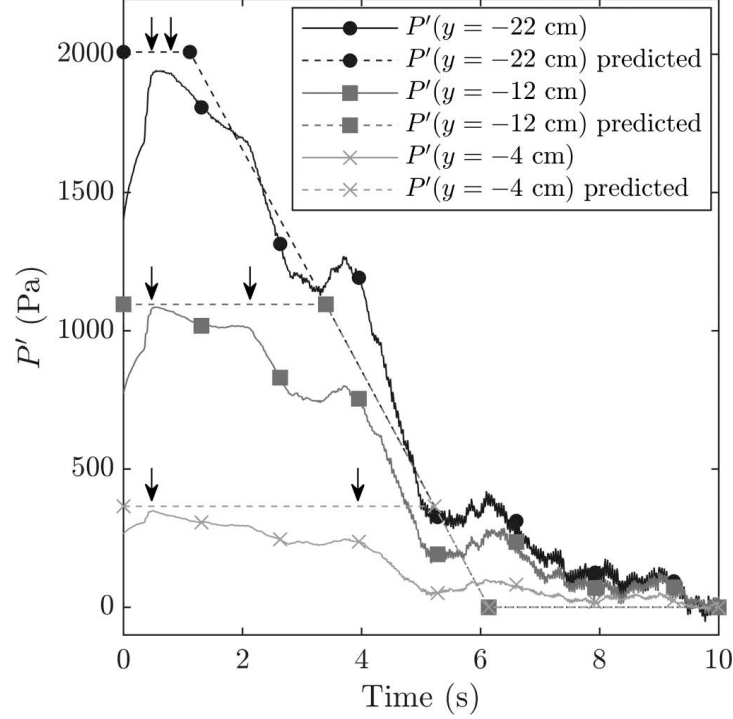


FIG. 9. Dynamic pore pressure (P') vs time during a high-acceleration simulation ($\Gamma = 0.25$ and $A = 0.0431$ cm) at three depths in the layer. The data are smoothed over a window of eight cycles. The dynamic pressure increases after a few cycles towards the effective static normal stress (depicted by the horizontal portions of the dashed lines) and then gradually decreases to 0. This high-pressure episode, whose approximated start and end points are depicted by black arrows, is sustained longer at shallower depths, as predicted by the compaction front model [Eqs. (20) and (24); dashed lines].

With the specified bottom boundary conditions, the vertical solid grain velocity is directly related to the compaction rate (see Appendix B for a detailed derivation),

$$u_{sy} = \frac{\partial \langle \phi(y, t) \rangle}{\partial t} \frac{H}{(1 - \phi_0)}, \quad (21)$$

where ϕ_0 is the initial porosity and $\frac{\partial \langle \phi(y, t) \rangle}{\partial t} = \frac{1}{H} \int_0^H \frac{\partial \phi(y, t)}{\partial t} dy$ is the depth-averaged compaction rate over a sublayer that extends from the bottom wall to height H above the bottom ($0 < H \leq |h|$).

Equations (20) and (21) reveal that the source of an elevated pore pressure in a drained layer is the vertical velocity of the solid grains, which is proportional to the rate of compaction. The vertical velocity, in turn, is set by a volume conservation consideration, which requires that the grain compaction rate must be balanced by the rate of fluid expulsion. The expulsion rate is controlled by the fluid viscosity, the layer permeability, and the evolving pressure gradients. More specifically, when the system compacts, the pore pressure rises, with gradients exceeding hydrostatic values. When the lithostatic limit for the pressure gradient, $\nabla P'_y = \nabla \sigma_0$, is reached, the solid stresses completely vanish and the net force on the grains is 0. At this point, the grains will maintain a constant downward velocity of

$$u_{sy} \approx (\kappa_0 / \eta) \nabla \sigma_0. \quad (22)$$

This steady-state compaction and pressurization phase ends when the porosity reaches some lower critical value. In our simulations, we find that this critical value corresponds to $\phi_c = 0.429 \pm (9.5 \times 10^{-4})$, which is higher than the reported 3D random close packing of spheres $\phi_{\text{RCP}}^{\text{3D}} = 0.36 \pm 0.02$ [70]. This higher value probably reflects our choice to measure the porosity as a 3D property over

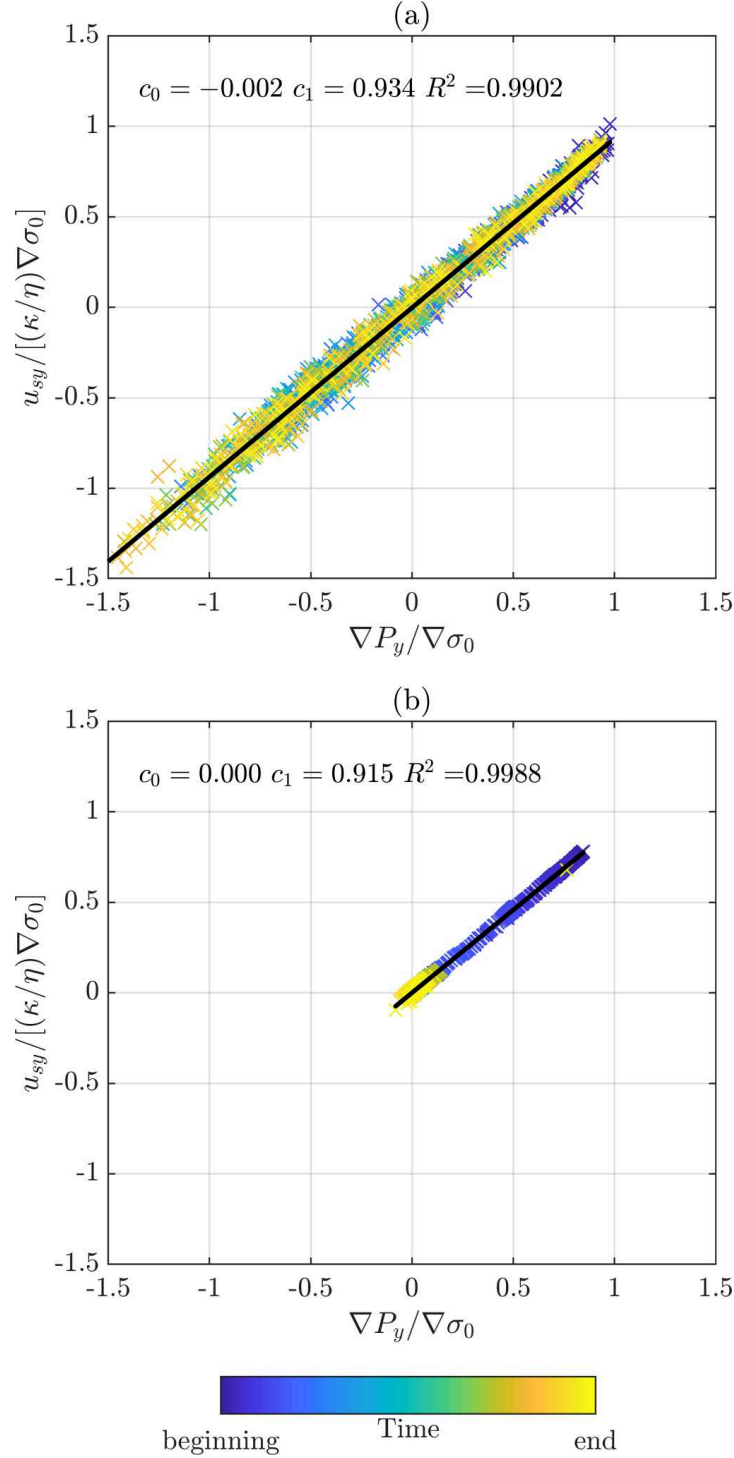


FIG. 10. Average vertical velocity of the solid grains, normalized by $(\kappa_0/\eta)\nabla\sigma_0$, vs vertical gradients of average dynamic pore pressure (normalized by $\nabla\sigma_0$) from high-acceleration, DPP simulation ($\Gamma = 0.25$, $A = 0.0431$ cm). The symbol color represents the time in the simulation: blue represents the beginning of the simulation, and yellow is the end. The data show that in well-drained systems, Eq. (20) captures the coupled grain compaction and fluid pressurization dynamics, both (a) for the instantaneous response as seen in the original data and (b) when the data are smoothed over a window of eight cycles. The numerical data fit well the black line with a slope of 1 (c_0 is the intersection and c_1 the slope).

a monolayer of spheres. The abrupt reduction in compaction rate once a lower critical porosity is reached agrees with [38], which is a study of vertical shaking.

Equation (20) also indicates that at any point in time, the pore pressure gradient is independent of the former porosity and state of pressure and, instead, is sensitive only to the instantaneous rate of skeleton compaction/dilation. At the same time, Eqs. (20)–(22) reveal that the rate of compaction is controlled by the permeability and is independent of the imposed shear parameters. The higher the permeability of the layer, the faster the grains compact.

These insights about the dependency between the rate of compaction, the pressure gradient, and the permeability for a fully drained system, when $De \ll 1$, are well demonstrated in our simulation results. Specifically, a clear distinction can be made between HPP and DPP simulations. In HPP simulations with high accelerations, the grains remain in contact with each other during the whole simulation, as witnessed by their ability to transmit the shear waves from the bottom wall [Figs. 6(a) and 6(c)]. In contrast, in DPP simulations of high accelerations, after a few shaking cycles, the dynamic pore pressure gradient becomes equal to the static effective stress gradient [$|\nabla P'_y/\nabla\sigma_0| \approx 1$; Fig. 8(b)]. The solid grain velocity is then maximal and proportional to the dynamic pore pressure gradient and to the permeability, as shown in Fig. 4. At this stage, the fluid pressure is equal to the lithostatic stress within the compacting zone, which means that the fluid (and not the grains) carries the load, solid stress chains vanish, and shear waves are not transmitted [see Figs. 6(b) and 7(d)].

Finally, this work identifies an upward-moving front that separates an upper pressurized compacting region from a lower, fully compacted zone. This front arises because the downward grain movement is restricted by the vertical stationarity of the bottom wall, which means that once grains near the bottom reach a higher packing density, the rate of compaction decreases. Since compaction is the driver for pressurization, when compaction stops, the pressure gradient in this fully compacted layer drops to a hydrostatic value. The pressurized layer is thus restricted to an upper layer, above the fully compacted region, and its thickness decreases over time. The rate at which the pressurized layer thickness decreases is dictated by the velocity of the “compaction front” that transmits upward the information about the stationary bottom wall. To find this velocity, we express the compaction front as a discontinuity and write the grain’s mass conservation over the front, in the front’s frame of reference,

$$\rho_s(1 - \phi_0)(u_{sy}^0 - u_{\text{front}}) = \rho_s(1 - \phi_c)(u_{sy}^c - u_{\text{front}}), \quad (23)$$

where u_{front} is the front’s velocity, ϕ_0 and $u_{s,y}^0$ are the porosity and grain velocity before the front arrives, respectively, and ϕ_c and $u_{s,y}^c$ are the porosity and grain velocity after the front arrives, respectively. Since $u_{s,y}^c \approx 0$ the velocity of the front is

$$u_{\text{front}} = \frac{\phi_0 - 1}{\phi_0 - \phi_c} u_{sy}^0. \quad (24)$$

Evaluating u_{front} in Eq. (24), with $u_{sy}^0 = (\kappa_0/\eta)\nabla\sigma_0 = (\kappa_0/\eta)(1 - \phi_0)(\rho_s - \rho_f)g$ as the solid vertical velocity during the full pressurization stage [Eq. (22)], leads to

$$u_{\text{front}} = \frac{\phi_0 - 1}{\phi_0 - \phi_c} \frac{\kappa_0}{\eta} \nabla\sigma_0, \quad (25)$$

which provides a good prediction for the front velocity in our simulations. The front velocity dictates the slope of the bottom boundary of the nearly zero horizontal grain velocity domain in Fig. 6(b), the maximum vertical grain velocity domain in Fig. 6(d), and the pressurized domain in Fig. 8(b) (all represented by a black line). The compaction front model, expressed by Eqs. (24), (25), and (20), predicts the dynamic pressure profiles in the layer over time. We express the front position as

$$y_{\text{front}} = y_0 + u_{\text{front}} \cdot t, \quad (26)$$

where y_0 is negative and indicates the depth at which the front first appears, and $y_{\text{front}} = 0$ means that the front has propagated all the way to the surface. With this definition, the pressure profile is

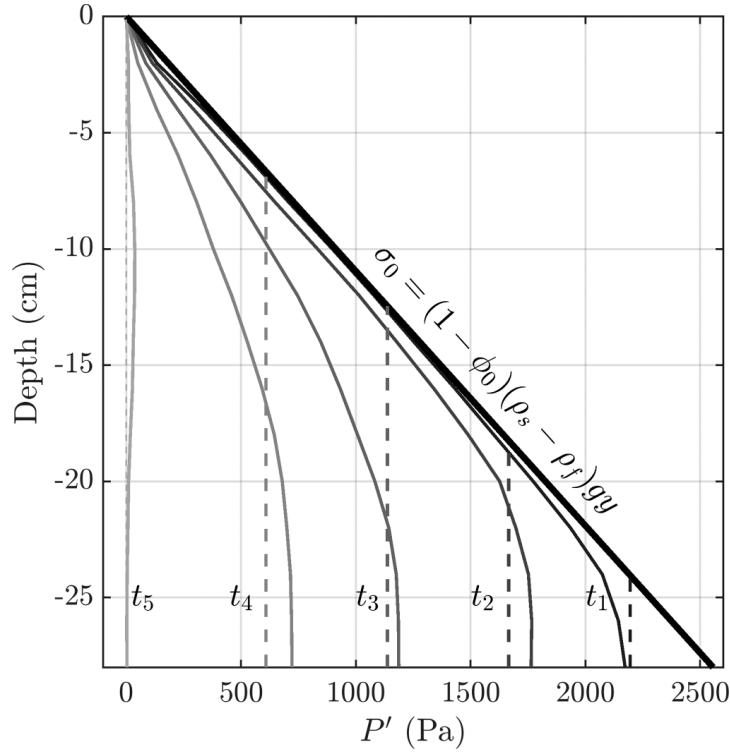


FIG. 11. Profiles of dynamic pore pressure (P') at different times ($t_1 = 0.65$ s, $t_2 = 1.97$ s, $t_3 = 3.29$ s, $t_4 = 4.62$ s, $t_5 = 9.47$ s) during a high-acceleration DPP simulation with $\Gamma = 0.25$ ($A = 0.0431$ cm). The bold black line shows the effective static normal stress. The dashed curves depict the dynamic pore pressure profiles, as predicted by the compaction front model [Eqs. (24)–(27)]. The thin solid curves are the numerically derived dynamic pore pressure profiles. The simulations and the model show a good agreement. See text for sources of deviations.

made of two linear segments:

$$P'(y, t) = \begin{cases} \sigma_0(y) & \text{for } y \geq y_{\text{front}}, \\ \sigma_0(y_{\text{front}}) & \text{for } y < y_{\text{front}}. \end{cases} \quad (27)$$

This means that in the upper part of the layer, before the front passes ($y > y_{\text{front}}$), the slope of the pressure profile is expected to be equal to the slope of the effective static normal stress. In the lower part of the layer, after the front has passed ($y < y_{\text{front}}$), we expect a zero slope, i.e., constant pressure with depth. The predicted profiles at different times during the simulation [Eqs. (26) and (27)] are presented in Fig. 11 as dashed lines and compared to the numerical profiles (solid lines). The predicted and observed profiles agree overall, and deviations may arise from (i) the finite thickness of the compaction front, which is not accounted for in the theory of Eq. (24); (ii) the bottom sublayer instantaneous compaction/dilatation around an average vertical stationarity; and (iii) the instantaneous grain velocity oscillations around the predicted compaction velocity. The overall physical picture of the compaction front with the distinct zones that it forms is summarized in Fig. 12.

As an implication, one can attempt to compare our modeling predictions to observations in earthquakes. Our simulated layer models a fully saturated soil layer that is shaken by seismic waves. An upward-propagating compaction front is predicted. Within the pressurized compacting sublayer, before the arrival of the compaction front, contact stresses between grains vanish and shear waves cannot be transmitted. We predict that this sublayer, which exhibits the properties of liquefaction [7], will become thinner with time and progressively confined to shallower depths. This prediction

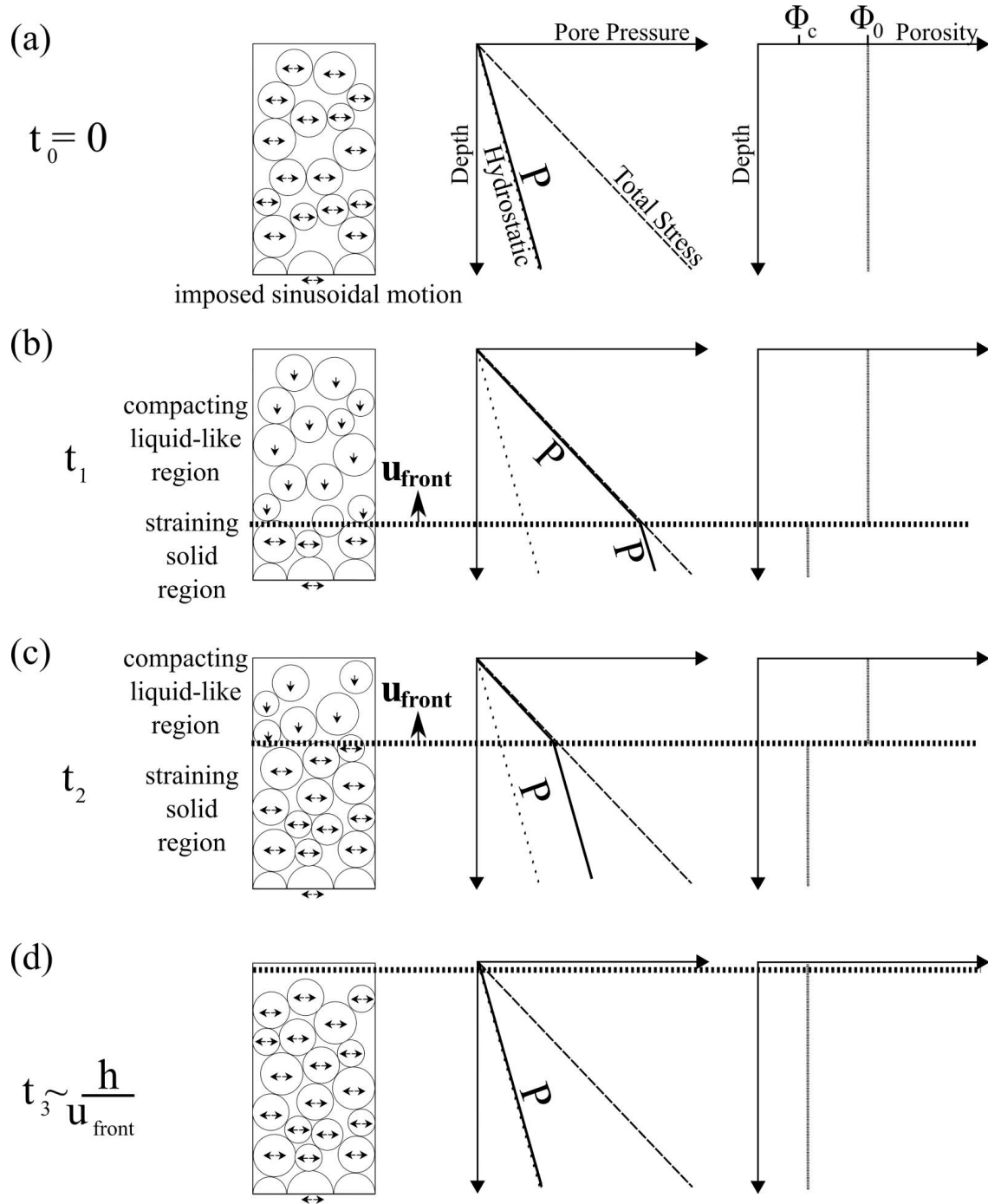


FIG. 12. Schematic summarizing the evolution of the coupled grain-fluid dynamics. (a) Initially, the layer has a porosity ϕ_0 and the grains move horizontally at a velocity u_{sx} , imposed by the cyclic shear of the bottom wall. The pore pressure is hydrostatic. (b) After a few shaking cycles, the grain layer is divided into two sublayers by a compaction front that moves upward at a rate u_{front} . The grains in the top sublayer settle at a velocity of u_{sy}^0 , their horizontal velocity is vanishingly low, and the pore pressure is elevated to the value of the initial total stress. The bottom sublayer has compacted to a porosity of ϕ_c , the grains move following the cyclical horizontal shear, and the pressure gradient is hydrostatic, although the pressure itself is elevated and set by the value of the pressure at the compaction front. (c) At a later time, the compaction front has progressed upward and, with it, the depth at which the pressure gradient becomes hydrostatic. (d) After some time (which depends on the compaction front velocity and the layer height), the compaction front has already passed, and the whole layer has a porosity of ϕ_c . The whole layer then follows the imposed cyclic shear at the bottom.

is supported by field observations by Holzer *et al.* [71], who measured the fluid pressure directly in the ground, during an earthquake. They found that high pore pressure and liquefaction decay from the bottom upward. Our results have another important implication for soil liquefaction that relates to the drainage conditions. Most commonly, liquefaction is assumed to initiate under undrained conditions [40,72], since it is believed that fluid flow relaxes the pore pressure. Our simulations and theory show that liquefaction can be initiated under well-drained conditions, in support of recent experiments [39]. This has critical implications for geophysical earthquake hazard assessment.

VI. SUMMARY

In the current work, we explore theoretically and numerically the coupled grain–interstitial pore fluid dynamics of a saturated granular layer, subject to low overburden stresses and to cyclic horizontal displacements. Targeting specifically a setting representative of an upper soil layer responding to an earthquake seismic excitation, our study focuses on the layer compaction, pore fluid pressurization, and fluid flow under well-drained conditions, whereby the pore fluid can flow out of the grain layer during the shaking period. A nondimensional analysis reveals that the drainage condition is a function of the nondimensional De number, which, in the current setting, is the ratio between the time scale of pore pressure diffusion and the shaking periodicity. It was previously thought that when fluid can easily flow out of the system ($De \ll 1$ conditions), the fluid pressure does not rise significantly and does not play a significant role in the dynamics of the system. By contrast, this work shows analytically and numerically that even when $De \ll 1$, the fluid pressure rises dramatically and the dynamics of the grains is significantly altered.

We identify two end-member behaviors, with a transition controlled by the shaking acceleration. At low accelerations, below a critical value, the system behaves rigidly, compaction is negligible, and the fluid pressure remains hydrostatic. At high accelerations, albeit still at a fraction of the gravitational acceleration, significant compaction occurs, coupled to high-fluid-pressure gradients that support the grains. Here, the compaction is initially rapid and linear in time, and we find that the compaction rate is governed by the rate of fluid drainage, which in itself is a function of the layer permeability and the fluid viscosity. This constant compaction rate is independent of the shaking forcing. The duration and location of the pressurization event are well described as a compaction front (Fig. 12) that propagates up from the base of the layer. Before the arrival of the front, the interstitial fluid is overpressurized to the level of the effective static normal stress, and it flows upward fully supporting the grains’ weight, which allows the grains to compact at a constant rate. After the front passage, grains are compacted and the fluid pressure gradient is hydrostatic. The good agreement between the numerical simulations and the compaction front model suggests that our theory can serve as a predictive tool to evaluate pressurization episodes in compacting, well-drained, grain-fluid systems.

Specifically, our results indicate that compaction, fluid flow, and pressurization are interdependent in horizontally shaken granular layers under drained conditions, with potential implications for earthquake-induced soil liquefaction.

ACKNOWLEDGMENTS

We thank K. J. Måløy, Y. H. Hatzor, V. Vidal, J. C. Géminard, E. G. Flekkøy, E. Altshuler, A. Batista-Leyra, and G. Sanchez-Colina for interesting discussions. S.B.-Z. acknowledges the support of Institut Français d’Israël and Campus France for the Chateaubriand Fellowship, as well as the University of Strasbourg. S.B.-Z. and E.A. are grateful for the support of ISF Grant No. 197/17. S.P. acknowledges Grant No. 19-21114Y from the Czech Science Foundation (GA CR). R.T. acknowledges the support of the INSU ALEAS program, of the LIA France-Norway D-FFRACT, IPGS, and of the ITN FlowTrans, funding from the European Union’s Seventh Framework Programme for research under Grant Agreement No. 316889.

APPENDIX A: PARAMETER SCALING IN THE COUPLED GRAIN-FLUID MODEL

The time step of the numerical solver was chosen to be small enough to resolve a single undissipated elastic collision between two grains, which lasts for $t_{\text{col}} = \sqrt{m/k_n}$, where m is the average grain mass and k_n is the grain normal stiffness (i.e., the spring constant used to compute the normal forces between grains in contact, using a linear displacement/force interaction model). We choose the time step to be $\Delta t = 0.1 \cdot t_{\text{col}}^{\text{min}}$, where $t_{\text{col}}^{\text{min}}$ is the collision time associated with the smallest grain in our system. Using our model parameters, this restriction yields $\Delta t \approx O(10^{-7})$ s. The periodicity of the imposed horizontal shaking in our simulations is within the range of $T \approx O(10^{-2})$ – $O(10^{-1})$ s. This means that the simulation time step is sufficiently small to fully resolve this external forcing.

The dependency between the time step and the grain size means that natural grain sizes could not be modeled in a reasonable simulation time. To overcome this limitation, we model grains that are larger than those found in nature. Since we are interested in the dynamics that occur within the natural range of permeabilities, we must decouple the permeability value from the modeled grain size. We do so by modeling the permeability as $\kappa = \kappa_1 \kappa'(x, y, t)$ [Eq. (19)], where $\kappa_1 = \alpha \langle r \rangle^2$ is a constant in each simulation, and $\kappa' = r'^2 \phi^3 / (1 - \phi)^2$ varies in space and time (through changes in ϕ and, to a lesser extent, changes in r'^2). Under the effect of a pore pressure field and intergranular contact forces, grains are set in relative motion, which induces deformation and changes the porosity field ϕ (and possibly r'^2). We assume that this changes κ' , without perturbing κ_1 . By varying α in Eq. (19) we directly control the order of magnitude of the permeability between different simulations, independent of the grain size. This decoupling approach was proposed and successfully compared to experiments in [50–53,56]. The “decoupled model” correctly captures the relevant dynamics because grain size does not dominate the physics. Instead, changes in the porosity and the order of magnitude of the permeability control the system behavior [Eqs. (21) and (22)]. The excellent agreement between theory and simulations further shows that the grain size does not affect the pore pressure evolution and the compaction rate, as predicted in Eqs. (22)–(26) and shown in Figs. 9–11.

The small time step places a restriction on the permeability of the granular skeleton. To correctly resolve the fluid pressure diffusion Eq. (13), on the superimposed grid, we use the Courant-Friedrichs-Lewy condition $\Delta t < 0.5 \cdot \Delta x^2 / D$. In our simulations, $\Delta x = 4 \cdot \langle r \rangle$, where $2 \cdot \langle r \rangle$ is the mean grain diameter, and $D = (\kappa_0) / (\beta \eta \phi)$ is the pore pressure diffusion coefficient. This restriction means that the permeability should be $\kappa < 10^{-10}$ m², and to ensure this, we set the α parameter in Eq. (19) to be $\alpha < 10^{-5}$.

APPENDIX B: VERTICAL SOLID GRAIN VELOCITY AND COMPACTION RATE

Reorganization of Eq. (3) shows that the divergence of the solid grain velocity can be related to the temporal and spatial change in porosity:

$$\nabla \cdot \mathbf{u}_s = \frac{1}{1 - \phi} \left(\frac{\partial \phi}{\partial t} + \mathbf{u}_s \cdot \nabla \phi \right). \quad (\text{B1})$$

Since we do not expect large spatial gradients in porosity we neglect the last term in Eq. (B1), and by reducing it to the vertical dimension we get

$$\frac{\partial u_{sy}(y, t)}{\partial y} \approx \frac{1}{1 - \phi(y, t)} \frac{\partial \phi(y, t)}{\partial t}. \quad (\text{B2})$$

Integration of Eq. (B2) from the bottom ($y = 0$) to an arbitrary height ($y = H$) gives

$$\begin{aligned}
 \int_0^H \frac{\partial u_{sy}}{\partial y} dy &= \int_0^H \frac{1}{1 - \phi(y, t)} \frac{\partial \phi(y, t)}{\partial t} dy \\
 &= - \int_0^H \frac{\partial}{\partial t} [\ln(1 - \phi(y, t))] dy \\
 &= - \int_0^H \frac{\partial}{\partial t} [\ln(1 - \phi_0 - \delta\phi(y, t))] dy \\
 &= - \int_0^H \frac{\partial}{\partial t} [\ln((1 - \phi_0)(1 - \delta\phi(y, t)/(1 - \phi_0)))] dy \\
 &= - \int_0^H \frac{\partial}{\partial t} [\ln(1 - \phi_0) + \ln(1 - \delta\phi(y, t)/(1 - \phi_0))] dy, \tag{B3}
 \end{aligned}$$

where $\delta\phi$ is a small change from the initial porosity.

Since $\delta\phi(y, t)/(1 - \phi_0) \ll 1$ we can expand a series $\ln(1 - \delta\phi(y, t)/(1 - \phi_0)) \approx -\delta\phi(y, t)/(1 - \phi_0) - \delta\phi^2(y, t)/2(1 - \phi_0)^2 + O(\delta\phi^3)$. Neglecting the high-order terms of the expansion, Eq. (B3) becomes

$$\begin{aligned}
 u_{sy}(H, t) - u_{sy}(0, t) &\approx - \int_0^H \frac{\partial [\ln(1 - \phi_0) - \delta\phi(y, t)/(1 - \phi_0)]}{\partial t} dy \\
 &= \frac{1}{1 - \phi_0} \int_0^H \frac{[\delta\phi(y, t)]}{\partial t} dy \\
 &= \frac{1}{1 - \phi_0} \int_0^H \frac{\partial [\phi(y, t) - \phi_0]}{\partial t} dy \\
 &= \frac{\partial \langle \phi(y, t) \rangle}{\partial t} \frac{H}{1 - \phi_0}, \tag{B4}
 \end{aligned}$$

where $\frac{\partial \langle \phi(y, t) \rangle}{\partial t} = \frac{1}{H} \int_0^H \frac{\partial \phi(y, t)}{\partial t} dy$ is the spatial average compaction rate over a layer that extends from the bottom wall to height H . Applying the boundary condition of $u_{sy}(0, t) = 0$ to Eq. (B4),

$$u_{sy}(y, t) = \frac{\partial \langle \phi(y, t) \rangle}{\partial t} \frac{H}{1 - \phi_0}, \tag{B5}$$

which correlates the solid grain flux over a surface with the change in porosity in a total medium volume.

-
- [1] C. Marone, Laboratory-derived friction laws and their application to seismic faulting, *Annu. Rev. Earth Planet Sci.* **26**, 643 (1998).
 - [2] J. K. Morgan and M. S. Boettcher, Numerical simulations of granular shear zones using the distinct element method: 1. Shear zone kinematics and the micromechanics of localization, *J. Geophys. Res.* **104**, 2703 (1999).
 - [3] K. Mair, K. M. Frye, and C. Marone, Influence of grain characteristics on the friction of granular shear zones, *J. Geophys. Res.* **107**, 2219 (2002).
 - [4] P. A. Johnson and X. Jia, Nonlinear dynamics, granular media and dynamic earthquake triggering, *Nature* **437**, 871 (2005).
 - [5] K. Mair and S. Abe, 3D numerical simulations of fault gouge evolution during shear: Grain size reduction and strain localization, *Earth Planet. Sci. Lett.* **274**, 72 (2008).

- [6] G. R. Martin, W. D. L. Finn, and H. B. Seed, Fundamentals of liquefaction under cyclic loading, *J. Geotech. Eng. Div.* **101**, 423 (1975).
- [7] H. B. Seed, J. Lysmer, and P. P. Martin, Pore-water pressure changes during soil liquefaction, *J. Geotech. Geoenviron. Eng. Div.* **102**, 323 (1976).
- [8] U. El Shamy and M. Zeghal, A micro-mechanical investigation of the dynamic response and liquefaction of saturated granular soils, *Soil Dynam. Earthquake Eng.* **27**, 712 (2007).
- [9] R. M. Iverson, The physics of debris flows, *Rev. Geophys.* **35**, 245 (1997).
- [10] D. Ertas and T. C. Halsey, Granular gravitational collapse and chute flow, *Europhys. Lett.* **60**, 931 (2002).
- [11] O. Katz, J. K. Morgan, E. Aharonov, and B. Dugan, Controls on the size and geometry of landslides: Insights from discrete element numerical simulations, *Geomorphology* **220**, 104 (2014).
- [12] A. Lucas, A. Mangeney, and J. P. Ampuero, Frictional velocity-weakening in landslides on Earth and on other planetary bodies, *Nat. Commun.* **5**, 3417 (2014).
- [13] S. Perez and E. Aharonov, Long runout landslides: A solution from granular mechanics, *Frontiers Phys.* **3**, 80 (2015).
- [14] S. Perez, E. Aharonov, and R. Toussaint, Unsteady granular flows down an inclined plane, *Phys. Rev. E* **93**, 042902 (2016).
- [15] H. J. Herrmann, J. Hovi, and S. Luding, *Physics of Dry Granular Media* (Springer Science & Business Media, Berlin, 1997).
- [16] E. Aharonov and D. Sparks, Rigidity phase transition in granular packings, *Phys. Rev. E* **60**, 6890 (1999).
- [17] E. Aharonov and D. Sparks, Shear profiles and localization in simulations of granular materials, *Phys. Rev. E* **65**, 051302 (2002).
- [18] E. Aharonov and D. Sparks, Stick-slip motion in simulated granular layers, *J. Geophys. Res.* **109**, 1 (2004).
- [19] P. Jop, Y. Forterre, and O. Pouliquen, A constitutive law for dense granular flows, *Nature* **441**, 727 (2006).
- [20] Y. Forterre and O. Pouliquen, Flows of dense granular media, *Annu. Rev. Fluid Mech.* **40**, 1 (2008).
- [21] G. Sánchez-Colina, L. Alonso-Llanes, E. Martínez-Román, A. Batista-Leyva, C. Clement, C. Flidner, E. Altshuler, and R. Toussaint, “Lock in accelerometry” to follow sink dynamics in shaken granular matter, *Rev. Sci. Instrum.* **85**, 126101 (2014).
- [22] L. Alonso-Llanes, G. Sánchez-Colina, E. Martínez, A. J. Batista-Leyva, R. Toussaint, and E. Altshuler, Intruder penetration in granular matter studied by lock-in accelerometry, *Revista Cubana Fis.* **33**, 95 (2016).
- [23] S. A. Miller, A. Nur, and D. L. Olgaard, Earthquakes as a coupled shear stress–high pore pressure dynamical system, *Geophys. Res. Lett.* **23**, 197 (1996).
- [24] L. Goren, E. Aharonov, D. Sparks, and R. Toussaint, Pore pressure evolution in deforming granular material: A general formulation and the infinitely stiff approximation, *J. Geophys. Res.: Solid Earth* **115**, B09216 (2010).
- [25] R. M. Iverson and R. G. LaHusen, Dynamic pore-pressure fluctuations in rapidly shearing granular materials, *Science* **246**, 796 (1989).
- [26] J. Desrues, R. Chambon, M. Mokni, and F. Mazerolle, Void ratio evolution inside shear bands in triaxial sand specimens studied by computed tomography, *Geotechnique* **46**, 529 (1996).
- [27] M. Nicolas, P. Duru, and O. Pouliquen, Compaction of a granular material under cyclic shear, *Eur. Phys. J. E* **3**, 309 (2000).
- [28] A. Skempton, The pore-pressure coefficients A and B, *Geotechnique* **4**, 143 (1954).
- [29] K. Terzaghi, *Theoretical Soil Mechanics* (John Wiley, New York, 1943).
- [30] D. M. Hanes and D. L. Inman, Observations of rapidly flowing granular-fluid materials, *J. Fluid Mech.* **150**, 357 (1985).
- [31] J. Samuelson, D. Elsworth, and C. Marone, Shear-induced dilatancy of fluid-saturated faults: Experiment and theory, *J. Geophys. Res.* **114**, 1 (2009).
- [32] F. Boyer, E. Guazzelli, and O. Pouliquen, Unifying Suspension and Granular Rheology, *Phys. Rev. Lett.* **107**, 188301 (2011).
- [33] L. Goren, E. Aharonov, D. Sparks, and R. Toussaint, The mechanical coupling of fluid-filled granular material under shear, *Pure Appl. Geophys.* **168**, 2289 (2011).

- [34] D. R. Hewitt, J. S. Nijjer, M. G. Worster, and J. A. Neufeld, Flow-induced compaction of a deformable porous medium, *Phys. Rev. E* **93**, 023116 (2016).
- [35] G. Gauthier and P. Gondret, Compaction of liquid immersed granular packings by small upward flows, *Phys. Rev. Fluids* **4**, 074308 (2019).
- [36] C. Lesaffre, V. Mineau, D. Picart, and H. Van Damme, Densification under vibration of a saturated granular packing, *C.R. Acad. Sci. Ser. IV Phys.* **1**, 647 (2000).
- [37] J. J. S. Jerome, N. Vandenberghe, and Y. Forterre, Unifying Impacts in Granular Matter From Quicksand to Cornstarch, *Phys. Rev. Lett.* **117**, 098003 (2016).
- [38] S. Kiesgen de Richter, C. Hanotin, P. Marchal, S. Leclerc, F. Demeurie, and N. Louvet, Vibration-induced compaction of granular suspensions, *Eur. Phys. J. E* **38**, 74 (2015).
- [39] O. Adamidis and G. Madabhushi, Experimental investigation of drainage during earthquake-induced liquefaction, *Geotechnique* **68**, 655 (2018).
- [40] A. Sawicki and J. Mierczynski, Developments in modeling liquefaction of granular soils, Caused by cyclic loads, *Appl. Mech. Rev.* **59**, 91 (2006).
- [41] R. Snieder and A. van den Beukel, The liquefaction cycle and the role of drainage in liquefaction, *Granular Matter* **6**, 1 (2004).
- [42] D. L. Lakeland, A. Rechenmacher, and R. Ghanem, Towards a complete model of soil liquefaction: The importance of fluid flow and grain motion, *Proc. R. Soc.* **470**, 20130453 (2014).
- [43] B. M. Das, *Principles of Soil Dynamics* (PWS-Kent, Boston, 1993).
- [44] S. L. Kramer, *Geotechnical Earthquake Engineering* (Prentice Hall, Upper Saddle River, NJ, 1996).
- [45] K. Ishihara, Liquefaction and flow failure during earthquakes, *Geotechnique* **43**, 351 (1993).
- [46] H. Darcy, *Les fontaines publiques de la ville de Dijon* (Victor Dalmont, Paris, 1856).
- [47] M. Reiner, The Deborah number, *Phys. Today* **17**(1), 62 (1964).
- [48] P. A. Cundall and O. D. Strack, A discrete numerical model for granular assemblies, *Geotechnique* **29**, 47 (1979).
- [49] E. G. Flekkøy, A. Malthe-Sørenssen, and B. Jamtveit, Modeling hydrofracture, *J. Geophys. Res. Solid Earth* **107**, ECV 1-1 (2002).
- [50] Ø. Johnsen, R. Toussaint, K. J. Måløy, and E. G. Flekkøy, Pattern formation during air injection into granular materials confined in a circular Hele-Shaw cell, *Phys. Rev. E* **74**, 011301 (2006).
- [51] J. L. Vinningland, Ø. Johnsen, E. G. Flekkøy, R. Toussaint, and K. J. Måløy, Granular Rayleigh-Taylor Instability: Experiments and Simulations, *Phys. Rev. Lett.* **99**, 048001 (2007).
- [52] J. L. Vinningland, Ø. Johnsen, E. G. Flekkøy, R. Toussaint, and K. J. Måløy, Experiments and simulations of a gravitational granular flow instability, *Phys. Rev. E* **76**, 051306 (2007).
- [53] J. L. Vinningland, Ø. Johnsen, E. G. Flekkøy, R. Toussaint, and K. J. Måløy, Size invariance of the granular Rayleigh-Taylor instability, *Phys. Rev. E* **81**, 041308 (2010).
- [54] M. J. Niebling, E. G. Flekkøy, K. J. Måløy, and R. Toussaint, Mixing of a granular layer falling through a fluid, *Phys. Rev. E* **82**, 011301 (2010).
- [55] M. J. Niebling, E. G. Flekkøy, K. J. Måløy, and R. Toussaint, Sedimentation instabilities: Impact of the fluid compressibility and viscosity, *Phys. Rev. E* **82**, 051302 (2010).
- [56] J. L. Vinningland, R. Toussaint, M. Niebling, E. G. Flekkøy, and K. J. Måløy, Family-Viscek scaling of detachment fronts in granular Rayleigh-Taylor instabilities during sedimentating granular/fluid flows, *Eur. Phys. J.: Spec. Topics* **204**, 27 (2012).
- [57] M. J. Niebling, R. Toussaint, E. G. Flekkøy, and K. J. Måløy, Dynamic aerofracture of dense granular packings, *Phys. Rev. E* **86**, 061315 (2012).
- [58] M. J. Niebling, R. Toussaint, E. G. Flekkøy, and K. J. Måløy, Numerical studies of aerofractures in porous media, *Revista Cubana Fis.* **29**, 1E66 (2012).
- [59] L. Goren, R. Toussaint, E. Aharonov, D. W. Sparks, and E. Flekkøy, A general criterion for liquefaction in granular layers with heterogeneous pore pressure, in *Poromechanics V: Proceedings of the Fifth Biot Conference on Poromechanics*, edited by C. Hellmich, B. Pichler, and D. Adam (American Society of Civil Engineers, Reston, VA, 2013), pp. 415–424.
- [60] E. Aharonov, L. Goren, D. W. Sparks, and R. Toussaint, Localization of shear in saturated granular media: Insights from a multi-scaled granular-fluid model, in *Poromechanics V: Proceedings of the Fifth Biot*

- Conference on Poromechanics*, edited by C. Hellmich, B. Pichler, and D. Adam (American Society of Civil Engineers, Reston, VA, 2013), pp. 471–480.
- [61] I. Ghani, D. Koehn, R. Toussaint, and C. W. Passchier, Dynamic development of hydrofracture, *Pure Appl. Geophys.* **170**, 1685 (2013).
- [62] A. Vass, D. Koehn, I. Ghani, S. Piazzolo, R. Toussaint, and A. Vass, The importance of fracture-healing on the deformation of fluid-filled layered systems, *J. Struct. Geol.* **67**, 94 (2014).
- [63] I. Ghani, D. Koehn, R. Toussaint, and C. W. Passchier, Dynamics of hydrofracturing and permeability evolution in layered reservoirs, *Frontiers Phys.* **3**, 1 (2015).
- [64] E. Bendror and L. Goren, Controls over sediment flux along soil-mantled hillslopes: Insights from granular dynamics simulations, *J. Geophys. Res. Earth Surface* **123**, 924 (2018).
- [65] S. Ben-Zeev, L. Goren, S. Perez, R. Toussaint, C. Clément, and E. Aharonov, The combined effect of buoyancy and excess pore pressure in facilitating soil liquefaction, in *Poromechanics VI: Proceedings of the Sixth Biot Conference on Poromechanics*, edited by M. Vandamme, P. Dangla, J. M. Pereira, and S. Ghabezloo (American Society of Civil Engineers, Reston, VA, 2017).
- [66] C. Clément, R. Toussaint, M. Stojanova, and E. Aharonov, Sinking during earthquakes: Critical acceleration criteria control drained soil liquefaction, *Phys. Rev. E* **97**, 022905 (2018).
- [67] P. C. Carman, Fluid flow through granular beds, *Trans., Inst. Chem. Eng.* **15**, 150 (1937).
- [68] See Supplemental Material at <http://link.aps.org/supplemental/10.1103/PhysRevFluids.5.054301> for a video of high-acceleration simulation.
- [69] N. Makedonska, D. W. Sparks, E. Aharonov, and L. Goren, Friction versus dilation revisited: Insights from theoretical and numerical models, *J. Geophys. Res.: Solid Earth* **116**, 1 (2011).
- [70] J. G. Berryman, Random close packing of hard spheres and disks, *Phys. Rev. A* **27**, 1053 (1983).
- [71] T. L. Holzer, T. L. Youd, and T. C. Hanks, Dynamics of liquefaction during the 1987 Superstition Hills, California, earthquake, *Science* **244**, 56 (1989).
- [72] National Academies of Sciences, Engineering and Medicine, *State of the Art and Practice in the Assessment of Earthquake-Induced Soil Liquefaction and Its Consequences* (National Academies Press, Washington, DC, 2016).

Chapter 2

Drainage explains soil liquefaction beyond the earthquake near-field

Article under revision for Nature Communications

Résumé

La liquéfaction du sol induite par les tremblements de terre est un phénomène courant et dévastateur par lequel les tremblements de terre provoquent une perte de rigidité du sol, produisant une compaction et une déformation du sol de type liquide. Les sols liquéfiés sont incapables de soutenir les infrastructures, causant des victimes, des pertes économiques et la destruction de systèmes de distribution et transports. Une observation déconcertante concernant la distribution spatiale de la liquéfaction du sol est que de nombreux événements de liquéfaction se produisent loin de l'épicentre du tremblement de terre, où la densité d'énergie sismique est faible. Le mécanisme classique de liquéfaction du sol, qui considère les sols comme un milieu effectivement non drainé pendant la durée du tremblement de terre, ne parvient pas à expliquer ces événements car on pense que la liquéfaction non drainée nécessite une densité d'énergie élevée.

Nous présentons ici un mécanisme d'initiation de la liquéfaction dans des conditions drainées, où l'écoulement de fluide à l'intérieur et à l'extérieur du sol pendant le tremblement de terre favorise les gradients de pression interstitielle excessive et la perte de résistance du sol. Les simulations et les expériences révèlent que l'initiation de la liquéfaction drainée n'est pas contrainte par un seuil de densité d'énergie, ce qui en fait un candidat de choix pour expliquer les événements de liquéfaction au-delà du champ proche du tremblement de terre. Nous constatons que la liquéfaction du sol drainé est déclenchée relativement rapidement et que la durée de l'événement est contrôlée par un front de compaction se propageant, dont la vitesse dépend du taux d'injection d'énergie sismique. Ces résultats expliquent en outre pourquoi les événements de liquéfaction ne sont pas observés à très petite énergie - la compaction est trop faible et l'événement est trop rapide pour être documenté. Nos résultats suggèrent que la liquéfaction du sol peut se produire dans un éventail complet de conditions de drainage, avec des implications critiques pour l'évaluation du potentiel de liquéfaction et des risques associés.

Drainage explains soil liquefaction beyond the earthquake near-field

Shahar Ben-Zeev^{1,2,*}, Liran Goren³, Renaud Toussaint^{2,4}, and Einat Aharonov^{1,4}

¹Institute of Earth Sciences, The Hebrew University of Jerusalem, 91904, Israel

²Université de Strasbourg, CNRS, ENGEES, Institut Terre & Environnement de Strasbourg, UMR7063, F-67000 Strasbourg, France

⁴PoreLab, the Njord Centre, Department of Physics, University of Oslo, P.O. Box 1048 Blindern, NO-0316 Oslo, Norway

³The Department of Earth and Environmental Sciences, Ben-Gurion University of the Negev, 84105, Israel

*Corresponding author: Shahar Ben-Zeev, shahar.benzeev@mail.huji.ac.il

December 8, 2022

Abstract

Earthquake-induced soil-liquefaction is a common and devastating phenomenon whereby earthquake-shaking induces loss of soil rigidity, producing compaction and liquid-like soil deformation. Liquefied soils are unable to support infrastructure, causing casualties, economic loss, and destruction of lifelines. A puzzling observation relating to the spatial distribution of soil liquefaction is that many liquefaction events occur far from the earthquake epicenter, where the seismic energy density is low. The classical mechanism for soil liquefaction, which views soils as an effectively undrained medium during the earthquake duration, fails to explain these events since undrained liquefaction is thought to require high energy density.

Here we present a mechanism for liquefaction initiation under drained conditions, where fluid flow within and out of the soil during the earthquake promotes excess pore pressure gradients and loss of soil strength. Simulations and experiments reveal that drained liquefaction initiation is not constrained by an energy density threshold, making it a prime candidate for explaining liquefaction events beyond the earthquake near-field. We find that drained soil liquefaction is triggered relatively rapidly, and the event duration is controlled by a propagating compaction front, whose velocity depends on the seismic energy injection rate. These findings further explain why liquefaction events are not observed at very small energy - compaction is too small, and the event is too rapid to be documented. Our results suggest that soil liquefaction may occur under a full spectrum of drainage conditions, with critical implications for the assessment of liquefaction potential and related hazards.

1 Introduction

Seismically induced soil liquefaction is a natural hazard that commonly occurs during earthquakes¹. During liquefaction, a soil that initially possessed an elasto-plastic rheology and was capable of supporting the load of infrastructure, loses its strength and stiffness in response to earthquake shaking, consequently exhibiting fluid-like rheology. Earthquake-induced soil liquefaction results in buildings and infrastructures sinking², floating and tilting², ground lateral spreading², settlement³, and landsliding⁴. Liquefaction damage often leads to extensive human casualties^{4,5}, destruction of lifelines^{2,6}, and economic losses⁶⁻⁹, that may result in complete abandonment of formerly inhabited areas⁷, posing a significant challenge to community resilience¹⁰.

The classical mechanism explaining seismically induced soil liquefaction¹ considers the soil as an "effectively undrained" medium. Upon cyclic shear, an initially loosely-packed soil tends to reduce its pore volume, as readily documented under dry and drained conditions¹¹. If the pore fluid flow rate is slow compared to the rate of porosity reduction, as is expected in an undrained soil response, the pore fluid is trapped within the contracting pores and its pressure increases. If the pore pressure builds up to the level of the overburden stress (commonly lithostatic values), then the effective stress reduces to zero¹², the soil loses its shear strength and stiffness and is said to be liquefied^{8,11}. Undrained lab experiments^{8,11,13,14} showed that during continuous shaking, and depending on the initial soil density and the applied shear stress, the pore pressure builds up gradually and reaches lithostatic values after several to tens of shear cycles.

Despite the overall success of the undrained perspective in describing the conditions leading to pore pressure rise and soil strength and stiffness loss during earthquakes, it struggles to explain soil liquefaction beyond the near-field, far from the earthquake's epicenter, where the seismic energy density input is small. Empirical inferences established a lower bound of 30 J/m³ for the seismic energy density required to induce liquefaction by "undrained consolidation"^{15,16}. Consequently, as the seismic energy decays away from the earthquake's epicenter, liquefaction events beyond the near-field should become uncommon. Nonetheless, the majority of the events in an extensive soil liquefaction compilation^{16,17} were triggered beyond the earthquake near field, where the seismic energy density is well below the 30 J/m³ threshold and as low as 0.1 J/m³ (Figure 1 in ref.¹⁶). The discrepancy between the leading theory and field observations of soil liquefaction indicates that our understanding of the conditions and processes associated with earthquake-induced soil liquefaction is incomplete.

The main attempt to reconcile theory and observations¹⁶ invokes seismically induced permeability enhancement^{7,18} between deeper aquifers and the liquefied layer. However, dynamic permeability increase and the availability of buried high fluid-pressure sources represent unique geometric and hydrologic settings, likely precluding it from being a general mechanism for liquefaction beyond the near field. Here, we adopt a different approach of exploring the feasibility and dynamics of liquefaction initiation under drained conditions, where consolidation is not expected to obey the undrained limit, and the previously established threshold energy density should not apply.

In a rare movie capturing soil liquefaction¹⁹ at the "Makuhari Seaside Park" in Chiba (Japan), during the Tohoku

earthquake (2011)²⁰, the photographer commented while pointing to the lawn: “... *there was water just coming up right there, on the ground... and the ground is just swaying right now*”. This testimony suggests that fluid drainage toward the surface during an earthquake could play an important role in the process of soil liquefaction, which agrees with recent theoretical and experimental studies proposing that rapid fluid flow could play a significant role in initiating liquefaction^{21–28}. This implies that the undrained liquefaction initiation mechanism does not necessarily cover the full spectrum of conditions leading to soil liquefaction.

A “Drained liquefaction” initiation implies that the timescale of fluid flow is shorter than the timescale associated with earthquake-induced soil deformation. In this scenario, porous fluid flow toward a drained boundary is accompanied by pore pressure gradients that exert seepage forces on the soil grains, supporting their weight, weakening grain contacts, and reducing soil strength. The notion that pressure gradients and seepage forces could fully support grains is, in itself, not novel. Static vertical pressure gradients supporting a layer of grains is known as quicksand conditions^{29,30}. Furthermore, interstitial fluid ejection leading to ground settlement is a known post-liquefaction failure mechanism^{31–33}. Here, we consider the case where in-situ pressure gradients and seepage forces emerge directly from seismic excitation during soil consolidation under drained conditions. Consequently, liquefaction initiates and is triggered as a drained phenomenon during the earthquake. We show that the drained liquefaction mechanism predicts liquefaction events triggered by low energy density. This, in turn, has critical implications for the physics of liquefaction, the conditions that can lead to liquefaction, and consequently, the evaluation of liquefaction potential and associated hazard.

2 Pore pressure evolution and the compaction front model

The evolution of the pore pressure in a deformable saturated granular media can be described by a diffusion equation with a source term related to the granular skeleton deformation^{21,22,27,34}:

$$\frac{\partial P'}{\partial t} - \frac{1}{\beta_f \eta \phi} \nabla \cdot [\kappa \nabla P'] + \frac{1}{\beta_f \phi} \nabla \cdot u_s = 0, \quad (1)$$

where P' is the dynamic pore pressure deviation from hydrostatic value ($P' = P - P_{hyd}$), β_f and η are the fluid compressibility and viscosity, respectively, κ is the permeability, t is time and ∇ is a spatial derivative. The third term in equation (1) describes the internal source for dynamic pore pressure, due to divergence of solid grain velocities (u_s). This term can be approximated^{22,27} as the rate of pore space compaction and dilation, $\nabla \cdot u_s \simeq \frac{1}{1-\phi} \frac{\partial \phi}{\partial t}$, where ϕ is the porosity.

Fluid drainage within the granular media is expected to obey Darcy’s flux law. Consequently, the characteristic velocity scale in equation (1) is identified with $u_0 = (\kappa_0/\phi\eta) \cdot (\sigma_0^h/h)$, where σ_0^h/h describes the initial effective lithostatic stress gradient, which is also the pressure gradient during liquefaction (σ_0^h is the initial effective lithostatic stress at depth h). κ_0 is the characteristic permeability. There are two length scales characterizing the system: Stress

and pressure change gradually over the layer depth, h , yet grains diverge and converge over a much shorter length scale, l , likely several grains wide, as seen in^{21,27}. Subsequently, non-dimensional parameters (represented by caret symbols, $\hat{\cdot}$) can be defined as follows: $\hat{\nabla} = \hat{\nabla}_l/l$ where $\hat{\nabla}$ appears as a divergence operator, $\hat{\nabla} = \hat{\nabla}_h/h$ where $\hat{\nabla}$ appears as a gradient operator, $\hat{u}_s = u_s/u_0$, $\hat{t} = t/t_0$, $\hat{P}' = P'/\sigma_0^h$, and $\hat{\kappa} = \kappa/\kappa_0$. Eq. 1 can then be re-written as:

$$\text{De} \frac{\partial \hat{P}}{\partial \hat{t}} - \hat{\nabla}_l \cdot [\hat{\kappa} \hat{\nabla}_h \hat{P}] + \frac{1}{\phi} \hat{\nabla}_l \cdot \hat{u}_s = 0 \quad (2)$$

The non-dimensional coefficient in front of the first term in equation (2) is known as the Deborah number (De)^{21,22,27,35,36}:

$$\text{De} = \frac{t_d}{t_0} = \frac{hl\beta_f\eta\phi}{T\kappa_0}, \quad (3)$$

which expresses the ratio between the timescale for pressure diffusion $t_d = \frac{hl}{D}$, where $D = \frac{\kappa_0}{\beta_f\eta\phi}$ is the pore pressure diffusion coefficient, and the timescale of deformation imposed by the shaking period, $t_0 = T$. Therefore, the De number provides a metric for evaluating the system's drainage conditions. When $\text{De} \ll 1$ and $t_d \ll T$, pore pressure diffusion is sufficiently rapid, so as to allow drainage during shaking. In this case, which we term "drained", the first term in equation (2) becomes negligible, and the diffusion term (second term) balances the source term (third term). When $\text{De} \gg 1$, the layer is "undrained", in which case the diffusion term is negligible, and the source term is balanced by the temporal derivative of the dynamic pressure²¹. Notably, contrary to previous studies that used the term 'drained' to describe an end-member with no change in fluid pressure^{8,37}, in the current study, 'drained' implies $\text{De} \ll 1$, and pore pressure gradients could emerge in response to skeleton deformation. For a discussion on drainage-related terminology and its relation to equation 2, see Appendix A.

To apply this general formulation to the deformation of a shallow soil column, we consider a layer of saturated cohesionless grains with a free and drained surface (where the pressure is maintained at a constant value, $P = 0$) and where no internal permeability barriers are present (Fig. 1). When such a soil layer is relatively loosely packed, with initial porosity ϕ_0 , and when it is subjected to horizontal shaking, an upward propagating compaction front (also referred to as a "solidification front") develops^{27,31,38,39}. The propagating compaction front separates two regions within the layer²⁷(Fig. 1a-b): a lower region, in which grains have compacted to porosity $\phi_c < \phi_0$ and are approximately stationary in the vertical direction. In this lower region, the pore pressure gradient is nearly hydrostatic, although the pore pressure itself is elevated to the value of the pressure at the front (Fig. 1c). In the region above the front, grains continuously settle at a uniform velocity while maintaining their initial porosity, ϕ_0 . The settling grains exchange place with the upward flowing pore fluid. The pore fluid pressure gradient above the front can, and normally will, become as high as lithostatic (Fig. 1c and Appendix B). This fluid pressure gradient is the source of an upward directed seepage forces that support the settling grains. Under these conditions, the upward front velocity, u_{front} , is

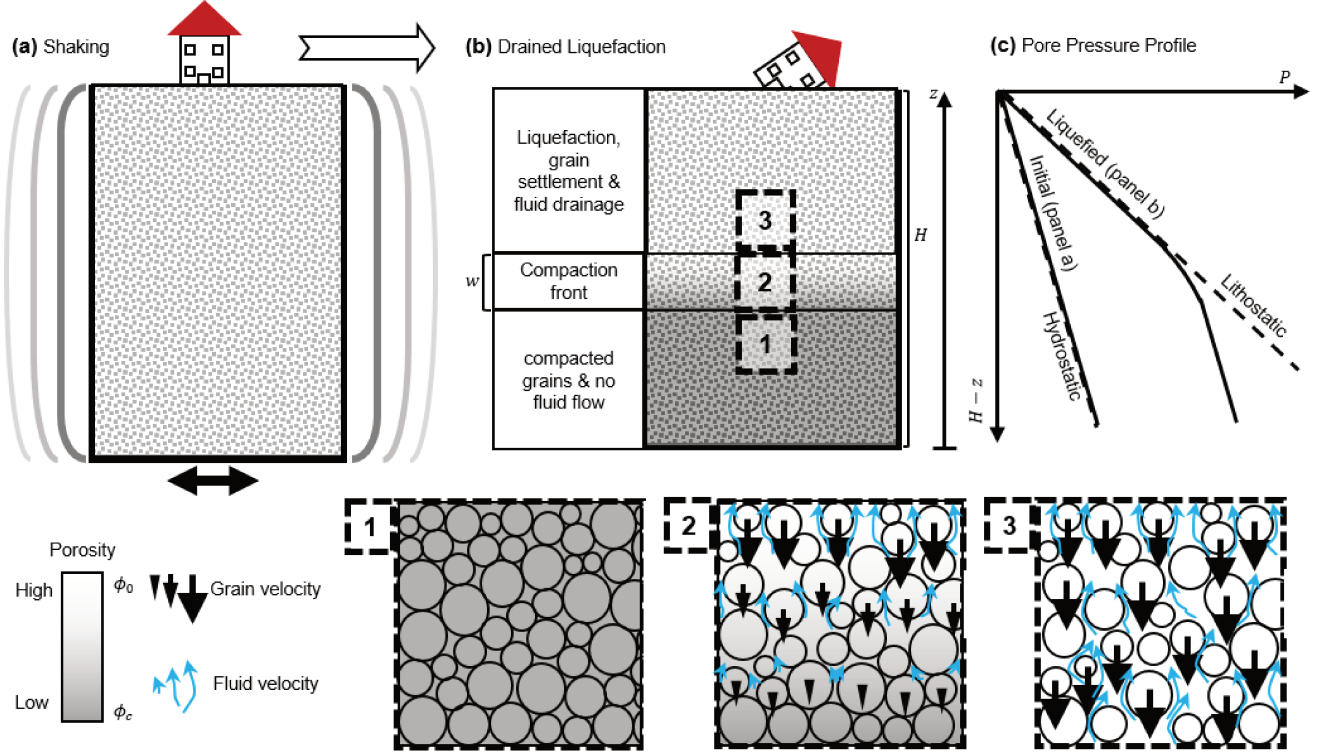


Figure 1: Schematics of the compaction front dynamics that develop under drained conditions. (a) An earthquake shakes a saturated soil layer of initial thickness H , and porosity ϕ_0 . (b) a compaction front swipes upwards, separating a (1) compacted region with porosity ϕ_c , and negligible grain vertical velocity and fluid flow, from (3) a liquefied region with porosity ϕ_0 , an upwards fluid flow and a downwards grain settling velocity. The transition between the regions occurs gradually along a compaction front (2), whose width is w . (c) The pore pressure gradient is initially hydrostatic. After the formation of the compaction front and the initiation of liquefaction, the pore pressure gradient above the front is equal to the lithostatic stress gradient. Below the front, the pressure gradient is hydrostatic (which causes no fluid flow), although the pressure itself is elevated.

theoretically predicted to be²⁷:

$$u_{\text{front}} = \frac{\phi_0 - 1}{\phi_0 - \phi_c} \frac{\kappa_0}{\eta} \frac{d\sigma_0}{dz}, \quad (4)$$

where $d\sigma_0/dz$ is the effective static normal stress gradient (Fig. 1).

The uniform porosities above (ϕ_0) and below (ϕ_c) the front imply that active compaction occurs only across the relatively narrow front. Furthermore, the upward propagating narrow front acts as an in-situ, migrating pressure source, which continuously forces upward fluid drainage²⁷ (Fig. 1).

This compaction front is in many aspects similar to previously described post-liquefaction "solidification fronts", which are preceded by an undrained liquefaction initiation and could result in consolidation^{31,38}. In the drained end-member described here, the compaction front forms and migrates co-seismically, and its very migration causes liquefaction above it, as demonstrated next.

3 Results

We performed grain-scale simulations and experiments of horizontally shaken layers of water-saturated cohesionless grains with a free surface. The simulations used a coupled Discrete Element Method (DEM) - Computational Fluid Dynamics (CFD) model⁴⁰ and the experiments were conducted in a transparent box, allowing inferences of grain motion and measurements of pore pressure by using an array of pressure transducers (see Methods). The simulations and experiments show the dynamics predicted by the compaction front model.

3.1 Evaluating the drainage conditions

The drainage conditions in the simulations and experiments were evaluated by estimating the De number following equation (3). The length scale controlling pressure gradients (and thus fluid fluxes) is conservatively chosen here as $h = H$, where H is the layer height⁴¹. In situations of homogeneous compaction and dilation⁴¹, H would also control the divergence of fluid flux and grain motion. However, when a compaction front is present, grain compaction and dilation are localized³⁶ at the front. A different natural length scale thus emerges for the divergence of fluid flux and grain motion as $l = w < H$, where w (Fig. 1) is the width of the compaction front. The simulations and experiments show that w spans several tens of grain diameters (≈ 20). As a consequence, the maximal value of De is $\sim 10^{-2}$ in the simulations and $\sim 10^{-4}$ in the experiments (see Table 1 for simulation and experiment parameters). This analysis indicates that the behavior we observed in the experiments and simulations arises from drained layer dynamics.

3.2 Liquefaction indicators in drained layers

Simulations and experiments determined to be controlled by drained dynamics show four indicators that are widely associated with soil liquefaction in the field and the lab: pore pressure rise, soil settlement, attenuation of shear waves, and degradation of shear modulus.

The dynamic pore pressure rises quickly in response to the onset of horizontal shaking and reaches approximately the value of the initial effective vertical solid stress (Fig. 2a). The duration at which the pore pressure remains elevated is a function of depth²⁷ and is set by the compaction front arrival. Once the front passes a certain depth, the pore pressure starts to decrease, so the closer a point is to the surface, the longer the pressure remains elevated at that point. The event ends at a time, t_e , which corresponds to the time it takes to initiate liquefaction, t_i , plus the time it takes the compaction front to propagate a distance $L \leq H$, from its initiation depth (Figs. 6 . 7) to the surface, $t_e = t_i + L/u_{\text{front}}$. The initiation time, t_i , is found here to be exceedingly short, with a conservative median value of 0.25 seconds in simulations and 2.5 seconds in experiments (see also section 10.4).

Concurrently with the pore pressure rise, the excited soil layer compacts continuously and linearly (Fig. 2b). Despite continued shaking, we find that the soil stops settling and reaches a new equilibrium configuration after time t_e .

Grains are shaken horizontally by the shear waves, which propagate from the excited layer base. Fig. 2c presents the mean horizontal grain velocity time series at different depths. Shortly after the onset of shaking, shear wave

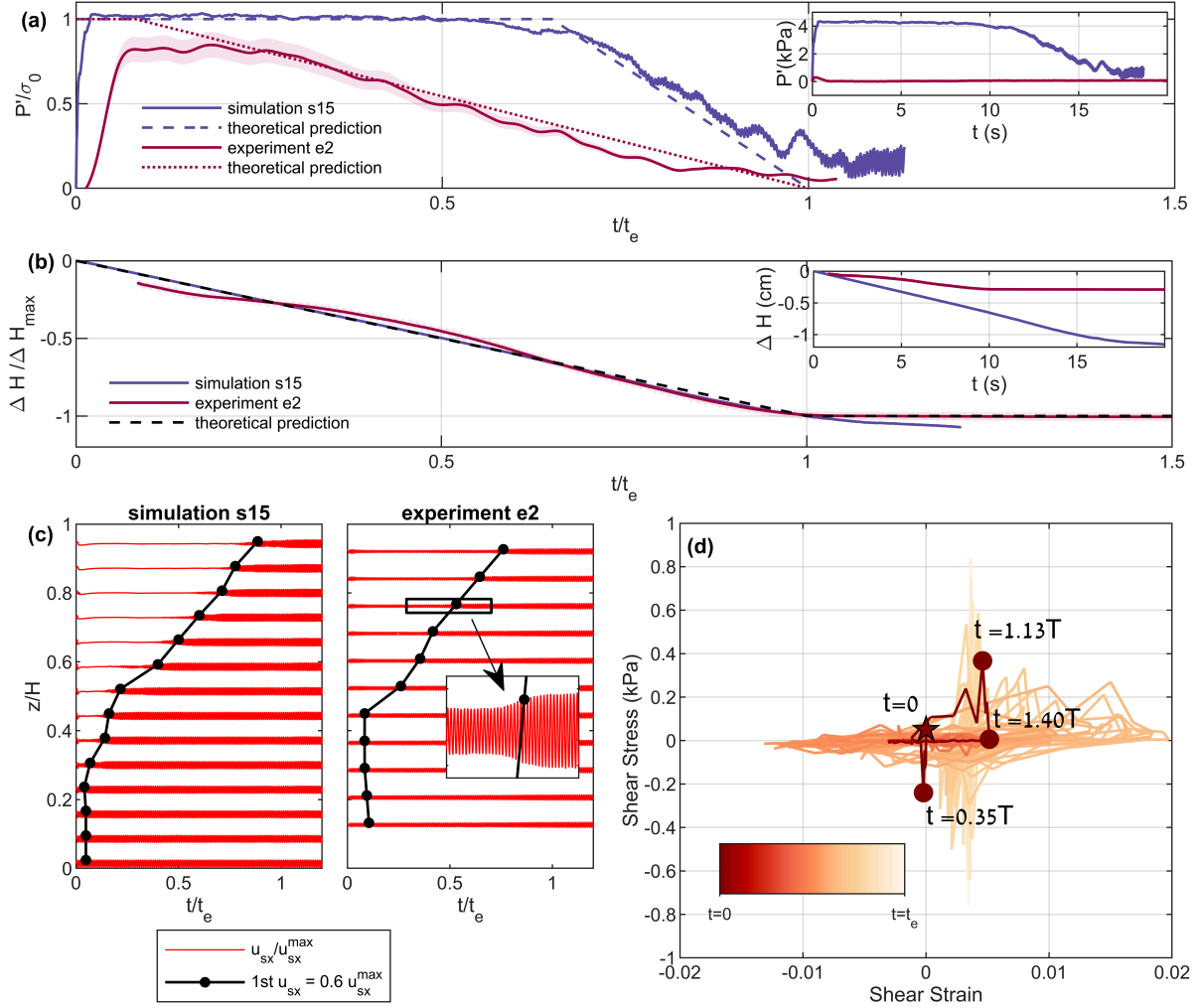


Figure 2: Liquefaction indicators in drained simulations and experiments. (a) Dynamic pore pressure at an approximately mid-depth of the grain layer. The axes are normalized to facilitate comparison between the simulation and experiment. t_e is defined based on panel b, as the time at which soil compaction significantly slows. Dashed and dotted lines represent theoretical predictions under the assumption of an infinitely narrow compaction front (equation 27 in ref. ²⁷), for the simulation and experiment, respectively. The shaded red background represents the uncertainty on the experimental pressure measurement. The pore pressure starts decreasing when the front passes past the measurement depth. Inset shows non-normalized values. (b) Grain settlement and whole layer compaction. ΔH_{max} refers to the end of the linear settlement phase. Dashed line depicts the theoretical prediction based on a time integral of Eq. 6. The shaded red background represents the uncertainty on the settlement measurement in the experiment. The inset shows non-normalized values. (c) Shear wave attenuation. The red velocigrams represent the grains' mean horizontal velocity at various depths, normalized by the maximum value. The black lines depict the first appearance of $u_{sx} = 0.6 u_{sx}^{max}$, approximating the arrival of the compaction front. Inset shows a vertical exaggeration of the black rectangle. The lower horizontal velocity, seen before front arrival, indicates a liquefied region which is unable to transmit shear waves. (d) Shear stress-strain curves in simulation s15. The color code corresponds to time in the simulations (the star marks $t = 0$). The slope of the stress-strain curves represents the shear modulus. The shear modulus degrades rapidly, within $\approx 1.4T$, where T is the shaking periodicity, and then gradually strengthens.

amplitudes become strongly attenuated throughout the layer, as expected from a fluid-like medium. At any given depth, attenuation persists until the compaction front arrives, after which shear-waves resume the amplitude of the input shear. The black lines in Fig. 2c follow the positions where the velocity amplitude increases back to $> 60\%$ of the maximum velocity (imposed at the bottom boundary), chosen here to depict the front position. The observed trend indicates that, similar to the pore pressure dynamics, attenuation lasts longer closer to the surface and overall continues up to $\sim t_e$.

Fig. 2d presents the relation between the shear stress and the shear strain at the mid-depth of a simulation layer. The mean slope of the stress-strain curve, known as the shear modulus, is used as a metric for the shear strength of a material^{42,43}. We observe that the stress-strain curve flattens soon after the application of shaking, over less than two shear cycles, indicating that the saturated soil layer has dynamically lost its shear strength. The soil progressively regains its strength as the front progresses upwards, displaying a finite stress-strain slope.

3.3 Drained liquefaction beyond the near field in simulations and experiments

The simulations and experiments were forced with a range of shaking amplitudes (A) and frequencies (ω) (Tables 2&3), leading to an energy density range of $0.07 - 7 \text{ J m}^{-3}$. The average seismic energy density in one shear cycle is calculated as $e = (\rho_s/4) PGV^2$ ^{16,44}, where $PGV = A\omega$ is the amplitude of the imposed harmonic cyclic velocity. Thus, the four liquefaction indicators emerged although the input energy density corresponded to low, far-field, values and was smaller than the previously established liquefaction triggering threshold of 30 J/m^3 ^{15,16}.

Analysis of simulation results further shows that the change in porosity across the compaction front, $\Delta\phi = \phi_0 - \phi_c$, correlates with the applied seismic energy density (Fig. 3a), and has an excellent correlation with the rate of the seismic energy density input (Fig. 3b), which can be evaluated as the seismic energy density over one period of shaking, e/T (or as the seismic power proportional to $PGV \cdot PGA$ in mono frequency harmonic oscillations).

Consistent with the prediction of equation (4), we further find that a larger porosity change is associated with a slower propagating compaction front (Fig. 3c) and a longer liquefaction event, $t_e \propto 1/u_{\text{front}}$.

Combining the above dependencies (Figs. 3a and 3c), a power-law relation emerges between the front velocity scaled by the permeability and the energy density (Fig. 3d). Forcing the system with a large energy density, yet lower than the predicted liquefaction triggering threshold, generates more compaction, a slower front velocity, and a longer liquefaction event. In contrast, a small energy density input induces only a small change in porosity across the front, leading to a rapid front propagation and a short-lived liquefaction event.

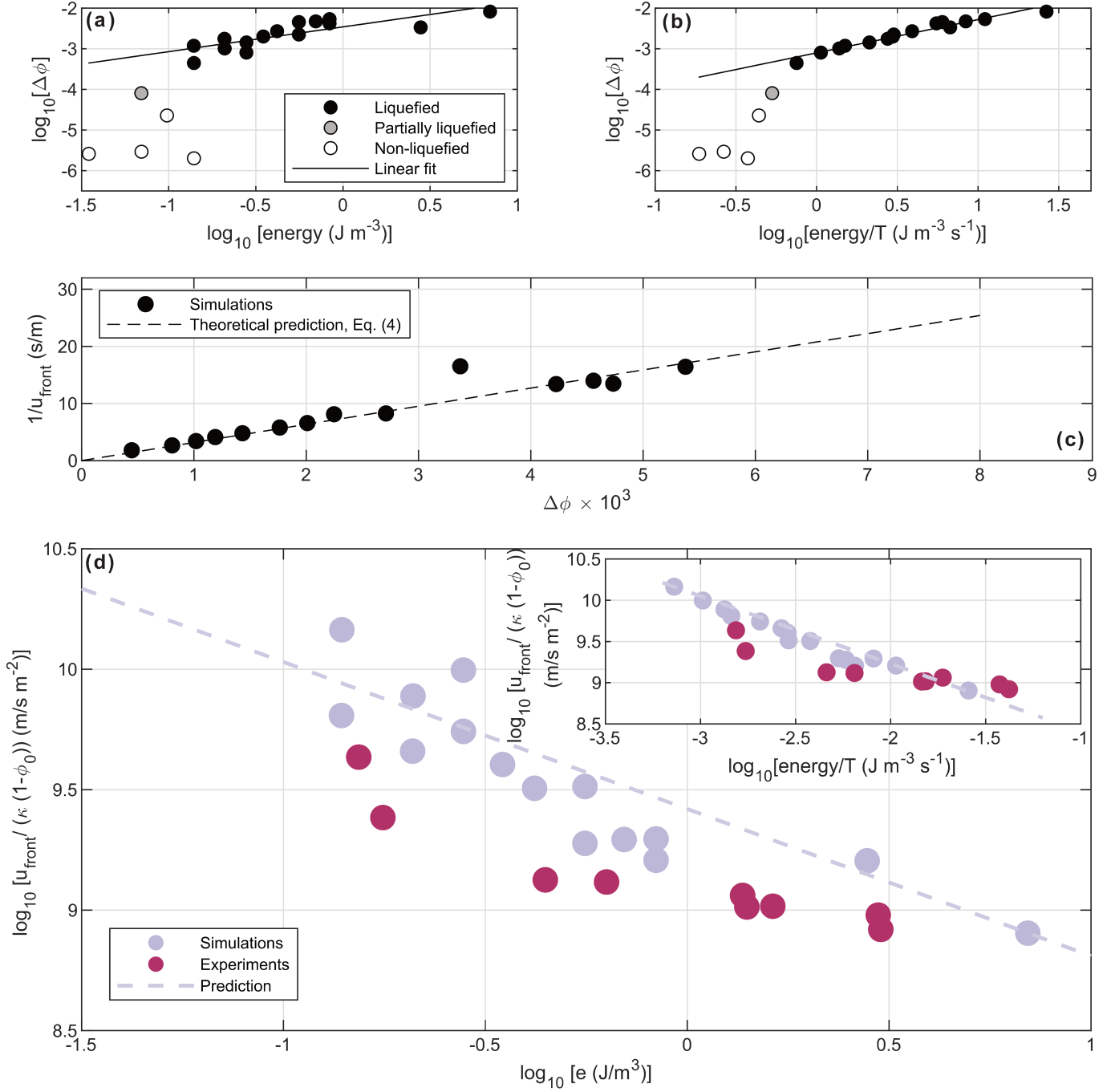


Figure 3: Relations between porosity change, seismic energy density, rate of energy density and compaction front velocity. (a) Change in porosity $\Delta\phi$ across the front, vs. the imposed seismic energy density in the simulations. A linear fit is depicted by the solid black line ($Y = 0.61 X - 2.46$; $R^2 = 0.66$). Gray and white markers were excluded from the linear fit. (b) Change in porosity vs. the rate of seismic energy density input (seismic power). The linear fit is $Y = 0.82 X - 3.1$; $R^2 = 0.95$. (c) Inverse compaction front mean velocity vs. $\Delta\phi$. The black dashed line is the theoretical prediction of Eq. 4. (d) Normalized front velocity vs. the imposed seismic energy density in simulations and experiments. The inset shows the normalized front velocity vs. the rate of the seismic energy density input (seismic power). Note that the energy densities (abscissa) used in the simulations and experiments, which showed the four liquefaction indicators, are below the undrained liquefaction triggering threshold of 30 J m^{-3} . The emerging trend shows that the compaction front propagates faster and the duration of the liquefaction event, t_e , is shorter, when the energy density (and seismic power) are lower. The prediction for the simulations (dashed line with a slope of -0.6) is based on Eq. 4 and the linear fit presented in Fig. 3a. The experimental data shows a similar power-law exponent (slope). The errors on the normalized front velocity are smaller than symbols size.

4 Discussion

4.1 The dynamics of drained liquefaction

The four liquefaction indicators observed in the low De number simulations and experiments demonstrate that liquefaction can initiate under drained conditions. In such cases, efficient drainage is key in facilitating the dynamic rheological change of the soil layer. The upward fluid flow between the compaction front and the free surface generated lithostatic pore pressure gradients (Fig. 2a) that supported the weight of the grains, so that granular contact forces vanished. The loss of grain contacts caused the shear modulus to drop (Fig. 2d) and the shear waves to attenuate (Fig. 2c). Ongoing evacuation of fluid from the compaction front facilitated homogeneous continuous layer settlement (Fig. 2b).

Relying on the inferred drained conditions ($De \ll 1$), Eq. 2, describing the pore pressure evolution can be simplified by neglecting the first term relative to the second and third terms. Consequently, it reduces to a two terms equation²⁷:

$$u_{sz} = \frac{\kappa_0}{\eta} \frac{\partial P'}{\partial z}, \quad (5)$$

where u_{sz} is the downward solid grains velocity. Equation (5) describes a compaction-pressurization feedback whereby the pressure gradient responds to instantaneous grain velocity and holds no memory of the previous pressure state²². In accordance with the prediction of the compaction front model, below the compaction front, where $u_{sz} \approx 0$, no dynamic pressure gradient develops and the total pressure gradient is approximately hydrostatic. Above the front, the grains settle at a uniform velocity, leading to a uniform pressure gradient. The compaction front coincides with the location where u_{sz} changes from finite to zero (Fig. 1b and insets).

Similar to the undrained end-member, drained liquefaction is triggered by shaking-induced destabilization of the granular skeleton through sliding and rolling over grain contacts. At the lowest position of failure, compaction occurs relative to the stable grains below, potentially prescribing the initiation depth of the compaction front, $z_{\text{front}}(t_i)$ (see Appendix C for more details). The pressure gradient and seepage forces that develop in response to this initial compaction only partially support the weight of the settling grains. As long as the pressure gradient remains smaller than lithostatic, the force balance on the settling grains promotes downward acceleration and faster settlement, leading to greater pressure gradients. Once the pressure gradient reaches lithostatic values, it fully supports the weight of the grains. The force balance over the settling grains is then zero, and the grains continue to settle at a constant, terminal velocity²⁷:

$$u_{szC} = \frac{\kappa_0}{\eta} \frac{d\sigma_0}{dz}, \quad (6)$$

where subscript C stands for a constant velocity. This terminal constant velocity dictates the linear compaction trend observed in Fig. 2b.

The timescale associated with pore pressure rise to lithostatic values in the simulations and experiments is short,

and likely related to a rapid downward propagating liquefaction front. Such a behavior, viewed as "unloading" fronts³⁸, was previously identified in experiments^{38,45,46} (see Methods section 10.4 and section A in the supplementary material). We observed that the deepest location to which the down-going liquefaction front reaches correlates with the imposed shaking frequency (Appendix C), and that the liquefaction front reaches this deepest location in less than two shear cycles, consistent with previous experiments conducted under drained conditions^{31,32}. Another timescale operating in the system is the time required for an isolated, fully immersed, grain (equation 5, Appendix B) to reach its terminal downward velocity. However, since this timescale is exceedingly small, $10^{-3} - 10^{-8}$ seconds, the acceleration of a single grain is not a rate-limiting process for triggering drained liquefaction. Recent cyclic triaxial experiments²⁸ found that the number of cycles required to initiate liquefaction under drained conditions is smaller than under undrained conditions, supporting the hypothesis that a pressurization time of the order of a few cycles could be indicative of drained liquefaction initiation. Such a consideration might apply to a recent ground motion analysis showing that, in some cases, the time for liquefaction triggering is as short as ~ 1.7 seconds from the onset of recorded shaking^{47,48}.

Different approaches have been proposed to evaluate soil liquefaction potential. Among these, the shear stress or the earthquake peak ground acceleration (PGA)²⁶ forms the theoretical basis for the widely used "simplified procedure for evaluating soil liquefaction potential"⁴⁹⁻⁵¹. Other approaches emphasize the shear strain¹⁴ or the seismic energy^{15,52-54} in identifying liquefaction triggering thresholds. Importantly, although the three approaches are mechanically linked, their predictions could differ⁵⁵. The current numerical liquefaction events show a good correlation between the seismic energy density (which follows PGV^2) and settlement magnitude (Fig. 3a). Furthermore, both numerical and experimental results show a good correlation between the seismic energy density and the front velocity (Fig. 3d). An even better correlation is found with the rate of seismic energy density input (seismic power, Fig. 3b,d). Both robust correlations emerged despite inherent differences in the boundary conditions and geometrical setup between the simulations and experiments, suggesting that, within the framework of drained liquefaction triggering, the seismic energy density, and possibly a new measure, the rate of seismic energy input (seismic power), can be considered as controlling parameters on the magnitude and duration of liquefaction events.

A leading energy-based approach for evaluating soil liquefaction potential uses the earthquake's Arias intensity⁵⁴. While the Arias intensity is a cumulative measure that accounts for the amplitude and frequency content throughout the duration of the earthquake, the rate of seismic energy density input (e/T), which we consider here, can be interpreted as a quasi-instantaneous Arias intensity or an average power of ground shaking over one shear cycle. The excellent performance of the rate of seismic energy density input in explaining the amount of compaction (Fig.3b) and the front velocity (Fig.3d inset), and in defining the clearest threshold between liquefied and non-liquefied simulations (Fig.3b) suggests that a dynamic process as drained liquefaction depends on the momentary power rather than on the cumulative power. This is likely in contrast to undrained liquefaction, which is a cumulative process in nature (the volumetric strain required to initiate liquefaction is accumulated over many shear cycles¹³), hence it might depend on a cumulative energy measure like Arias intensity.

4.2 Drained liquefaction beyond the near field in nature

Our simulations and experiments show that drained liquefaction (with $De \ll 1$) is triggered when forced with an energy density $< 30 \text{ J m}^{-3}$ and as small as 0.1 J m^{-3} . The De number (Eq. 3) can be evaluated to be smaller than one in many natural settings. For example, using representative values of a 5 meters deep soil layer, comprising 1 mm diameter grains, and assuming a 20 grains thick compaction front, gives $De = 10^{-4} - 10^{-1}$, when the permeability range is $\kappa_0 = 10^{-9} - 10^{-12} \text{ m}^2$. Consequently, drained liquefaction initiation can be invoked as a general mechanism to explain field observations of liquefaction beyond the earthquake near field, accounting for the previously puzzling 61% of the events reviewed in ref.^{16,17} (Fig 4a).

We propose that the compaction-pressurization feedback, inherent to the drained compaction front dynamics²⁷, is a pivotal player in neutralizing the energy density threshold. With this feedback, small compaction induced by low energy density⁵⁶ (or more precisely, low rate of energy density input, e/T), presumably facilitated by failure of the weakest grain contacts^{57,58}, generates the initial pressure gradient. The associated seepage forces partially support the weight of the surrounding grains, weakening their contacts and promoting further sliding between grains, compaction, and pressurization, until a lithostatic pressure gradient is achieved and complete liquefaction occurs.

The data of field liquefaction events^{16,17} show that the number of recorded events decays relatively rapidly below $e = 1 \text{ J m}^{-3}$ and no events are recorded when $e < 0.1 \text{ J m}^{-3}$ (Fig. 4a). Others⁵⁹ observed a similar trend regarding the decay of field liquefaction events with low PGV (proportional to the square root of the seismic energy density⁴⁴), where no liquefaction was observed below $PGV = 0.03 \text{ m s}^{-1}$ ($e \approx 0.5 \text{ J m}^{-3}$). The links we find between the input energy density and the layer permeability, on the one hand, and the compaction front velocity, on the other hand, could explain these observations. With a lower energy density or a larger permeability, the front velocity increases (Eq. 4), producing a short-lived liquefaction event (Fig. 4b), that is less likely to be observed or recorded. Furthermore, with a lower energy density, compaction across the front, $\phi_0 - \phi_c$, is smaller (Fig. 3a) and less ground settlement occurs (Fig. 4c), potentially reducing the associated hazard. The decay of the number of events and the limit on documented liquefaction event^{16,17} could therefore be explained within the drained liquefaction triggering framework as a combination of an asymptotically shorter-lived (Fig. 4b) and smaller-settlement events (Fig. 4c), and a seismic energy threshold below which liquefaction does not occur (Fig. 3a-b). Alternatively, it is possible to define a PGA threshold^{26,27,60} for liquefaction triggering in the current simulation set, which we find to have an exceptionally low value of $A\omega/g \approx 0.05$ (see Table 2).

The analysis above does not account for the finite duration of earthquakes, t_{EQ} , which can be shorter or longer than the event termination time, t_e (dictated by the front velocity, as discussed above). After time t_{EQ} , the seismic energy input drops to zero. The post-seismic evacuation of the excess pore pressure occurs at a rate that depends mainly on the permeability and, in our simulations and experiments, is accompanied by negligible residual compaction. The real duration of a drained liquefaction event is thus the minimum between t_e and t_{EQ} , where t_{EQ} is typically of the order of tens of seconds for moderate to large earthquakes (Fig. 4b-c). When the permeability is high and the seismic

energy low, $t_e < t_{EQ}$, the total compaction is dictated by the front passing through the whole layer, converting the porosity from ϕ_0 to ϕ_c , where $\Delta\phi$ is controlled by seismic energy density (sloping gray line in Fig. 4c). However, when the permeability is low, and the seismic energy is high, $t_e > t_{EQ}$, the front does not have sufficient time to sweep the whole layer during the earthquake. The total compaction, in this case, is independent of seismic energy density, and instead depends on permeability. The permeability controls the settling velocity of grains in the liquefied sub-layer, and the total compaction is then the integral of the settling velocity over time t_{EQ} (horizontal lines in Fig. 4c).

4.3 Complicated geometries

In our simulations and experiments, the water table was taken to coincide with the grain layer free surface. In such settings, fluid expulsion out of the soil layer will start concurrently with drained liquefaction initiation. However, if the water table lies much below the surface, fluid expulsion out of the soil during drained liquefaction initiation could be delayed. In cases where the water table is sufficiently deep, and the energy density is relatively low (inducing only a small $\Delta\phi$), the water table might not reach the surface during liquefaction, and no fluid expulsion out of the surface would be observed. Coseismic settling of the ground surface, on the other hand, will take place even in the absence of fluid expulsion. Other liquefaction indicators could still persist, even if not documented. Delayed fluid expulsion should therefore, not be a-priori considered as an indication for undrained liquefaction initiation followed by a breach of low permeability barrier, or as an indicator for liquefaction by pore pressure diffusion from a distant source^{7,16,18}. Instead, it could also be consistent with a drained initiation if the water table was originally relatively deep (see Appendix D).

In nature, a soil column might not be homogeneous as in our simulations and experiments and may comprise interchanges between sub-layers with variable permeability. Centrifuge experiments⁶¹ and numerical simulations⁶² show that a water-film may form below a low permeability seam. If the fluid flow upwards across the seam is slow and the seam is not broken yet, the water-film may change its volume to preserve a constant lithostatic water pressure boundary condition for the layer below the seam (by "pushing" the seam upwards⁶¹). This promotes a behavior very similar to the presented drained compaction front relative to the seam, where the higher permeability sub-layer below the seam is compacting and the fluid drains towards the water film (rather than directly to the surface). A further investigation of such a setting is needed to examine the initial pressurization process and its sensitivity to the seismic energy density.

5 Conclusions

Our analysis reveals that earthquake-induced soil liquefaction should be seen as a field phenomenon rather than a synonym for the single undrained pressurization mechanism. Particularly, liquefaction can occur under a full spectrum of drainage conditions. Low permeability and large depths contribute to an effectively undrained soil response, leading to $De \gg 1$. High shaking frequency (short periodicity, T) which is associated with high seismic energy density,

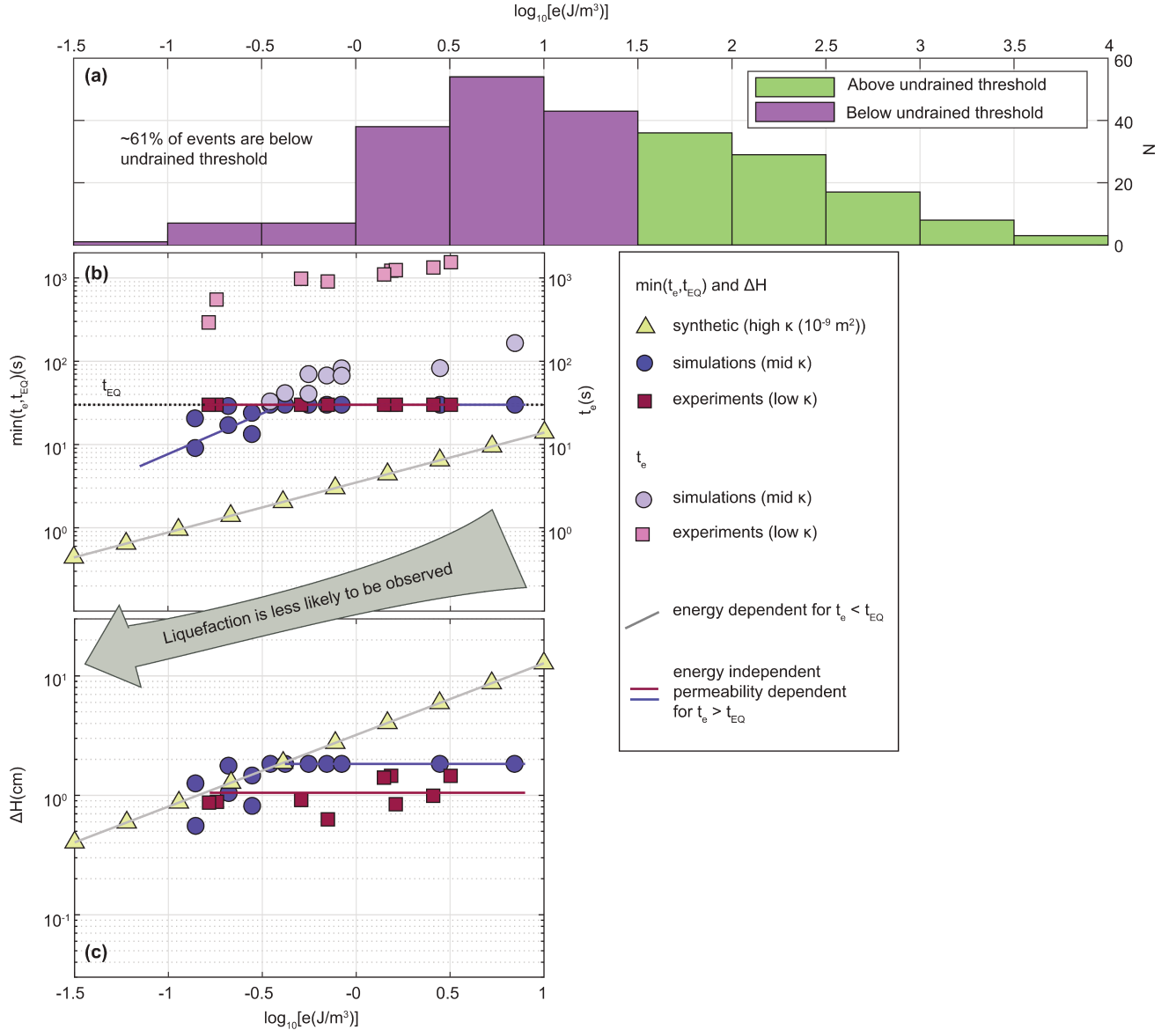


Figure 4: The duration and magnitude of drained liquefaction explain the distribution of field data beyond the near field. (a) Liquefaction data from ref.¹⁷ classified by seismic energy density, e , shows 61% of documented field events occur below the undrained liquefaction threshold and are therefore unexplained by the undrained process. In contrast, the numerical and experimental liquefaction events depicted in panels b and c, all occur below the undrained threshold. (b) Event duration, $t_e = H/u_{\text{front}}$ (see section 3.2) calculated for $H = 5$ m as function of the energy density of the imposed cyclic shear. The black horizontal line depicts a typical duration of a moderate to large earthquake, $t_{EQ} = 30$ s. Light coloured markers and the RHS axis show the predicted events duration if they were unbounded by the earthquake duration. Darker shaded markers and LHS axis present the duration of the potentially recordable liquefaction event, $\min(t_e, t_{EQ})$. Yellow markers are synthetic data with assumed higher permeability. (c) Calculated surface settlement, assuming a five meter deep soil column ($H = 5$ m). For high permeability soils and low energy density, $t_e < t_{EQ}$, and compaction increases with energy density (symbols that follow the gray line). When the permeability is lower and energy density is higher, $t_e > t_{EQ}$, drained liquefaction ceases after t_{EQ} and the total settlement is independent of the energy and depends on the permeability (symbols following the red and blue horizontal lines). Overall, liquefaction is less likely to be observed under low energy input due to its short duration and smaller surface settlement.

contributes as well to an effectively undrained soil response, suggesting that the undrained initiation end-member likely dominates close to the earthquake epicenter (near-field). On the other hand, permeable soils and shallow depths contribute to effectively drained conditions, with $De \ll 1$. Lower shaking frequency (long periodicity T), which is associated with smaller energy density, contributes as well to effectively drained conditions, suggesting that the drained initiation end-member likely dominates far away from the earthquake epicenter (intermediate to far-field).

The discovery that high permeability, well-drained soils should not be apriori assumed liquefaction resistant, and that low energy density input, corresponding to the earthquake far-field conditions, could induce soil liquefaction should reform how liquefaction potential and risk are evaluated, and how the associated hazard is accounted for.

6 Acknowledgements

S.B.-Z : Thanks Alain Steyer and Miloud Talib for technical assistance with the experiments, Martine Trautmann for granulometry and the support of Institut Français d’Israël and Campus France via the Chateaubriand Fellowship. S.B.-Z and E.A. wish to thank Assaf Klar and Eitan Cohen for a fruitful discussion. R.T. wishes to thank Eirik Flekkøy for fruitful discussions L.G. acknowledges support from ISF grant 562/19. E.A thanks ISF grant #910/17. R.T acknowledges the support of the CNRS INSU ALÉAS and CESSUR programs, the CNRS MITI program, the Universities of Strasbourg and Oslo and the Research Council of Norway through its Centre of Excellence funding scheme, project number 262644.

7 Author contributions

S.B.-Z. conducted the experiments under the supervision of R.T., and the numerical simulations under the supervision of L.G. and E.A.. S.B.-Z. produced the figures with the aid of L.G.. S.B.-Z. led the writing and all authors contributed to writing and editing the manuscript.

8 Competing interests

The authors declare no competing interests.

9 Additional information

Correspondence and requests for materials should be addressed to S.B.-Z.

10 Methods

10.1 A general description of the grain-fluid system

We study the coupled grain-fluid dynamics of a fully saturated granular layer subjected to 1D horizontal harmonic shear displacement. The top of the layer is unconfined. Horizontal cyclic shear is applied to the base of the layer, which acts as a no-flow boundary for the fluid. This geometry represents a shallow soil layer overlaying a bedrock that is agitated by an upward traveling horizontally polarized seismic shear wave.

10.2 Numerical simulations

The numerical approach is described in^{22,27}. Here, we repeat its main details. We use a two-phase coupled model. The grains are modeled using the discrete element method⁶³, and the interstitial pore fluid is modeled as a continuum on a superimposed Eulerian grid^{34,40,64–67}.

Grain velocity and position are resolved by time integration of the linear and rotational momentum conservation equations²⁷:

$$m_i \dot{\mathbf{u}}_{\mathbf{s},i} = m_i \mathbf{g} - V_{\text{imm},i} \rho_f \mathbf{g} + \sum_j \mathbf{F}_{ij} - \frac{\nabla P' \cdot V_i}{1 - \phi} \quad (7)$$

$$I_i \dot{\boldsymbol{\omega}}_{\mathbf{s},i} = \sum_j R_i \hat{\mathbf{n}}_{ij} \times \mathbf{F}_{ij}, \quad (8)$$

where $\dot{\mathbf{u}}_{\mathbf{s},i}$ and $\dot{\boldsymbol{\omega}}_{\mathbf{s},i}$ are the translational and rotational accelerations of grain i (dot notation indicates time derivative) and m_i and I_i are the mass and moment of inertia of grain i . R_i is the radius of grain i and $\hat{\mathbf{n}}_{ij}$ is a unit vector along the direction connecting the centers of grains i and j . In Eq. 7, the first term on the right hand side is the gravitational force, where \mathbf{g} is the gravitational acceleration. The second term is the buoyancy force, whose magnitude depends on the grain immersed volume $V_{\text{imm},i}$ and the fluid density ρ_f ²⁶. The third term is the sum of contact forces (\mathbf{F}_{ij}) over all grains j that are in contact with grain i , calculated with a linear contact model⁶³. The fourth term represents the seepage force exerted by the gradient of the dynamic pore pressure, $\nabla P'$, where V_i is the volume of grain i .

The evolution of the interstitial fluid pressure is represented by Eq. 1²², which is solved by using an implicit scheme over a square grid, with grid spacing of two average grain diameters^{21,22,34,65}. No a-priori assumption is made regarding the value of the De number (Eq. 3) and the relative importance of the three terms in the equation.

The two-way coupling between the grains and the fluid is implemented as follows. The fourth term on the right hand side of equation (7) is evaluated via a bilinear interpolation of $\nabla P'/(1 - \phi)$ from the surrounding grid nodes to grain i . The second and third terms of Eq. (1) are evaluated by defining smooth fields of grain velocity and porosity over the grid through a bi-linear interpolation of grain radius and velocity from individual grains surrounding each

grid node. The permeability, κ , in Eq. (1) is calculated based on a three dimensional Kozeny-Carman relation⁶⁸:

$$\kappa = \kappa_1 \kappa'(x, y, t) = \alpha r^2 \frac{\phi^3}{(1 - \phi)^2}, \quad (9)$$

where r^2 is the bi-linearly interpolated squared grain radii in the surroundings. $\kappa_1 = \alpha \langle r \rangle^2$ is a constant prefactor, and $\kappa' = r'^2 f(\phi)$ captures permeability variations in space and time. $\langle r \rangle$ is the mean grain radius in the system and r' is the local deviation from it, such that $r = \langle r \rangle r'$. In the original Kozeny-Carman relation, $\alpha = 1/45$ ⁶⁸ is a geometrical prefactor for spheres. In our simulations, we vary α to directly control the order of magnitude of the permeability independent of the grain size^{22,27}.

The geometry of the numerical layer (Fig. 5a) is a Hele-Shaw cell comprising spherical grains with grain radii between 0.8 – 1.2 cm, drawn from a normal distribution with a mean of 1 cm and a standard deviation of 1 cm. The system's horizontal dimension is 0.4 m. The layer is prepared as follows: First, a target height is specified. Then, grains are sedimented under gravity onto the bottom wall in a fluid-free environment. Next, to slightly compact the layer, a short horizontal shaking phase is applied over 0.62 seconds with $f = 12$ Hz and amplitude of $A = 0.0431$ centimeters, followed by 0.13 s relaxation, where no external forces aside from gravity are applied. Finally, the fluid is added, so its height approximately coincides with the top of the grain layer. In the simulations presented here, the initial layer height, following the preparation stage, is $H \approx 1.44$ m.

The bottom wall of the numerical Hele-Shaw cell is made of half grains glued together. The boundary condition for the bottom wall is zero velocity in the vertical direction ($u_{sz}(z = \text{bottom}, t) = 0$) and sinusoidal displacement in the horizontal direction, $x(z = \text{bottom}, t) = A(1 - \cos(\omega t))$, where A and ω are the shearing amplitude and angular frequency, respectively. At the top boundary, there are no normal or shear stresses. The boundary conditions for the fluid phase are no flow boundary at the bottom ($\partial P'/\partial z(z = \text{bottom}, t) = 0$) and constant pressure boundary at the top ($P'(z = \text{top}, t) = 0$). The water level is maintained at its initial height throughout the simulation. The side boundaries are periodic for the grains and pore fluid, mimicking a laterally infinitely long layer.

Table 1 summarizes the simulations' parameters. Table 2 lists the simulations presented here with their applied shear amplitude and frequency. The pressure signal in Fig. 2a is smoothed over a window of two cycles. The compaction in Fig. 2b is calculated as the time integral of the mean vertical velocity of grains in the topmost sub-layer.

10.3 Experiments

The experiments (Fig. 5b-e) comprise a $12 \times 12 \times 12$ cm³ transparent box. The box is attached to a horizontal shaker (Tira[®] S51120) fed with a harmonic signal from a signal generator (Agilent[®] 33220A) through an amplifier (BAA500). The box's face perpendicular to the shaking direction is filmed by a high-speed camera (Photron[®] SA5) at a rate of 250 frames per second. The frames are analyzed by using MATLAB[®] image processing toolbox and PIVlab^{69,70}, an open-source MATLAB[®] toolbox, to identify changes in the layer's height and define instantaneous grain velocity. An array of three pressure transducers (Honeywell 24PC) is mounted vertically on the opposite parallel face of the box at

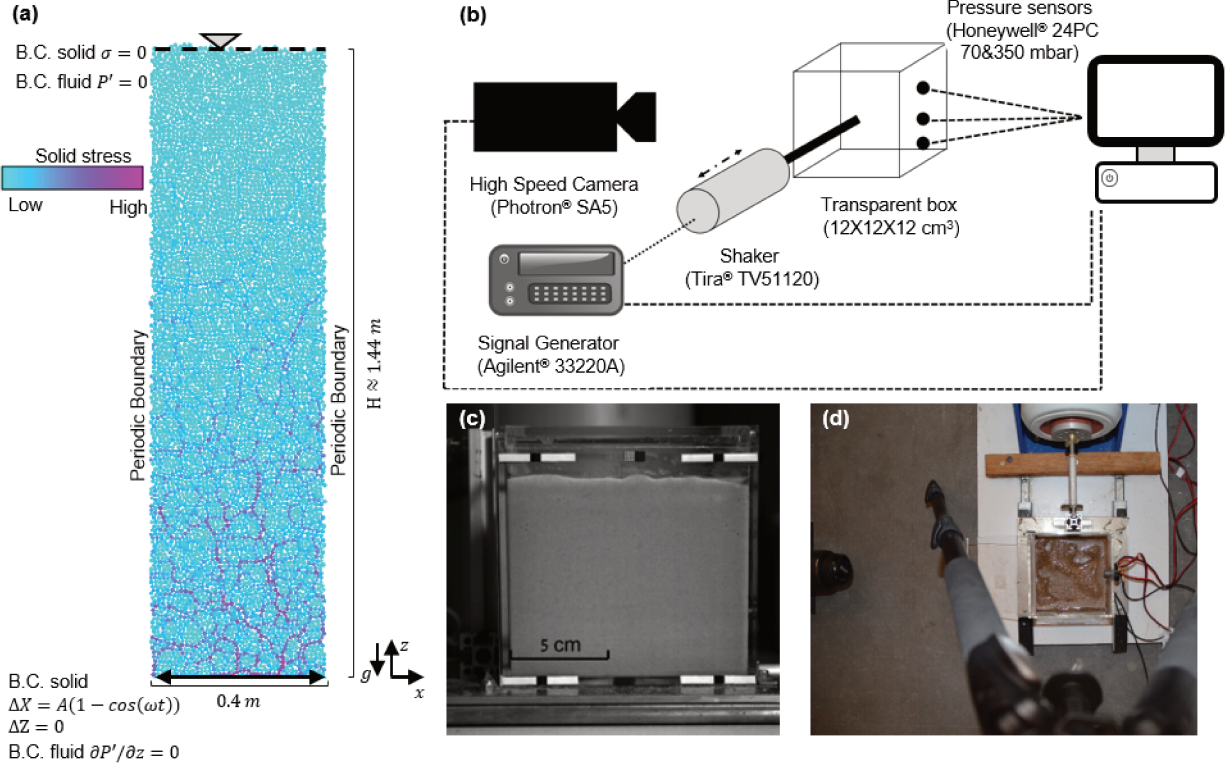


Figure 5: (a) Schematics of the simulations setup and boundary conditions. (b) Schematics of the experimental setup. (c) The front face of the experiment box (a frame from the high speed camera used for velocimetry). (d) Top view of the experiment box. The shaker is seen at the top of the photo and the high speed camera lenses are at the left.

Table 1: Physical parameters in simulations and experiments

Parameter	Simulations	Experiments	Units
mean grain density (ρ_s)	2,640	2,650	kg m ⁻³
fluid density (ρ_f)	1,000	$\sim 1,000$	kg m ⁻³
mean grain radius (r_s)	0.5	0.01	cm
fluid compressibility (β_f)	$4.5 \cdot 10^{-10}$	$\sim 4.5 \cdot 10^{-10}$	Pa ⁻¹
fluid dynamic viscosity (η)	10^{-3}	$\sim 10^{-3}$	Pa s
mean initial porosity (ϕ_0)	0.4337	~ 0.4 (mean)	-
characteristic permeability (κ_0)	$6.6 \cdot 10^{-11}$	$\sim 6.6 \cdot 10^{-12}$	m ²

Table 2: List of simulations

ID	Amplitude (cm)	frequency (Hz)	energy (J/m ³)	energy rate (J m ⁻³ s ⁻¹)	PGV (m/s)	PGA/g	Liquefied
s1	0.0431	5.38	0.1395	0.751	0.0145	0.05	Yes
s2	0.0431	7.61	0.2791	2.124	0.0206	0.1	Yes
s3	0.0431	9.32	0.4186	3.901	0.0252	0.15	Yes
s4	0.0431	10.77	0.5581	6.011	0.0291	0.2	Yes
s5	0.0431	12.04	0.6976	8.399	0.0325	0.25	Yes
s6	0.0431	13.19	0.8372	11.043	0.0356	0.3	Yes
s7	0.431	2.41	2.7906	6.725	0.065	0.1	Yes
s8	0.431	3.81	6.9764	26.580	0.1028	0.25	Yes
s9	0.0431	3.81	0.0698	0.266	0.0103	0.025	No
s10	0.0431	6.59	0.2093	1.379	0.0178	0.075	Yes
s11	0.0431	8.51	0.3488	2.968	0.023	0.125	Yes
s12	0.0215	7.61	0.0696	0.530	0.0103	0.05	Partially
s13	0.0215	10.77	0.1392	1.499	0.0145	0.1	Yes
s14	0.0215	13.19	0.2088	2.754	0.0178	0.15	Yes
s15	0.0862	6.59	0.8372	5.517	0.0356	0.15	Yes
s16	0.0862	5.38	0.5581	3.003	0.0291	0.1	Yes
s17	0.0862	3.81	0.2791	1.063	0.0206	0.05	Yes
s18	0.0862	2.68	0.1395	0.374	0.0145	0.025	No
s19	0.0215	5.38	0.0348	0.187	0.0073	0.025	No
s20	0.0431	4.49	0.0977	0.439	0.0122	0.035	No

depths of 1, 3.6, and 6.1 cm above the box base.

Before the experiment starts, the experimental box is filled with tap water, and the pressure transducers are calibrated under hydrostatic conditions. Then, sand grains with a mean diameter of 200 micrometers (SIFRACO N34) and density $\rho_s = 2650 \text{ kg/m}^3$ are gradually poured into the box. We aim for a situation where the water table and the top grains approximately coincide. Horizontal shaking is applied for 30 seconds with a displacement amplitude of at least one mean grain diameter. The pore pressure is measured at a frequency of 10^4 Hz from 30 s before the application of shaking and until 240 s after shaking stops. The pressure at the top is atmospheric, making the top boundary fully drained. All the other box faces exert no flow conditions.

Table 1 summarizes the experiments' parameters. Table 3 lists the experiments presented here with their applied shear amplitude and frequency. The initial porosity, ϕ_0 , presented in Table 3 is evaluated as follows: First, the pore water volume is evaluated as the difference between the water volume used in the experiment and the volume of the thin water film above the grains. Then, the pore water volume is divided by the total volume of the saturated grains based on the height of the grain layer as recorded by the first high-speed camera image.

The mean value of the pre-shaking pressure measurements is used to determine the hydrostatic pressure reference. The pressure signal in Fig. 2a is filtered using a low pass filter, with a cutoff frequency of 1 Hz. The shaded red area in Fig. 2a, representing the uncertainty on the pressure, follows the 95% confidence bounds on the parameters of the linear regression between voltage and pressure based on the pressure transducers calibration stage.

The calculation of the normalized compaction in Fig. 2b is based on an edge detection algorithm that identifies the top boundary (edge) of the grain layer in individual images. The algorithm was executed several times while

varying the top boundary of the search frame within which the algorithm searches for the edge. From search frame 211 (corresponding to a scaled time of $t/t_e = 0.084$) and on, the edge becomes independent of the search frame height, and thus Fig. 2b (red curve) shows the compaction trend only from frame 221. The red curve represents the normalized mean edge topography within the search frame (smoothed by a moving average window of 0.8 seconds). The shaded red band represents the uncertainty on the normalized edge height based on the standard error of the edge topography. The mean and standard error of the edge topography in the first search frame are based on a manual edge extraction.

The instantaneous grain velocity field is measured in every frame by using PIVlab^{69,70}, which relies on sub-frame correlation between timely-adjacent frames. The vertical velocity is then averaged over sub-layers, yielding the vertical velocity of grains as a function of depth and time (see section 10.4). To minimize boundary effects from the box’s walls, the averaging is done only close to the box’s center (approximately in the middle 2/4 of the box’s total width).

The energy, e , in Fig. 4c, is based on an estimation of the imposed PGV in the experiments. The input shaking frequency was accurately controlled by setting the frequency of the shaker. The shaking amplitude was estimated based on four markers placed close to the corners of the experiment box. Markers’ position was traced across frames. The temporal mean of markers position was subtracted from the position time series of each marker, and the four position time series were averaged. Then, the peaks of the combined, averaged time series were extracted, and the shaking amplitude was estimated as the average over the absolute value of the peaks through time $t = [0, t_e]$. The uncertainty in evaluating PGV is related to the standard error of the absolute value of the peaks time series. The error propagated to $\log_{10}[e]$ is smaller than the symbol size in Fig. 4c.

The permeability in the experiments was evaluated based on five static permeability tests. A constant head was applied across a saturated sand layer in each test, prepared similarly and with the same geometry as the shaking experiments. The outlet point that was located 1.4 cm above the base of the box imposed a 3D porous flow field in the box. The cumulative outflow was measured through time, and its time derivative was used as the discharge (with units of m^3/s) in a 1D Darcy’s law to determine the permeability. A correction factor from a true 1D porous flow to the specific 3D flow structure in these tests was derived by simulating the two geometries in COMSOL Multiphysics. For the same material permeability, the discharge in the 3D geometry was smaller by a factor of 10 with respect to its 1D counterpart. The permeability of each experiment was then estimated as being larger by a factor of 10 with respect to the measured quantity. The hydraulic head was varied between the five experiments, and the permeability used in Fig. 4c is the mean over the five measurements. The uncertainty on the permeability is evaluated as the standard error over the five permeability measurements. When propagated to the y-axis of Fig. 4c, $\log_{10}[u_{\text{front}}/(\kappa(1 - \phi_0))]$, the uncertainty is smaller than the symbol size.

Table 3: List of experiments

ID	Amplitude (cm)	frequency (Hz)	energy (J/m ³)	energy rate (J m ⁻³ s ⁻¹)	PGV (m/s)	PGA/g	Height (m)	ϕ_0
e1	0.0789	10	1.6293	16.293	0.0496	0.318	0.106	0.4
e2	0.0413	10	0.4452	4.452	0.0259	0.166	0.072	0.42
e3	0.0733	10	1.4054	14.054	0.0461	0.295	0.07	0.4
e4	0.0491	10	0.6313	6.313	0.0309	0.198	0.077	0.36
e5	0.0767	14	3.0158	42.221	0.0675	0.605	0.074	0.41
e6	0.0762	14	2.9728	41.619	0.067	0.601	0.071	0.4
e7	0.0517	14	1.3714	19.200	0.0455	0.408	0.075	0.4
e8	0.026	10	0.1763	1.763	0.0163	0.104	0.07	0.43
e9	0.0242	10	0.1536	1.536	0.0152	0.098	0.073	0.4

10.4 Evaluating the compaction front velocity (u_{front}) and the duration of liquefaction event (t_e)

The compaction front velocity is defined based on the ratio between the horizontally averaged vertical grain velocity and the grain terminal velocity defined by equation (6). Averaging is performed over sub-layers of two average grain diameter thickness. The averaged velocity is smoothed in time using a running average window of ~ 0.67 seconds in the simulations and ~ 1.2 seconds in the experiments. In the simulations, we further smooth the vertical dimension using a running average window of 10 centimeters. Plotting the averaged, smoothed and normalized velocity as a function of depth and time, $u_{sz}^{\text{norm}}(z, t)$ results in a map that highlights settling vs. stagnant grains (Fig. 6).

The compaction front depth at each time, t , is extracted by scanning $u_{sz}^{\text{norm}}(z, t)$ from the bottom upward and identifying the first depth where $u_{sz}^{\text{norm}}(z, t) \geq 0.5$ in simulations and ≥ 0.01 in experiments. This depth is defined as the front location at time t , $z_{\text{front}}(t)$. Finally, we manually pick the time when the front starts migrating upward continuously (t_i) and the time of front arrival to the top of the layer (t_f). In some experiments and simulations, $z_{\text{front}}(t)$ loses its coherent slope at some stage, and we choose t_f to be the last time step showing a coherent slope. The average front velocity is calculated as the average slope of the front depth-time curve between these two times.

The time of liquefaction event termination, t_e , used as the timescale factor in Fig. 2, is determined as the time at which the soil compaction slows down significantly (see Fig. 2b), as an approximation of $t_e = t_i + L/u_{\text{front}}$, where L is the distance to the surface from $z_{\text{front}}(t = t_i)$. In most cases, t_i is negligible in comparison to L/u_{front} since the downward moving liquefaction front (Fig. 6 inset) is very fast.

Appendix A Terminology

Some commonly used terms in the soil liquefaction literature do not uniquely signify the physical processes that underlie observations. Here, we address two terminology issues that emerge from the current research.

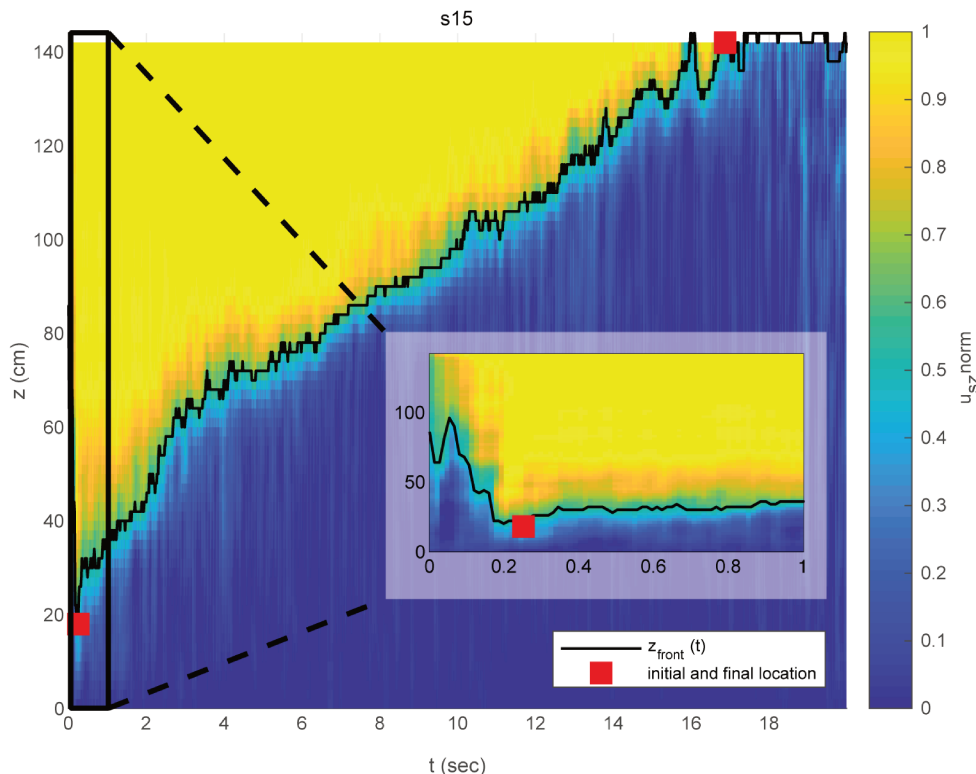


Figure 6: Example of compaction front detection and calculation of the average front velocity u_{front} . The vertical axis represents height above the bottom wall and the horizontal axis is time. The color map shows the normalized averaged and smoothed vertical grain velocity, u_{sz}^{norm} . The black curve depicts the inferred front location ($z_{\text{front}}(t)$). The front velocity is calculated as the average slope of the black curve, between the manually picked initial and final times (red squares). The inset shows the first second of the simulation (corresponding to the black rectangle in the main panel). The downward moving liquefaction front is observed in the first $\simeq 0.2$ seconds.

A.1 Drained, partially drained and undrained

Experimental observations of liquefaction accompanied by a syn-shaking soil settlement^{23,25}, and experimental setups with boundary conditions that allow fluid flow^{25,28,71} were denoted in previous studies as *partially drained*. In the current study, we refer to these settings as showing a *drained* response if $De \ll 1$, as explained below.

The non-dimensional analysis, equation (2) and the non-dimensional Deborah number, De , equation 3 define competing coupled grain-fluid effects in response to pore space changes as a function of the fluid ability to drain at the timescale of change. These competing effects lead to two end-member responses^{21,22,27}. The first end-member occurs when $De \gg 1$, fluid cannot flow out of or into a changing pore space during the change, and the pore pressure response is undrained. The second end-member occurs when $De \ll 1$, as in our simulations and experiments. Here, fluid has sufficient time to flow in and out of the changing pore space, the fluid may be considered as incompressible, and the pore pressure response is drained. We propose that partially-drained (or partially-undrained) should be reserved for a case where $De = \mathcal{O}(1)$. This terminology choice is consistent with several previous studies^{21,22,24}.

The choice of some studies to refer to $De \ll 1$ as partially drained might reflect the dominance of the undrained paradigm for liquefaction triggering, where 'partially' is added to reconcile observations of fluid flow simultaneously

with high pore fluid pressure and liquefaction. However, the coexistence of flow and pressurization is inherent to Darcy’s law, which relates interstitial fluid flow (drainage) to fluid pressure gradients and thus to non-hydrostatic, elevated pore pressure.

A.2 Liquefaction and fluidization

The term *liquefaction* is used to describe a rheological change from a solid-like to a fluid-like soil behavior. The term *fluidization* is more commonly used when the rheological change is imposed by an externally-sourced fluid flux that enters through a (lower) boundary and via its upward-flow supports and lifts the grains^{40,72}.

We believe that the term *liquefaction* should be used to describe the dynamics emerging here in the drained simulations and experiments for several reasons. First, as demonstrated in figure 2, the same field and experimental observations that are widely used to identify soil liquefaction, and which are commonly interpreted within the undrained liquefaction framework, are also observed here under drained conditions. Therefore, we suggest that the term *liquefaction* should be used to describe the observational phenomena, rather than a particular physical process. Second, the bottom boundaries of the simulations and experiments reported here are impermeable. No external fluid flux crosses the boundary to induce the syn-seismic pressure gradient that support and liquefy grains above the compaction front. In drained shaking, the high pressure gradients that liquefy the soil emerge dynamically and in-situ due to the process of internal compaction, rendering the term *fluidization* inconsistent.

Appendix B Liquefaction initiation timescale

There are two main candidate timescales for controlling t_i , the time to initiate drained liquefaction. The timescale of a single grain to fall down the fluid, and the time for an unloading front³⁸ to reach the liquefaction initiation depth.

We first explore the timescale associated with grain settlement and pressurization under drained conditions by considering the force balance over a single grain in the vertical direction:

$$\rho_s V \dot{u}_{sz} = \rho_s V g - \rho_f V g - \frac{V}{1 - \phi} \frac{dP'}{dz}. \quad (\text{B.1})$$

According to equation (B.1), the forces acting on such a grain are gravity, buoyancy and seepage by dynamic pore pressure gradient. To simplify the calculation, contact forces are not considered here. While contact forces are expected to be significant at the initial stages, when the pressure gradient rises, the grain becomes suspended and the magnitude of the contact forces likely drops.

Assigning the coupling between the pressure gradient and the grain’s vertical velocity (Eq. 5) in Eq. B.1 and solving for the grain velocity with the initial condition $u_{sz}(t = 0) = 0$:

$$u_{sz}(t) = \frac{\kappa}{\eta} (1 - \phi) (\rho_s - \rho_f) g (1 - e^{-\frac{t}{\tau}}) \quad (\text{B.2})$$

where $\tau = \frac{\kappa \rho_s (1-\phi)}{\eta}$ is the exponential timescale for approaching terminal velocity. Assigning parameters for water and a natural sand, $\eta = 10^{-3}$ Pa s, $\rho_s = 2600$ kg m⁻³, $\phi = 0.5$ and $\kappa = 10^{-9} - 10^{-14}$ m², we find that $\tau \approx 10^{-3} - 10^{-8}$ s, is a fraction of a second. The pore pressure gradient follows a similar exponential evolution, with the same timescale, τ

$$\frac{dP'}{dz} = (1 - \phi)(\rho_s - \rho_f)g (1 - e^{-\frac{t}{\tau}}). \quad (\text{B.3})$$

Our simulations and experiments show that both the grain settlement (downward) velocity and the pressurization approach their asymptotic values over a short timescale, yet much longer than τ . Thus the dynamics of a single grain falling in a fluid is probably not the rate limiting process in initiating liquefaction. Our results indicate that t_i may be controlled by the descending "unloading" liquefaction front that precedes the upward compaction front. Liquefaction initiation is only complete once this unloading front reaches the compaction front initiation depth, as seen in Fig. 6 and in section A in the supplementary materials.

Appendix C Compaction front initiation height

A careful analysis of the simulation results reveals that the height above the bottom boundary, from which the compaction front initiates, z_0 , is not constant. z_0 is the thickness of the layer above the bottom wall that remains non-liquefied through shaking. Figure 7 shows that the initiation height of the compaction front correlates well with the imposed shaking frequency ($R^2 = 0.79$), where under higher input frequency, the compaction front starts closer to the bottom wall. We did not find another parameter that correlates as well with the initiation height ($PGV : R^2 = 0.06$; $PGA : R^2 = 0.33$, $e/T : R^2 = 0.03$).

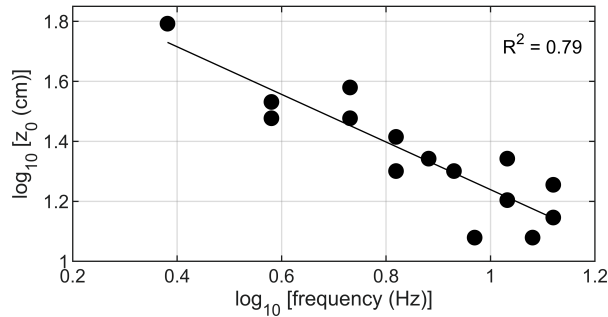


Figure 7: The height at which the compaction front initiates above the bottom boundary, z_0 , as a function of imposed shaking frequency. The black line represents the best linear fit ($Y = -0.79 X + 2$, $R^2 = 0.79$).

Appendix D Delay of fluid expulsion where the water level is below the surface

When the water level is located below the surface, different scenarios could emerge for the interactions between the compaction front, the water level and the surface. To define these interactions, we start by dividing the excited soil column to three regions: (1) below the compaction front, where the grain and fluid vertical velocities are approximately zero ($u_{sz}^{(1)} = u_{fz}^{(1)} \approx 0$), (2) above the compaction front and below the water level. Here, downward grain velocity is expressed by Eq. 6 as $u_{sz}^{(2)} = u_{szC} = (\kappa/\eta)(d\sigma_0/dz)$ ($d\sigma_0/dz < 0$), and the upward fluid velocity is $u_{fz}^{(2)} = -((1 - \phi_0)/\phi_0) u_{szC}$, and (3) above the water level where we assume that the downward grain velocity follows that of the second layer, $u_{sz}^{(3)} = u_{szC}$.

Next, we define the time dependent height of the top boundaries of the three regions with respect to the layer's base: (1) the height of the compaction front is expressed as $z_{\text{front}}(t) = z_0 + u_{\text{front}} \cdot t$, where u_{front} is defined in Eq. 4 and $z_0 = z_{\text{front}}(t = 0)$, (2) the height of the water table is $WL(t) = WL_0 + u_{fz}^{(2)} \cdot t$, where $WL_0 = WL(t = 0)$, and (3) the height of the soil layer is $h(t) = H + u_{sz}^{(3)} \cdot t$, where $H = h(t = 0)$, and $u_{sz}^{(3)}$ is negative.

A competition between the earthquake's duration, t_{EQ} , the time for the front to arrive to the water level, t_{front}^{WL} , and the time for the water level to arrive to the surface, t_{WL}^{surface} , controls the potential for different observations, where:

$$t_{\text{front}}^{WL} = \frac{WL_0 - z_0}{u_{\text{front}} - u_{fz}^{(2)}} = \frac{WL_0 - z_0}{\frac{\kappa}{\eta} \frac{d\sigma_0}{dz} \left(\frac{\phi_0 - 1}{\phi_0 - \phi_c} + \frac{1 - \phi_0}{\phi_0} \right)}, \quad (\text{D.1})$$

and

$$t_{WL}^{\text{surface}} = \frac{H - WL_0}{u_{fz}^{(2)} - u_{sz}^{(3)}} = \frac{H - WL_0}{-\frac{\kappa}{\eta} \frac{d\sigma_0}{dz} \left(\frac{1 - \phi_0}{\phi_0} + 1 \right)}. \quad (\text{D.2})$$

When the water level is initially close to surface, as is the case in coastal and riverbank sediments, then for a wide range of parameter sets, $t_{WL}^{\text{surface}} < \min(t_{EQ}, t_{\text{front}}^{WL})$, and fluid will seep co-seismically at the surface, making liquefaction easily detectable. For example, consider a 10 meter deep soil column ($H = 10$ m) with $\kappa = 2 \times 10^{-9}$ m², an initial water level that is located 30 cm below the surface ($WL_0 = 9.7$ m), and excitation that induces $\Delta\phi = 9 \times 10^{-3}$, the water will seep at the surface after $t_{WL}^{\text{surface}} \simeq 7$ seconds, while the whole liquefaction event will last for $t_{\text{front}}^{WL} \simeq 8.5$.

However, if the permeability is lower, the excitation is weaker (leading to a smaller $\Delta\phi$), or the initial water level is deeper, then $t_{\text{front}}^{WL} < t_{WL}^{\text{surface}}$, and the liquefaction event may terminate before water reaches and seeps out of the surface. For example, consider the parameters used above, but when the initial water level is 2 meters below the surface ($WL_0 = 8$ m), than the event will terminate after $t_{\text{front}}^{WL} \simeq 14$ seconds without a co-seismic seepage, since $t_{WL}^{\text{surface}} \simeq 90$ seconds.

References

- [1] Kramer, S. L. *Geotechnical Earthquake Engineering* (1996).

- [2] Ishihara, K., Araki, K. & Bradley, B. Characteristics of Liquefaction-Induced Damage in the 2011 Great East Japan Earthquake. In *International Conference on Geotechnics for Sustainable Development - Geotec Hanoi, Vietnam.*, 22 (2011).
- [3] Bray, J., EERI, M., Cubrinovski, M., Zupan, J. & Taylor, M. Liquefaction Effects on Buildings in the Central Business District of Christchurch. *earthquake spectra* **30**, 85–109 (2014).
- [4] Bradley, K. *et al.* Earthquake-triggered 2018 Palu Valley landslides enabled by wet rice cultivation. *Nature Geoscience* **12**, 935–940 (2019). URL <http://dx.doi.org/10.1038/s41561-019-0444-1>.
- [5] Gautam, D., Magistris, F. S. D. & Fabbrocino, G. Soil liquefaction in Kathmandu valley due to 25 April 2015 Gorkha, Nepal earthquake. *Soil Dynamics and Earthquake Engineering* **97**, 37–47 (2017). URL <http://dx.doi.org/10.1016/j.soildyn.2017.03.001>.
- [6] Cubrinovski, M., Henderson, D. & Bradley, B. Liquefaction Impacts in Residential Areas in the 2010-2011 Christchurch Earthquakes. *Proceedings of the International Symposium on Engineering Lessons Learned from the 2011 Great East Japan Earthquake* 811–824 (2012).
- [7] Cox, S. C. *et al.* Hydrological effects of the M.W 7.1 Darfield (Canterbury) earthquake , 4 September 2010 , New Zealand. *New Zealand Journal of Geology and Geophysics* **55**, 231–247 (2012).
- [8] National Academies of Sciences, Engineering & Medicine. State of the Art and Practice in the Assessment of Earthquake-Induced Soil Liquefaction and Its Consequences. Tech. Rep., Washington, DC (2016). URL <https://www.nap.edu/catalog/23474>.
- [9] Wood, A., Noy, I. & Parker, M. The Canterbury rebuild five years on from the Christchurch earthquake. *Reserve Bank of New Zealand Bulletin* **79**, 1–16 (2016).
- [10] Jones, K., Pascale, F., Wanigarathna, N., Morga, M. & Sargin, S. Critical evaluation of the customisation process of the UNDRR disaster resilience scorecard for cities to earthquake - induced soil liquefaction disaster events. *Bulletin of Earthquake Engineering* **19**, 4115–4143 (2021). URL <https://doi.org/10.1007/s10518-020-00993-y>.
- [11] Martin, G. R., Finn, W. L. & Seed, H. B. Fundamentals of Liquefaction Under Cyclic Loading. *Journal of the geotechnical engineering division* **101**, 423–438 (1975).
- [12] Terzaghi, K. *Theoretical Soil Mechanics* (John Wiley, New York, 1943).
- [13] de Alba, P. A., Chan, K. C. & Seed, H. B. Sand liquefaction in large-scale simple shear tests. *Journal of Geotechnical and Geoenvironmental Engineering* **102**, 909–927 (1976).
- [14] Dobry, R., Ladd, R., Yokel, F., Chung, R. & Powell, D. *Prediction of Pore Water Pressure Buildup and Liquefaction of Sands During Earthquakes by the Cyclic Strain Method* (US department of commerce, National Bureau of Standards, Gaithersburg, MD, 1982).

- [15] Green, R. A. & Mitchell, J. K. Energy-based evaluation and remediation of liquefiable soils. *Geotechnical Special Publication* 1961–1970 (2004). URL <http://www.scopus.com/inward/record.url?eid=2-s2.0-10944245321&partnerID=tZ0tx3y1>. arXiv:1011.1669v3.
- [16] Wang, C. Y. Liquefaction beyond the Near Field. *Seismological Research Letters* **78**, 512–517 (2007).
- [17] Wang, C. Y. & Manga, M. Chapter 11 Liquefaction. In *Water and Earthquakes*, chap. 11 (Springer Cham, 2021).
- [18] Manga, M. *et al.* Changes in permeability caused by transient stresses: Field observations, experiments, and mechanisms. *Reviews of Geophysics* **50** (2012).
- [19] Kooi, B. Great Eastern Japan Earthquake - Liquefaction in Makuhari (2011). URL https://www.youtube.com/watch?v=rn3oAvmZY8k&ab_channel=BrentKooi.
- [20] Konagai, K., Kiyota, T., Suyama, S. & Asakura, T. Maps of soil subsidence for Tokyo bay shore areas liquefied in the March 11th, 2011 off the Pacific Coast of Tohoku Earthquake. *Soil Dynamics and Earthquake Engineering* **53**, 240–253 (2013). URL <http://dx.doi.org/10.1016/j.soildyn.2013.06.012>.
- [21] Goren, L., Aharonov, E., Sparks, D. W. & Toussaint, R. Pore pressure evolution in deforming granular material: A general formulation and the infinitely stiff approximation. *Journal of Geophysical Research: Solid Earth* **115**, 1–19 (2010).
- [22] Goren, L., Aharonov, E., Sparks, D. W. & Toussaint, R. The Mechanical Coupling of Fluid-Filled Granular Material Under Shear. *Pure and Applied Geophysics* **168**, 2289–2323 (2011).
- [23] Madabhushi, G. S. P. & Haigh, S. K. How Well Do We Understand Earthquake Induced Liquefaction? **42**, 150–160 (2012).
- [24] Lakeland, D. L., Rechenmacher, A. & Ghanem, R. Towards a complete model of soil liquefaction : the importance of fluid flow and grain motion. *Proceedings of the royal society* **470** (2014).
- [25] Adamidis, O. & Madabhushi, G. Experimental investigation of drainage during earthquake-induced Experimental investigation of drainage during earthquake-induced liquefaction. *Geotechnique* **68**, 655–665 (2018).
- [26] Clément, C., Toussaint, R., Stojanova, M. & Aharonov, E. Sinking during earthquakes: critical acceleration criteria control drained soil liquefaction. *Physical Review E* **97**, 022905 (2018). arXiv:1802.08528v1.
- [27] Ben-Zeev, S., Aharonov, E., Toussaint, R., Perez, S. & Goren, L. Compaction front and pore fluid pressurization in horizontally shaken drained granular layers. *Physical Review Fluids* **054301**, 1–25 (2020).
- [28] Adamidis, O. & Anastasopoulos, I. Cyclic liquefaction resistance of sand under a constant inflow rate. *Geotechnique* (2022).
- [29] Briaud, J.-L. *Geotechnical engineering: unsaturated and saturated soils* (John Wiley & Sons., 2013).

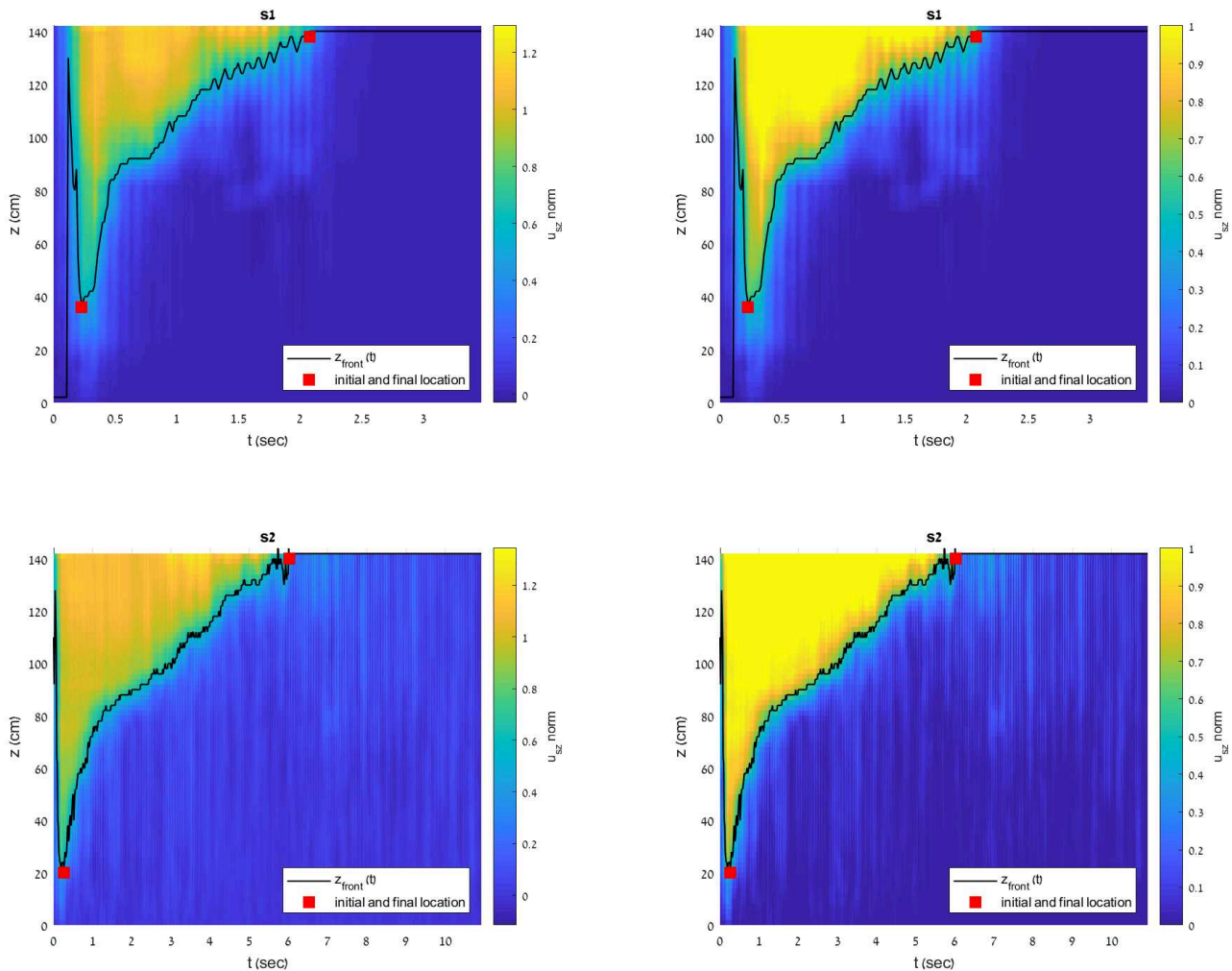
- [30] Paldor, A. *et al.* Coastal topography and hydrogeology control critical groundwater gradients and potential beach surface instability during storm surges. *Hydrology and Earth System Sciences* **26**, 5987–6002 (2022).
- [31] Wang, B. *et al.* Excess pore pressure dissipation and solidification after liquefaction of saturated sand deposits. Excess pore pressure dissipation and solidification after liquefaction of saturated sand deposits. *Soil Dynamics and Earthquake Engineering* **49**, 157–164 (2013). URL <http://dx.doi.org/10.1016/j.soildyn.2013.02.018>.
- [32] Adamidis, O. & Madabhushi, G. S. P. Post-liquefaction reconsolidation of sand. *Proceedings of the royal society* **472** (2016).
- [33] Chiaradonna, A. & Emilio, O. Assessment of post-liquefaction consolidation settlement. *Bulletin of Earthquake Engineering* **17**, 5825–5848 (2019). URL <https://doi.org/10.1007/s10518-019-00695-0>.
- [34] Niebling, M. J., Flekkøy, E. G., Måløy, K. J. & Toussaint, R. Sedimentation instabilities: Impact of the fluid compressibility and viscosity. *Physical Review E* **82**, 051302 (2010).
- [35] Reiner, M. The Deborah Number. *Physics today* **17**, 62 (1964).
- [36] Kasmalkar, I., Damsgaard, A., Goren, L. & Suckale, J. Shear variation at the ice-till interface changes the spatial distribution of till porosity and meltwater drainage. *Journal of Geophysical Research Earth Surface* **126**, 1–29 (2021).
- [37] M. Manga & C.-Y. Wang. In *Treatise on Geophysics*, chap. 4.12 (Oxford).
- [38] Florin, V. & Ivanov, P. Liquefaction of Saturated Sandy Soils. In *Proceedings of the 5th international conference on soil mechanics and foundation engineering*, 107–11 (1961).
- [39] El Shamy, U. & Zeghal, M. A micro-mechanical investigation of the dynamic response and liquefaction of saturated granular soils. *Soil Dynamics and Earthquake Engineering* **27**, 712–729 (2007).
- [40] McNamara, S., Flekkøy, E. G. & Måløy, K. J. Grains and gas flow: molecular dynamics with hydrodynamic interactions. *Physical review E* **61**, 4054—4059 (2000). URL <http://www.ncbi.nlm.nih.gov/pubmed/11088197>.
- [41] Iverson, R. M. *et al.* Acute Sensitivity of Landslide Rates to Initial Soil Porosity. *Science* **290**, 513–516 (2000).
- [42] Silver, M. L. & Seed, H. B. Deformation characteristics of sand under cyclic loading. *Journal of the Soil Mechanics and Foundations Division* **97**, 1081–1098 (1971).
- [43] Hardin, B. O. & Drnevich, V. Shear Modulus and Damping in Soils: Measurement and Parameter Effects. *Journal of the Soil Mechanics and Foundations Division* **98**, 603–624 (1972).
- [44] Lay, T. & Wallace, T. C. *Modern global seismology* (Elsevier, 1995).
- [45] Sharp, M. k. & Dobry, R. sliding block analysis of lateral spreading based on centrifuge results. *International journal of physical modeling in geotechnics* 13–32 (2002).

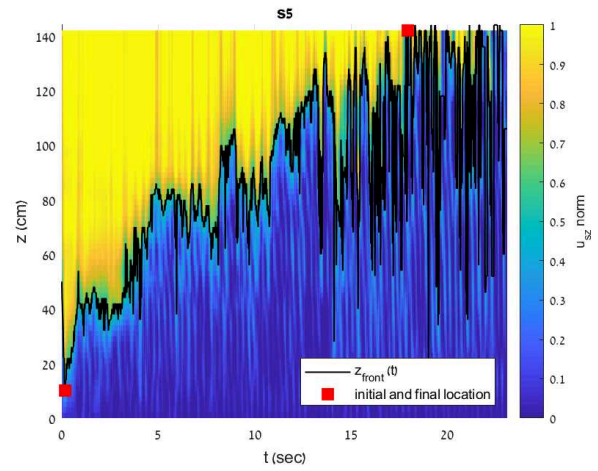
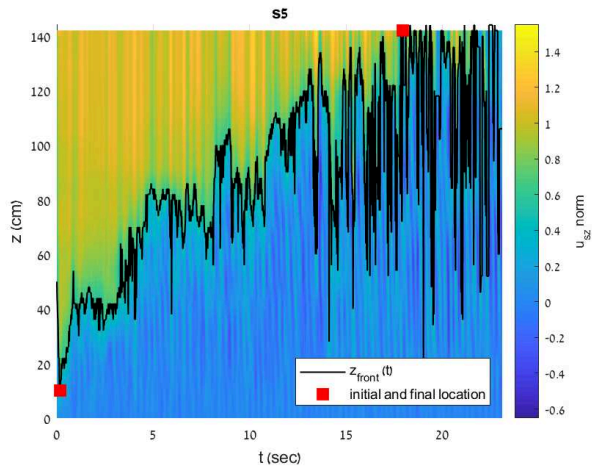
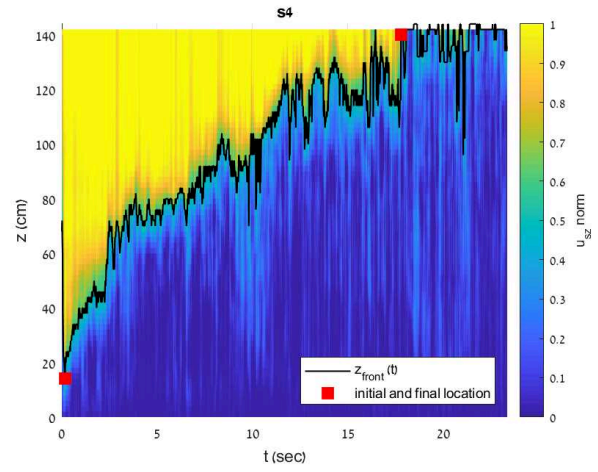
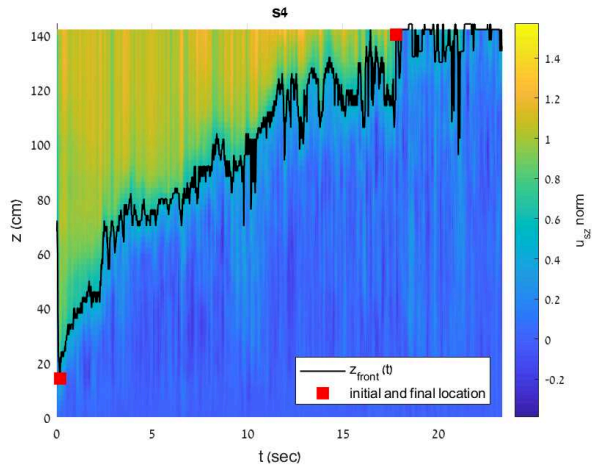
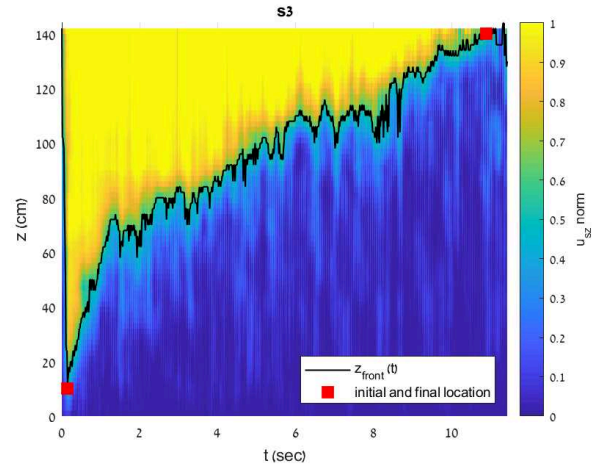
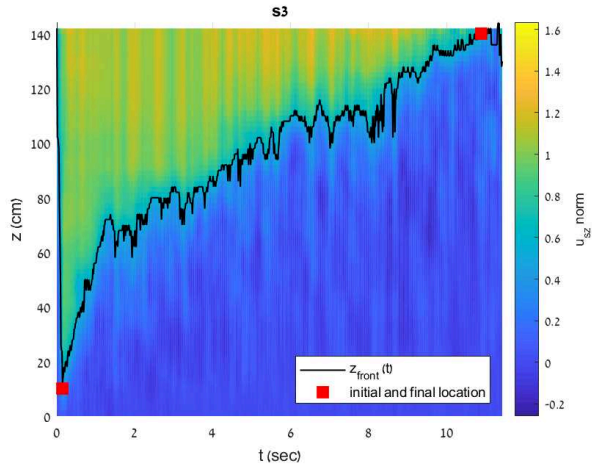
- [46] Gonzalez, L., Abdoun, T., Zeghal, M., Kallou, V. & Sharp, M. k. Physical modeling and visualization of soil liquefaction under high confining stress. *Earthquake Engineering and engineering vibration* **4**, 47–57 (2005).
- [47] Greenfield, M. W. *Effects of long-duration ground motions on liquefaction hazards*. Ph.D. thesis, University of Washington (2017).
- [48] Ozener, P. T., Greenfield, M. W., Sideras, S. S. & Kramer, S. L. Identification of time of liquefaction triggering. *Soil Dynamics and Earthquake Engineering* **128** (2020).
- [49] Seed, H. B. & Idriss, I. M. Simplified procedure for evaluating soil liquefaction potential. *Journal of the Soil Mechanics and Foundations Division* **97**, 1249–1273 (1971).
- [50] Ishihara, K. Liquefaction and flow failure during earthquakes. *Geotechnique* **43**, 351–415 (1993).
- [51] Youd, T. L. *et al.* Liquefaction resistance of soils: Summary report from the 1996 NCEER and 1998 NCEER/NSF Workshops on Evaluation of Liquefaction Resistance of Soils. *Journal of Geotechnical and Geoenvironmental Engineering* **127**, 817–833 (2001).
- [52] Nemat-Nasser, S. & Shokooh, A. A unified approach to densification and liquefaction of cohesionless sand in cyclic shearing. *Canadian Geotechnical Journal* **16**, 659–678 (1979).
- [53] Berrill, J. & Davis, R. Energy dissipation and seismic liquefaction of sands: revised model. *Soils and Foundations* **25**, 106–118 (1985).
- [54] Kayen, R. E. & Mitchell, J. k. Assessment of liquefaction potential during earthquakes by arias intensity. *Journal of Geotechnical and Geoenvironmental Engineering* **123**, 1162–1174 (1997).
- [55] Kokusho, T. Liquefaction potential evaluations: energy-based method versus stress-based method. *Canadian Geotechnical Journal* **50**, 1088–1099 (2013).
- [56] Nicolas, M., Duru, P. & Pouliquen, O. Compaction of a granular material under cyclic shear. *The European Physical Journal E* **3**, 309–314 (2000). URL <http://link.springer.com/10.1007/s101890070001.0006252>.
- [57] Aharonov, E. & Sparks, D. W. Shear profiles and localization in simulations of granular materials. *Physical Review E* **65**, 051302 (2002).
- [58] Aharonov, E. & Sparks, D. W. Stick-slip motion in simulated granular layers. *Journal of Geophysical Research* **109**, 1–12 (2004).
- [59] Zhu, J., Baise, L. G. & Thompson, E. M. An Updated Geospatial Liquefaction Model for Global Application. *Bulletin of the Seismological Society of America* **107** (2017).

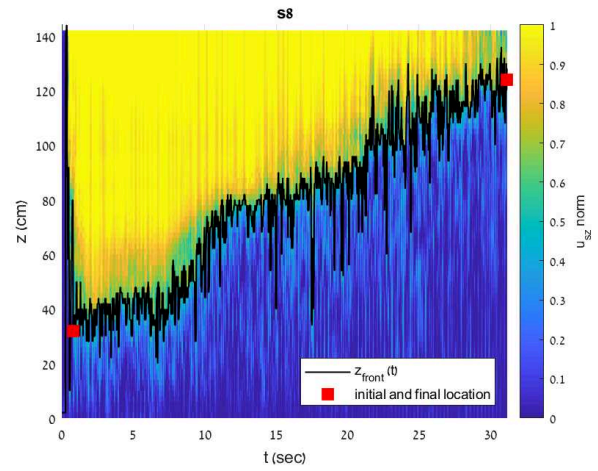
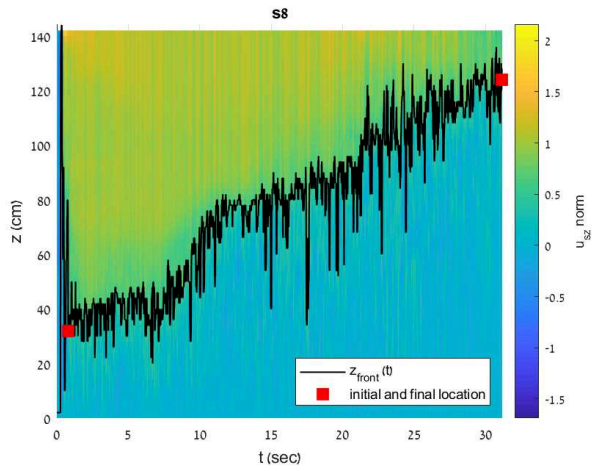
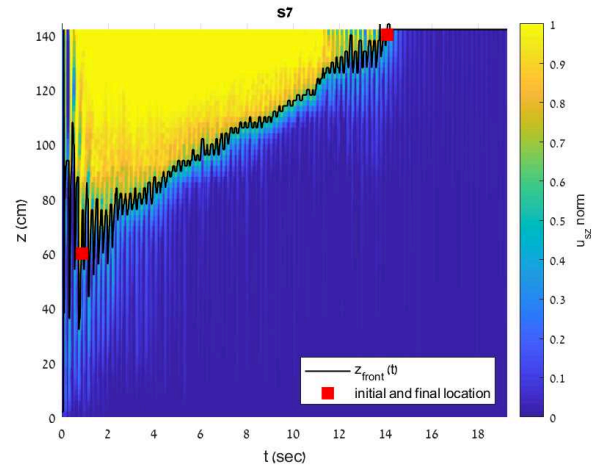
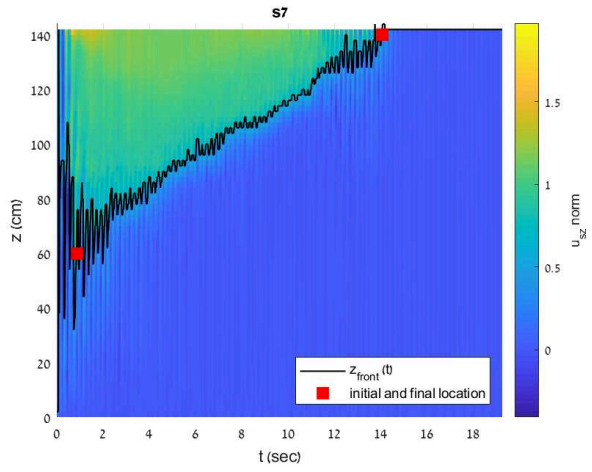
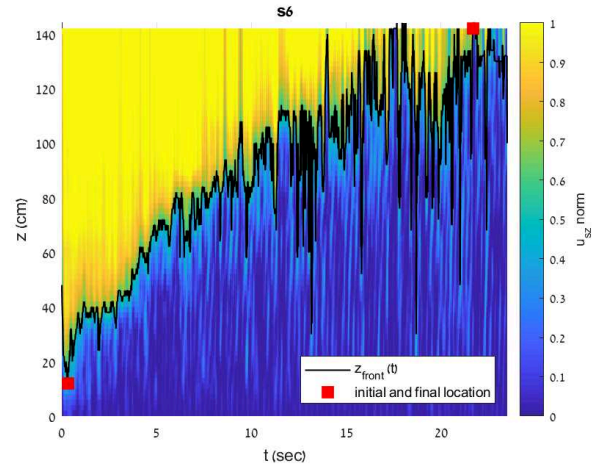
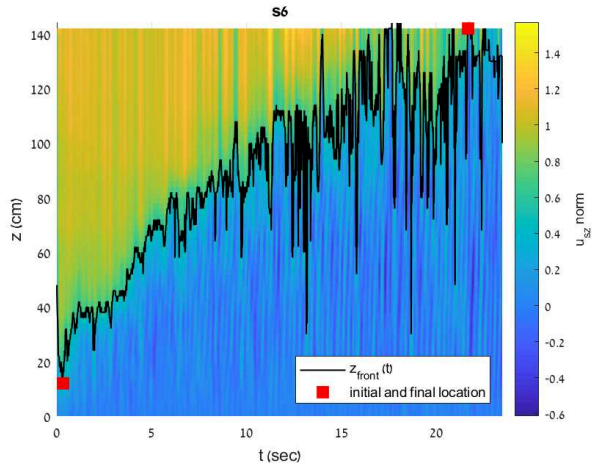
- [60] de Magistris, S. F., Lanzano, G., Forte, G. & Fabbrocino, G. A database for PGA threshold in liquefaction occurrence. *Soil Dynamics and Earthquake Engineering* **54**, 17–19 (2013). URL <http://dx.doi.org/10.1016/j.soildyn.2013.07.011>.
- [61] Brennan, A. J. & Madabhushi, G. Liquefaction and Drainage in Stratified Soil. *Journal of Geotechnical and Geoenvironmental Engineering* **0241** (2005).
- [62] Kokusho, T. & Kojima, T. Mechanism for Postliquefaction Water Film Generation in Layered Sand. *Journal of Geotechnical and Geoenvironmental Engineering* **128**, 129–137 (2002).
- [63] Cundall, P. A. & Strack, O. D. A discrete numerical model for granular assemblies. *Geotechnique* **29.1**, 47–65 (1979).
- [64] Johnsen, Ø., Toussaint, R., Måløy, K. J. & Flekkøy, E. G. Pattern formation during air injection into granular materials confined in a circular Hele-Shaw cell. *Physical Review E* **74**, 011301 (2006).
- [65] Niebling, M. J., Flekkøy, E. G., Måløy, K. J. & Toussaint, R. Mixing of a granular layer falling through a fluid. *Physical Review E* **82**, 011301 (2010).
- [66] Vinningland, J. L., Johnsen, Ø., Flekkøy, E. G., Toussaint, R. & Måløy, K. J. Granular Rayleigh-Taylor Instability: Experiments and Simulations. *Physical Review Letters* **99**, 048001 (2007). [arXiv:0706.0122v2](https://arxiv.org/abs/0706.0122v2).
- [67] Vinningland, J. L., Johnsen, Ø., Flekkøy, E. G., Toussaint, R. & Måløy, K. J. Experiments and simulations of a gravitational granular flow instability. *Physical Review E* **76**, 051306 (2007).
- [68] Carman, P. C. Fluid flow through granular beds. *Trans. Inst. Chem. Eng.* **15**, 150–166 (1937). URL [http://dx.doi.org/10.1016/S0263-8762\(97\)80003-2](http://dx.doi.org/10.1016/S0263-8762(97)80003-2).
- [69] Thielicke, W. & Stamhuis, E. J. PIVlab – Towards User-friendly , Affordable and Accurate Digital Particle Image Velocimetry in MATLAB. *journal of open research software* **2** (2014).
- [70] Thielicke, W. & Sonntag, R. Particle Image Velocimetry for MATLAB : Accuracy and enhanced algorithms in PIVlab. *journal of open research* **9** (2021).
- [71] Kamai, R. & Boulanger, R. W. Single-element simulations of partial-drainage effects under monotonic and cyclic loading. *Soil Dynamics and Earthquake Engineering* **35**, 29–40 (2012). URL <http://dx.doi.org/10.1016/j.soildyn.2011.10.002>.
- [72] Haigh, S., Eadington, J. & Madabhushi, S. P. G. Permeability and stiffness of sands at very low effective stresses. *Geotechnique* **62**, 69–75 (2012).

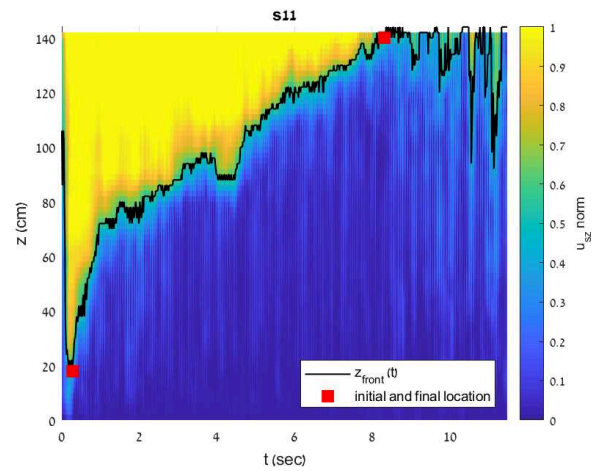
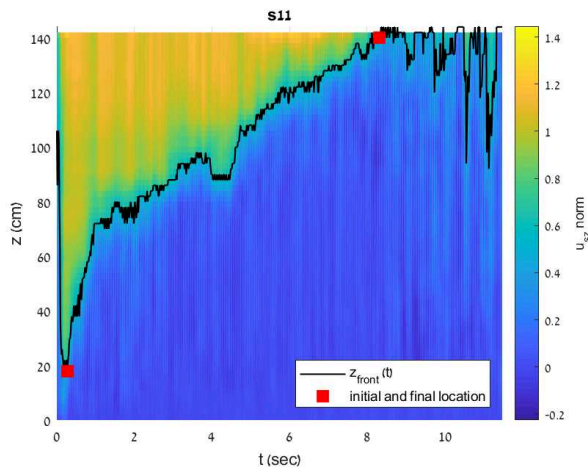
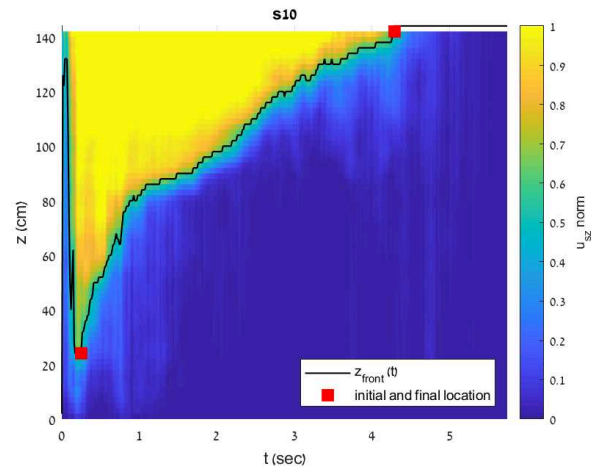
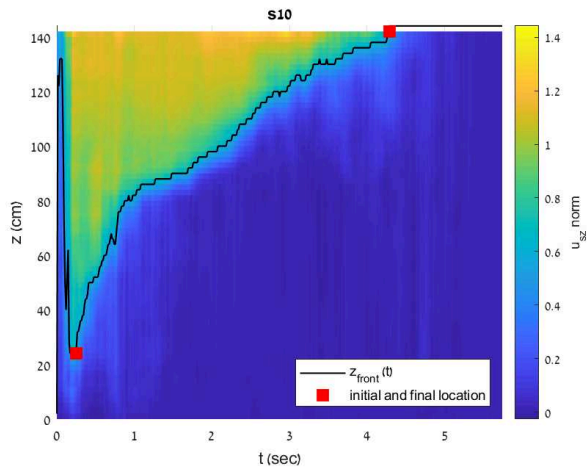
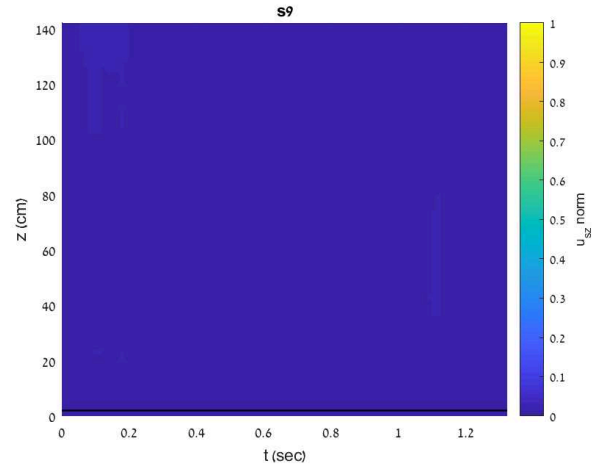
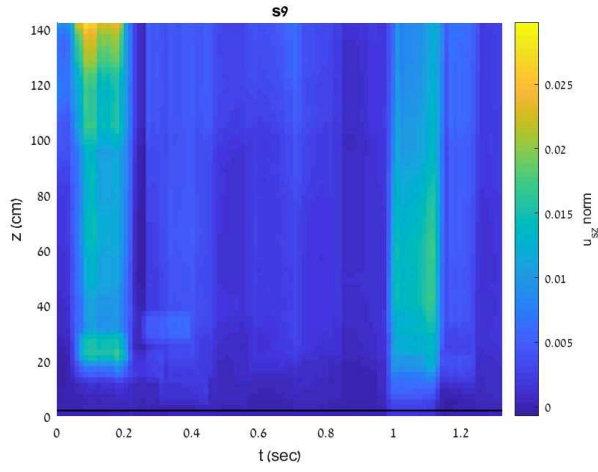
A Supplementary material for "Drainage explains soil liquefaction beyond the earthquake near-field" - grain velocity maps

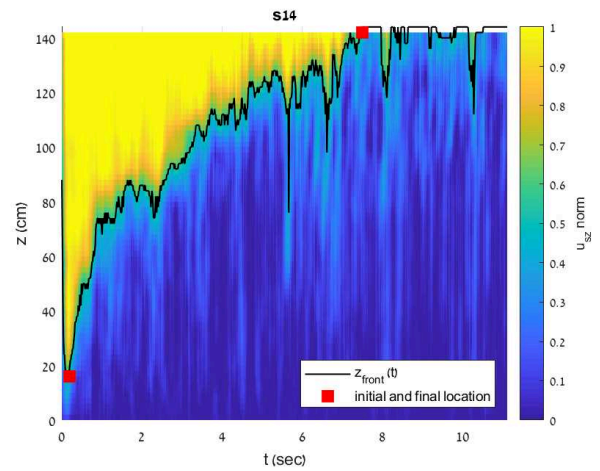
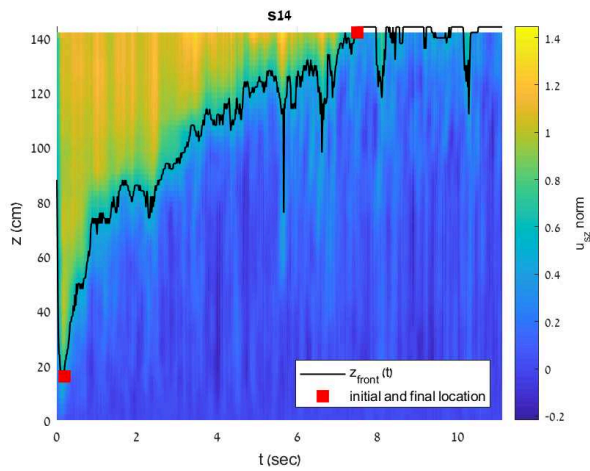
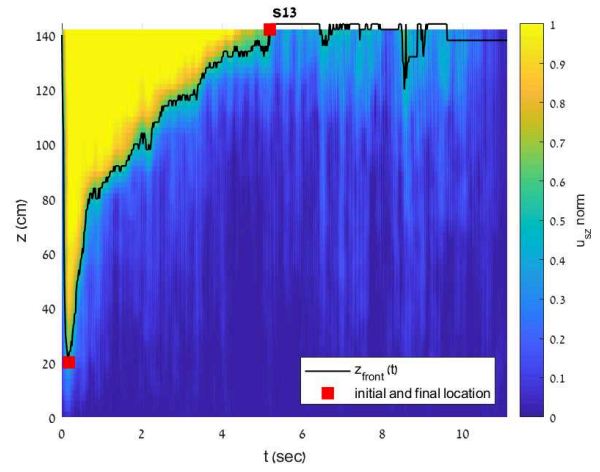
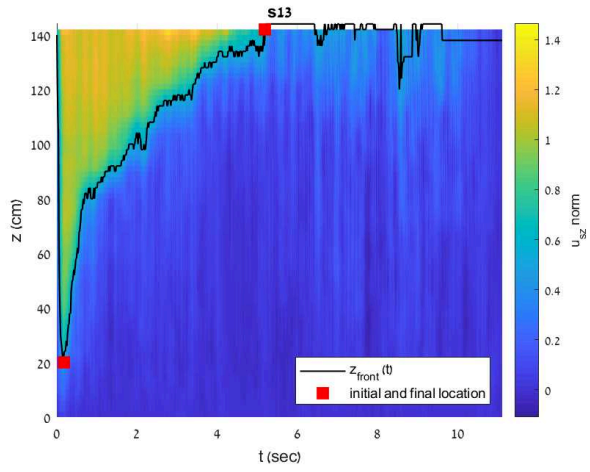
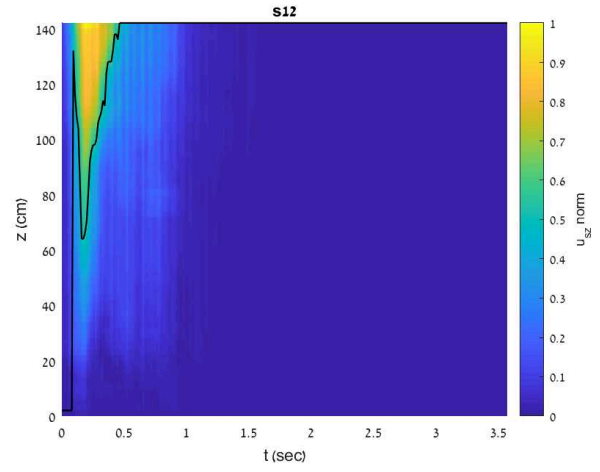
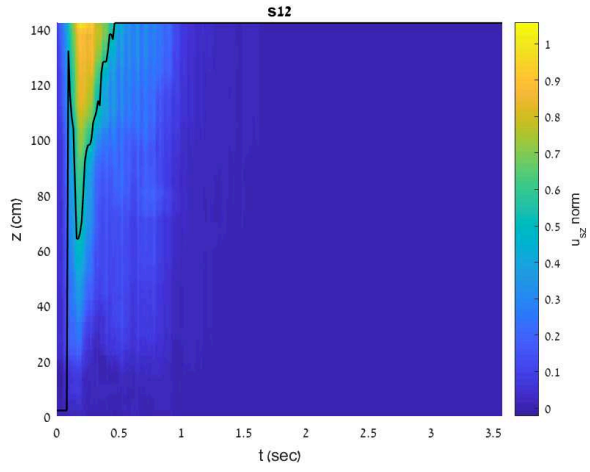
Here, we show grain velocity maps (see Table 3), normalized by the theoretical terminal velocity, following (Eq. 6). The black lines depict the compaction front location over time ($z_{\text{front}}(t)$) and the red markers show the initial and final locations used for the calculation of the front velocity (see section 10.4). The velocity signal is smoothed following the procedure described in section 10.4. For each simulation, the raw normalized velocity values are presented on the left panel, and the values subjected to a 0 – 1 threshold are shown on the right panel. Grains settlement at an approximately constant terminal velocity is shown in yellow, and grains that are approximately vertically stagnant are in blue. The vertical velocity of grains is proportional to the pore pressure gradients (Eq. 5), hence yellow areas in the maps means complete liquefaction. In some of the simulations, the fast downward propagating "liquefaction front" which precedes the "compaction front", can be observed.

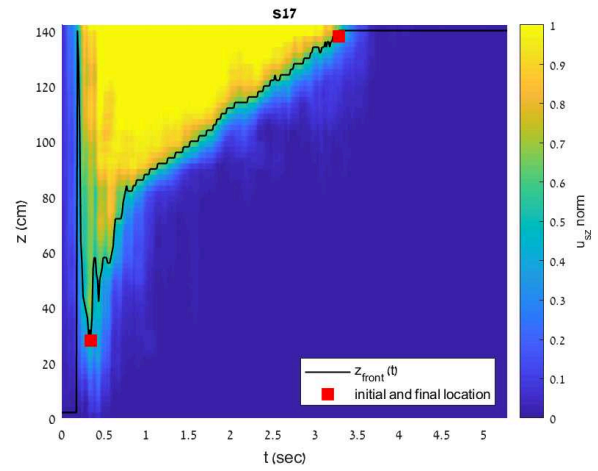
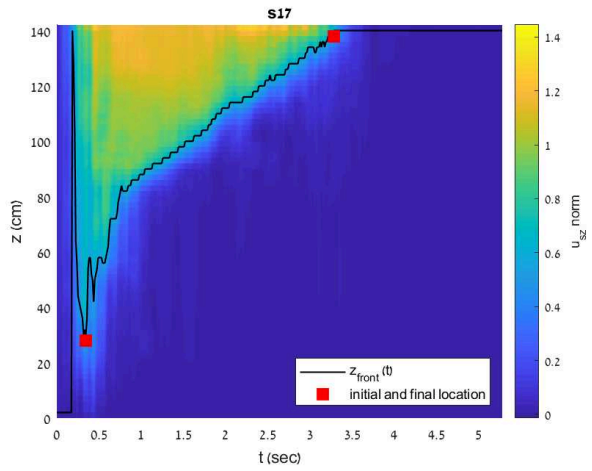
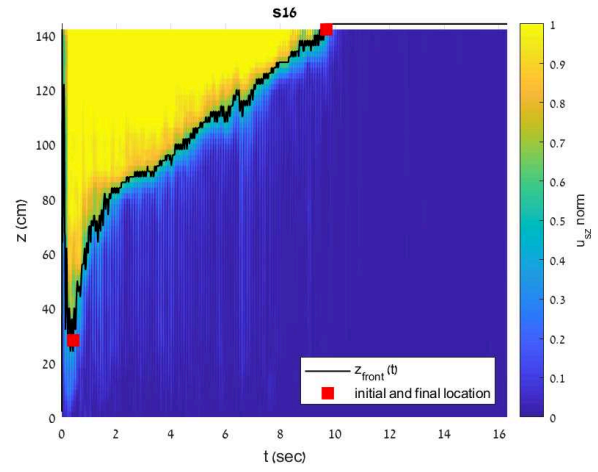
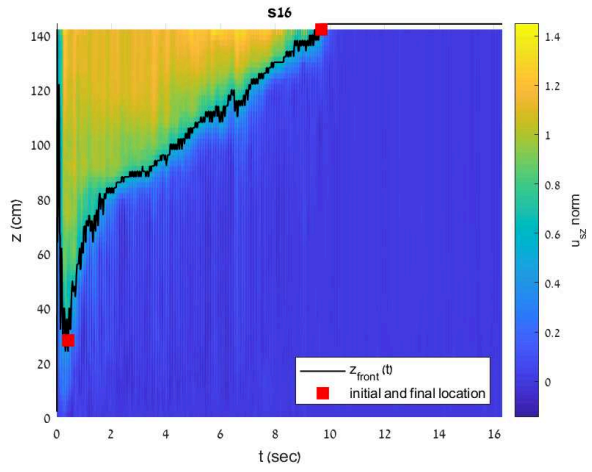
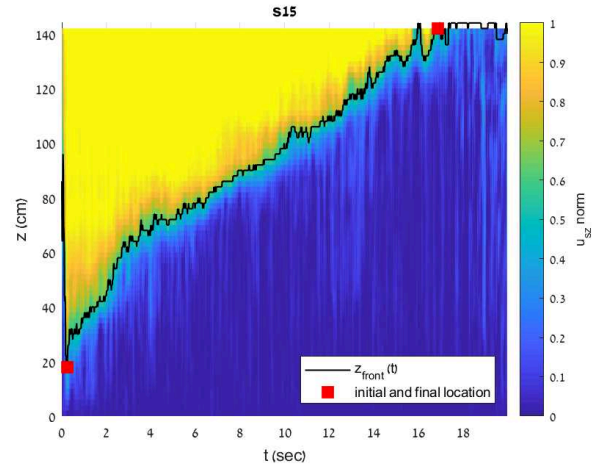
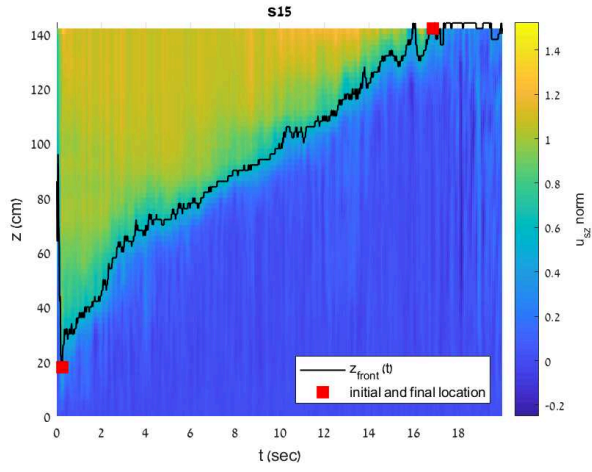


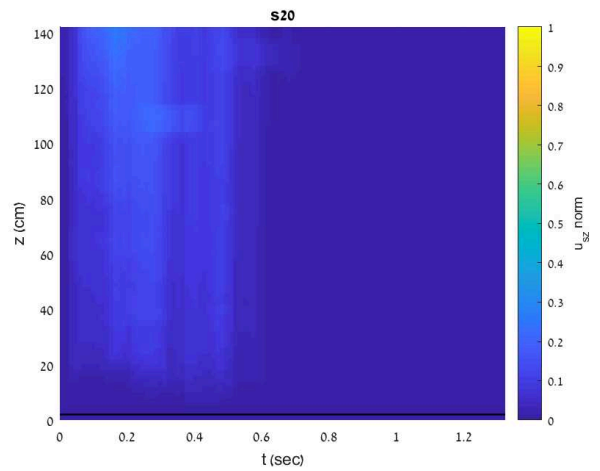
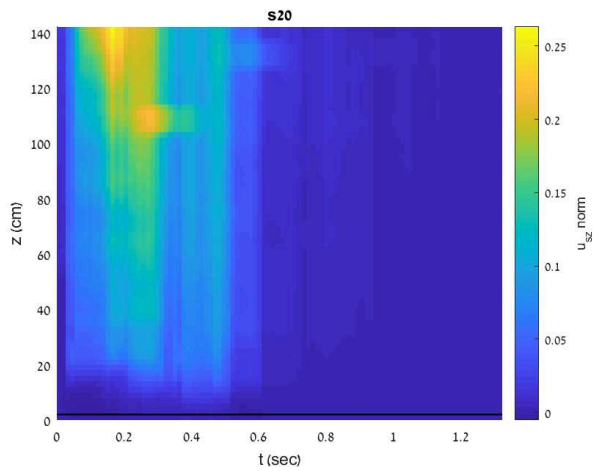
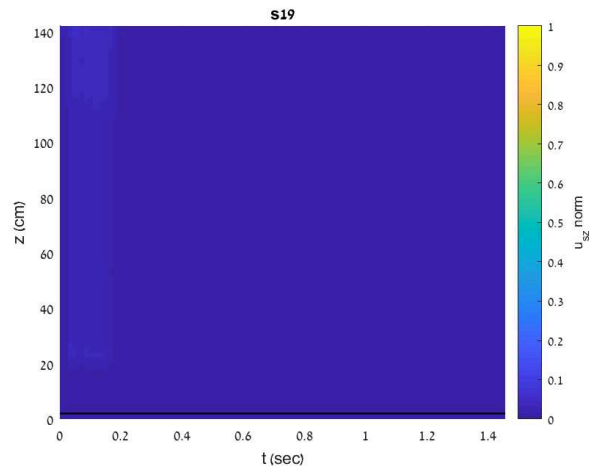
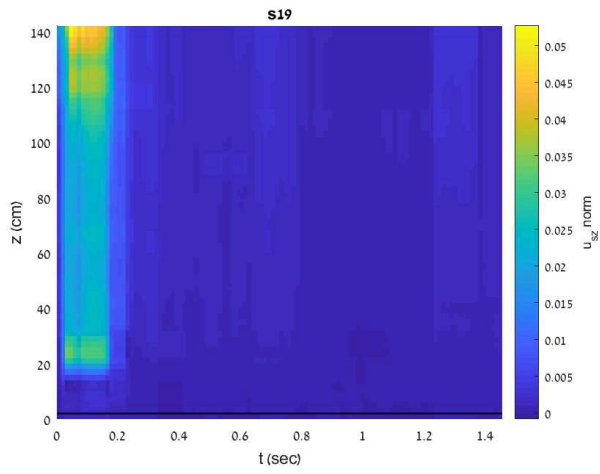
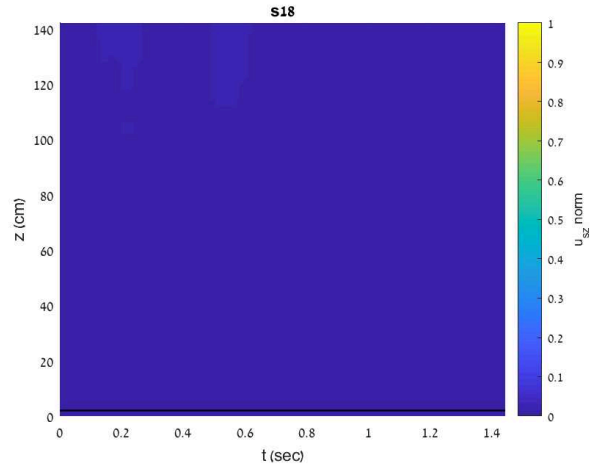
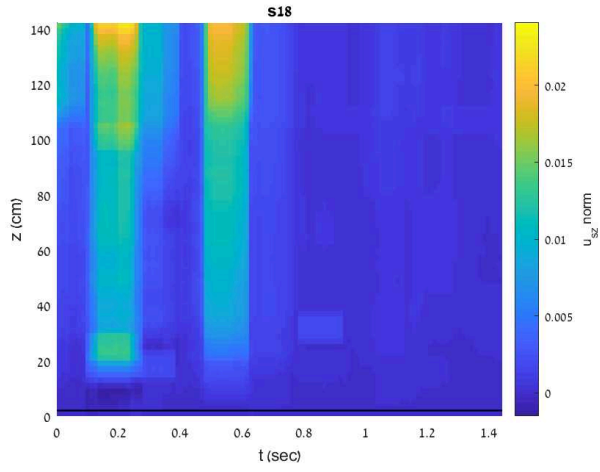












Chapter 3

Recurrent soil liquefaction under drained conditions

Article unpublished - to be submitted to Geophysical Research Letters

Résumé

La liquéfaction des sols induite par les tremblements de terre est un phénomène courant et souvent dévastateur, entraînant de graves pertes économiques et des victimes. Au cours de la liquéfaction, les sols saturés, auparavant stables, deviennent liquides, perdant leur capacité à supporter des structures telles que des bâtiments ou des ponts. Souvent, la liquéfaction se produit de manière récurrente, de sorte que les sols qui ont été liquéfiés par un tremblement de terre se liquéfient à nouveau en réponse à un tremblement de terre ultérieur. Cette re-liquéfaction est énigmatique, car l'un des paramètres importants contrôlant la susceptibilité à la liquéfaction des sols est leur densité relative, c'est-à-dire la compacité du sol par rapport à son état de compaction ultime, où le sol meuble est plus sujet à la liquéfaction que le sol densément tassé. Étant donné que la liquéfaction entraîne la compaction du sol (réduction de la densité relative pendant ou après l'événement), un événement de liquéfaction aurait dû fournir une remédiation naturelle contre la liquéfaction future, et la liquéfaction récurrente aurait dû être rare.

Dans cette lettre, nous montrons que le nouveau mécanisme de liquéfaction drainée et sa relation avec le taux d'apport d'énergie sismique, qui contrôlent le changement de porosité et l'étendue verticale de la compaction pendant la liquéfaction, suggèrent que dans de nombreux cas, seule une compaction partielle se produit dans un premier temps et la re-liquéfaction est presque inévitable lors de futurs tremblements de terre suffisamment forts.

Recurrent soil liquefaction under drained conditions

Shahar Ben-Zeev^{1,2}, Liran Goren³, Renaud Toussaint^{2,4}, Einat Aharonov^{1,4}

¹Institute of Earth Sciences, The Hebrew University of Jerusalem, 91904, Israel

²Université de Strasbourg, CNRS, ENGEES, Institut Terre & Environnement de Strasbourg, UMR7063,
F-67000 Strasbourg, France

³The Department of Earth and Environmental Sciences, Ben-Gurion University of the Negev, 84105, Israel

⁴PoreLab, the Njord Centre, Department of Physics, University of Oslo, P.O. Box 1048 Blindern, NO-0316
Oslo, Norway

Key Points:

- We utilize theory and numerical simulations to harness the novel drained liquefaction mechanism and the associated compaction front dynamics to explain recurrent soil liquefaction.
- Reliquefaction can be the result of a larger shaking intensity in a second shaking event that drives further compaction.
- Reliquefaction can be the result of the vertical spatial distribution of the degree of compaction in the aftermath of the first shaking event.

Corresponding author: Shahar Ben-Zeev, shahar.benzeev@mail.huji.ac.il

Abstract

During seismically-induced soil-liquefaction saturated solid soils transform into liquid-like media in response to earthquake shaking and due to dynamic pore fluid pressurization. A key parameter controlling liquefaction susceptibility is the relative density of soils, where loose soils are more susceptible to liquefaction. A commonly observed outcome of liquefaction is soil densification, which is expected to act as a natural remediation against recurrent liquefaction. Despite this expectation, liquefaction often occurs recurrently at the same site during earthquake sequences. Here we show that within the framework of drained liquefaction initiation, recurrent liquefaction is a foreseeable outcome. Coupled grains-fluid numerical simulations and theory reveal that in drained liquefaction, the rate of seismic energy input controls the change in porosity and the vertical extent of compaction during liquefaction. This suggests that in many cases, only partial compaction occurs in a first event, and reliquefaction is almost inevitable during future, strong enough, earthquakes.

Plain Language Summary

Soil liquefaction is an earthquake hazard in which solid soils become liquid-like, losing their ability to support infrastructure. During liquefaction, fluid-filled voids within the soil reduce their volume in response to earthquake shaking, and the fluid pressure is increased. Consequently, the overburden is supported by the fluid instead of the grains. Dense soils are less susceptible to liquefaction, and since soils usually turn denser in the aftermath of a liquefaction event, liquefaction should have been natural remediation against reliquefaction. Yet, previously liquefied soils are widely documented to liquefy again in a subsequent earthquake. We suggest reconciling the reliquefaction puzzle by invoking the new drained liquefaction mechanism. Using theory and computer simulations, we show that in drained liquefaction, the amount and extent of compaction are controlled by the seismic power, and when only partial compaction occurs during the first liquefaction event, the soil can reliquefy in a future earthquake.

1 Introduction

Seismically induced soil liquefaction is a natural hazard that commonly occurs during earthquakes (Kramer, 1996). Under static conditions, the elasto-plastic rheology of soils allows them to support the load of man-made infrastructures, as well as gravitational forces exerted by sloping surfaces. During earthquake-induced soil liquefaction, the soil partly or fully loses its strength and stiffness, transitioning into a fluid-like material that cannot support infrastructure and gravitational loads. The rheological change associated with liquefaction is mainly attributed to a dynamic increase of the pore fluid pressure in response to pore space reduction (Martin et al., 1975), causing a decrease and even loss of the effective stress and the soil's shear strength. Liquefaction may result in various failure modes, including (Ishihara et al., 2011) sinking, floating, and tilting of infrastructure, ground lateral spreading and settlement (Bray et al., 2014), and landsliding (Bradley et al., 2019).

The relative density of soils, namely, their density with respect their most compacted state, is considered key in controlling liquefaction susceptibility. More specifically, undrained lab experiments (de Alba et al., 1976) showed that loose soils tend to liquefy after fewer shearing cycles than dense soils. Consequently, due to the finite duration of the earthquake's strong motion, denser soils are less likely to liquefy, all else being equal. Geotechnical remedial measures against liquefaction exploit this property by actively increasing the soil's relative density, e.g., via vibro-compaction and explosion (Besharat, 2012)).

It is not uncommon for soil liquefaction to recur at the same site during successive seismic events (Yasuda & Tohno, 1988; Sims & Garvin, 1995; Obermeier, 1996; Wakamatsu, 2011, 2012; Quigley et al., 2013; National Academies of Sciences, Engineering & Medicine, 2016; Papathanassiou et al., 2016; Tuttle et al., 2017). One example of recurring

liquefaction was documented during the Canterbury earthquake sequence in 2010-2011 (New Zealand), where large areas within and outside the city of Christchurch were liquefied several times (Quigley et al., 2013) during the main and aftershock events. A second, well-studied example is the reliquefaction of lake sediments in Watsonville, California, as part of the 1989 Loma Prieta earthquake sequence (Sims & Garvin, 1995). Liquefaction recurrence is highly consequential for evaluating liquefaction potential and severity of future events and for the correct interpretation of paleoseismicity markers (Obermeier, 1996; Maurer et al., 2019). However, despite its pervasiveness and importance, recurrent liquefaction is at odds with the dominant view of liquefaction physics, as explained below.

Two main factors are considered to contribute to the liquefaction resistance of previously-liquefied soils (Olson et al., 2005). Soils that were not disturbed for a sufficiently long duration experience aging effects, which can arise mechanically, i.e., through minor changes in the granular skeleton that progress onto a more stable configuration, and chemically, i.e., through cementation (Olson et al., 2005). Once an aged soil is liquefied, its geotechnical age is reset due to soil fabric destruction, and its susceptibility to reliquefaction is expected to increase. Therefore, a liquefaction - reliquefaction sequence of aged soils is not perplexing. In contrast, young and less cohesive soils are expected to densify during and after liquefaction (Obermeier, 1996; Olson et al., 2005), and so previously liquefied young soils are expected to develop some resistance to future reliquefaction (de Alba et al., 1976; Obermeier, 1996; National Academies of Sciences, Engineering & Medicine, 2016). Hence, a liquefaction event of young or rejuvenated soils is expected to reduce their reliquefaction potential, acting as a natural remedial measure. Sequences of liquefaction and reliquefaction events of young and rejuvenated soils thus present an enigma.

In the current study, we will not consider aging effects, but instead focus on either relatively young soil layers, that did not age yet (including man-made fill, and reclaimed lands), or, rejuvenated soils reset by at least one prior liquefaction event.

Liquefaction is classically considered as an undrained phenomena (Martin et al., 1975; Kramer, 1996), whereby the rate of pore pressure dissipation, and fluid flow in and out of the pore space is much slower than the deformation rate of the solid soil matrix. Recent studies, however, established that there is another path to liquefaction, which has been previously overlooked: liquefaction can also initiate under drained conditions (Goren et al., 2010, 2011; Madabhushi & Haigh, 2012; Lakeland et al., 2014; Adamidis & Madabhushi, 2018; Clément et al., 2018; Ben-Zeev et al., 2020, 2022). Here we explore the conditions and parameters that facilitate recurring liquefaction events in young and rejuvenated soils within the framework of drained-liquefaction triggering.

In drained liquefaction, the timescale for pressurized pore fluid evacuation is much shorter than that of the earthquake forcing that induces skeleton compaction. The fluid flow toward a drained boundary during shaking is the driving mechanism for the formation of elevated pore pressure gradients and excess pore pressure above hydrostatic values. The "drained liquefaction" mechanism was recently invoked (Ben-Zeev et al., 2022) to explain triggering of liquefaction by remote earthquakes (Wang, 2007), revealing its potential prevalence in liquefaction catalogues (Ben-Zeev et al., 2022). The "drained liquefaction" process has been described in (Ben-Zeev et al., 2020, 2022), and we summarize its essence here: Drained liquefaction is characterized by a co-seismic settlement of the granular layer (Madabhushi & Haigh, 2012; Ben-Zeev et al., 2020, 2022), at a rate that is coupled to the rate of fluid flow and mainly depends on the soil permeability, κ (Ben-Zeev et al., 2020):

$$\frac{dH}{dt} = u_{sz} = \frac{\kappa}{\eta} \frac{\partial P'}{\partial z}, \quad (1)$$

where H is the layer's height, u_{sz} is the vertical velocity of grains, η is the fluid viscosity, and $\partial P'/\partial z$ the dynamic pore pressure gradient (the pressure in excess of hydrostatic) in

the vertical direction. During liquefaction, equation 1 becomes:

$$\frac{dH}{dt} \simeq u_{szC} = \frac{\kappa}{\eta} \frac{d\sigma}{dz}, \quad (2)$$

where u_{szC} is the terminal settling velocity of the top region of grains, and $d\sigma/dz < 0$ is the initial vertical effective normal stress gradient.

In drained liquefaction, compaction is not uniform throughout the layer. Instead, it is localized within an upward-moving narrow compaction front (Fig. 1b) (Ben-Zeev et al., 2020). The magnitude of compaction, i.e., the change in porosity across the front, $\Delta\phi = \phi_0 - \phi_c$, (where ϕ_0 and ϕ_c are the porosity above and below the compaction front, respectively), was found in Ben-Zeev et al. (2022) to depend mainly on the rate of the seismic energy density imposed by shaking (Fig. 1e), which we term the *seismic power* ($Sp = e_n/T$, where e_n is the average seismic energy density in one shear cycle, and $T = f^{-1}$ is the periodicity of shaking, the inverse of the frequency). High Sp causes a large porosity decrease ($\Delta\phi$) across the front, and low Sp produces a small $\Delta\phi$. In the limit of $Sp \rightarrow 0$, the change in porosity will drop to zero. A reasonably good correlation was also found (Ben-Zeev et al., 2022) between $\Delta\phi$ and PGV (and thus also with energy), and between $\Delta\phi$ and PGA.

The propagation velocity of the compaction front is (Ben-Zeev et al., 2020):

$$u_{\text{front}} = \frac{(\phi_0 - 1)}{\Delta\phi} \frac{dH}{dt} = \frac{(\phi_0 - 1)}{\Delta\phi} \frac{\kappa}{\eta} \frac{d\sigma}{dz}, \quad (3)$$

The theoretical liquefaction duration is the time it takes the front to sweep through the whole layer:

$$t_e = \frac{L}{u_{\text{front}}}, \quad (4)$$

where $L \leq H$ is the depth from which the liquefaction front starts propagating. A small $\Delta\phi$ across the front, arising from a small input Sp , produces faster front progression (Eq. 3), resulting in a potentially shorter liquefaction event (Eq. 4). A large $\Delta\phi$ across the front, arising from a high input Sp , produces slower front progression (Eq. 3), resulting in a potentially longer liquefaction event (Eq. 4). The permeability of the layer also plays a significant role, where the front will be slower in a less permeable layer, resulting in a longer liquefaction event.

If seismic shaking stops before the compaction front has reached the top of the soil layer, $Sp = 0$, the change in porosity ($\Delta\phi$) will be negligible compared to the syn-shaking porosity change, and the post-shaking front will propagate significantly faster than the former syn-shaking front (Eq. 3), resulting in a quick cessation of the liquefaction event (Eq. 4) after the arrest of shaking.

Since earthquakes have a finite duration (t_{EQ}), and the dynamics are expected to halt after the shaking ceased ($Sp = 0$), the effective duration of a drained liquefaction event is

$$t_e^* = \min[t_e, t_{EQ}]. \quad (5)$$

If $t_e < t_{EQ}$, the compaction front has time to swipe through the whole layer, compacting it into a stable configuration with ϕ_c dictated by the Sp (Fig. 1c,e). If $t_e > t_{EQ}$, only the bottom sub-layer, through which the front has swiped, will compact into the new Sp -dependent stable porosity, ϕ_c , while the top sub-layer will remain at its' original porosity, ϕ_0 (Fig. 1d).

The unique interplay between the seismic power (Sp), $\Delta\phi$, compaction front velocity, and the earthquake duration could lead to a wide range of scenarios, in which a liquefied layer will not become liquefaction resistant in the aftermath of an earthquake. Motivated by these insights, we hypothesize that recurrent liquefaction sequences could represent predictable dynamics associated with drained liquefaction under varying Sp input and earthquake duration in a series of successive earthquakes.

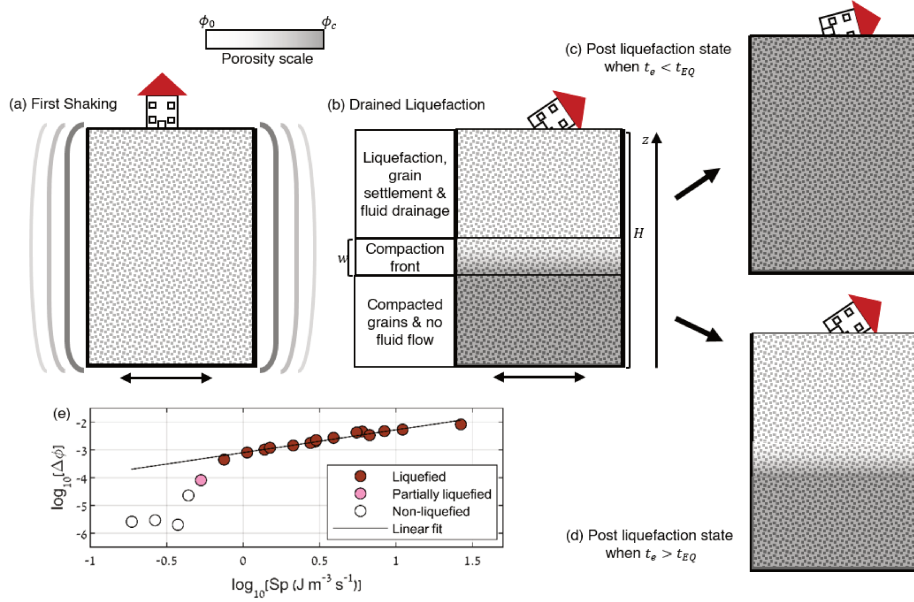


Figure 1. Cartoon describing the drained liquefaction process. (a) a layer of initial porosity ϕ_0 is shaken under seismic power Sp . (b) A compaction front of width w divides the layer into a lower solidified zone, compacted to porosity ϕ_c , and an upper zone that is liquefied and is continuously settling with porosity ϕ_0 . (c) If the theoretical duration of liquefaction (t_e) was shorter than the earthquake duration (t_{EQ}), the front has swiped all the way up during the earthquake, and the whole layer will achieve the compacted porosity, ϕ_c , dictated by the Sp from the earthquake. (d) If the theoretical duration of liquefaction (t_e) was longer than the earthquake duration (t_{EQ}), the front did not have time to swipe all the way up, so that at the end of shaking the layer will be divided into two sub-layers: a top layer with the initial porosity ϕ_0 , and a bottom layer compacted to ϕ_c (where the value of ϕ_c is dictated by Sp , as shown in panel e). (e) The change in porosity, $\Delta\phi = \phi_0 - \phi_c$ vs. the input seismic power (data from Ben-Zeev et al. 2022). The equation for the best fit is $Y = 0.82 X - 3.1$; $R^2 = 0.95$.

2 Coupled Grains and Fluid Numerical Simulations

We use a two-phase coupled model, where the solid grains are modeled using the discrete element method (DEM, (Cundall & Strack, 1979)), and the fluid phase is modeled as a continuum on a superimposed Eulerian grid (McNamara et al., 2000; Johnsen et al., 2006; Niebling et al., 2010a, 2010b; Vinningland et al., 2007b, 2007a). The fluid equation solved on the superimposed grid is a pore pressure diffusion equation (Goren et al., 2010, 2011), with a source term that relates dilation and compaction of the pore space due to grain skeleton deformation to pore pressure change. The dynamics of the solid grains are affected by the pore pressure gradients via the incorporation of pore pressure drag force in their linear momentum conservation equation. Within this numerical framework, drained or undrained behavior is not pre-determined, but rather emerges during the simulation in response to the assigned parameters and boundary conditions. The method and code were recently validated by comparing the emergent grains and fluid dynamics between the numerical model, experiments, and theory under harmonic shaking excitation (Ben-Zeev et al., 2022). For a detailed description of the numerical method, see Text S1 and Figure S1 in Supporting Information.

We explore the possibility and dynamics of recurrent liquefaction events under drained conditions by executing a series of nine simulations (Table S1 in the Supporting Information). In each simulation, a saturated, drained granular layer is shaken by two successive shaking events punctuated by a period of relaxation, when no shaking is applied. Each shaking event is characterised by an input power (Sp), denoted as Sp_1 and Sp_2 , for the first and second shaking events, respectively. Three predetermined Sp values are used in the simulation series: (1) low $Sp = 1.39 \text{ J m}^{-3}\text{s}^{-1}$ ($PGV = 0.018 \text{ m/s}$; $PGA = 0.075g$), (2) medium $Sp = 3.92 \text{ J m}^{-3}\text{s}^{-1}$ ($PGV = 0.025 \text{ m/s}$; $PGA = 0.15g$) and (3) high $Sp = 11.1 \text{ J m}^{-3}\text{s}^{-1}$ ($PGV = 0.036 \text{ m/s}$; $PGA = 0.3g$). The applied shaking signals share an equal displacement amplitude of $A = 0.0431 \text{ cm}$ (4.31% average grain diameter), and the Sp values are controlled by modifying the shaking frequency (6.6, 9.3 and 13.2 Hz). The first shaking event (with Sp_1) is stopped once the compaction front reaches the layer mid-depth ($\sim H/2$). Then we wait a relaxation period of $\simeq 1$ second so that residual compaction ceases and excess pore pressure fully dissipates before starting a second shaking event with Sp_2 .

3 Results

To demonstrate liquefaction-reliquefaction dynamics under drained conditions, Fig. 2 presents results from simulation sim3 (Table S1 in the Supporting Information), which was shaken with $Sp_2 > Sp_1$ (Fig. 2a). Panels b-d show different aspects of the saturated grain layer dynamic, revealing two consecutive liquefaction events of the same saturated grain layer. Fig. 2b shows that the dynamic pore pressure, P' , normalized by the initial effective lithostatic stress, σ_0 , at different depths, (Fig. 2b) reaches a value of one during both shaking events, indicating that P' became equal to the initial effective lithostatic overburden, a prominent liquefaction indicator. High P' is recorded over longer duration at depth closer to the surface. Fig. 2c depicts the vertical grain velocity normalized by the theoretical critical value (u_{szC} , Eq. 2) through depth and time. The figure shows that the layer is divided into two. In the upper region, grains settle at their maximal theoretical speed (yellow region), during both the first and second shaking events, which coincide with the durations of the high P' presented in Fig. 2b. During each of the two events, the upper settling region shrinks with time, due to the upward migrating compaction front that separates the upper region (yellow) from a lower (blue) region. In the lower region, grains are approximately stagnant in the vertical direction (Fig. 1b). The black solid line in Fig. 2c depicts the depth in which $u_{sz}/u_{szC} = 0.5$, which is defined here as the compaction front location over time. Only across the transition zone between the upper and lower regions, within the finite thickness of the compaction front, does active compaction take place. The slope of the front location defines the front velocity. Ben-Zeev et al. (2022) demonstrated that the front velocity u_{front} is inversely dependent on the input power, Sp . This relation emerges from the control of

Sp on $\Delta\phi$ (Fig.1e), and the inverse relation between $\Delta\phi$ and u_{front} as predicted by equation (3). u_{front} is fastest when shaking is stopped ($Sp = 0, \Delta\phi \rightarrow 0$) between the two shaking events (marked by a dotted black line).

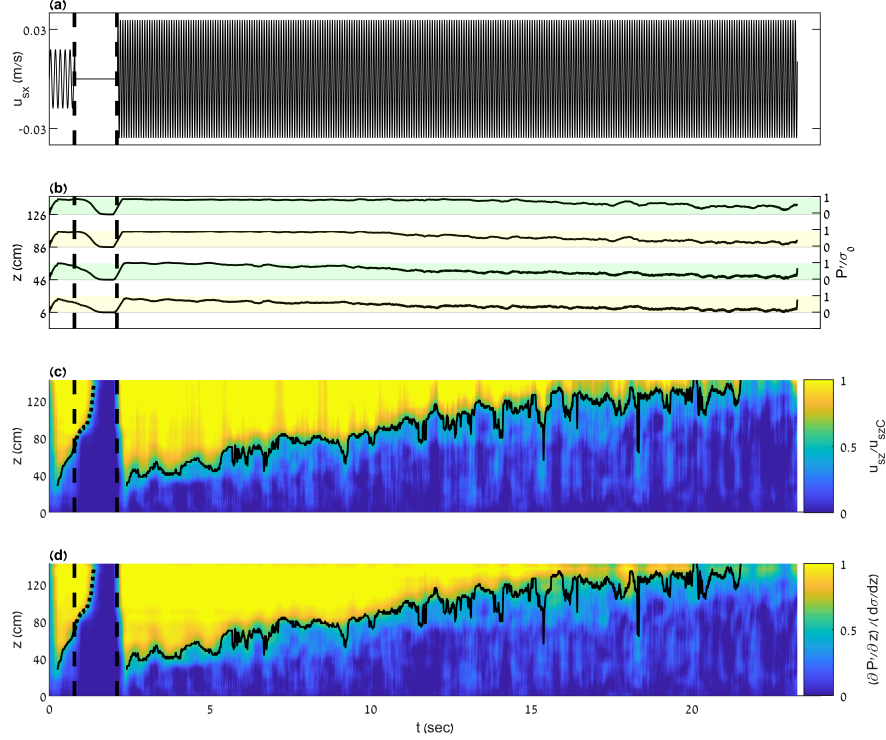


Figure 2. Results from a representative simulation of $Sp_2 > Sp_1$ (sim3 in Table S1). The results show an emergent sequence of liquefaction - reliquefaction of a saturated grain layer by two consecutive shaking events. (a) The imposed horizontal velocity at the base of the grain layer shows a first event ($Sp_1 = 1.39 \text{ J m}^{-3}\text{s}^{-1}$), followed by a relaxation period (delineated by the dashed lines), and a second shaking event with a higher PGV and frequency, producing a higher power of $Sp_2 = 11.1 \text{ J m}^{-3}\text{s}^{-1}$. (b) Dynamic pore pressure normalized by the initial effective stress, at different depths. The pressure rises, and the layer is liquefied ($P'/\sigma_0 = 1$) quickly after the onset of shaking in both events. (c) Normalized vertical grain velocity as a function of depth and time. The black line marks the compaction front location over time, chosen here to be at $u_{sz}/u_{szC} = 0.5$. The slope of the compaction front location is the front velocity (u_{front}). (d) Dynamic pore pressure gradient in the vertical direction normalized by the initial effective stress gradient. The front location (black line) is a replica of the front location from panel (c), revealing the strong correspondence and coupling between pressure gradient and grain velocity, following equations 1 and 2. The region above the front is seen to be liquefied and to narrow through time. Notice that the layer is reliquefied during the second shaking event.

Fig. 2d presents the dynamic pore pressure gradient normalized by the initial effective lithostatic stress gradient ($(\partial P'/\partial z)/(\partial \sigma/\partial z)$). The similarity between the grains vertical

velocity pattern presented in Fig. 2c and the normalized pore pressure gradient pattern is striking, and it demonstrates the strong coupling between the pore pressure gradient and the grains velocity following the predictions of equations 1 and 2. More specifically, when the settling vertical velocity of the grains is equal to the theoretical terminal value (yellow in Fig. 2c), the dynamic pore pressure gradient is equal to the initial effective lithostatic stress gradient, the grains are fully supported by the pore pressure and the region is liquefied (yellow in Fig. 2d). When the vertical velocity of the grains is close to zero (blue in Fig. 2c), the dynamic pore pressure gradient is close to zero as well (blue in Fig. 2d). Consequently, the front defines the border between liquefied and settling sub-layer at the top and non-liquefied stagnant sub-layer at the bottom.

Importantly, grain settling and pore pressure gradient dynamics are similar across the two shaking events despite the difference in the imposed Sp . Particularly, grain settlement and lithostatic pore pressure gradients are observed to initiate at approximately the same depth in both events, even though the bottom sub-layer was already compacted prior to the second event.

Figure 3 extends the insights developed based on Figure 2 across the entire simulation set. Each sub-panel in Figure 3a presents the normalized vertical grain velocity (similar to Figure 2c), where the shaking velocity associated with the two shaking events is depicted at the base for each panel. The panels are organized such that the vertical axis of Fig. 3 represents the first shaking phase (Sp_1), and the horizontal axis represents the second shaking phase (Sp_2). The duration of the first shaking event is set so that at the end of the event, the front reaches the layer's mid-depth ($H/2$). This means that at the end of the first shaking event, the sub-layer below $H/2$ is compacted to $\phi_c(Sp_1)$, while the sub-layer above this depth retains its initial porosity ϕ_0 . Since the front velocity varies inversely with the input Sp , we increase the first event duration with increasing Sp_1 . Fig. 3b is organized similarly to Fig. 3a. Each sub-panel shows the normalized dynamic pore pressure (as in Figure 2b) for the corresponding events in Fig. 3a. The full simulation set presented in Fig. 3 reveals that the two consecutive shaking events produced liquefaction-reliquefaction sequences across all the explored combinations of Sp_1 and Sp_2 . We identify liquefaction events based on grain settlement at the terminal velocity (predicted by equation 2) and complete pressurization of the interstitial pore fluid.

The simulation set presented in Fig. 3 can be categorized into two end-members based on the relative values of the input powers during the two shaking events. The two end-member behaviors primarily differ by the initiation depth of the reliquefaction (second event) compaction front. The first end-member is when $Sp_2 \leq Sp_1$ (green and red dots, on and above the diagonal). Here, the front of the second event starts approximately at the depth where the front of the first event stopped (slightly higher, in most cases, due to residual compaction during the relaxation period). The dynamic pore pressure during the second event rises to lithostatic values only above the location of the new front (Fig. 3b). When $Sp_2 = Sp_1$ (green dots), it is apparent that the second event front velocity is approximately equal (the slope of the black line) to that of the first event. When $Sp_2 < Sp_1$ (red dots), the front velocity during the second event is faster than that of the first event. Overall, when $Sp_2 \leq Sp_1$, the second shaking event induces reliquefaction, but only within the top sub-layer, which did not experience compaction during the first event.

The second end-member behavior occurs when $Sp_2 > Sp_1$ (blue dots, below the diagonal). Here, the front produced by the second event initiates deeper than where the first front stopped. Therefore, also sub-layers that were compacted during the first event re-compact and reliquefy. Here again, the dynamic pore pressure rises to lithostatic values above the new front location (Fig. 3b).

4 Discussion

Reliquefaction occurs ubiquitously around the globe, but it is not well explained by the conventional liquefaction mechanism. Here we show that reliquefaction could be expected under the "drained" mechanism (Goren et al., 2010, 2011; Ben-Zeev et al., 2020, 2022). Drained and undrained liquefaction both perceive the process of pressurization as an outcome of porosity evolution, driven by the soils' tendency to compact under cyclic forcing when the initial porosity (or the equivalent relative density) is sufficiently large. The two mechanisms differ both in their compaction mechanism and in their fluid pressurization mechanism. Pressurization in undrained liquefaction arises from the cumulative porosity decrease and the compressibility of the fluid, while in drained liquefaction, the pressurization is controlled by the *rate* of porosity change (Goren et al., 2010, 2011), which, in itself, is linked to the rate of fluid drainage out of the compacting pore space. The latter is a function of the skeleton permeability and fluid viscosity. A crucial component of the drained liquefaction physics is that porosity reduction (i.e. compaction) does not occur uniformly across the soil layer, as is often implicitly assumed for the undrained liquefaction end-member, but it is localized along the upward migrating compaction front (Ben-Zeev et al., 2020, 2022). As a consequence, in undrained liquefaction a homogeneous layer is expected to liquefy uniformly, while in drained liquefaction only the progressively shrinking sub-layer above the ascending compaction front will liquefy.

The drained liquefaction theory and the current simulations of a soil layer response to two consecutive simulated earthquakes (two shaking events), reveal that the possibility for reliquefaction within the drained liquefaction framework is tightly linked to the compaction front dynamics. More specifically, two properties of the front dynamics predispose the soil layer for reliquefaction.

The first is the control of the shaking power on the equilibrium porosity of the compacted sublayer, $\phi_c(S_p)$. Figure 4a demonstrates how the average porosity (below the compaction front) changes in the course of the two successive shaking events. After the first shaking event, the compacted bottom sub-layer achieved porosity ϕ_{c1} , lower than its initial porosity, ϕ_0 . The value of ϕ_{c1} (black dots in Figure 4a) decreases with increasing Sp_1 . The white circles in Figure 4a show the porosity of the compacted sub-layer after the second event. If $Sp_2 \leq Sp_1$ the porosity of the compacted sub-layer remains unchanged, so that $\phi_{c2} \approx \phi_{c1}$. If however $Sp_2 > Sp_1$, the porosity of this sublayer, ϕ_{c2} , is further reduced in the second shaking event. Consequently, the final porosity, ϕ_{c2} , after a shaking sequence is a function of the maximal Sp experienced by the soil during the seismic sequence (Fig. 4b). The results in Fig. 4b agree with Fig. 1e, i.e., the reduction in porosity due to passage of a compaction front increases with Sp that causes this compaction. This control means that any soil compacted under a certain Sp could be further compacted and consequently reliquefied in response to a higher Sp event (Fig. 5a).

The second property of the front dynamics that facilitates reliquefaction emerges from its finite velocity (Fig. 5b). If a shaking event terminates before the front reaches the top of the soil column, the sublayer above the final front position did not have a chance to reduce its porosity. The tendency of this top sublayer to reliquefy is, therefore, equal to the tendency of the whole soil layer to liquefy before the first event. Reliquefaction of the top sublayer is expected to occur under any Sp that would have liquefied the whole soil layer in the first event, including under $Sp_2 < Sp_1$.

Since the front velocity depends on the soil skeleton permeability and inversely on the shaking power Sp (as can be deduced from equation 3 and Figure 1 (Ben-Zeev et al., 2022)), relatively low-permeable soils and high Sp_1 events are expected to produce slow migrating compaction fronts, increasing the potential for $t_{EQ} < t_e$. This leaves the top sublayer uncompacted following the first event, preserving its susceptibility to liquefy in future shaking event, even when $Sp_2 < Sp_1$.

It is noted that the seismic power (Sp) experienced at a site could vary in between consecutive seismic events, as it is determined by the earthquake’s magnitude and the distance to the source (assuming a simple earth velocity model and neglecting specific site effects) (Wang, 2007). More specifically, excitation of one site by variable Sp values in different seismic events can be the outcome of two possible scenarios: (1) Varying earthquake magnitudes on the same source (e.g., a preshock-mainshock-aftershock sequence), and (2) Excitation from various source location relative to the site of the liquefiable soil (e.g., different segments of a single fault or a complex faults system).

Our numerical and theoretical insights are consistent with the recent experimental series of Ha et al. (2011) conducted with a drained top boundary. The authors studied reliquefaction by conducting shaking table experiments of five consecutive shaking events with equal excitation parameters over five different sands. By defining the number of shear cycles required to liquefy and reliquefy the soil as a metric for liquefaction susceptibility, Ha et al. (2011) found that the susceptibility of the top sublayers did not significantly change from the second shaking event and onward (the first event rejuvenated the soil, a process that is not accounted for in the current study), even though the average relative density of the soil (accounting for the whole layer, from the bottom) decreases between shaking events. We can explain these findings as an outcome of the second property of front dynamics (Fig. 5b). The experimental top sublayers were presumably left under-compacted for the given magnitude of excitation because the compaction front did not reach the top of the layer, leaving them susceptible to reliquefy even under similar excitation.

An important outcome of our new understanding is that drained reliquefaction resistance could be achieved only if the compaction front has reached the top of the soil layer during the first shaking event, $t_e < t_{EQ}$, and only against later shaking events with a smaller or equal power S_p , i.e., $Sp_2 \leq Sp_1$ (see Fig. 5).

5 Conclusions

We performed numerical simulations of coupled grain dynamics and pore fluid flow and pressurization under drained conditions, whereby fluid can flow out of a compacting layer at the timescale of compaction. Simulation results of drained liquefaction triggering and theory predict the occurrence of reliquefaction in an earthquake sequence. The seismic power (Sp) controls the amount of compaction and its vertical extent. The latter is regulated by an upward migrating compaction front whose velocity is a function of Sp . Consequently, reliquefaction can be the outcome of two factors. First, reliquefaction can occur when the Sp of the second event is larger than that of the first event, forcing the soil to further compact and pressurize during the second event (Fig. 5a). Second, arrest of the compaction front migration at mid-depth due to cessation of the seismic event leaves the top sub-layers under-compacted, allowing them to reliquefy even under a second lower Sp seismic event (Fig. 5b). These new understandings provide a fuller perspective of soil reliquefaction susceptibility than the commonly used relative density. The new theory links the final density of liquefied sub-layers (porosity in this study) to the magnitude of the excitation sequence, allowing assessing the vertical extent of non-resistant sub-layers. Furthermore, understanding the drained path for reliquefaction is highly consequential for liquefaction resistance assessments of sites that were artificially remediated by increasing the soil density. Our insights are also expected to contribute to paleo-seismicity studies. The assessment of paleo-ground motion and paleo-earthquake magnitude from observations of soft-sediment deformation relies on geotechnical procedures. The links we propose between reliquefaction events and sequences of seismic power could provide new ways of interpreting reliquefaction sequences in the geological record.

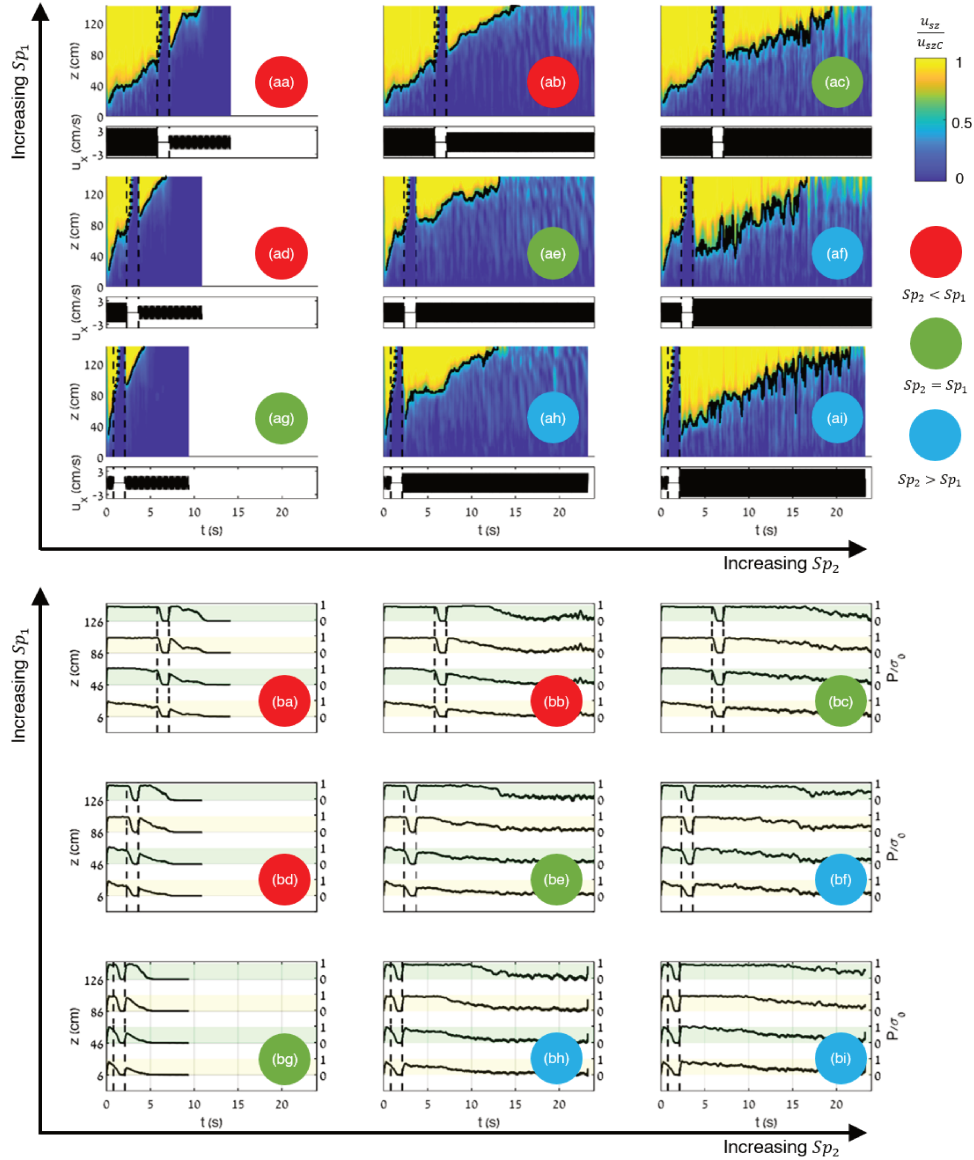


Figure 3. Overview of the entire simulation set, showing sequences of two shaking events, separated by a relaxation period (start and end times are depicted by vertical dashed lines). Three power (Sp) values are used for the first and second shaking events. Each row represents different Sp_1 for the first event (the bottom row shows the smallest Sp_1). Each column represents a different value of Sp_2 for the second event (left column is the smallest Sp_2). (a) Normalized vertical velocity of grains as a function of depth vs. time. The input horizontal velocity is depicted below each sub-panel. The black line marks the compaction front location over time (dotted during relaxation). The yellow color marks terminal grain velocity, corresponding to liquefied grains, and the blue colors mark grains that are approximately stagnant in the vertical direction, and are not supported by fluid pressure gradient that reach lithostatic values. (b) Dynamic pore pressure normalized by the initial effective stress, at different depths (colored rectangles enclose the 0 – 1 range at each depth). Two end members behaviors emerge. When $Sp_2 \leq Sp_1$ (green and red dots, on and above the diagonal), the second event induces reliquefaction only within the top sub-layer, without reliquefying the compacted bottom sub-layer. When $Sp_2 > Sp_1$ (blue dots, below the diagonal), deep regions within the layer reliquefy during the second shaking phase, reliquefying also sub-layers that were compacted in the first event.

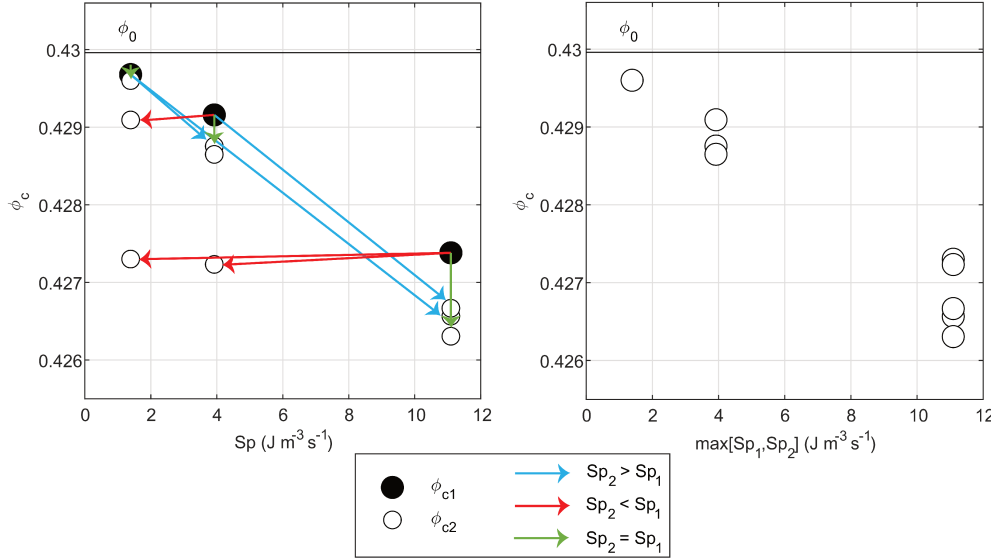


Figure 4. (a) Average porosity as a function of the seismic power. The average porosity is calculated below the final position of the compaction front following the first event ($0 \leq z < H/2$), measured at the final time step of the first (ϕ_{c1}) and second (ϕ_{c2}) events. The initial porosity (ϕ_0) is depicted by a horizontal black line. The arrows are pointing from Sp_1 to Sp_2 . When $Sp_2 > Sp_1$ the porosity decreases in the second phase (blue arrows pointing downward and to the right). When $Sp_2 \leq Sp_1$ the porosity remains almost constant despite the second shaking (horizontal red and vertical green arrows). (b) Average porosity (as defined in (a)) plotted against the maximal Sp in a shaking sequence, which controls the final critical porosity, regardless of its position in the shaking sequence. This result is a consequence of the basic relation between compaction and Sp shown in Fig. 1e.

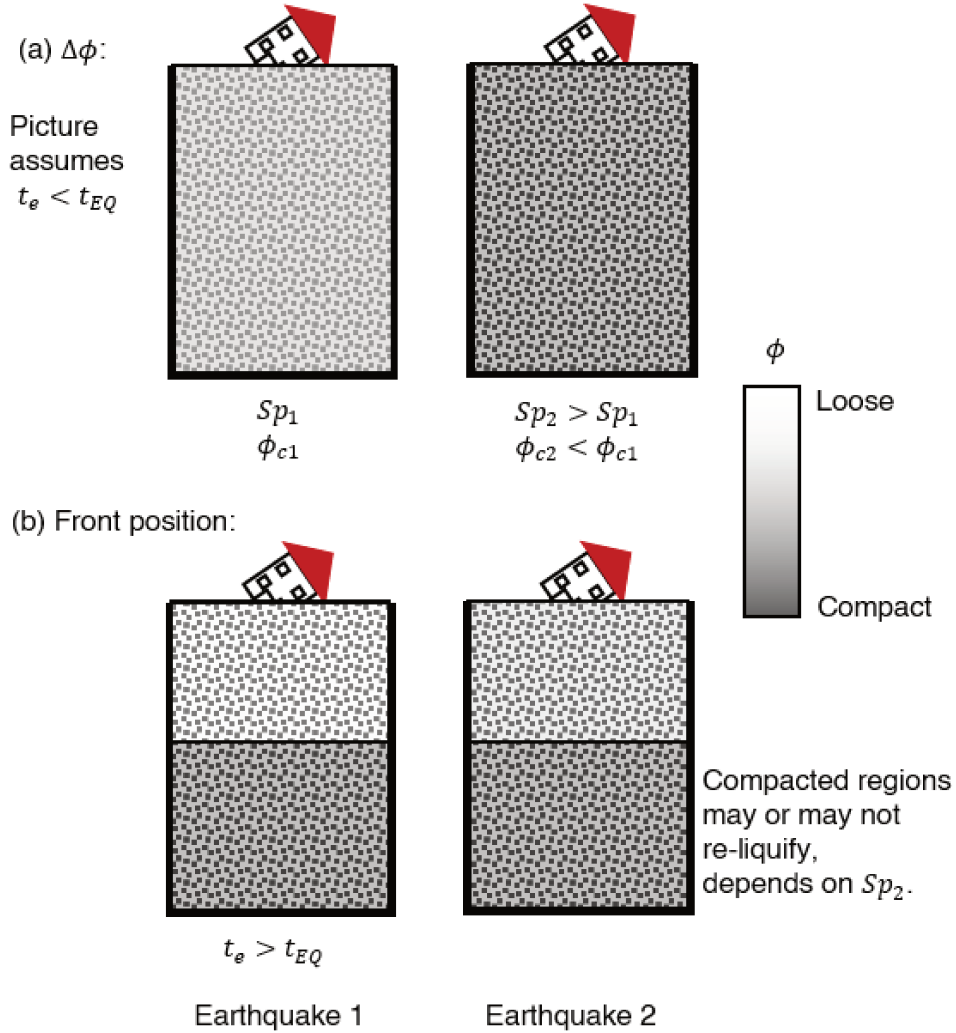


Figure 5. The two paths for reliquefaction. (a) Forcing with a higher power in the second earthquake ($Sp_2 > Sp_1$) drives the layer to compact to a denser, ϕ_{c2} configuration, fully reliequifying it in the second event. (b) A partial progression of the compaction front in the first earthquake leaves the topmost sub-layer under-compacted, making it prone to reliquefaction in a second earthquake, even if $Sp_2 \leq Sp_1$. Rliquefaction can be achieved by a combination of the two ingredients or by one of them.

References

- Adamidis, O., & Madabhushi, G. (2018). Experimental investigation of drainage during earthquake-induced Experimental investigation of drainage during earthquake-induced liquefaction. *Geotechnique*, *68*(8), 655–665. doi: 10.1680/jgeot.16.p.090
- Ben-Zeev, S., Aharonov, E., Toussaint, R., Perez, S., & Goren, L. (2020). Compaction front and pore fluid pressurization in horizontally shaken drained granular layers. *Physical Review Fluids*, *054301*, 1–25. doi: 10.1103/PhysRevFluids.5.054301
- Ben-Zeev, S., Goren, L., Toussaint, R., & Aharonov, E. (2022). Drainage explains soil liquefaction beyond the earthquake near-field. *under revision for Nature Communications*.
- Besharat, V. (2012). The Methods of Remediation of Existing Underground Structure Against Liquefaction. In *15th word conference on earthquake engineering*.
- Bradley, K., Mallick, R., Andikagumi, H., Hubbard, J., Meilianda, E., Switzer, A., ... Hill, E. M. (2019). Earthquake-triggered 2018 Palu Valley landslides enabled by wet rice cultivation. *Nature Geoscience*, *12*(November), 935–940. Retrieved from <http://dx.doi.org/10.1038/s41561-019-0444-1> doi: 10.1038/s41561-019-0444-1
- Bray, J., EERI, M., Cubrinovski, M., Zupan, J., & Taylor, M. (2014). Liquefaction Effects on Buildings in the Central Business District of Christchurch. *earthquake spectra*, *30*(1), 85–109. doi: 10.1193/022113EQS043M
- Clément, C., Toussaint, R., Stojanova, M., & Aharonov, E. (2018). Sinking during earthquakes: critical acceleration criteria control drained soil liquefaction. *Physical Review E*, *97*(2), 022905. doi: 10.1103/PhysRevE.97.022905
- Cundall, P. A., & Strack, O. D. (1979). A discrete numerical model for granular assemblies. *Geotechnique*, *29.1*, 47–65. doi: 10.1680/geot.1979.29.1.47
- de Alba, P. A., Chan, K. C., & Seed, H. B. (1976). Sand liquefaction in large-scale simple shear tests. *Journal of Geotechnical and Geoenvironmental Engineering*, *102*(GT9), 909–927.
- Goren, L., Aharonov, E., Sparks, D. W., & Toussaint, R. (2010). Pore pressure evolution in deforming granular material: A general formulation and the infinitely stiff approximation. *Journal of Geophysical Research: Solid Earth*, *115*(9), 1–19. doi: 10.1029/2009JB007191
- Goren, L., Aharonov, E., Sparks, D. W., & Toussaint, R. (2011). The Mechanical Coupling of Fluid-Filled Granular Material Under Shear. *Pure and Applied Geophysics*, *168*(12), 2289–2323. doi: 10.1007/s00024-011-0320-4
- Ha, I.-s., Olson, S. M., Seo, M.-w., & Kim, M.-m. (2011). Evaluation of reliquefaction resistance using shaking table tests. *Soil Dynamics and Earthquake Engineering*, *31*(4), 682–691. Retrieved from <http://dx.doi.org/10.1016/j.soildyn.2010.12.008> doi: 10.1016/j.soildyn.2010.12.008
- Ishihara, K., Araki, K., & Bradley, B. (2011). Characteristics of Liquefaction-Induced Damage in the 2011 Great East Japan Earthquake. In *Internatioanl conference on geotechnics for sustainable development - geotec hanoi, vietnam*. (p. 22).
- Johnsen, Ø., Toussaint, R., Måløy, K. J., & Flekkøy, E. G. (2006). Pattern formation during air injection into granular materials confined in a circular Hele-Shaw cell. *Physical Review E*, *74*(1), 011301. doi: 10.1103/PhysRevE.74.011301
- Kramer, S. L. (1996). *Geotechnical Earthquake Engineering*.
- Lakeland, D. L., Rechenmacher, A., & Ghanem, R. (2014). Towards a complete model of soil liquefaction : the importance of fluid flow and grain motion. *Proceedings of the royal society*, *470*(2165). doi: <https://doi.org/10.1098/rspa.2013.0453>
- Madabhushi, G. S. P., & Haigh, S. K. (2012). How Well Do We Understand Earthquake Induced Liquefaction? , *42*(September), 150–160. doi: 10.1007/s40098-012-0018-2
- Martin, G. R., Finn, W. L., & Seed, H. B. (1975). Fundamentals of Liquefaction Under Cyclic Loading. *Journal of the geotechnical engineering division*, *101*(GT5), 423–438.
- Maurer, B. W., Eeri, M., Green, R. A., Eeri, M., Wotherspoon, L. M., Eeri, M., & Bastin, S. (2019). The Stratigraphy of Compound Sand Blows at Sites of Recurrent Liquefaction : Implications for Paleoseismicity Studies. *Earthquake Spectra*, *35*(3), 1421–1440. doi: 10.1193/041818EQS097M

- McNamara, S., Flekkøy, E. G., & Måløy, K. J. (2000). Grains and gas flow: molecular dynamics with hydrodynamic interactions. *Physical review E*, *61*(4), 4054—4059. Retrieved from <http://www.ncbi.nlm.nih.gov/pubmed/11088197> doi: 10.1103/PhysRevE.61.4054
- National Academies of Sciences, Engineering, & Medicine. (2016). *State of the Art and Practice in the Assessment of Earthquake-Induced Soil Liquefaction and Its Consequences* (Tech. Rep.). Washington, DC. Retrieved from <https://www.nap.edu/catalog/23474> doi: 10.17226/23474
- Niebling, M. J., Flekkøy, E. G., Måløy, K. J., & Toussaint, R. (2010a). Mixing of a granular layer falling through a fluid. *Physical Review E*, *82*(1), 011301. doi: 10.1103/PhysRevE.82.011301
- Niebling, M. J., Flekkøy, E. G., Måløy, K. J., & Toussaint, R. (2010b). Sedimentation instabilities: Impact of the fluid compressibility and viscosity. *Physical Review E*, *82*(5), 051302. doi: 10.1103/PhysRevE.82.051302
- Obermeier, S. F. (1996). Use of liquefaction-induced features for paleoseismic analysis — An overview of how seismic liquefaction features can be distinguished from other features and how their regional distribution and properties of source sediment can be used to infer the locat. *Engineering Geology*, *44*(1-4), 1–76. Retrieved from <http://www.sciencedirect.com/science/article/pii/S0013795296000403> doi: 10.1016/S0013-7952(96)00040-3
- Olson, S. M., Green, R. A., & Obermeier, S. F. (2005). Geotechnical analysis of paleoseismic shaking using liquefaction features : a major updating. , *76*, 235–261. doi: 10.1016/j.enggeo.2004.07.008
- Papathanassiou, G., Ganas, A., & Valkaniotis, S. (2016). Recurrent liquefaction-induced failures triggered by 2014 Cephalonia, Greece earthquakes: Spatial distribution and quantitative analysis of liquefaction potential. *Engineering Geology*, *200*, 18–30. Retrieved from <http://dx.doi.org/10.1016/j.enggeo.2015.11.011> doi: 10.1016/j.enggeo.2015.11.011
- Quigley, M. C., Bastin, S., & Bradley, B. A. (2013). Recurrent liquefaction in Christchurch, New Zealand, during the Canterbury earthquake sequence. *Geology*, *41*(4), 419–422. doi: 10.1130/G33944.1
- Sims, J. D., & Garvin, C. D. (1995). Recurrent Liquefaction Induced by the 1989 Loma Prieta Earthquake and 1990 and 1991 Aftershocks : Implications for Paleoseismicity Studies. , *85*(1), 51–65.
- Tuttle, M. P., Villamor, P., Almond, P., Bastin, S., Bucci, G., Langridge, R., . . . Hardwick, C. M. (2017). Liquefaction Induced during the 2010 – 2011 Canterbury , New Zealand , Earthquake Sequence and Lessons Learned for the Study of Paleoliquefaction Features. , *88*(5), 1403–1414. doi: 10.1785/0220170073
- Vinningland, J. L., Johnsen, Ø., Flekkøy, E. G., Toussaint, R., & Måløy, K. J. (2007a). Experiments and simulations of a gravitational granular flow instability. *Physical Review E*, *76*(5), 051306. doi: 10.1103/PhysRevE.76.051306
- Vinningland, J. L., Johnsen, Ø., Flekkøy, E. G., Toussaint, R., & Måløy, K. J. (2007b). Granular Rayleigh-Taylor Instability: Experiments and Simulations. *Physical Review Letters*, *99*(4), 048001.
- Wakamatsu, K. (2011). Recurrence of Liquefaction at the Same Site Induced by the 2011 Great East Japan Earthquake Compared with Previous Earthquakes. In *Proc. of the 15th world conf. on earthquake engineering*.
- Wakamatsu, K. (2012). Recurrent liquefaction induced by the 2011 Great East Japan earthquake compared with the 1987 earthquake. *Proceedings of the International Symposium on Engineering Lessons Learned from the 2011 Great East Japan Earthquake, March 1-4, 2012, Tokyo, Japan*, 675–686.
- Wang, C. Y. (2007). Liquefaction beyond the Near Field. *Seismological Research Letters*, *78*(5), 512–517. doi: 10.1785/gssrl.78.5.512
- Yasuda, S., & Tohno, I. (1988). Sites of Reliquefaction Caused by the 1983 Nihonkai-Chubu Earthquake. *Soils and Foundations*, *28*(2), 61–72. doi: <https://doi.org/10.3208/>

sandf1972.28.2_61

Supporting Information for ”Recurrent soil liquefaction under drained conditions”

Shahar Ben-Zeev^{1,2}, Liran Goren³, Renaud Toussaint^{2,4}, Einat Aharonov^{1,4}

¹Institute of Earth Sciences, The Hebrew University of Jerusalem, 91904, Israel

²Université de Strasbourg, CNRS, ENGEES, Institut Terre & Environnement de Strasbourg, UMR7063, F-67000 Strasbourg, France

³The Department of Earth and Environmental Sciences, Ben-Gurion University of the Negev, 84105, Israel

⁴PoreLab, the Njord Centre, Department of Physics, University of Oslo, P.O. Box 1048 Blindern, NO-0316 Oslo, Norway

Contents of this file

1. Text S1
2. Figure S1
3. Tables S1 to S2

Introduction In Text S1 we provide details regarding the numerical method. Text S2 provides essential details regarding the post-processing of the numerical results. Figure S1 shows the numerical setup as a supplement for Text S1. Table S1 summarizes the simulations’ parameters. Table S2 lists the simulations presented here with their applied seismic power input and frequency.

Text S1. The numerical approach is described in (Goren et al., 2011; Ben-Zeev et al., 2020). Here, we repeat its main details. We use a two-phase coupled model. The grains are modeled using the discrete element method (Cundall & Strack, 1979), and the interstitial pore fluid is modeled as a continuum on a superimposed Eulerian grid (McNamara et al., 2000; Johnsen et al., 2006; Niebling et al., 2010a, 2010b; Vinningland et al., 2007b, 2007a).

Grain velocity and position are resolved by time integration of the linear and rotational momentum conservation equations (Ben-Zeev et al., 2020):

$$m_i \dot{\mathbf{u}}_{s,i} = m_i \mathbf{g} - V_{imm,i} \rho_f \mathbf{g} + \sum_j \mathbf{F}_{ij} - \frac{\nabla P' \cdot V_i}{1 - \phi} \quad (1)$$

$$I_i \dot{\boldsymbol{\omega}}_{s,i} = \sum_j R_i \hat{\mathbf{n}}_{ij} \times \mathbf{F}_{ij}, \quad (2)$$

where $\dot{\mathbf{u}}_{s,i}$ and $\dot{\boldsymbol{\omega}}_{s,i}$ are the translational and rotational accelerations of grain i (dot notation indicates time derivative) and m_i and I_i are the mass and moment of inertia of grain i . R_i is the radius of grain i and $\hat{\mathbf{n}}_{ij}$ is a unit vector along the direction connecting the centers of grains i and j . In Eq. 1, the first term on the right hand side is the gravitational force, where \mathbf{g} is the gravitational acceleration. The second term is the buoyancy force, whose magnitude depends on the grain immersed volume $V_{imm,i}$ and the fluid density ρ_f (Clément et al., 2018). The third term is the sum of contact forces (\mathbf{F}_{ij}) over all grains j that are in contact with grain i , calculated with a linear contact model (Cundall & Strack, 1979). The fourth term represents the seepage force exerted by the gradient of the dynamic pore pressure, $\nabla P'$, where V_i is the volume of grain i .

The evolution of the interstitial fluid pressure is represented by (Goren et al., 2011):

$$\frac{\partial P'}{\partial t} - \frac{1}{\beta_f \eta \phi} \nabla \cdot [\kappa \nabla P'] + \frac{1}{\beta_f \phi} \nabla \cdot u_s = 0, \quad (3)$$

where P' is the dynamic pore pressure deviation from hydrostatic value ($P' = P - P_{hyd}$), β_f and η are the fluid compressibility and viscosity, respectively, κ is the permeability, t is time and ∇ is a spatial derivative. The third term in equation (3) describes the internal source for dynamic pore pressure, due to divergence of solid grain velocities (u_s). That equation is solved by using an implicit scheme over a square grid, with grid spacing of two average grain diameters (Goren et al., 2010, 2011; Niebling et al., 2010a, 2010b).

The two-way coupling between the grains and the fluid is implemented as follows. The fourth term on the right hand side of equation (1) is evaluated via a bilinear interpolation of $\nabla P'/(1 - \phi)$ from the surrounding grid nodes to grain i . The second and third terms of Eq. (3) are evaluated by defining smooth fields of grain velocity and porosity over the grid through a bi-linear interpolation of grain radius and velocity from individual grains surrounding each grid node. The permeability, κ , in Eq. (3) is calculated based on a three dimensional Kozeny-Carman relation (Carman, 1937):

$$\kappa = \kappa_1 \kappa'(x, y, t) = \alpha r^2 \frac{\phi^3}{(1 - \phi)^2}, \quad (4)$$

where r^2 is the bi-linearly interpolated squared grain radii in the surroundings. $\kappa_1 = \alpha < r >^2$ is a constant prefactor, and $\kappa' = r'^2 f(\phi)$ captures permeability variations in space and time. $< r >$ is the mean grain radius in the system and r' is the local deviation from it, such that $r = < r > r'$. In the original Kozeny-Carman relation, $\alpha = 1/45$ (Carman, 1937) is a geometrical prefactor for spheres. In our simulations, we vary α to directly

control the order of magnitude of the permeability independent of the grain size (Goren et al., 2011; Ben-Zeev et al., 2020).

The geometry of the numerical layer (Fig. S1) is a Hele-Shaw cell comprising spherical grains with grain radii between 0.8 – 1.2 cm, drawn from a normal distribution with a mean of 1 cm and a standard deviation of 1 cm. The system’s horizontal dimension is 0.4m. The layer is prepared as follows: First, a target height is specified. Then, grains are sedimented under gravity onto the bottom wall in a fluid-free environment. Next, to slightly compact the layer, a short horizontal shaking phase is applied over 0.62 seconds with $f = 12$ Hz and amplitude of $A = 0.0431$ centimeters, followed by 0.13s relaxation, where no external forces aside from gravity are applied. Finally, the fluid is added, so its height approximately coincides with the top of the grain layer. In the simulations presented here, the initial layer height, following the preparation stage, is $H \approx 1.44$ m.

The bottom wall of the numerical Hele-Shaw cell is made of half grains glued together. The boundary condition for the bottom wall is zero velocity in the vertical direction ($u_{sz}(z = \text{bottom}, t) = 0$) and sinusoidal displacement in the horizontal direction, $x(z = \text{bottom}, t) = A(1 - \cos(\omega t))$, where A and ω are the shearing amplitude and angular frequency, respectively. At the top boundary, there are no normal or shear stresses. The boundary conditions for the fluid phase are no flow boundary at the bottom ($\partial P'/\partial z(z = \text{bottom}, t) = 0$) and constant pressure boundary at the top ($P'(z = \text{top}, t) = 0$). The water level is maintained at its initial height throughout the simulation. The side boundaries are periodic for the grains and pore fluid, mimicking a laterally infinitely long layer.

Table S1 summarizes the simulations' parameters. Table S2 lists the simulations presented here with their applied seismic power input and frequency.

Text S2. The numerical grains' kinematics and dynamics, and the fluid pressure values are resolved in 2D during a simulation. In post-processing of the simulations results, in each time step, those quantities are averaged over thin horizontal sublayers (with a width of 2 grain diameters), in order to produce the figures that display them as a function of depth and time (Figs. 2-3 in the main text). Specifically, the grains' vertical velocity presented per depth and time is the average velocity of all the grains occupying all the numerical cells in a specific depth and time step. The pressure and pressure gradient values presented per depth and time are the average values solved on the fluid grid in a specific depth and time step.

The consequent grain velocity, fluid pressure, and fluid pressure gradient data are smoothed using a moving average with a moving window of 0.264 seconds in the temporal dimension, and a moving window of 10 cm in the spatial vertical dimension.

The porosity value in Figure 4 is produced by the same averaging approach described above, from the porosity values on the numerical grid. Here we further average the porosity over a thickness between the height of the bottom wall ($z = 0$) to height $z = H/2$ which is the maximum height to which the front reach at the end of the first shaking event. We perform this averaging before the simulation begins (ϕ_0), at the end of the first shaking event (ϕ_{c1}), and at the end of the second liquefaction event (ϕ_{c2}).

References

Ben-Zeev, S., Aharonov, E., Toussaint, R., Perez, S., & Goren, L. (2020). Compaction

- front and pore fluid pressurization in horizontally shaken drained granular layers. *Physical Review Fluids*, 054301, 1–25. doi: 10.1103/PhysRevFluids.5.054301
- Carman, P. C. (1937). Fluid flow through granular beds. *Trans. Inst. Chem. Eng.*, 15, 150–166. Retrieved from [http://dx.doi.org/10.1016/S0263-8762\(97\)80003-2](http://dx.doi.org/10.1016/S0263-8762(97)80003-2) doi: 10.1016/S0263-8762(97)80003-2
- Clément, C., Toussaint, R., Stojanova, M., & Aharonov, E. (2018). Sinking during earthquakes: critical acceleration criteria control drained soil liquefaction. *Physical Review E*, 97(2), 022905. doi: 10.1103/PhysRevE.97.022905
- Cundall, P. A., & Strack, O. D. (1979). A discrete numerical model for granular assemblies. *Geotechnique*, 29.1, 47–65. doi: 10.1680/geot.1979.29.1.47
- Goren, L., Aharonov, E., Sparks, D. W., & Toussaint, R. (2010). Pore pressure evolution in deforming granular material: A general formulation and the infinitely stiff approximation. *Journal of Geophysical Research: Solid Earth*, 115(9), 1–19. doi: 10.1029/2009JB007191
- Goren, L., Aharonov, E., Sparks, D. W., & Toussaint, R. (2011). The Mechanical Coupling of Fluid-Filled Granular Material Under Shear. *Pure and Applied Geophysics*, 168(12), 2289–2323. doi: 10.1007/s00024-011-0320-4
- Johnsen, Ø., Toussaint, R., Måløy, K. J., & Flekkøy, E. G. (2006). Pattern formation during air injection into granular materials confined in a circular Hele-Shaw cell. *Physical Review E*, 74(1), 011301. doi: 10.1103/PhysRevE.74.011301
- McNamara, S., Flekkøy, E. G., & Måløy, K. J. (2000). Grains and gas flow: molecular dynamics with hydrodynamic interactions. *Physical review E*, 61(4), 4054—4059.

Retrieved from <http://www.ncbi.nlm.nih.gov/pubmed/11088197> doi: 10.1103/PhysRevE.61.4054

Niebling, M. J., Flekkøy, E. G., Måløy, K. J., & Toussaint, R. (2010a). Mixing of a granular layer falling through a fluid. *Physical Review E*, *82*(1), 011301. doi: 10.1103/PhysRevE.82.011301

Niebling, M. J., Flekkøy, E. G., Måløy, K. J., & Toussaint, R. (2010b). Sedimentation instabilities: Impact of the fluid compressibility and viscosity. *Physical Review E*, *82*(5), 051302. doi: 10.1103/PhysRevE.82.051302

Vinningland, J. L., Johnsen, Ø., Flekkøy, E. G., Toussaint, R., & Måløy, K. J. (2007a). Experiments and simulations of a gravitational granular flow instability. *Physical Review E*, *76*(5), 051306. doi: 10.1103/PhysRevE.76.051306

Vinningland, J. L., Johnsen, Ø., Flekkøy, E. G., Toussaint, R., & Måløy, K. J. (2007b). Granular Rayleigh-Taylor Instability: Experiments and Simulations. *Physical Review Letters*, *99*(4), 048001.

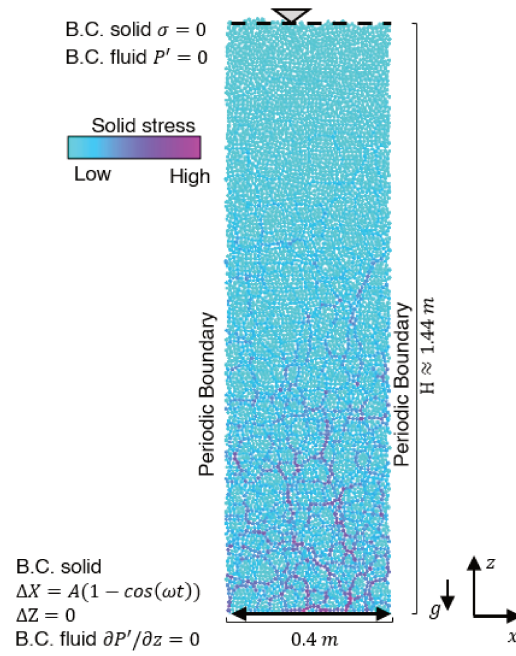


Figure S1. Schematics of the simulations setup and boundary conditions.

Table S1. Physical parameters in simulations

Parameter	Value	Units
mean grain density (ρ_s)	2,640	kgm ⁻³
fluid density (ρ_f)	1,000	kgm ⁻³
mean grain radius (r_s)	0.5	cm
fluid compressibility (β_f)	$4.5 \cdot 10^{-10}$	Pa ⁻¹
fluid dynamic viscosity (η)	10^{-3}	Pas
mean initial porosity (ϕ_0)	0.4337	-
characteristic permeability (κ_0)	$6.6 \cdot 10^{-11}$	m ²

Table S2. List of simulations

ID	Description	Power ₁ ($J/(m^3s)$)	frequency ₁ (Hz)	Power ₂ ($J/(m^3s)$)	frequency ₂ (Hz)
sim1	low-low	1.39	6.59	1.39	6.59
sim2	low-mid	1.39	6.59	3.92	9.32
sim3	low-high	1.39	6.59	11.1	13.19
sim4	mid-low	3.92	9.32	1.39	6.59
sim5	mid-mid	3.92	9.32	3.92	9.32
sim6	mid-high	3.92	9.32	11.1	13.19
sim7	high-low	11.1	13.19	1.39	6.59
sim8	high-mid	11.1	13.19	3.92	9.32
sim9	high-high	11.1	13.19	11.1	13.19

Discussion, future perspectives, and conclusions

Discussion

This dissertation presents a study of drained soil liquefaction. The following questions were defined as the basis for the study:

1. Can liquefaction occur under drained conditions? And what is this drained mechanism?
2. What are the controlling dynamics and parameters of drained liquefaction and how do they differ from the dynamics of undrained liquefaction?
3. Can drained liquefaction explain observed, but previously unexplained, intermediate-field and far-field liquefaction cases?
4. Can drained liquefaction explain observed, previously enigmatic, recurrent liquefaction events and define the conditions that favor reliquefaction?

Liquefaction initiation is classically perceived as the outcome of undrained conditions, assuming that pore fluid pressurization will occur only if porous fluid flow is restricted during the earthquake shaking. The current work puts forward a new perspective that perceives pore fluid pressurization and soil liquefaction as outcomes of a spectrum of drainage conditions defined between drained and undrained end members. To accurately define the end-member cases, the Deborah number (De , eq. (2)) framework (Reiner, 1964; Goren et al., 2010, 2011)

is invoked. A consistent and precise definition of a system as "drained" or "undrained" is achieved by identifying the time scale of pore pressure diffusion, the time scale of the shaking forcing, and their ratio. The De number framework (eq. (2)) (Goren et al., 2010, 2011) was adjusted in Chapter 1 and refined in Chapter 2 to specifically evaluate the drainage conditions in a horizontally shaken unconfined saturated soil layer. The exact definition of the De number will be further discussed later in this chapter.

The numerical simulation results of liquefied granular material presented in Chapter 1 were all characterized by $De \ll 1$, and evaluated as "drained". Furthermore, the simulated dynamics were successfully predicted by the "drained" two terms form of eq. (1) without a-priori assumption regarding the simulation's drainage condition, supporting and validating the De number framework. The theory presented in Chapter 1, supported by the numerical simulations, demonstrates that liquefaction can occur under drained conditions. It shows, that allowing the pore fluid to flow in and out of the deforming pores does not preclude pressurization. In fact quite the opposite, this flow serves as the pressurization driver. While the fluid flows, pore pressure gradients must form to drive the flow following Darcy's law (Darcy, 1856). The grains, which are initially stagnant and supported by their contacts, become instead partially to fully supported by seepage forces, induced by the dynamic pore pressure gradient. The supported grains settle downwards within the fluid, which exchanges place with the grains and flows upwards, towards the free surface. The seepage forces, which lift the grains, liquefy the layer, and decrease its shear strength. Ultimately, the grains are fully supported by the seepage forces and the dynamic pore pressure gradient in the vertical direction ($\partial P'/\partial z$) becomes equal to the initial effective lithostatic stress gradient ($d\sigma/dz$). At this stage, the soil layer co-seismically settles at a constant rate (u_{szC}) which is primarily dependent on the soil's permeability (κ):

$$u_{szC} = \frac{\kappa}{\eta} \frac{d\sigma}{dz}, \quad (3)$$

where η is the pore fluid viscosity.

Compaction front controls drained liquefaction dynamics

The layer's instantaneous settlement rate, given by eq. (3) does not tell the whole story of drained liquefaction. The key feature of drained liquefaction that was identified in Chapter 1 is that the co-seismic compaction is not homogeneous throughout the layer, but rather localized into a narrow region termed the "compaction front". The front divides the layer into an upper liquefied and settling, yet not internally compacting sub-layer, from a lower currently non-liquefied and nearly vertically stagnant sub-layer. The front moves upward at a velocity that depends on the grains instantaneous settlement velocity (eq. (3)) and the change in porosity across the front ($\Delta\phi = \phi_0 - \phi_c$):

$$u_{\text{front}} = \frac{(\phi_0 - 1)}{\Delta\phi} u_{szC} = \frac{(\phi_0 - 1)}{\Delta\phi} \frac{\kappa}{\eta} \frac{d\sigma}{dz}, \quad (4)$$

where ϕ_0 is the initial porosity (dominant in the upper sub-layer) and ϕ_c is the final critical porosity, which characterizes the lower compacted sub-layer. This theoretical prediction of the front velocity (eq. (4)) was confirmed by the numerical simulations and experiments presented in Chapter 2. The agreement with experiments (Figure 3d in Chapter 2) serves as another validation of the numerical and theoretical models.

The width of the compaction front (w) was shown in Chapter 2 to be the length scale over which velocities converge (see Figure 1 in Chapter 2), i.e., the length scale associated with the source term of the pore pressure diffusion equation (eq. (1)). The layer's depth (h) is the length scale associated with the gradient fields (of solid stress and pore pressure) and together they control the time scale of pressure diffusion. The shaking periodicity (T , the reciprocal of the frequency) is conservatively chosen to represent the time scale of forcing. Therefore, De number (eq. (2)) becomes (eq. (3) in Chapter 2):

$$\text{De} = \frac{hw\beta_f\eta\phi}{T\kappa_0}. \quad (5)$$

The De number in the field

To demonstrate a possible application of the De number framework in field conditions, Fig. 7 shows how the refined De number (eq. (5)) changes with depth (down to 20 meters deep, considered as the maximum depth for potential soil liquefaction) for a range of representative permeabilities. The calculation assumes a front width of 20 grains, each 1 mm in diameter and ignores a possible relation between the grain size and the permeability (e.g., Kozeny-Carman relation). For the low frequency end-member of earthquake shaking (panel a, $f = 0.1$ Hz) $De \ll 1$ for all the examined permeabilities and depths, i.e., drained dynamics are expected even for deeply buried layers. For the high end-member of frequencies (panel b, $f = 10$ Hz), drained dynamics with $De \ll 1$ are not expected under low permeability, even at shallow depths (left of the black line that marks $De = 1$). Yet, under relatively high permeability, drained behavior is expected even at deeply buried layers (right of the black line).

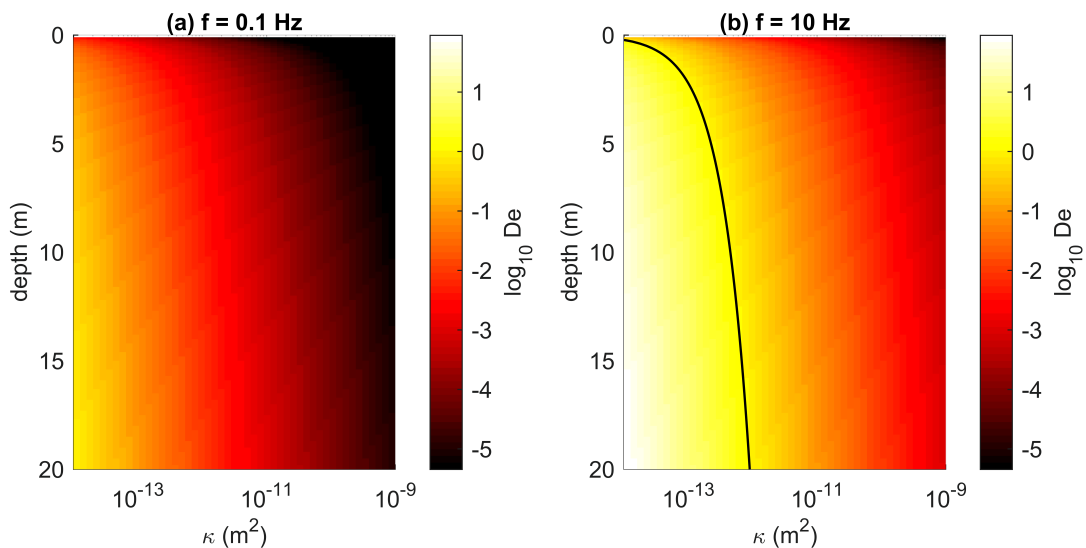


Figure 7: The De number as a function of depth and permeability for (a) 0.1 and (b) 10 Hz shaking. The black line marks $De = 1$. At high permeability drained dynamics are expected even under very high shaking frequency.

The onset of drained liquefaction

The parameter space of the input ground motion was studied extensively in the simulations and experiments presented in Chapter 2. The rate of input of seismic energy density (the seismic power, $Sp = e/T$ where $e = (\rho_s/4) PGV^2$ is the average seismic energy density in one shear cycle (Lay and Wallace, 1995), and T is the periodicity of shaking) was identified (Figure 3b in Chapter 2) as the best shaking parameter that controls the equilibrium critical porosity (ϕ_c). Consequently, Sp controls the magnitude of the change in porosity and hence the velocity of the co-seismic compaction front (eq. (4), Figure 3d inset in Chapter 2). Low seismic power (Sp) yields a smaller change in porosity across the front, leading to a faster moving compaction front (eq. (4)), shorter liquefaction event, and less soil settlement in total. Additionally, a threshold Sp was identified (Figure 3b in Chapter 2) which separated liquefied from non-liquefied simulations.

In harmonic motion, the seismic power ($Sp = (\rho/4) A^2\omega^3$) is proportional to the Arias intensity (section 0.3) if taken over one shear cycle instead of over the entire duration shaking ($I_A = (\pi/2g) \int_0^T a(t)^2 dt = (\pi^2/2g) A^2\omega^3$). Arias intensity is a cumulative energy measure, and hence probably suited to control the cumulative volumetric strain leading to undrained liquefaction (Fig. 4a). The seismic power on the other hand can be seen as the quasi-instantaneous Arias intensity. This agrees with a dynamic process, such as drained liquefaction, which is expected to be independent of the cumulative energy, and rather depend on the instantaneous power.

A major aspect that is unique to drained liquefaction is the initiation almost immediately after the onset of shaking, during the very first shear cycles. This in contrast to undrained liquefaction (section 0.1) that requires at least few shear cycles (for the most susceptible soil conditions, see Fig. 3) in order to facilitate the volumetric strain required to initiate liquefaction (Goren et al., 2010, 2011). This expectation is embedded in simplified liquefaction evaluation procedures via a factor that represents the expected strong motion duration (see section 0.3). In agreement with the current study, recent cyclic triaxial ex-

periments (Adamidis and Anastasopoulos, 2022) showed that for a given relative density and applied shear stress, less shear cycles are required to initiate soil liquefaction when drainage is allowed. Furthermore, under drained conditions, a given number of shear cycles and a given cyclic shear stress amplitude will liquefy denser soils than in the undrained counterpart. This suggests that the assumed higher resistance to liquefaction of dense soils should be questioned under drained conditions.

Liquefaction beyond the near-field

All of the drained simulations and experiments in Chapter 2 were conducted under seismic energy density input ($e = \rho_s/4 PGV^2$ (Lay and Wallace, 1995; Wang, 2007)) which is lower than the minimum energetic threshold to induce liquefaction via "undrained consolidation" (Green and Mitchell, 2004; Wang, 2007). Yet, liquefaction in those simulations and experiments is observed. Hence it is concluded that drained liquefaction is not limited by the undrained energetic threshold, and could be invoked to explain the previously enigmatic many liquefaction occurrences beyond the earthquake near-field, where the seismic energy density is low (see section 0.3.1). Furthermore, similarly to the seismic power, albeit less robust, the seismic energy density was found to be correlated with the change in porosity and the velocity of the compaction front. An asymptotic approach towards very fast front progression under low seismic energy density and a seismic energy threshold below which liquefaction does not occur were identified in the simulations and experiments in Chapter 2. This provides a possible explanation for the decaying trend in the number of documented liquefaction events with decreased seismic energy density and the limit on documented events.

Recurrent liquefaction

The duration of drained liquefaction is dictated by the minimum time between the time it takes for the compaction front to arrive at the surface (t_e) and the duration of the earthquake (t_{EQ}). When $t_e \simeq u_{\text{front}}/H$ is much longer than the duration of the earthquake, due to low

permeability, large seismic energy density excitation or if the layer is very thick, the actual duration of drained liquefaction will be limited by the earthquake duration. In contrast, if the permeability is high, the seismic energy density is low, or the layer is thin, the actual duration will be set by the time it takes for the front to swipe up across the layer (u_{front}/H). Consequently, a liquefaction event can terminate in one of two final states: (1) if the front has swiped all the way through the layer (after duration t_e), the whole layer will compact to the equilibrium porosity (ϕ_c) of the applied Sp . (2) if the front has halted before reaching the top of the layer (after duration t_{EQ}), the bottom sub-layer will be compacted to the equilibrium porosity (ϕ_c) of the applied Sp , and the top sub-layer will maintain its initial porosity ϕ_0 .

Site response to earthquakes can vary significantly between different earthquakes, i.e., the same site can be excited with different seismic energy density and seismic power values. With this understanding, Chapter 3 extends the theory to identify the conditions leading to recurrent liquefaction when liquefaction is drained (utilizing simulations for demonstration). A layer that in the first event, under seismic power Sp_1 , has compacted completely to a new denser porosity ϕ_{c1} can be assumed liquefaction resistance under any further shaking of a smaller or equal SP ($Sp_2 \leq Sp_1$). This layer is still prone to reliquefaction under a higher Sp in a second shaking, since its equilibrium porosity (ϕ_{c2}) is expected to be smaller than ϕ_{c1} . Under the higher Sp_2 the additional compaction will lead further pressurization, as expected on the drained path to liquefaction (Figure 5a in Chapter 3). A second scenario is of a layer where only its bottom sub-layer has compacted to ϕ_{c1} in the first shaking event under Sp_1 shaking. Its top sub-layer maintains the higher initial porosity ϕ_0 . Hence, the top sub-layer will liquefy again in a subsequent shaking under any Sp_2 that would have liquefied the layer in its initial state, possibly even lower than Sp_1 . The bottom sub-layer on the other hand, will liquefy again only under a higher Sp_2 (Figure 5b in Chapter 3). Overall, the unique dynamics of drained liquefaction and the compaction front are shown to dictate the layer (or sub-layer) susceptibility to reliquefaction. Specifically, unless the whole

layer has compacted to ϕ_c which is stable under the highest possible Sp , the layer should be susceptible to reliquefaction.

Future perspective

The De number framework has the potential to serve as a general metric to predict the expected mechanism for liquefaction initiation in a given field site. In cases where $De \ll 1$, the described drained dynamics can be used as a constitutive law (which will be easier and more cost-effective to apply than discrete element simulations). While this work has utilized a physics-driven approach to emphasize the role of drainage in soil liquefaction, several aspects are identified for further investigation.

As expected from previous work about drained liquefaction (Clément et al., 2018), a peak ground acceleration threshold for liquefaction can be defined. The threshold identified in this work was an order of magnitude lower than the recommendations of the design codes (e.g., Eurocode 8, 2004), making drained liquefaction a promising candidate mechanism for explaining liquefaction events that were observed (de Magistris et al., 2013) to occur under a PGA smaller than the design codes threshold (e.g., Eurocode 8, 2004). Yet, the exact value of a PGA, or perhaps a power threshold, under drained conditions should be the focus of a future designated work.

The seismic ground motion frequency (f) plays an important role in the drainage conditions evaluation, such that low frequency (high periodicity) is more likely to lead to drained conditions ($De \ll 1$, eq. (2), Fig. 7). The frequency is also embedded in the seismic power of harmonic motion ($Sp \propto A^2 (2\pi f)^3$) which was found to be a key parameter in drained liquefaction. Another dependency between the frequency and the drained liquefaction dynamics was presented in Chapter 2, where the compaction front initiation height above the bottom wall was found to correlate best with the frequency. This probably relates to the typical wavelength of the shear wave, which is expected to depend on the frequency of shaking

(similarly to the "Stokes boundary layer" of viscous fluid flow with oscillatory boundary). A further detailed examination of the effect of frequency (at typical seismic ground motion frequencies) on drained liquefaction is of importance, since generally the role of frequency in liquefaction is unclear (Kostadinov and Towhata, 2002; Wong and Wang, 2007).

The shaking in this work was harmonic, with a single frequency and amplitude. While this simplification has the advantage when comparing simulations and experiments to theory and when exploring the parameter space, it is a crude simplification of natural seismic ground motion signal. Yet, since drained liquefaction has been shown to initiate in few shear cycles and under a relatively low intensity of excitation, it is postulated that drained liquefaction will be initiated within the first strong enough cycles, after the shear wave arrival. Furthermore, since the seismic power here was taken for a single period of a monochromatic wave, examination of the power effect of real signal decomposed into all the significant oscillation modes is required. It is postulated that the compaction front velocity will not be constant, and would instead depend on the power of the momentary motion.

In this study, the granular layer (both in simulations and experiments) was homogeneous and fully saturated. Two scenarios of more complicated geometries were discussed theoretically in chapter 2. Future research could explore the influence of more complicated geometries (e.g., tilted, a low permeability cap layer etc.), composition and permeability variations, and variations in the degree of saturation (e.g., partly or non saturated sub-layers). Furthermore, a more complete understanding of drained liquefaction in a setup that is closer to a natural soil profile will allow direct comparison of the model to field study cases.

The time scales for complete liquefaction in the simulations can be resolved more accurately by incorporating an "added mass" force on the simulated grains, i.e., changing the grain mass into a fluid-coated grain mass in order to incorporate the fluid inertia into the model. This is not expected to alter the dynamics in general, yet, as suggested by the analysis of Niebling et al. (2010a) (who compared simulations with and without the "added mass"), I expect that the time scales for grain and fluid accelerations to their terminal velocity might

be underestimated when this force is neglected.

The geometry of the numerical setup used in this study was of a "Hele-Shaw" cell, which is essentially a 2D setup. A possible path of research is to conduct real 3D coupled numerical simulations (El Shamy and Zeghal, 2007; Dorostkar and Carmeliet, 2018) of a similar setup and boundary conditions as in the current study. The extra degrees of freedom in 3D are not expected to alter the general dynamics (as the agreement between the 2D simulations and the 3D experiments suggests) but rather to modulate emergent parameters such as the equilibrium porosity under Sp , or liquefaction thresholds in input motion parameters.

Conclusions

In this work, I showed that liquefaction can be initiated under drained conditions. The compaction front was identified as a key dynamic component of drained liquefaction. The short initiation time scale, the seismic power as a controlling parameter on liquefaction threshold, kinematics, and dynamics, and the initiation under very low seismic energy density were shown to be distinguishing properties of drained liquefaction over the undrained prevailing approach. A possible path for recurrent liquefaction events under the drained view was suggested to be the outcome of those unique characteristics.

In contrast to undrained liquefaction, drained liquefaction is triggered under lower shaking intensity, does not require energy or strain accumulation and hence can be initiated after a shorter excitation. Overall, drained liquefaction is easier to trigger, suggesting that the current liquefaction risk analysis procedures which are mainly based on the undrained hypothesis are not conservative enough and may underestimate liquefaction risk. For the same reasons, paleo-seismicity studies may overestimate ground motion (and consequently earthquakes magnitude or distance to source) of paleo-earthquakes, in order to explain soft sediment deformations in the geological record.

Appendix A

The Combined Effect of Buoyancy and Excess Pore Pressure in Facilitating Soil Liquefaction

Ben-Zeev, S., Goren, L., Perez, S., Toussaint, R., Clement, C. & Aharonov, E. (2017). The Combined Effect of Buoyancy and Excess Pore Pressure in Facilitating Soil Liquefaction. *Poromechanics VI: Proceedings of the Sixth Biot Conference on Poromechanics*, 107-116.

doi:10.1061/9780784480779.013

Published article in *Poromechanics VI: Proceedings of the Sixth Biot Conference on Poromechanics*.

(Published on July 6, 2017. doi:10.1061/9780784480779.013)

The Combined Effect of Buoyancy and Excess Pore Pressure in Facilitating Soil Liquefaction

S. Ben Zeev¹; L. Goren²; S. Perez³; R. Toussaint⁴; C. Clément⁵; and E. Aharonov⁶

¹Institute of Earth Science, Hebrew Univ. of Jerusalem, Israel. E-mail:

shahar.benzeev@mail.huji.ac.il

²Geological & Environmental Science, Ben-Gurion Univ. of the Negev, Israel.

³Univ. of Chemistry and Technology Prague, The Czech Republic.

⁴Université de Strasbourg, CNRS, Institut de Physique du Globe de Strasbourg, UMR7516, F-67000 Strasbourg, France.

⁵Université de Strasbourg, CNRS, Institut de Physique du Globe de Strasbourg, UMR7516, F-67000 Strasbourg, France.

⁶Institute of Earth Science, Hebrew Univ. of Jerusalem, Israel.

Abstract

Soil liquefaction is a devastating earthquake hazard, commonly causing tilting, sinking and floating of infrastructure. The classical mechanism for liquefaction requires undrained and loosely packed soil, that upon shear experiences elevated, lithostatic, pore pressure and consequently zero effective stress. However, some field and experimental observations cannot be explained by this mechanism. These include liquefaction of pre-compacted soils, liquefaction under drained conditions, repeated liquefaction events, and liquefaction triggered by small seismic energy density. A recent study suggests a new mechanism for soil liquefaction that arises only from buoyancy effects of fluids plus grain accelerations, where the term “liquefaction”, used as its phenomenological field definition, refers to a macroscopic transition from rigid to fluid-like behavior. We extend that study and seek a unifying mechanism for field observed liquefaction that accounts both for the buoyancy effect and for elevated pore pressure, though not necessarily with lithostatic values. To achieve this goal, we use a coupled fluid flow and granular dynamics numerical model to study the effect of pore pressure on the sinking of a large object (“intruder”) into a drained densely packed granular system, undergoing cyclic shearing. Results show that despite the drained conditions pore pressure rises during shaking. Although pore pressure remains well below lithostatic values, the soil liquefies, as identified macroscopically by intruder sinking to its isostatic position. Even simulations with buoyancy effects alone show liquefaction and intruder sinking under certain conditions, yet inclusion of pore-pressure effects add to the buoyancy effect, and is seen to enhance liquefaction and promote intruder sinking.

INTRODUCTION

Soil liquefaction is a natural hazard that accompanies many earthquakes, with potentially destructive consequences that include tilting, sinking and uplifting of infrastructure. Two different definitions are commonly used for liquefaction: The first is a phenomenological definition, used practically in the field. It identifies liquefaction via observations of macro-scale changes in the rheological response of soils, from rigid to a fluid-like slurry during or following an earthquake. In contrast, the second definition is mechanistic in nature. It is used in laboratory tests and relates liquefaction to rheological change caused by pore pressure rise to lithostatic levels (Youd & Idriss 2001, Martin et al. 1975). Clément et al. 2017 a,b suggested that the two definitions do not always coincide, and that many of the field-observed liquefaction events may occur at relatively low pore pressure. Indeed, the pore pressure (PP) mechanism for liquefaction requires soils that are initially loose and effectively undrained (Youd & Idriss 2001). The loose soil skeleton compacts during shaking, decreasing pore volume and increasing PP. The undrained conditions prevent fluid escape from the compacting pore volume, allowing PP to reach lithostatic values. Yet, this PP mechanism fails to explain many field and experimental observations of liquefaction: (1) Liquefaction in pre-compacted soils (Soga 1998), (2) Under drained conditions, see e.g. demo at <https://www.youtube.com/watch?v=cONq231dn6w>, (3) Repeated liquefaction events (Obermeier 1996), and (4) Far-field liquefaction that occurs despite small seismic energy input (Wang 2007).

Thus Clément et al. 2017a,b, suggested an alternative liquefaction mechanism, that may explain those previously unexplained occurrences of liquefaction. This new mechanism for liquefaction requires fluid, but does not require PP increase. To test the new mechanism, Clément et al. (2017a,b) probed the conditions for the onset of liquefaction using the macroscale sinking pattern of an “intruder” (a big grain), placed on the top of a saturated layer composed of smaller grains, to horizontal cyclic shear. This was done using theoretical analysis, experiments and numerical simulations. The simulations were based on the Discrete Element Method algorithm (DEM) (Cundall & Strack 1979), modified to include the buoyancy force of the fluid as it acts on the grains and the intruder, proportional to their immersed volume in the fluid. The results of that work show an alternative mechanism for liquefaction that arises from grain acceleration and buoyancy forces alone, as PP (deviating from hydrostatic) was not included in the Clément et al. theory and simulations, but liquefaction in the phenomenological sense, was still observed. Thus, it appears that PP rise is not a

necessary condition for liquefaction. However, as many field observations show evidence for elevated PP during liquefaction [e.g. Obermeier 1996, Holzer et al. 1989], we hypothesize that PP rise can enhance liquefaction and expand the dynamic regime over which buoyancy-acceleration triggered liquefaction occurs. It is therefore suggested that the new buoyancy-acceleration mechanism and the more classical elevated PP mechanism combine to span a spectrum of conditions that can lead to soil liquefaction.

In the current work, we explore this idea by extending the numerical work of Clément et al. to include beyond hydrostatic pore pressure effects. We present preliminary results from the extended buoyancy - pore pressure model, showing the capacity of elevated pore pressure, even when significantly lower than the lithostatic stress, to enhance the sinking of an intruder.

RESULTS FROM CLÉMENT ET AL. 2017

Clément et al. 2017a,b simulated the response of a densely packed saturated granular media to earthquake shaking using a modified DEM, accounting only for the buoyancy effect of the fluid but not including PP. In their simulations, they identified the onset of soil liquefaction both via micromechanics and via the sinking of an intruder lying on top of a saturated granular layer, which undergoes horizontal cyclic shaking. Liquefaction in the simulations was defined by following the intruder sinking pattern, in a similar way to phenomenological field observations of liquefaction during and following earthquakes. Their simulation results show that the dynamic response of the grains and the intruder depends on the horizontal acceleration. For low acceleration, the grains and the intruder move together with almost no sliding along granular contacts. As a result, the intruder doesn't sink at all. At higher horizontal acceleration, high relative velocity between the grains is observed, with the exception of the region surrounding the intruder, where the grains move semi synchronously with the intruder. The outcome of this dynamics is that the intruder sinks towards its isostatic position. Intruder sinking is facilitated by grain-grain contact sliding that allows rearrangement of the medium surrounding the intruder. With the buoyancy effect, granular sliding is easier, as the normal contact force between grains is reduced with respect to a dry layer. Less sliding occurs in the vicinity of the intruder because the intruder is only partially immersed, and the buoyancy force acting to reduce the normal contact forces between the intruder and its neighboring grains is smaller. Since these simulations don't include PP, their results demonstrate that liquefaction, with sinking structures, can occur without elevated PP rise beyond hydrostatic values. This buoyancy

dependent liquefaction mechanism may explain liquefaction of pre-compacted soil, under drained conditions and repeated liquefaction events. It further predicts liquefaction with low energy and low earthquake-induced peak ground accelerations, that can possibly explain far field liquefaction events that occurred despite small seismic energy input (Wang 2007).

INTRUDER AND PORE PRESSURE SIMULATION METHOD

Solid Phase. In our new simulations we use a similar DEM for the grains as in Clément et al. 2017a,b, but add to it the pore pressure effect. The grains are modeled as spheres with a linear elastic contact model. A velocity dependent damping is added to the normal contact force, and a threshold friction law is added to the tangential force that allows sliding when the shear force surpasses a frictional criterion. Grain motion is determined by time integration of the linear (eq. 1) and rotational (eq. 2) momentum conservation equations.

$$m_i \dot{u}_i = m_i g - V_{imm} \rho_f g + \sum_j F_{ij} - \frac{\nabla P \cdot V_i}{1-\phi} \quad (1)$$

$$I_i \dot{\omega} = \sum_j R_i \hat{n}_{ij} \times F_{ij} \quad (2)$$

In equation (1), the left-hand side is the inertia of grain i . In the right hand side, the first term is the gravitational force, the second term is the buoyancy force whose magnitude depends on the immersed volume of the grain V_{imm} , and on the fluid density ρ_f , the third term is the sum of contact forces with all grains j that are in contact with grain i , and the fourth term, which was not included in Clément et al. 2017a,b, represents the drag force exerted by the fluid pressure gradient, ∇P , where P is the pore pressure deviation from hydrostatic values and V_i is the volume of grain i .

Fluid Phase. The interstitial fluid is modeled as a continuum on a superimposed Eulerian grid (McNamara et al. 2000). The grid spacing is set to be two grain diameters, to both respect Darcy's law over each grid cell and to allow sufficient resolution for the fluid solver (Goren et al. 2011). The fluid pressure equation is (Goren et al. 2010, 2011, Niebling et al. 2010a,b):

$$\frac{\partial P}{\partial t} = \frac{1}{\beta \phi \eta} \nabla \cdot [k \nabla P] - \frac{1}{\beta \phi} \nabla \cdot \bar{u}_s \quad (3)$$

The left-hand side of equation (3) represents the temporal derivative of the pore pressure. On the right-hand side, the first term represents pore pressure diffusion, where k is the permeability, β is the fluid compressibility, and η is the fluid dynamic viscosity. The second term represents a source for pore pressure due to the solid grain velocity divergence.

Coupling Between the Solid and The Fluid Phases. In order to achieve two-way coupling between the two phases, the relevant quantities are interpolated between the grains and the fluid grid. The porosity and the solid grain velocity are defined on the fluid grid via a bi-linear interpolation scheme that assures smooth porosity and solid velocity fields. This allows solving eq. (3) for the spatially and temporally variable PP. In addition, to solve eq. (1), the pressure gradient is interpolated back from the fluid grid to the grains together with the porosity ϕ using the same bi-linear scheme. In our model, the permeability and porosity are connected by the 3D Carman-Kozeny relationship:

$$k = \alpha \overline{r^2} \frac{\phi^3}{(1-\phi)^2} \quad (4)$$

Where $\overline{r^2}$ is the average of the squared grain radii in the surroundings, and α is a constant that allows us to vary permeability between different simulations, while keeping the characteristic time scale of pressure diffusion across grid spacing longer than model time step.

Treating the Intruder. As the intruder is larger than the grid spacing, we cannot directly use the previously described solid-fluid interpolation scheme to account for its contribution to porosity and solid velocity on grid nodes, and for the back interpolation of defining the pressure gradient over it based on the surrounding grid nodes. To overcome this limitation, we treat the intruder as a cluster of polygonal grains glued together, where each polygon corresponds to the area of intersect between the intruder and a cell (see Fig 1). To achieve this, we define virtual grains with mass, volume, and center of mass based on the volume and location of each polygon that results from intersecting the intruder with a particular cell, where virtual grains velocity is equivalent to the intruder velocity. Then, the virtual intruder equivalent grains can be treated as normal grains in the interpolation scheme of solid grains to fluid grid. For numerical stability reasons, we assign a finite porosity of $\phi = 0.001$ in cells that are fully covered by the intruder. This low porosity ensures that the permeability inside the intruder as calculated in eq. 4, will be sufficiently small relative to the permeability in the rest of the medium. The fluid pressure equation (3) can thus be solved continuously over the full domain, including the intruder, that acts as a low permeability barrier for fluid flow.

The pressure gradient force on the center of mass of the intruder is calculated using the mean value of pressure gradient on grid nodes that are covered by the intruder. This arises from the discretization of the volume integral over the pressure gradient (eq. 5):

$$\left(\frac{\nabla P \cdot V_i}{1 - \phi}\right)_{intruder} = \frac{1}{1 - \phi} \int \nabla P dV = \frac{1}{1 - \phi} \sum_k^n \nabla P_k \frac{V}{n} = \frac{V}{(1 - \phi)} \cdot \frac{1}{n} \sum_k^n \nabla P_k \quad (5)$$

where V is the volume of the intruder and n is the number of grid cells that intersect with it. For other aspects of the calculation such as the solution of equations (1) and (2), the intruder is treated as a thin disc with thickness of one average grain diameter.

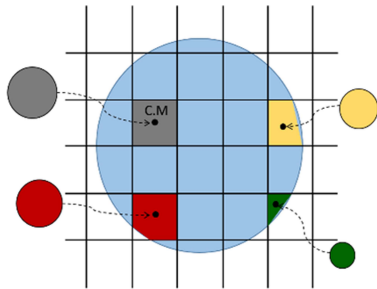


Figure 1. Partitioning the intruder into virtual grains. Each polygon that forms from the intersection between the grid and the intruder translates into a virtual grain with equivalent area, mass, center of mass (C.M) and velocity. In the next stage, these virtual grains contribute their quantities to the fluid nodes using the bi-linear interpolation scheme.

Simulation Setup. The numerical system (Fig. 2) represents a thin columnar (Hele-Shaw) cell of densely packed spheres with an intruder on top. The cell is horizontally periodic. Dynamics is induced by cyclically shearing the bottom wall at a pre-defined amplitude and frequency. The water table level is maintained at a constant height. For the buoyancy effect the water level sets the degree of immersion of the grains and the intruder, and for the PP effect it is used as the top zero pressure boundary, which allows efficient fluid drainage across the top. The base of the cell is set as a no flow boundary. The physical parameters of the simulation are provided in table 1.

Grain density	$\rho_s = 2,640 \text{ kg} \cdot \text{m}^{-3}$	Fluid compressibility	$\beta_f = 4.5 \cdot 10^{-10} \text{ Pa}^{-1}$
Intruder density	$\rho_{int} = 1,980 \text{ kg} \cdot \text{m}^{-3}$	Fluid viscosity	$\eta = 10^{-3} \text{ Pa} \cdot \text{s}$
Fluid density	$\rho_f = 1,000 \text{ kg} \cdot \text{m}^{-3}$	Average grain diameter	$d = 0.01 \text{ m}$
Young modulus	$E = 10^{10} \text{ Pa}$	Intruder diameter	$D = 0.06 \text{ m}$
Friction coefficient	$\mu = 0.5$	Permeability (order of magnitude)	$\kappa \sim 10^{-9} - 10^{-10} \text{ m}^2$

Table 1. Physical parameters used in the simulations.

PRELIMINARY RESULTS FROM SIMULATIONS WITH PORE PRESSURE

Figure 3 shows results of simulations with horizontal shaking frequency of 12Hz, that differ in their shaking amplitude and thus in their Peak Ground Acceleration (PGA) provided by the bottom wall. We quantify the amount of intruder sinking by measuring its normalized emerged volume, defined as the ratio between its instantaneous emerged volume (V_{em}) to its initial emerged volume ($V_{em}(0)$). We observe that as the PGA increases from 0.01g to 0.1g, the emerged volume decreases and the intruder sinks

further. Comparing simulations with and without the PP effect, we find that intruder sinking is enhanced in simulations that include dynamically induced PP (depicted by solid black lines) compared to simulations in which only the buoyancy effect is included (depicted by dashed light blue lines) as in Clément et al. 2017a,b work. While at the lower PGA the enhanced sinking is negligible, at higher PGA values, sinking becomes increasingly more significant. The RHS of Fig 3 shows the ratio of PP (in excess of hydrostatic) to effective normal stress ($\sigma_{eff} = (\rho_s - \rho_f)gh$, where h is the depth with respect to the water table, and ρ_s the bulk density of the grains) at three depths (locations shown in Fig 2), for simulations that include PP. As the PGA increases this ratio increases and is sustained longer at all depths, but importantly, this ratio never equals 1. This means that although the total PP never reaches lithostatic values, still the elevated values of PP makes the granular layer more liquefied. This is testified by the enhanced intruder sinking, relative to the case of buoyancy alone (which in itself promotes liquefaction, but at higher PGA).

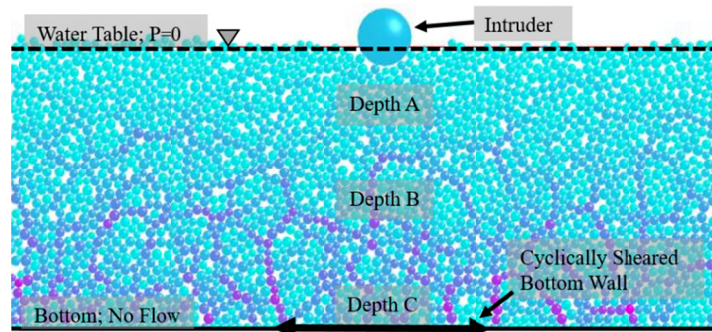


Figure 2. Numerical system setup

CONCLUSIONS

In the current work, we study mechanisms for liquefaction. For that, we adopt the field scale phenomenological definition that identifies liquefaction with observations of macro-scale changes in the rheological response of a soil, as it changes from a solid skeleton to a liquefied slurry. Here, we follow the sinking of an intruder (simulating a building) into a saturated dense and drained soil during horizontal shaking. The preliminary modeling results show that liquefaction, as testified by the intruder sinking towards its isostatic position, occurs under specific shaking conditions in saturated soils. Liquefaction does not require loose sediments, neither does it require pore pressure reaching lithostatic values. Instead, it requires the correct combination of mechanistic effects: horizontal grain accelerations, fluid buoyancy and pore-pressure rise. Clément et al. 2017a,b have shown that some sinking can occur already at relatively low PGAs, solely due to the effect of buoyancy. Yet, here we find that

sinking is enhanced significantly by dynamically induced PP. This occurs even when the PP value remains below the effective normal stress, i.e., even when the classical laboratory scale liquefaction criterion of pore pressure becoming equal to the lithostatic stress, is not met.

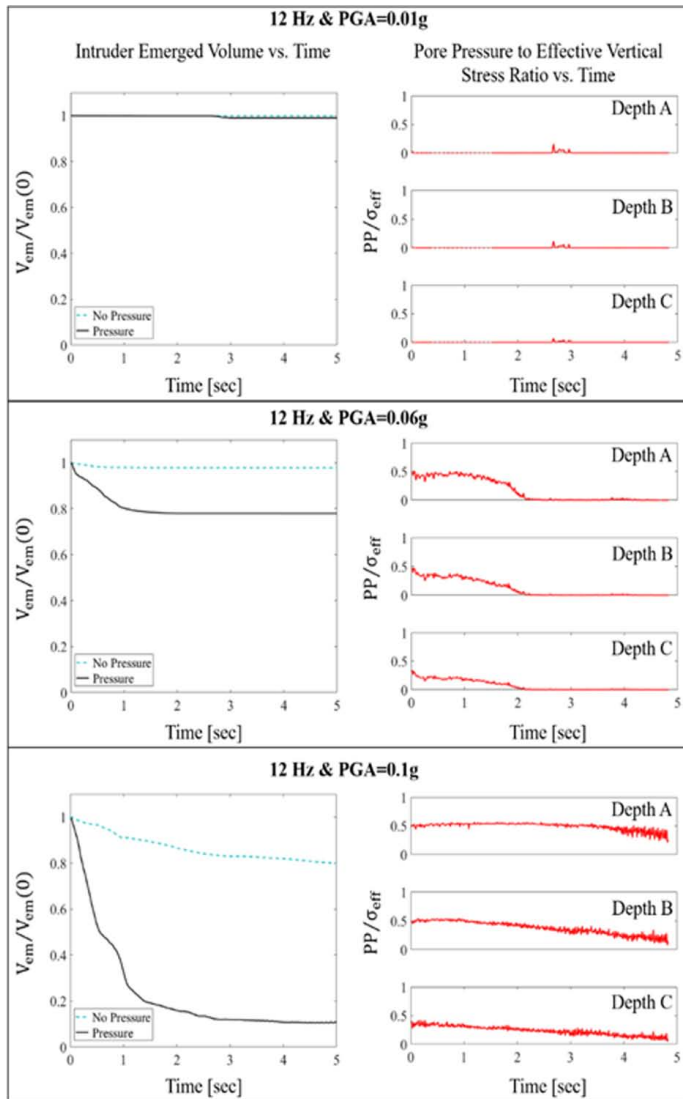


Figure 3. LHS- normalized emerged volume of the intruder vs. time for simulations with dynamically induced pore pressure (black lines) and simulations with only buoyancy effect (dashed blue lines). Sinking increases with increasing PGA. Sinking is observed even in runs with the buoyancy effect only, provided shaking is strong enough, but is enhanced when the PP effect is included. RHS- average ratio of PP to the effective normal stress for chosen depths that are depicted in Fig 2. The pore pressure stays always below the effective normal stress and yet liquefaction occurs, causing sinking of the intruder.

To conclude, liquefaction can occur due to high enough driving force, which overcomes the strength of the soil, or from the opposite perspective, of lowering the strength of the soil itself. The fluid effect is two-fold: The buoyancy force reduces the strength of the soil statically and uniformly, while the PP effect reduces the strength by forming dynamically.

REFERENCES

- Clément, C., Toussaint, R., and Aharonov, E. (2017). "Shake and sink: liquefaction without pressurization." *under-review*.
- Clément, C., Toussaint, R., Stojanova, M., and Aharonov, E. (2017). "The art of sinking intruder during earthquakes." *under-review*.
- Cundall, P.A., and Strack, O.D. (1979). "A discrete numerical model for granular assemblies." *Geotechnique*, 29(1), 47-65.
- Goren, L., Aharonov, E., Sparks, D., and Toussaint, R. (2010). "Pore pressure evolution in deforming granular material: A general formulation and the infinitely stiff approximation." *Journal of Geophysical Research*, 115(B9).
- Goren, L., Aharonov, E., Sparks, D., and Toussaint, R. (2011). "The mechanical coupling of fluid-filled granular material under shear." *Pure and Applied Geophysics*, 168(12), 2289-2323.
- Holzer, T.L., Youd, T.L., and Hanks, T.c. (1989). "Dynamics of liquefaction during the 1987 superstition hills, california, earthquake." *Science*, 244(4900), 56-59.
- Martin, G.R., Finn, W.L., and Seed, H.B. (1975). "Fundamentals of liquefaction under cyclic loading." *Journal of Geotechnical and Geoenvironmental Engineering*, 101(ASCE# 1123 Proceedings).
- McNamara, S., Flekkøy, E.G., and Måløy, K.J. (2000). "Grains and gas flow: molecular dynamics with hydrodynamic interactions." *Physical Review E*, 61(4), 4054.
- Niebling, M.J., Flekkøy, E.G., Måløy, K.J., and Toussaint, R. (2010). "Mixing of a granular layer falling through a fluid." *Physical Review E*, 82(1), 011301.
- Niebling, M.J., Flekkøy, E.G., Måløy, K.J., and Toussaint, R. (2010). "Sedimentation instabilities: Impact of the fluid compressibility and viscosity." *Physical Review E*, 82(1), 051302.
- Obermeier, S.F. (1996). "Use of liquefaction-induced features for paleoseismic analysis — An overview of how seismic liquefaction features can be distinguished from other features and how their regional distribution and properties of source sediment can be used to infer the location and strength of Holocene paleo-earthquakes." *Engineering Geology*, 44(1), 1-76.
- Soga, K. (1998). "Soil liquefaction effects observed in the Kobe earthquake of 1995." *Proceedings of the ICE Geotechnical Engineering*, 131, 34-51.

- Wang, Y.C. (2007). "Liquefaction beyond the near field." *Seismological Research Letters*, 78, 512-517.
- Youd, T.L., and Idriss, I.M. (2001). "Liquefaction Resistance of Soils: Summary Report from the 1996 NCEER and 1998 NCEER/NSF Workshops on Evaluation of Liquefaction Resistance of Soils." *Journal of Geotechnical and Geoenvironmental Engineering*, 127(10), 817-83

Bibliography

- O. Adamidis and I. Anastasopulis. Cyclic liquefaction resistance of sand under a constant inflow rate. *Geotechnique*, 2022. doi:10.1680/jgeot.21.00082.
- O. Adamidis and G. Madabhushi. Experimental investigation of drainage during earthquake-induced Experimental investigation of drainage during earthquake-induced liquefaction. *Geotechnique*, 68(8):655–665, 2018. doi:10.1680/jgeot.16.p.090.
- D. C. A. Andrews and G. R. Martin. Criteria for liquefaction of silty soils. In *12th world conference on earthquake engineering*, pages 1–8, Auckland, New Zealand, 2000. URL <https://www.iitk.ac.in/nicee/wcee/article/0312.pdf>.
- J. Berrill and R. Davis. Energy dissipation and seismic liquefaction of sands: revised model. *Soils and Foundations*, 25(2):106–118, 1985. doi:https://doi.org/10.3208/sandf1972.25.2_106.
- V. Besharat. The methods of remediation of existing underground structure against liquefaction. In *15th World Conference on earthquake engineering*, 2012. URL https://www.iitk.ac.in/nicee/wcee/article/WCEE2012_{_}3225.pdf.
- C. Z. Beyzaei, J. D. Bray, S. V. Ballegooy, M. Cubrinovski, and S. Bastin. Depositional environment effects on observed liquefaction performance in silt swamps during the Canterbury earthquake sequence. *Soil Dynamics and Earthquake Engineering*, 107(December 2017):303–321, 2018. ISSN 0267-7261. doi:<https://doi.org/10.1016/j.soildyn.2018.01.035>.

- K. Bradley, R. Mallick, H. Andikagumi, J. Hubbard, E. Meilianda, A. Switzer, N. Du, G. Brocard, D. Alfian, B. Benazir, G. Feng, S.-h. Yun, J. Majewski, S. Wei, and E. M. Hill. Earthquake-triggered 2018 Palu Valley landslides enabled by wet rice cultivation. *Nature Geoscience*, 12(November):935–940, 2019. ISSN 1752-0908. doi:10.1038/s41561-019-0444-1. URL <http://dx.doi.org/10.1038/s41561-019-0444-1>.
- J. Bray, M. EERI, M. Cubrinovski, J. Zupan, and M. Taylor. Liquefaction effects on buildings in the Central Business District of Christchurch. *earthquake spectra*, 30(1):85–109, 2014. doi:<https://doi.org/10.1193/022113EQS043M>.
- C. Clément, R. Toussaint, M. Stojanova, and E. Aharonov. Sinking during earthquakes: critical acceleration criteria control drained soil liquefaction. *Physical Review E*, 97(2): 022905, 2018. doi:<https://doi.org/10.1103/PhysRevE.97.022905>.
- S. C. Cox, H. K. Rutter, A. Sims, M. Manga, J. J. Weir, T. Ezzy, P. A. White, T. W. Horton, and D. Scott. Hydrological effects of the M_w 7.1 Darfield (Canterbury) earthquake , 4 September 2010 , New Zealand. *New Zealand Journal of Geology and Geophysics*, 55(3): 231–247, 2012. doi:<https://doi.org/10.1080/00288306.2012.680474>.
- M. Cubrinovski, D. Henderson, and B. Bradley. Liquefaction impacts in residential areas in the 2010-2011 Christchurch earthquakes. *Proceedings of the International Symposium on Engineering Lessons Learned from the 2011 Great East Japan Earthquake*, pages 811–824, 2012a. URL https://ir.canterbury.ac.nz/bitstream/handle/10092/6712/12639573_{_}Cubrinovski_{_}GEJE2011_{_}TohokuSpecialConference_{_}Paper183_{_}2012.pdf;sequence=1.
- M. Cubrinovski, K. Robinson, M. Taylor, M. Hughes, and R. Orense. Lateral spreading and its impacts in urban areas in the 2010-2011 Christchurch earthquakes. *New Zealand Journal of Geology and Geophysics*, 55(3):255–269, 2012b. doi:<https://doi.org/10.1080/00288306.2012.699895>.

- P. A. Cundall and O. D. Strack. A discrete numerical model for granular assemblies. *Geotechnique*, 29.1:47–65, 1979. ISSN 0016-8505. doi:<https://doi.org/10.1680/geot.1979.29.1.47>.
- H. Darcy. *Les fontaines publiques de la ville de Dijon*. Victor Dalmont, Paris, 1856.
- P. A. de Alba, K. C. Chan, and H. B. Seed. Sand liquefaction in large-scale simple shear tests. *Journal of Geotechnical and Geoenvironmental Engineering*, 102(GT9):909–927, 1976. doi:<https://doi.org/10.1061/AJGEB6.0000322>.
- S. F. de Magistris, G. Lanzano, G. Forte, and G. Fabbrocino. A database for PGA threshold in liquefaction occurrence. *Soil Dynamics and Earthquake Engineering*, 54:17–19, 2013. ISSN 0267-7261. doi:<http://dx.doi.org/10.1016/j.soildyn.2013.07.011>.
- S. F. de Magistris, G. Lanzano, G. Forte, and G. Fabbrocino. A peak acceleration threshold for soil liquefaction : lessons learned from the 2012 Emilia earthquake (Italy). *Natural Hazards*, 74:1069–1094, 2014. doi:<https://doi.org/10.1007/s11069-014-1229-x>.
- H. M. Dief and J. L. Figueroa. Liquefaction assessment by the unit energy concept through centrifuge and torsional shear tests. *Canadian Geotechnical Journal*, 44(11):1286–1297, 2007. ISSN 0008-3674. doi:<https://doi.org/10.1139/T07-059>.
- R. Dobry and T. Abdoun. Cyclic Shear Strain Needed for Liquefaction Triggering and Assessment of Overburden Pressure Factor K_σ . *Journal of Geotechnical and Geoenvironmental Engineering*, 141(11):04015047, 2015. doi:[https://doi.org/10.1061/\(ASCE\)GT.1943-5606.0001342](https://doi.org/10.1061/(ASCE)GT.1943-5606.0001342).
- R. Dobry, R. Ladd, F. Yokel, R. Chung, and D. Powell. *Prediction of Pore Water Pressure Buildup and Liquefaction of Sands During Earthquakes by the Cyclic Strain Method*. US department of commerce, National Bureau of Standards, Gaithersburg, MD, 1982.
- O. Dorostkar and J. Carmeliet. Potential energy as metric for understanding stick–slip dynamics in sheared granular fault gouge: A coupled CFD–DEM study.

- Rock Mechanics and Rock Engineering*, 51:3281–3294, 2018. ISSN 1434-453X.
doi:<https://doi.org/10.1007/s00603-018-1457-6>.
- U. El Shamy and M. Zeghal. A micro-mechanical investigation of the dynamic response and liquefaction of saturated granular soils. *Soil Dynamics and Earthquake Engineering*, 27(8):712–729, 2007. ISSN 02677261. doi:<https://doi.org/10.1016/j.soildyn.2006.12.010>.
- Eurocode 8. Eurocode 8: Design of structures for earthquake resistance. Technical report, European Committee for Standardization, 2004.
- G. L. Fiegel and B. L. Kutter. Liquefaction mechanism for layered soils. *journal of geotechnical engineering*, 120(4):737–755, 1994. doi:[https://doi.org/10.1061/\(ASCE\)0733-9410\(1994\)120:4\(737\)](https://doi.org/10.1061/(ASCE)0733-9410(1994)120:4(737)).
- J. L. Figueroa, A. S. Saada, L. Liang, and N. M. Dahisaria. Evaluation of soil liquefaction by energy principles. *journal of geotechnical engineering*, 120(9):1554–1569, 1994. doi:[https://doi.org/10.1061/\(ASCE\)0733-9410\(1994\)120:9\(1554\)](https://doi.org/10.1061/(ASCE)0733-9410(1994)120:9(1554)).
- D. Gautam, F. S. D. Magistris, and G. Fabbrocino. Soil liquefaction in Kathmandu valley due to 25 April 2015 Gorkha, Nepal earthquake. *Soil Dynamics and Earthquake Engineering*, 97(October 2016):37–47, 2017. ISSN 0267-7261. doi:<http://dx.doi.org/10.1016/j.soildyn.2017.03.001>.
- L. Goren, E. Aharonov, D. W. Sparks, and R. Toussaint. Pore pressure evolution in deforming granular material: A general formulation and the infinitely stiff approximation. *Journal of Geophysical Research: Solid Earth*, 115(9):1–19, 2010. ISSN 21699356. doi:<https://doi.org/10.1029/2009JB007191>.
- L. Goren, E. Aharonov, D. W. Sparks, and R. Toussaint. The mechanical coupling of fluid-filled granular material under shear. *Pure and Applied Geophysics*, 168(12):2289–2323, 2011. ISSN 00334553. doi:<https://doi.org/10.1007/s00024-011-0320-4>.

- R. A. Green. *Energy-Based Evaluation and Remediation of Liquefiable Soils*. PhD thesis, Virginia Polytechnic Institute and State University, 2001.
- R. A. Green and J. K. Mitchell. A closer look at Arias intensity-based liquefaction evaluation procedures. In *2003 Pacific Conference on Earthquake Engineering*, number 13, page 15, 2003. URL <https://www.nzsee.org.nz/db/2003/Print/Paper094p.pdf>.
- R. A. Green and J. K. Mitchell. Energy-based evaluation and remediation of liquefiable soils. In *Geotechnical Engineering for Transportation Projects*, 2004. doi:[https://doi.org/10.1061/40744\(154\)191](https://doi.org/10.1061/40744(154)191).
- M. W. Greenfield. *Effects of long-duration ground motions on liquefaction hazards*. PhD thesis, University of Washington, 2017.
- I.-s. Ha, S. M. Olson, M.-w. Seo, and M.-m. Kim. Evaluation of reliquefaction resistance using shaking table tests. *Soil Dynamics and Earthquake Engineering*, 31(4):682–691, 2011. ISSN 0267-7261. doi:<http://dx.doi.org/10.1016/j.soildyn.2010.12.008>.
- K. Ishihara, K. Araki, and B. Bradley. Characteristics of liquefaction-induced damage in the 2011 Great East Japan earthquake. In *International Conference on Geotechnics for Sustainable Development - Geotec Hanoi, Vietnam.*, page 22, 2011. doi:<http://hdl.handle.net/10092/6249>.
- Y. Jafarian, R. Vakili, A. S. Abdollahi, and M. H. Baziar. Simplified soil liquefaction assessment based on cumulative kinetic energy density: Attenuation law and probabilistic analysis. *International Journal of Geomechanics*, 14(2):267–281, 2014. doi:[https://doi.org/10.1061/\(ASCE\)GM.1943-5622.0000317](https://doi.org/10.1061/(ASCE)GM.1943-5622.0000317).
- Ø. Johnsen, R. Toussaint, K. J. Måløy, and E. G. Flekkøy. Pattern formation during air injection into granular materials confined in a circular Hele-Shaw cell. *Physical Review E*, 74(1):011301, 2006. doi:<https://doi.org/10.1103/PhysRevE.74.011301>.

- K. Jones, F. Pascale, N. Wanigarathna, M. Morga, and S. Sargin. Critical evaluation of the customisation process of the UNDRR disaster resilience scorecard for cities to earthquake - induced soil liquefaction disaster events. *Bulletin of Earthquake Engineering*, 19(10): 4115–4143, 2021. ISSN 1573-1456. doi:<https://doi.org/10.1007/s10518-020-00993-y>.
- P. Jop, Y. Forterre, and O. Pouliquen. A constitutive law for dense granular flows. *Nature*, 441(June):727–730, 2006. doi:<https://doi.org/10.1038/nature04801>.
- R. E. Kayen and J. k. Mitchell. Assesment of liquefaction potential during earthquakes by Arias intensity. *Journal of Geotechnical and Geoenvironmental Engineering*, 123(12): 1162–1174, 1997. doi:[https://doi.org/10.1061/\(ASCE\)1090-0241\(1997\)123:12\(1162\)](https://doi.org/10.1061/(ASCE)1090-0241(1997)123:12(1162)).
- T. Kokusho and T. Kojima. Mechanism for postliquefaction water film generation in layered sand. *Journal of Geotechnical and Geoenvironmental Engineering*, 128(February):129–137, 2002. doi:[https://doi.org/10.1061/\(ASCE\)1090-0241\(2002\)128:2\(129\)](https://doi.org/10.1061/(ASCE)1090-0241(2002)128:2(129)).
- K. Konagai, T. Kiyota, S. Suyama, and T. Asakura. Maps of soil subsidence for Tokyo bay shore areas liquefied in the March 11th, 2011 off the Pacific Coast of Tohoku Earthquake. *Soil Dynamics and Earthquake Engineering*, 53:240–253, 2013. ISSN 0267-7261. doi:<http://dx.doi.org/10.1016/j.soildyn.2013.06.012>.
- B. Kooi. Great Eastern Japan Earthquake - Liquefaction in Makuhari, 2011. URL https://www.youtube.com/watch?v=rn3oAvmZY8k&ab_channel=BrentKooi.
- M. V. Kostadinov and I. Towhata. Assessment of liquefaction-inducing peak ground velocity and frequency of horizontal ground shaking at onset of phenomenon. *Soil Dynamics and Earthquake Engineering*, 22(4):309–322, 2002. doi:[https://doi.org/10.1016/S0267-7261\(02\)00018-0](https://doi.org/10.1016/S0267-7261(02)00018-0).
- S. L. Kramer. *Geotechnical Earthquake Engineering*. Prentice Hall, Upper Saddle River, New Jersey, 1996. ISBN 0133749436.

- D. L. Lakeland, A. Rechenmacher, and R. Ghanem. Towards a complete model of soil liquefaction : the importance of fluid flow and grain motion. *Proceedings of the royal society*, 470(2165), 2014. doi:<https://doi.org/10.1098/rspa.2013.0453>.
- K. Law, Y. Cao, and G. He. An energy approach for assessing seismic liquefaction potential. *Canadian Geotechnical Journal*, 1990. doi:<https://doi.org/10.1139/t90-043>.
- T. Lay and T. C. Wallace. *Modern global seismology*. Elsevier, 1995. ISBN 9780127328706.
- L. Liang, J. L. Figueroa, and A. S. Saada. Liquefaction under random loading: Unit energy approach. *Journal of geotechnical engineering*, 1995. doi:[https://doi.org/10.1061/\(ASCE\)0733-9410\(1995\)121:11\(776\)](https://doi.org/10.1061/(ASCE)0733-9410(1995)121:11(776)).
- M. Manga and C.-Y. Wang. Earthquake Hydrology. In G. Schubert, editor, *Treatise on Geophysics*, volume 4, chapter 4.12, pages 305–328. Elsevier, Oxford, second edition, 2015. ISBN 978-0-444-53803-1. doi:<https://doi.org/10.1016/B978-0-444-53802-4.00082-8>.
- G. S. P. Madabhushi and S. K. Haigh. How well do we understand earthquake induced liquefaction? *Indian Geotechnical Journal*, 42(September):150–160, 2012. doi:<https://doi.org/10.1007/s40098-012-0018-2>.
- M. Manga, I. Beresnev, E. E. Brodsky, J. E. Elkhoury, D. Elsworth, S. E. Ingebritsen, D. C. Mays, and C.-y. Wang. Changes in permeability caused by transient stresses: Field observations, experiments, and mechanisms. *Reviews of Geophysics*, 50(2), 2012. doi:<https://doi.org/10.1029/2011RG000382>.
- K. D. Marano, D. J. Wald, and T. I. Allen. Global earthquake casualties due to secondary effects : a quantitative analysis for improving rapid loss analyses. *Natural Hazards*, 52: 319–328, 2010. doi:<https://doi.org/10.1007/s11069-009-9372-5>.
- G. R. Martin, W. L. Finn, and H. B. Seed. Fundamentals of liquefaction under cyclic

- loading. *Journal of the geotechnical engineering division*, 101(GT5):423–438, 1975.
doi:<https://doi.org/10.1061/AJGEB6.0000164>.
- S. McNamara, E. G. Flekkøy, and K. J. Måløy. Grains and gas flow: molecular dynamics with hydrodynamic interactions. *Physical review E*, 61(4):4054—4059, 2000. ISSN 1063-651X.
doi:<https://doi.org/10.1103/PhysRevE.61.4054>.
- National Academies of Sciences Engineering and Medicine. State of the Art and Practice in the Assessment of Earthquake-Induced Soil Liquefaction and Its Consequences. Technical report, The National Academies of Sciences Engineering and Medicine, Washington, DC, 2016.
- S. Nemat-Nasser and A. Shokoh. A unified approach to densification and liquefaction of cohesionless sand in cyclic shearing. *Canadian Geotechnical Journal*, 16(4):659–678, 1979.
doi:<https://doi.org/10.1139/t79-076>.
- M. J. Niebling, E. G. Flekkøy, K. J. Måløy, and R. Toussaint. Mixing of a granular layer falling through a fluid. *Physical Review E*, 82(1):011301, 2010a. ISSN 15393755.
doi:<https://doi.org/10.1103/PhysRevE.82.011301>.
- M. J. Niebling, E. G. Flekkøy, K. J. Måløy, and R. Toussaint. Sedimentation instabilities: Impact of the fluid compressibility and viscosity. *Physical Review E*, 82(5):051302, 2010b. ISSN 15393755. doi:<https://doi.org/10.1103/PhysRevE.82.051302>.
- S. F. Obermeier. Use of liquefaction-induced features for paleoseismic analysis — An overview of how seismic liquefaction features can be distinguished from other features and how their regional distribution and properties of source sediment can be used to infer the locat. *Engineering Geology*, 44(1-4):1–76, 1996. ISSN 00137952. doi:[https://doi.org/10.1016/S0013-7952\(96\)00040-3](https://doi.org/10.1016/S0013-7952(96)00040-3).
- S. M. Olson, S. F. Obermeier, and T. D. Stark. Interpretation of penetration resistance for

- back-analysis at sites of previous liquefaction. *Seismological Research Letters*, 72(1):46–59, 2001. doi:<https://doi.org/10.1785/gssrl.72.1.46>.
- S. M. Olson, R. A. Green, and S. F. Obermeier. Geotechnical analysis of paleoseismic shaking using liquefaction features : a major updating. *Engineering Geology*, 76:235–261, 2005. doi:<https://doi.org/10.1016/j.enggeo.2004.07.008>.
- Oregon State University. Japan Earthquake 2011 Liquefaction Damage, 2011. URL https://www.youtube.com/watch?v=GviJkVEMfwQ&ab_channel=OregonStateUniversity.
- S. Parez, T. Travnickova, M. Svoboda, and E. Aharonov. Strain localization in planar shear of granular media: the role of porosity and boundary conditions. *The European Physical Journal E*, 44(134):1–17, 2021. ISSN 1292-895X. doi:<https://doi.org/10.1140/epje/s10189-021-00138-2>.
- M. C. Quigley, S. Bastin, and B. A. Bradley. Recurrent liquefaction in Christchurch, New Zealand, during the Canterbury earthquake sequence. *Geology*, 41(4):419–422, 2013. ISSN 00917613. doi:<https://doi.org/10.1130/G33944.1>.
- R. A. Rasanen, N. A. Marafi, and B. W. Maurer. Compilation and forecasting of paleoliquefaction evidence for the strength of ground motions in the U.S. Pacific Northwest. *Engineering Geology*, 292(July):106253, 2021. ISSN 0013-7952. doi:<https://doi.org/10.1016/j.enggeo.2021.106253>.
- M. Reiner. The Deborah Number. *Physics today*, 17(1):62, 1964. doi:<https://doi.org/10.1063/1.3051374>.
- A. Sawicki and J. Mierczynski. Developments in modeling liquefaction of granular soils, caused by cyclic loads. *Applied Mechanics Reviews*, 59(2):91–106, 2006. ISSN 00036900. doi:<https://doi.org/10.1115/1.2130362>.

- J. H. Schmertmann. The mechanical aging of soils. *journal of geotechnical engineering*, 117(1):1288–1330, 1991. doi:[https://doi.org/10.1061/\(ASCE\)0733-9410\(1991\)117:9\(1288\)](https://doi.org/10.1061/(ASCE)0733-9410(1991)117:9(1288)).
- H. B. Seed and I. M. Idriss. Simplified procedure for evaluating soil liquefaction potential. *Journal of the Soil Mechanics and Foundations Division*, 97(9):1249–1273, 1971. doi:<https://doi.org/10.1061/JSFEAQ.0001662>.
- D. Sengupta, R. Chen, and M. E. Meadows. Building beyond land : An overview of coastal land reclamation in 16 global megacities. *Applied Geography*, 90(May 2017):229–238, 2018. ISSN 0143-6228. doi:<https://doi.org/10.1016/j.apgeog.2017.12.015>.
- J. D. Sims and C. D. Garvin. Recurrent liquefaction induced by the 1989 Loma Prieta earthquake and 1990 and 1991 aftershocks: Implications for paleoseismicity studies. *Bulletin of the Seismological Society of America*, 85(1):51–65, 1995. doi:<https://doi.org/10.1785/BSSA0850010051>.
- K. Soga. Soil liquefaction effects observed in the Kobe earthquake of 1995. *Proceedings of the ICE Geotechnical Engineering*, 131:34–51, 1998. doi:<https://doi.org/10.1680/igeng.1998.30004>.
- W. Thielicke and R. Sonntag. Particle Image Velocimetry for MATLAB : Accuracy and enhanced algorithms in PIVlab. *journal of open research*, 9(12), 2021. doi:<https://doi.org/10.5334/jors.334>.
- W. Thielicke and E. J. Stamhuis. PIVlab – Towards user-friendly , affordable and accurate digital Particle Image Velocimetry in MATLAB. *journal of open research software*, 2(1), 2014. doi:<http://doi.org/10.5334/jors.bl>.
- M. P. Tuttle, R. Hartleb, L. Wolf, and P. W. Mayne. Paleoliquefaction studies and the evaluation of seismic hazard. *Geosciences*, 9(7):311, 2019. doi:<https://doi.org/10.3390/geosciences9070311>.

- J. L. Vinningland, Ø. Johnsen, E. G. Flekkøy, R. Toussaint, and K. J. Måløy. Granular Rayleigh-Taylor Instability: Experiments and simulations. *Physical Review Letters*, 99(4): 048001, 2007a. doi:<https://doi.org/10.1103/PhysRevLett.99.048001>.
- J. L. Vinningland, Ø. Johnsen, E. G. Flekkøy, R. Toussaint, and K. J. Måløy. Experiments and simulations of a gravitational granular flow instability. *Physical Review E*, 76(5): 051306, 2007b. doi:10.1103/PhysRevE.76.051306.
- C. Y. Wang. Liquefaction beyond the Near Field. *Seismological Research Letters*, 78(5): 512–517, 2007. ISSN 0895-0695. doi:10.1785/gssrl.78.5.512.
- C. Y. Wang and M. Manga. Hydrologic responses to earthquakes and a general metric. *Frontiers in Geofluids*, pages 206–216, 2011. ISSN 14688115. doi:10.1002/9781444394900.ch14.
- C. Y. Wang and M. Manga. Chapter 11: Liquefaction. In *Water and Earthquakes*, chapter 11. Springer Cham, 2021. ISBN 9783030643089. doi:10.1007/978-3-030-64308-9.
- A. Wong and C.-Y. Wang. Field relations between the spectral composition of ground motion and hydrological effects during the 1999 Chi-Chi (Taiwan) earthquake. *Journal of Geophysical Research: Solid Earth*, 112(B10):1–19, 2007. doi:10.1029/2006JB004516.
- A. Wood, I. Noy, and M. Parker. The Canterbury rebuild five years on from the Christchurch earthquake. *Reserve Bank of New Zealand Bulletin*, 79:1–16, 2016. URL <https://ideas.repec.org/a/nzb/nzbbul/feb201603.html>.
- L. M. Wotherspoon, R. P. Orense, M. Jacka, R. A. Green, B. R. Cox, and C. M. Wood. Seismic performance of improved ground sites during the 2010 – 2011 Canterbury earthquake sequence. *Earthquake Spectra*, 30(1):111–129, 2014. doi:10.1193/082213EQS236M.
- F. Yamashita, E. Fukuyama, and K. Omura. Estimation of fault strength: Reconstruction of stress before the 1995 Kobe earthquake. *Science*, 306(October):261–264, 2004. doi:<https://doi.org/10.1126/science.1101771>.

- T. L. Youd and N. S. Hoose. Liquefaction susceptibility and geologic setting. In *6th World Conference on Earthquake Engineering*, pages 2189–2194, Englewood Cliffs, NJ, 1977. Prentice Hall. URL https://www.iitk.ac.in/nicee/wcee/article/6{}_vol13{}_2189.pdf.
- T. L. Youd and D. M. Perkins. Mapping liquefaction-induced ground failure potential. *Journal of the geotechnical engineering division*, 104(4), 1978. doi:<https://doi.org/10.1061/AJGEB6.0000612>.
- T. L. Youd, I. M. Idriss, R. D. Andrus, I. Arango, G. Castro, J. T. Christian, R. Dobry, W. D. L. Finn, L. F. H. Jr, M. E. Hynes, K. Ishihara, J. P. Koester, S. S. C. Liao, W. F. M. Iii, G. R. Martin, J. K. Mitchell, Y. Moriwaki, M. S. Power, P. K. Robertson, R. B. Seed, and K. H. S. Ii. Liquefaction resistance of soils: Summary report from the 1996 NCEER and 1998 NCEER/NSF Workshops on Evaluation of Liquefaction Resistance of Soils. *Journal of Geotechnical and Geoenvironmental Engineering*, 127(10):817–833, 2001. doi:[https://doi.org/10.1061/\(ASCE\)1090-0241\(2001\)127:10\(817\)](https://doi.org/10.1061/(ASCE)1090-0241(2001)127:10(817)).

תקציר

התנזלות קרקע ברעידת אדמה היא תופעה נפוצה והרסנית שגורמת להפסדים כלכליים ואבידות בנפש. בזמן התנזלות רעידת האדמה גורמת לאובדן קשיחות קרקעות, התנהגות נוזלית ואובדן פתאומי של יכולת הקרקע לשאת מעמסת תשתיות שגורמות לכשל של מבנים וגשרים. התנזלות קרקע מזוהה גם ברקורד הגיאולוגי כמעוות של סדימנט רך. המכניזם הקלאסי שמשמש להסבר התופעה מניח תגובה לא מנוקזת של הקרקע. כלומר, בזמן רעידת האדמה נקבובי הקרקע המלאים במים נוטים לקרוס ולהתכווץ מהר מאוד כך שהנוזל לא יכול לצאת מהם ולכן לחץ המים עולה. מעמסת משקל הקרקע עוברת מהמגעיים בין הגרגרים למי הנקבים שאינם יכולים להתנגד לגזירה. מחקרים מהזמן האחרון הטילו ספק בכך שתגובה לא מנוקזת היא המכניזם היחיד שיכול לגרום להתנזלות. בפרט, הנחת תגובה לא מנוקזת לא מסבירה תצפיות של התנזלות רחוק ממוקד רעידת האדמה היכן שצפיפות האנרגיה הסייסמית מאוד נמוכה, ומתקשה בהסבר של מקרי התנזלות חוזרים ונשנים של קרקע ברעידות אדמה שונות. מודל אי הניקוז מתקשה גם בהסבר תצפיות של יציאת מים בפני הקרקע בזמן רעידת האדמה, שקיעת קרקע בזמן הרעדה במעבדה ותחזיות תיאורטיות שמאפשרות עליית לחץ מים תחת ניקוז מיטבי.

באמצעות תובנות העולות מתיאוריה פיסיקלית של התפתחות לחץ מי נקבים בשכבת גרגרים מתעוותת, מודלים ספרתיים וניסויי הרעדה, עבודה זו מראה שעליית לחץ מי הנקבים יכולה להתרחש באמצעות מקרה קצה של ניקוז מיטבי, בנוסף למקרה הקצה המוכר של עליית לחץ בתנאי אי-ניקוז. זרימת מים ביחס לגרגרי הקרקע היא מחויבת המציאות תחת תנאי ניקוז מיטבי. הזרימה נתמכת על ידי גרדיאנט לחץ מי נקבים עודף ולחץ מי נקבים עודף שמנוזלים את הקרקע. דינמיקת ההתנזלות תחת ניקוז מיטבי נשלטת על ידי חזית דחיסה המתקדמת במעלה שכבת הקרקע ומפרידה בין תת השכבה התחתונה הדחוסה ולא מנוזלת, לבין תת השכבה העליונה המנוזלת ונעה כלפי מטה. חזית הדחיסה נעה מעלה במהירות שמוכתבת על ידי קצב כניסת האנרגיה הסייסמית באתר (ההספק הסייסמי). תחת ניקוז מיטבי, משך ההתנזלות ותהליך דחיסת הקרקע נמצאו כתלויים בעיקר ביחסים בין ההספק הסייסמי, מהירות החזית, עובי שכבת הקרקע ומידת חדירותה לזרימת מים.

התנזלות קרקע תחת ניקוז מיטבי מתרחשת אפילו תחת צפיפות אנרגיה סייסמית מאוד נמוכה ובכך מספקת הסבר לתצפיות מבלבלות של התנזלות במרחק גדול מאוד ממוקד רעידת האדמה. יחסי הגומלין בין כמות הדחיסה להספק הסייסמי בזמן רעידת אדמה יכולים גם להסביר מקרי התנזלות חוזרים ונשנים, המתרחשים למרות הציפייה שהתנזלות תהווה טיוב טבעי לקרקע כנגד התנזלות נוספת.

ההשלכות המעשיות של עבודה זו הן שאין להניח מראש עמידות להתנזלות של קרקעות מנוקזות היטב (למשל בשל חדירות גבוהה), אתרים שבהם לא מצופה תנודת קרקע גדולה מאוד, ואתרים שהתנזלו בעבר.

עבודה זו נעשתה בהדרכתם של

פרופ' עינת אהרונוב

פרופ' לירן גורן

פרופ' רנו טוסה

התנזלות קרקע ברעידת אדמה תחת ניקוז מיטבי

חיבור לשם קבלת תואר דוקטור בפילוסופיה

מאת

שחר בן זאב

הוגש לסנט האוניברסיטה העברית ולאוניברסיטת שטרסבורג

דצמבר 2022

התנזלות קרקע ברעידת אדמה תחת ניקוז מיטבי

חיבור לשם קבלת תואר דוקטור בפילוסופיה

מאת

שחר בן זאב

הוגש לסנט האוניברסיטה העברית ולאוניברסיטת שטרסבורג

דצמבר 2022

Liquéfaction du sol induite par tremblement de terre dans des conditions drainées

Résumé

La liquéfaction du sol induite par les tremblements de terre, une cause majeure de dommages aux infrastructures, est traditionnellement expliquée par un mécanisme « non drainé ». Ce travail remet en question ce point de vue en utilisant la théorie, les simulations et les expériences, en proposant un mécanisme « drainé » où l'écoulement des fluides dans le sol peut conduire à une augmentation de la pression interstitielle et à la liquéfaction, même en cas de faible énergie sismique. Ce mécanisme drainé permet d'expliquer des événements de liquéfaction non-expliqués au-delà du champ proche du tremblement de terre et de liquéfaction fréquente.

Mots clés: Liquéfaction des sols, tremblements de terre, milieux granulaires, dynamique des fluides

Résumé en anglais

Earthquake-induced soil liquefaction, a major cause of infrastructure damage, is traditionally explained by an "undrained" mechanism. This work challenges this view using theory, simulations, and experiments, proposing a "drained" mechanism where fluid flow within soil can lead to pore pressure increase and liquefaction, even under low seismic energy. This drained mechanism explains puzzling liquefaction events beyond the earthquake near-field and recurrent liquefaction.

Keywords: Soil liquefaction, earthquakes, granular media, fluid dynamics